EPFL

Thèse n° 8392

Light-active Metal-Organic Frameworks for Photocatalytic Hydrogen Evolution.

Présentée le 11 septembre 2020

à la Faculté des sciences de base
Laboratoire de simulation moléculaire
Programme doctoral en chimie et génie chimique

pour l'obtention du grade de Docteur ès Sciences

par

Stavroula KAMPOURI

Acceptée sur proposition du jury

Prof. A. Züttel, président du jury
Prof. B. Smit, Dr K. Stylianou, directeurs de thèse
Prof. H. García, rapporteur
Prof. A. Fateeva, rapporteuse
Prof. A. Hagfeldt, rapporteur

École polytechnique fédérale de Lausanne

2020

Acknowledgements

Carrying out my doctoral studies for the last four years in Switzerland has been a wonderful adventure. For that I need to thank all the people that made this experience so special with their support in all its different forms.

First, I would like to express my gratitude to my supervisors Prof. Berend Smit and Kyriakos Stylianou. Berend, I am grateful for all your support, guidance and inspiring advice. Working with you has been a very constructive experience and I learned a lot. Kyriakos, thank you for all your help, you were always available for discussions, with your knowledge and positive energy inspiring me and keeping my motivation always high. I would also like to thank my informal supervisor, Dr. Christopher Ireland for his support and guidance. Chris, thank you for your help and advice from the first day of my studies. I will always cherish our first scientific discussions.

I would also like to thank all my collaborators that significantly assisted me in successfully implementing my research projects. More specifically, I would like to thank Prof. Andreas Züttel, Prof. Kevin Sivula, Prof. László Forró, Dr. Christopher Ireland, Dr. Maria Fumanal, Mish Ebrahim, Bardiya Valizadeh, Dr. Tu Nguyen, Dr. Mariana Spodaryk, Dr. Emad Oveisi, Dr. Pascal Schouwink, Dr. Mounir Mensi, Dr. Natalia Gasilova, Dr. Gloria Capano, Daniele Ongari, Dr. Amber Mace, Dr. Andrzej Sienkiewicz and Dr. Robert Palgrave. Furthermore, I want to express my appreciation to Prof. Raffaella Buonsanti and Prof. Mohammad Nazeeruddin for accessing their groups' infrastructure. Moreover, I would like to thank Evelyne Ludi, Laurent Seydoux, Annabelle Coquoz, Cédric Passerini, Jean Perruchoud, Robin Délèze, Stéphane Voeffray and Anne Lene Odegaard, for administrative and IT support, as well as running the chemical store.

I would also like to express my gratitude to my special friends and colleagues that I shared with them not only the office and laboratory, but also beautiful moments outside work, Pelin, Sam, Arun, Andrzej, Bardiya, Chris, Tu, Peanut and Luna. During a Ph.D., there are always some more challenging times, with extra pressure and stress. However, having my amazing friend Mish on my side made those periods pass fast and me feeling even nostalgic about them. Thank you for all your support, for all our girl's nights and for being such a great friend!

Last but not least, I would like thank my family that has always been supporting me. More specifically, my parents Maria and Giorgos, my grand-parents Leftheris and Megali Alina, my aunts Vasso and Toula, my almost brother and sister, Giorgos and Katerina and my puppies Paris and Lila. Mom and dad, you offered me endless love and prepared me to overcome any challenges on my way. Grandpa thank you for always passionately believing in my abilities since I was a kid. Grandma thank you for

comparing me with Marie Curie whenever I felt tired, you always cheered me up regardless how stressed I was. Having Lila in my life was a huge asset for my studies, since she could make all my stress disappear just by looking at her. Most importantly, I want to express my gratitude to my soul-mates Errika and Noris. Noris, thank you for using your amazing skills to help me during my Ph.D, by proofreading and correcting my manuscripts, or by patiently listening to me practicing innumerable presentations. Errika, you have always been so supportive through every step and every obstacle I faced during my studies, you are my everything! I would never have made it if it weren't for both of you and I am extremely lucky having you in my life.

ABSTRACT

The general scope of this thesis lies in the application of MOFs in photocatalysis. MOFs demonstrate inherent properties – such as high porosity, tunable optoelectronic and catalytic properties, which render them promising candidates for photocatalysis. The main research activity relative to this thesis aims at the advancement of MOF-based photocatalytic systems in terms of activity, cost and sustainability. This was achieved by employing different strategies that can lead to the favorable modification of the three major photocatalytic steps of light absorption, charge separation-migration and catalysis, which govern the overall performance of a photocatalytic system.

More specifically, Chapter 2 describes the impact of different co-catalysts on the photocatalytic activity of a MOF-based system, based on the well-known MIL-125-NH_2. Variation of the co-catalysts can significantly influence the two major photocatalytic steps of charge separation and the catalytic reaction. All the metal oxide and phosphide co-catalysts investigated are found to significantly improve the activity of MIL-125-NH_2, with the system using Ni_2P nanoparticles (NPs) exhibiting a high H_2 evolution rate (1230 μmol h^{-1} g^{-1}) and an apparent quantum yield of 6.6% at 450 nm, which is comparable to the state of the art. Comparison of Ni_2P with Pt showed that the noble-metal-free Ni_2P/MIL-125-NH_2 system significantly outperforms Pt/MIL-125-NH_2. These results are attributed to the enhanced electronic interactions between MIL-125-NH_2 and Ni_2P, and prove that earth abundant co-catalysts can challenge the commonly used noble metals.

The low cost and high efficiency of Ni_2P/MIL-125-NH_2 prompted me to focus on another component used in photocatalytic systems, which is the electron donor. Chapter 3 shows that variation of the electron donors highly influences the activity of Ni_2P/MIL-125-NH_2, with triethylamine significantly boosting the H_2 evolution rate. However, the utilization of electron donors is another factor hindering the industrialization of such systems, since these substances can be toxic and expensive. Inspired by this challenge, we then replaced the electron donor with rhodamine B (RhB) – a simulant organic pollutant – envisioning dual-functional photocatalysis for simultaneous H_2 generation and organic pollutant degradation. This research project revealed the first example of a MOF-based dual-functional photocatalytic system able to generate H_2 in a high rate and degrade RhB under visible-light.

Chapter 4 describes a strategy for enhancing the photocatalytic performance of MOF-based systems by favourably altering the photocatalytic steps of light harvesting and charge separation. This was achieved by developing MOF/MOF heterojunctions. The combination of MIL-125-NH_2 with MIL-167 – a Ti-based MOF with complementary light absorption properties – leads to the formation of a type II heterojunction MIL-167/MIL-125-NH_2, with enhanced optoelectronic properties. MIL-

167/MIL-125-NH_2 significantly outperforms its single components MIL-167 and MIL-125-NH_2, in terms of photocatalytic H_2 production. This strategy contributes to the discovery of novel MOF-based photocatalytic systems that can harvest the solar energy and exhibit high catalytic activities in the absence of co-catalysts.

Finally, Chapter 5 shows an alternative role of MOFs in the photocatalysis field, which lies in their utilization as precursors for the synthesis of highly active metal-oxide semiconductor photocatalysts. MIL-125-NH_2 was calcined to form pure and mixed anatase-rutile phase TiO_2 NPs. The MIL-125-NH_2-derived TiO_2 with anatase to rutile ratio of approximately 3/1 exhibits higher photocatalytic H_2 evolution rates than the commercial P25 Degussa, TiO_2 synthesized from precipitated titanium hydroxide and MIL-167-derived TiO_2. This is attributed to the templated morphology of MIL-125-NH_2-derived TiO_2, which forces the anatase and rutile NPs into effective contact with each other, leading to an efficient electron-hole separation.

Keywords

Photocatalysis, Metal-Organic Frameworks, Water Reduction, Dual-Functional Photocatalysis, Organic Pollutants Photo-oxidation, Heterojunctions, MOF-Mediated Synthesis

RESUME

La portée générale de cette thèse réside dans l'utilisation des MOFs pour des applications photocatalytiques. Les MOFs présentent des propriétés inhérentes – telles qu'une porosité élevée, des propriétés optoélectroniques et catalytiques accordables – qui en font des candidats prometteurs pour la photocatalyse. La principale activité de recherche relative à cette thèse vise à faire progresser les systèmes photocatalytiques basés sur MOFs en termes d'activité, de coût et de durabilité. Cela a été réalisé en employant différentes stratégies qui peuvent conduire à l'amélioration des trois principales étapes photocatalytiques qui régissent les performances globales d'un système photocatalytique : l'absorption de la lumière, la séparation-migration de charge et la catalyse.

Plus précisément, le Chapitre 2 décrit l'impact de différents co-catalyseurs sur l'activité photocatalytique d'un système basé sur le MOF bien connu MIL-125-NH_2. La variation des co-catalyseurs peut influencer de manière significative les deux principales étapes photocatalytiques de séparation des charges et la réaction catalytique. Tous les co-catalyseurs d'oxyde et de phosphure métalliques étudiés améliorent considérablement l'activité du MIL-125-NH_2, le système utilisant des nanoparticules de Ni_2P (NPs) présentant un taux d'évolution élevé de H_2 (1230 μmol h^{-1} g^{-1}) et un rendement quantique apparent de 6,6% à 450 nm, ce qui est comparable à l'état de l'art. La comparaison du Ni_2P avec le Pt a montré que le système Ni_2P/MIL-125-NH_2 sans métal noble surpasse de manière significative le système Pt/MIL-125-NH_2. Ces résultats sont attribués aux interactions électroniques améliorées entre le MIL-125-NH_2 et le Ni_2P, et démontrent que les co-catalyseurs à base de matériaux abondants peuvent remplacer les métaux nobles couramment utilisés.

Le faible coût et la haute efficacité du système Ni_2P/MIL-125-NH_2 m'ont incité à me concentrer sur un autre composant utilisé dans les systèmes photocatalytiques, qui est le donneur d'électrons. Le Chapitre 3 montre que la variation des donneurs d'électrons influence fortement l'activité du Ni_2P/MIL-125-NH_2, la triéthylamine augmentant considérablement le taux d'évolution de H_2. Cependant, l'utilisation de donneurs d'électrons est un autre facteur entravant l'industrialisation de tels systèmes, car ces substances peuvent être toxiques et coûteuses. Inspirés par ce défi, nous avons ensuite remplacé le donneur d'électrons par de la rhodamine B (RhB) - un polluant organique simulant - envisageant une photocatalyse à double fonction pour la génération simultanée de H_2 et la dégradation des polluants organiques. Ce projet de recherche a révélé le premier exemple d'un système photocatalytique à double fonction basé sur un MOF capable de générer du H_2 à un taux élevé et de dégrader le RhB sous la lumière visible.

Le Chapitre 4 décrit une stratégie pour améliorer les performances photocatalytiques des systèmes à base de MOF en modifiant favorablement les étapes photocatalytiques de l'absorption de lumière et de la séparation des charges. Ceci a été réalisé en développant des hétérojonctions MOF/MOF. La combinaison de MIL-125-NH_2 avec le MIL-167 – un MOF à base de Ti avec des propriétés d'absorption de lumière complémentaires – conduit à la formation d'une hétérojonction de type II MIL-167/MIL-125-NH_2, avec des propriétés optoélectroniques améliorées. MIL-167/MIL-125-NH_2 surpasse considérablement ses composants simples MIL-167 et MIL-125-NH_2, en termes de production de photocatalytique H_2. Cette stratégie contribue à la découverte de nouveaux systèmes photocatalytiques à base de MOF qui peuvent récolter l'énergie solaire et présenter des activités catalytiques élevées en l'absence de cocatalyseurs.

Enfin, le Chapitre 5 montre un rôle alternatif des MOF dans le domaine de la photocatalyse, qui réside dans leur utilisation comme précurseurs pour la synthèse de photocatalyseurs semi-conducteurs à oxyde métallique très actifs. Le MIL-125-NH_2 a été calciné pour former des NPs TiO_2 en phase anatase-rutile purs et mélangés. Le TiO_2 dérivé de MIL-125-NH_2 avec un rapport anatase/rutile d'environ 3/1 présente des taux d'évolution photocatalytique de H_2 plus élevés que le matériel commercial Degussa P25, un TiO_2 synthétisé à partir d'hydroxyde de titane précipité et TiO_2 dérivé de MIL-167. Cela est attribué à la morphologie basée sur des modèles de TiO_2 dérivé de MIL-125-NH_2, qui force les NPs anatase et rutile à entrer en contact efficace les uns avec les autres, conduisant à une séparation efficace électron-trou.

Mots-clés

Photocatalyse, Structure Métal-Organique, Réduction de l'Eau, Photocatalyse Bifonctionnelle, Photo-oxydation des Polluants Organiques, Hétérojonctions, Synthèse Médiée par le MOF

TABLE OF CONTENTS

ACKNOWLEDGEMENTS ..... **I**

ABSTRACT ..... **III**

KEYWORDS IV

RESUME ..... **V**

MOTS-CLES VI

LIST OF FIGURES ..... **IX**

LIST OF ABBREVIATIONS AND SYMBOLS ..... **XIV**

CHAPTER 1 INTRODUCTION **1**

1.1 INTRODUCTION TO PHOTOCATALYSIS 2
1.2 FUNDAMENTAL PRINCIPLES OF PHOTOCATALYSIS 3
1.2.1 First Major Photocatalytic Step: Light harvesting *4*
1.2.2 Second Major Photocatalytic Step: Charge Separation and Migration *5*
1.2.3 Third Major Photocatalytic Step: Catalytic Redox Reaction *6*
1.3 PHOTOCATALYTIC HYDROGEN EVOLUTION 7
1.4 PHOTOCATALYTIC OXIDATION OF ORGANIC COMPOUNDS 10
1.5 DUAL-FUNCTIONAL PHOTOCATALYSIS 12
1.6 METAL-ORGANIC FRAMEWORKS FOR PHOTOCATALYSIS 14
1.6.1 MOFs stability under water splitting conditions *15*
1.6.2 MOFs' Optical Response *16*
1.6.3 MOF-based Photocatalytic Systems for Water reduction *16*
1.7 OBJECTIVES OF THIS THESIS 20

CHAPTER 2 VARIATION OF ABUNDANT CO-CATALYSTS IN A METAL-ORGANIC FRAMEWORK PHOTOCATALYTIC SYSTEM **21**

2.1 INTRODUCTION 22
2.2 SYNTHESIS AND CHARACTERIZATION 23
2.3 PHOTOCATALYTIC ACTIVITY 26
2.4 MECHANISM 28
2.5 COMPARISON OF Ni_2P TO PT 29
2.6 SUMMARY AND CONCLUSIONS 31

CHAPTER 3 VARIATION OF ELECTRON-DONORS AND DUAL-FUNCTIONAL PHOTOCATALYSIS **32**

3.1 INTRODUCTION 33
3.2 VARIATION OF ELECTRON-DONORS 34
3.3 DUAL-FUNCTIONAL PHOTOCATALYTIC ACTIVITY 35
3.4 SUMMARY AND CONCLUSIONS 38

CHAPTER 4 DESIGN OF MOF/MOF HETEROJUNCTIONS **40**

4.1 INTRODUCTION 41
4.2 SYNTHESIS AND CHARACTERIZATION 42
4.3 PHOTOCATALYTIC ACTIVITY 43
4.4 MECHANISM 44
4.5 HETEROJUNCTION WITH UIO-66-NH_2 AND MIL-125-NH_2 48
4.6 SUMMARY AND CONCLUSIONS 49

CHAPTER 5 MOF-DERIVED TITANIUM DIOXIDE FOR PHOTOCATALYSIS; THE IMPACT OF THE TEMPLATED MORPHOLOGY **51**

5.1 INTRODUCTION 52
5.2 SYNTHESIS AND CHARACTERIZATION 54
5.3 PHOTOCATALYTIC ACTIVITY 60

5.4 COMPARISON OF MIL-125-NH_2-DERIVED TiO_2 TO OTHER TiO_2 SAMPLES 62
5.5 SUMMARY AND CONCLUSIONS 65

CHAPTER 6 CONCLUSIONS AND OUTLOOK **66**

APPENDIX **67**

REFERENCES **107**

CURRICULUM VITAE **119**

List of Figures

Chapter 1 Introduction

Figure 1.1: *Images illustrating current environmental problems: growing air and water pollution, aridity, climate change, wildfires. Credits to Markus Spiske, Chris LeBoutillier and Leonid Danilov from Pexels.* *2*
Figure 1.2: *Major photocatalytic fields.* *3*
Figure 1.3*: (A) Band gap diagram of conductors, semiconductors and insulators. (B) Schematic illustration of major photocatalytic steps. Step 1: Light absorption, Step 2: Generation of electron-hole pairs and their migration to the surface of the photocatalyst and Step 3: Surface redox reactions.* *4*
Figure 1.4: *Soral irradiance spectra (G-173). Blue, gray and black lines represent the extraterrestrial, the global total on 37° sun-facing tilted surface and the direct normal spectral irradiance, respectively. The ultraviolet (UV), visible (Vis) and infrared (IR) regions are highlighted. Data taken from the American Society for Testing and Materials (ASTM).*[15] *5*
Figure 1.5: *Spatial separation of the photogenerated charge carriers within a type II heterojunction with a staggered gap.* *6*
Figure 1.6: *Calculated free energy diagram for H_2 evolution at a potential U = 0 relative to the standard H_2 electrode at pH = 0. Reprinted with permission from Ref 20. Copyright 2005 American Chemical Society.* *7*
Figure 1.7: *Energy diagrams of photocatalytic water splitting relative to NHE, at pH = 0, with the H_2 evolution and O_2 evolution reactions redox potentials.* *8*
Figure 1.8: *Schematic illustration of the possible constituents of a photocatalytic H_2 evolution system.* *9*
Figure 1.9: *Schematic representation of the photoexcitation of a photocatalyst in the presence of organic pollutants. The mechanism for the generation of anion superoxide and hydroxyl radicals, as well as that for the direct organic pollutant's oxidation is also illustrated.* *11*
Figure 1.10: *Schematic representation of the mechanism for dual-functional photocatalysis for H_2 generation coupled with oxidation of organic pollutants to either achieve full degradation of hazardous organic contaminants or to synthesize useful organic molecules.* *13*
Figure 1.11: *Schematic representation of MOFs' constituents.* *14*
Figure 1.12: *Schematic illustration of the proposed mechanism for photocatalytic H_2 and O_2 evolution over Cd-TBAPy. Reprinted with permission from Ref. 81 Copyright © 2018 John Wiley and Sons.* *17*
Figure 1.13: *Schematic representation of proposed mechanism for photocatalytic H_2 generation over Rhodamine B (RhB) sensitized Pt/UiO-66 under visible-light. Reproduced from Ref. 84 with permission from The Royal Society of Chemistry.* *18*
Figure 1.14: *Schematic representation of the synthesis procedure of UiO-66-NH_2 with encapsulated Pt NPs (Pt@UiO-66-NH_2) and of Pt NPs deposited on the exterior surface of the MOF (Pt/UiO-66-NH_2), with the mechanism for photocatalytic H_2 production over Pt@UiO-66-NH_2 being highlighted. Reprinted with permission from Ref. 85a Copyright © 2016 John Wiley and Sons.* *19*

Chapter 2 Variation of Abundant Co-catalysts in a Metal-Organic Framework Photocatalytic System

Figure 2.1: (*A) PXRD patterns, (B) N_2 adsorption-desorption isotherm and (C) SEM image of the as-synthesized MIL-125-NH_2. (D) UV-Vis absorbance of free ligand H_2BDC-NH_2 and Kubelka-Munk representation of diffuse reflectance of MIL-125-NH_2.* *23*
Figure 2.2: *Schematic illustration of the synthetic procedure employed for the generation of transition metal oxide and phosphide NPs.* *24*
Figure 2.3: *PXRD patterns of MOF-derived NiO, Fe_2O_3, Co_3O_4, CoP, Ni_2P and CuO NPs.* *25*
Figure 2.4: *High-resolution TEM images of: (A) NiO, (B) Fe_2O_3, (C) Co_3O_4, (D) CoP, (E) Ni_2P and (F) CuO NPs.* *25*
Figure 2.5: *Comparison of H_2 evolution rates (with respect to MIL-125-NH_2) of 9.2 wt.% Ni_2P/MIL-125-NH_2, 8.6 wt.% NiO/MIL-125-NH_2, 7.9 wt.% Co_3O_4/MIL-125-NH_2, 8.8 wt.% CoP/MIL-125-NH_2, 10.2 wt.% Fe_2O_3/MIL-125-NH_2 and 7.9 wt.% CuO/MIL-125-NH_2 under visible light irradiation for 8 hours.* *27*
Figure 2.6: *Recycling photocatalytic performance of (A) Ni_2P/MIL-125-NH_2 and (B) NiO/MIL-125-NH_2 for 3 consecutive cycles.* *27*
Figure 2.7: *PL spectra of the suspensions of MIL-125-NH_2 with different amounts of: (A) Ni_2P, (B) CoP, (C) Co_3O_4, (D) Fe_2O_3, (E) CuO and (F) NiO. The excitation wavelength was 420 nm.* *28*
Figure 2.8: *Comparison of the photocatalytic activity of MIL-125-NH_2 with optimized amounts of Ni_2P (green) and Pt (gray) NPs as co-catalysts.* *30*

Figure 2.9: *(A) Comparison of the PL spectra of MIL-125-NH_2 with and without various amounts of Pt NPs (solid lines) and the corresponding amounts of Ni_2P NPs (dotted lines). Excitation at 420 nm. (B) Photocurrent responses of MIL-125-NH_2 with the optimized amounts of Ni_2P (9.2 wt.%, green) and Pt (2.05 wt.%, black).* *30*

Chapter 3 Variation of Electron-Donors and Dual-Functional Photocatalysis

Figure 3.1: *(A) Comparison of H_2 evolution rates of Ni_2P/MIL-125-NH_2 with different electron donors, under visible light irradiation for 8 h, (B) PXRD patterns of 9.2 wt.% Ni_2P/MIL-125-NH_2 after the photocatalytic test with different electron donors.* *34*

Figure 3.2: *(A) Photocatalytic H_2 evolution rates of Ni_2P/MIL-125-NH_2 in 17 mL of photocatalytic solutions with different concentration of RhB under visible light irradiation for 8 h. Inset: photograph showing the difference in the color of the photocatalytic solution before and after the photocatalytic test, with initial RhB concentration of 1.2 ppm. (B) UV-Vis spectra of reference samples and supernatants after the photocatalytic RhB decolorization process.* *36*

Figure 3.3: *Control experiments: (A) UV-vis spectra of 1.2 ppm RhB solution (reference), the supernatant of the same solution combined with Ni_2P/MIL-125-NH_2 after 24 h in the dark and after the photocatalytic test. (B) UV-Vis spectra of 1.2 ppm RhB solution (reference) and same solution after 3 h irradiation with visible light.* *37*

Figure 3.4: *The impact of the incorporation of TEOA as hole scavenger and tert-butanol as •OH radical scavenger on the RhB degradation rate after 3 h photocatalytic test.* *38*

Chapter 4 Construction of MOF/MOF Heterojunctions

Figure 4.1: *Schematic representation of three different types of heterojunctions: (A) type I, with straddling gap (B) type II with staggered gap and (C) type III with broken gap.* *41*

***Figure 4.2**: Schematic representation of the synthetic protocol of the MIL-167/MIL-125-NH_2 heterojunction. MIL-125-NH_2 is synthesized in the presence of MIL-167 crystals.* *43*

Figure 4.3: *SEM images of (A) MIL-167, (B) MIL-125-NH_2, (C) and (D) MIL-167/MIL-125-NH_2, with different magnification.* *43*

Figure 4.4: *Photocatalytic performance of MIL-125-NH_2 (yellow), MIL-167 (red), 3 wt.% (light orange), 8 wt.% (orange), and 13 wt.% (dark orange) MIL-167/MIL-125-NH_2. The heterojunctions are represented with solid fill, while the corresponding physical mixtures with patterned fill.* *44*

Figure 4.5: *(A) UV-vis absorption spectra and (B) PL emission of MIL-125-NH_2 (yellow), MIL-167 (red), MIL-167/MIL-125-NH_2 heterojunctions (solid lines, mustard: 3 wt.%, orange: 8 wt.% and dark orange 13 wt.%) and corresponding physical mixtures (dotted lines, mustard: 3 wt.%, orange: 8 wt.% and dark orange: 13 wt.%). The excitation wavelength was 420 nm.* *45*

Figure 4.6: *SEM images comparing the morphology of (A) the 8 wt.% MIL-167/MIL-125-NH_2 heterojunction sample with that of (B) its analogous physical mixture of MIL-167 and MIL-125-NH_2.* *46*

Figure 4.7: *(A) Computed electronic band alignment relative to the vacuum level of MIL-167 and MIL-125-NH_2. (B) Schematic representation of a type II heterojunction with MIL-167 and MIL-125-NH_2.* *46*

Figure 4.8: *(A) Computed electronic band alignment relative to the vacuum level of UIO-66-NH_2 and MIL-125-NH_2. (B) UV-vis absorption spectra of MIL-125-NH_2 (yellow), UIO-66-NH_2 (black) and UIO-66-NH_2/MIL-125-NH_2 materials (dark-light gray).* *48*

Figure 4.9: *(A) Photocatalytic performance and (B) PL spectra of MIL-125-NH_2 (yellow), UIO-66-NH_2 (black) and UIO-66-NH_2/MIL-125-NH_2 heterojunctions (dark-light gray).* *49*

Chapter 5 Construction of MOF-derived TiO_2 Photocatalyst; The Impact of the templated Morphology

Figure 5.1: *(A) TGA curve of MIL-125-NH_2 obtained under airflow with a heating rate of 5 °C min^{-1}. (B) PXRD patterns of the as-synthesized MIL-125-NH_2-derived TiO_2.* *54*

Figure 5.2: *(A) Variable temperature PXRD patterns of MIL-125-NH_2 heated up to 810 °C and (B) Full Width Half Maximum (FWHM) values of the TiO_2 anatase and rutile peaks derived from the variable temperature PXRD patterns of MIL-125-NH_2.* *55*

Figure 5.3: *(A) TGA curve of precipitated TiH_4O_4 obtained under airflow with a heating rate of 5 °C min^{-1}. (B) PXRD patterns of TiH_4O_4-derived TiO_2. (C) Variable temperature PXRD patterns of TiH_4O_4 heated up to 810 °C. (D) FWHM values of the TiO_2 anatase and rutile peaks derived from the variable temperature PXRD patterns of amorphous titanium hydroxide (TiH_4O_4).* *57*

Figure 5.4: *Kubelka-Munk representation of the UV-Vis diffuse Rrflectance of (A) MIL-125-NH_2-derived and (B) TiH_4O_4-derived TiO_2.* *58*
Figure 5.5: *SEM images of (A) MIL-125-NH_2 and MIL-125-NH_2-derived TiO_2 samples synthesized at (B) 400 °C, (C) 500 °C, (D) 600 °C and (E) 700 °C for 1 h. The images are of the same magnification except that of MIL-125-NH_2, which is of 5 times less magnification in order to display the morphology of the larger MOF crystals.* *59*
Figure 5.6: *(A) and (B) Bright-field TEM images, and (C) selected area electron diffraction pattern of MIL-125-NH_2-derived TiO_2 synthesized through calcination at 600°C for 1 h. Simulated electron diffraction patterns of anatase and rutile phases (ring sampling diffraction planes) are shown at the down part of image (C).* *59*
Figure 5.7: *(A) SEM, (B) bright-field TEM and (C) dark-field TEM images of the TiH_4O_4-derived TiO_2 sample synthesized at 500 °C.* *60*
Figure 5.8: *Comparison of H_2 evolution rates of (A) MIL-125-NH_2-derived TiO_2 samples synthesized at different temperatures and B) TiH_4O_4-derived TiO_2 samples synthesized at 600°C (anatase), 700°C (anatase-rutile) and 800°C (anatase-rutile).* *61*
Figure 5.9: *(A) Recycling photocatalytic experiments and (B) SEM image of MIL-125-NH_2-derived TiO_2 (with optimum TiO_2 anatase to rutile ratio of 66:34) after recycling experiments.* *61*
Figure 5.10: *(A) PXRD patterns of the MIL-167- and MIL-125-NH_2- derived TiO_2, synthesized through calcination at 600°C. SEM images of MIL-167-derived TiO_2 at (B) smaller and (C) larger magnification.* *62*
Figure 5.11: *(A) TEM image and (B) selected area electron diffraction pattern of MIL-167-derived TiO_2.* *62*
Figure 5.12: *(A) Comparison of photocatalytic activity and (B) SEM images of the MIL-125-NH_2- derived, MIL-167-derived, TiH_4O_4-derived TiO_2 and P25 Degussa. Inset: Photograph of the light-blue-colored P25 Degussa (left) and the MIL-125-NH_2-derived TiO_2 (right), after the photocatalytic test.* *64*
Figure 5.13: *(A) N_2 sorption isotherms for the best performing MIL-125-NH_2-derived, TiH_4O_4-derived, MIL-167-derived and P25 Degussa TiO_2 and corresponding BET surface areas. (B) Kubelka-Munk representation of UV-Vis diffuse reflectance of MIL-167-derived, MIL-125-NH_2-derived, TiH_4O_4-derived TiO_2 and P25 Degussa. Inset: band gap values for each of the materials, extrapolated from the linear section of the Tauc plot for an indirect bandgap.* *64*

Appendix

Figure S.1: *Schematic illustration of the photocatalytic set-up used.* *70*
Figure S.2: *Photocatalytic H_2 evolution rates of MIL-125-NH_2 (17.0 mg) against different adding amounts of (a) NiO, (b) Co_3O_4, (c) CoP, (d) Fe_2O_3 and (e) CuO NPs under visible light irradiation for 8 h.* *72*
Figure S.3: *PXRD patterns of the as-synthesized MIL-125-NH_2 and the different co-catalysts, and the co-catalyst/MIL-125-NH_2 systems after the photocatalytic test.* *75*
Figure S.4: *XPS data on the CuO/MIL-125-NH_2 (left) and CoP/MIL-125-NH_2 system (right) after photocatalysis, confirming that the co-catalysts are stable.* *75*
Figure S.5: *(a) SEM images after photocatalytic test and corresponding EDX elemental analysis for (a) Ni_2P/MIL-125-NH_2 (b) NiO/MIL-125-NH_2, (c) CoP/MIL-125-NH_2, (d) Co_3O_4/MIL-125-NH_2, (e) Fe_2O_3/MIL-125-NH_2 and (f) CuO/MIL-125-NH_2. Scale bar: 1 μm.* *76*
Figure S.6: *N_2 adsorption-desorption isotherms of Ni_2P/MIL-125-NH_2 (green) (a) before (with a calculated BET surface area of 1175 m^2 g^{-1}) and (b) after the photocatalytic experiments (with a calculated BET surface area of 1176 m^2 g^{-1}). N_2 adsorption-desorption isotherms of NiO/MIL-125-NH_2 (orange), (c) before (with a calculated BET surface area of 1288 m^2 g^{-1}) and (d) after the photocatalytic experiments (with a calculated BET surface area of 1233 m^2 g^{-1}).* *77*
Figure S.7: *FTIR spectra of Ni_2P/MIL-125-NH_2 before (red) and after (blue) photocatalytic test.* *78*
Figure S.8: *PXRD patterns of (a) Ni_2P/MIL-125-NH_2 and (b) NiO/MIL-125-NH_2.* *78*
Figure S.9: *PL spectra of the MIL-125-NH_2 and the suspensions of MIL-125-NH_2 with the optimized amounts of: NiO (orange), CuO (blue), Fe_2O_3 (red), Co_3O_4 (violet) CoP (navy blue) and Ni_2P (green, optimized for photocatalytic hydrogen evolution). The co-catalyst-induced quenching of the PL follows the descending order of $Ni_2P > CoP \approx Co_3O_4 > Fe_2O_3 > CuO > NiO$. The excitation wavelength was 420 nm.* *79*
Figure S.10: *(a) Time Resolved PL decay curves and (b) lifetime of MIL-125-NH_2 and MIL-125-NH_2 with different co-catalysts. The excitation wavelength was 420 nm. Since the lifetimes of the co-catalyst/MIL-125-NH_2 systems were not highly different from each other, drawing further conclusions based on these results might be inconclusive.* *79*
Figure S.11: *Cathodic polarization curves of the electrodes with Ni_2P and NiO NPs obtained by linear scan voltammetry.* *80*
Figure S.12: *(a) PXRD patterns of the simulated (blue) and as-synthesized (red) Pt NPs. (b) N_2 adsorption-desorption isotherm of Ni_2P NPs.* *81*

Figure S.13: *(a) TEM image and (b) electron diffraction pattern of Pt NPs. The size of Pt NPs is estimated to be around 20-30 nm.* *81*
Figure S.14: *H_2 evolution rate of 17.0 mg MIL-125-NH_2 against different adding amounts of Pt NPs.* *82*
Figure S.15: *PXRD patterns of MIL-125-NH_2 simulated (dark gray), Pt NPs as-synthesized (light gray) and 2 (± 0.4) wt.% Pt/MIL-125-NH_2 after photocatalytic test.* *82*
Figure S.16: *(a) SEM image of 2 (± 0.4) wt.% Pt/MIL-125-NH_2 after photocatalytic testing, and corresponding EDX maps of (b) Titanium, (c) Pt and (d) both Ti and Pt.* *83*
Figure S.17: *Cyclic voltammograms of (a) blank electrolyte (0.1 M TBAP in acetonitrile) at 20 mV s^{-1}, (b) TEA, (c) TEOA, (d) EtOH, (e) MeOH and (f) L-ascorbic acid in the same solution.* *87*
Figure S.18: *(a) Photocatalytic H_2 production of Ni_2P/MIL-125-NH_2 in aqueous acetonitrile solution with variant concentrations of Rhodamine B (RhB), (b) PXRD patterns of the as-synthesized MIL-125-NH_2 and Ni_2P, and the Ni_2P/MIL-125-NH_2 after the photocatalytic test in 17 mL solution with 0.02 mg of RhB (1.2 ppm).* *88*
Figure S.19: *(a) Trapping experiments of active species: UV-Vis spectra of 1.2 ppm RhB solution (blank) and supernatants after photocatalytic test of the same solution with 0.01 M TEOA (e^- scavenger), 0.01 M tert-butanol (•OH radical scavenger) and no scavenger, and (b) corresponding PXRD patterns. The duration of the photocatalytic tests was 3 h.* *88*
Figure S.20: *Control experiment: H_2 evolution of Ni_2P/MIL-125-NH_2 in an aqueous acetonitrile solution, without any RhB or other electron donors, after 3 h visible light irradiation (solid red line). This result was compared with the photocatalytic performance of Ni_2P/MIL-125-NH_2 in aqueous acetonitrile solution with variant concentration of RhB (dashed lines).* . *89*
Figure S.21: *Calibration curve of RhB in acetonitrile solution with water (5 v/v% H_2O). Absorbance peak at 543 nm...* *89*
Figure S.22: *TGA curve of a) MIL-125-NH_2 and b) MIL-167 obtained under airflow with a heating rate of 5 °C min^{-1}.* *90*
Figure S.23: *PXRD patterns of a) the as-synthesized (light colors) and simulated (dark colors) MIL-125-NH_2 (yellow) and MIL-167 (red), b) MIL-125-NH_2 synthesized in the presence of increasing amounts of MIL-167 (5 - 100 mg, increasing toward the top of the figure) and c) MIL-125-NH_2 synthesized in the presence of 20, 40 and 60 mg of MIL-167.* *91*
Figure S.24: *SEM image of MIL-167/MIL-125-NH_2 heterojunction sample. In this case, prior to microscopy the samples were added in a MeOH solution, sonicated and then drop-casted on the SEM holder, which was allowed to dry.* *91*
Figure S. 25: *SEM images of a), b): 3 wt.% MIL-167/MIL-125-NH_2, c), d): 8 wt.% MIL-167/MIL-125-NH_2 and d), e) 13 wt.% MIL-167/MIL-125-NH_2, with different magnification. The samples were prepared by spreading a small amount of the MIL-167/MIL-125-NH_2 dry powder on a carbon type SEM holder and then blowing the it with N_2 to remove excess material.* *92*
Figure S.26: *a) PXRD patterns of 8 wt.% MIL-167/MIL-125-NH_2 before and after photocatalysis, and b) N_2 sorption isotherms of the as-synthesized MIL-125-NH_2 and MIL-167, and 8 wt.% MIL-167/MIL-125-NH_2 after photocatalysis. The BET (Brunauer-Emmett-Teller) surface area of the 8 wt.% MIL-167/MIL-125-NH_2 is smaller than that of the as-synthesized MIL-125-NH_2 (1230 versus 1560 m^2 g^{-1}), which is associated with the presence of the non-porous MIL-167, contributing to the overall mass of the sample.* *93*
Figure S.27: *Photocatalytic recycling experiments of MIL-167/MIL-125-NH_2 for three consecutive cycles of 12 h each. MIL-167/MIL-125-NH_2 consistently produces hydrogen for more than 36 h.* *93*
Figure S.28: *PXRD patterns of a) the as-synthesized (light colors) and simulated (dark colors) MIL-125-NH_2 (yellow) and UIO-66-NH_2 (gray), and b) MIL-125-NH_2 synthesized in the presence of 10, 20, 40 and 60 mg of UIO-66-NH_2.* *98*
Figure S.29: *a) SEM image of UIO-66-NH_2 and b) 58 wt.% UIO-66-NH_2/MIL-125-NH_2.* *99*
Figure S.30: *PXRD patterns of UIO-66-NH_2, 16 wt.%, 28 wt.% and 46 wt.% UIO-66-NH_2/MIL-125-NH_2 after photocatalysis.* *99*
Figure S.31: *XPS showing the Ti 2p binding energy of a) the best performing MIL-125-NH_2-derived TiO_2 sample (synthesized at 600 °C) and b) the best performing TiH_4O_4 sample (synthesized at 700 °C). Included is the fitting for the TiO_2 anatase and rutile phase, determined using 2 Voigt functions; insert is the relative area of the fits related to each line.* *101*
Figure S.32: *a) Bright-field and b) dark-field TEM images of MIL-125-NH_2-derived TiO_2 synthesized through calcination at 400°C for 1 h. c) Selected Area Electron Diffraction (SAED) pattern. Dark-field TEM image was acquired from the reflections shown by a circle on the SAED pattern.* *102*
Figure S.33: *a) Bright-field and b), c), d) dark-field TEM images of MIL-125-NH_2-derived TiO_2 synthesized through calcination at 600°C for 1 h. e) SAED pattern. For the acquisition of the dark-field images, the incident electrons beam is tilted so that only reflections of specific diffracting crystallographic planes contribute to image formation. Depending on the angle of diffraction, specific nano-sized particles are illuminated, manifesting the multi-particle nature of the template. Dark-field TEM images correspond to the diffracting planes shown by a green circle in the SAED pattern.* *102*
Figure S.34: *SEM image of the TiH_4O_4-derived TiO_2 samples synthesized at a) 500 °C, b) 600 °C and c) 700 °C for 1 h. The images are of the same magnification.* *102*

Figure S.35: *a) Bright-field TEM image and b) SAED pattern of TiH_4O_4-derived TiO_2 synthesized through calcination at 500°C for 1 h.* *103*
Figure S.36: *PXRD pattern of MIL-125-NH_2- derived TiO_2 (with optimum TiO_2 anatase to rutile ratio of 66:34) before and after recycling experiments.* *103*
Figure S.37: *TGA curve of MIL-167 obtained under airflow with a heating rate of 5 °C min^{-1}.* *104*
Figure S.38: *Dependence of the H_2 evolution on the concentration of photocatalyst in solution, for the best-performing MIL-125-NH_2-derived and P25 Degussa TiO_2.* *105*
Figure S.39: *PL spectra of the MIL-167-derived, TiH_4O_4-derived, MIL-125-NH_2-derived TiO_2 and P25 Degussa. The excitation wavelength was at 340 nm.* *105*

List of Abbreviations and Symbols

º	Degree
Å	Ångström
•OH	Hydroxyl radical
ºC	Degree Celsius
BDC	Terephthalic acid
CB	Conduction Band
CH_3CN	Acetonitrile
CO_2	Carbon dioxide
COF	Covalent-organic frameworks
DMF	Dimethylformamide
e.g.	Exempla gratia
e^-	Electron
EDX	Energy Dispersive X-ray Spectroscopy
EPR	Electron paramagnetic resonance
EtOH	Ethanol
eV	Electronvolt
g	Gram
h	Hour
h^+	Hole
H^+	Proton
H_2	Hydrogen
HOCOs	Highest occupied crystalline orbitals
HOMO	Highest occupied molecular orbital
i.e.	Id est
LUCOs	Lowest unoccupied crystalline orbitals
LUMO	Lowest unoccupied molecular orbital
M	Molar (mol L^{-1})
MeOH	Methanol
mg	Milligram
MIL	Material from Institute Lavoisier
min	Minutes
mL	Millilitre

MOF	Metal-organic framework
MW	Molecular weight
N_2	Nitrogen
NHE	Normal Hydrogen Electrode
NPs	Nanoparticles
NH_2-BDC	2-Aminorephthalic acid
$(NH_2)_2$-BDC	2,5-Diaminoterephthalic acid
nm	Nanometer
O_2	Oxygen
$O_2^{\bullet-}$	Superoxide radicals
OH-BDC	2-Hydroxyterephthalic acid
$(OH)_2$-BDC	2,5-Dihydroxyterephthalic acid
PL	Photoluminescence
ppm	Parts per million
PXRD	Powder X-ray Diffraction
ref.	Reference
RhB	Rhodamine B
SEM	Scanning Electron Microscopy
t	Time
T	Temperature
TEA	Triethylamine
TEM	Transmission Electron Microscopy
TEOA	Triethanolamine
TGA	Thermogravimetric Analysis
TPL	Transient photoluminescence
UIO	University of Oslo
UV	Ultraviolet
VB	Valence band
Vs	Versus
ΔG	Gibbs free energy
λ	Wavelength
μmol	Micromole

Note: additional abbreviations for specific compounds are defined within the thesis.

Chapter 1 Introduction

Parts of this chapter are based on published work:

'*Dual-Functional Photocatalysis for Simultaneous Hydrogen Production and Oxidation of Organic Substances*'

S. Kampouri, K. C. Stylianou, ACS Catal. 2019, 5, 4247 - 4270

Reprinted in an adapted version with permission of Ref. 1, Copyright © 2019, American Chemical Society

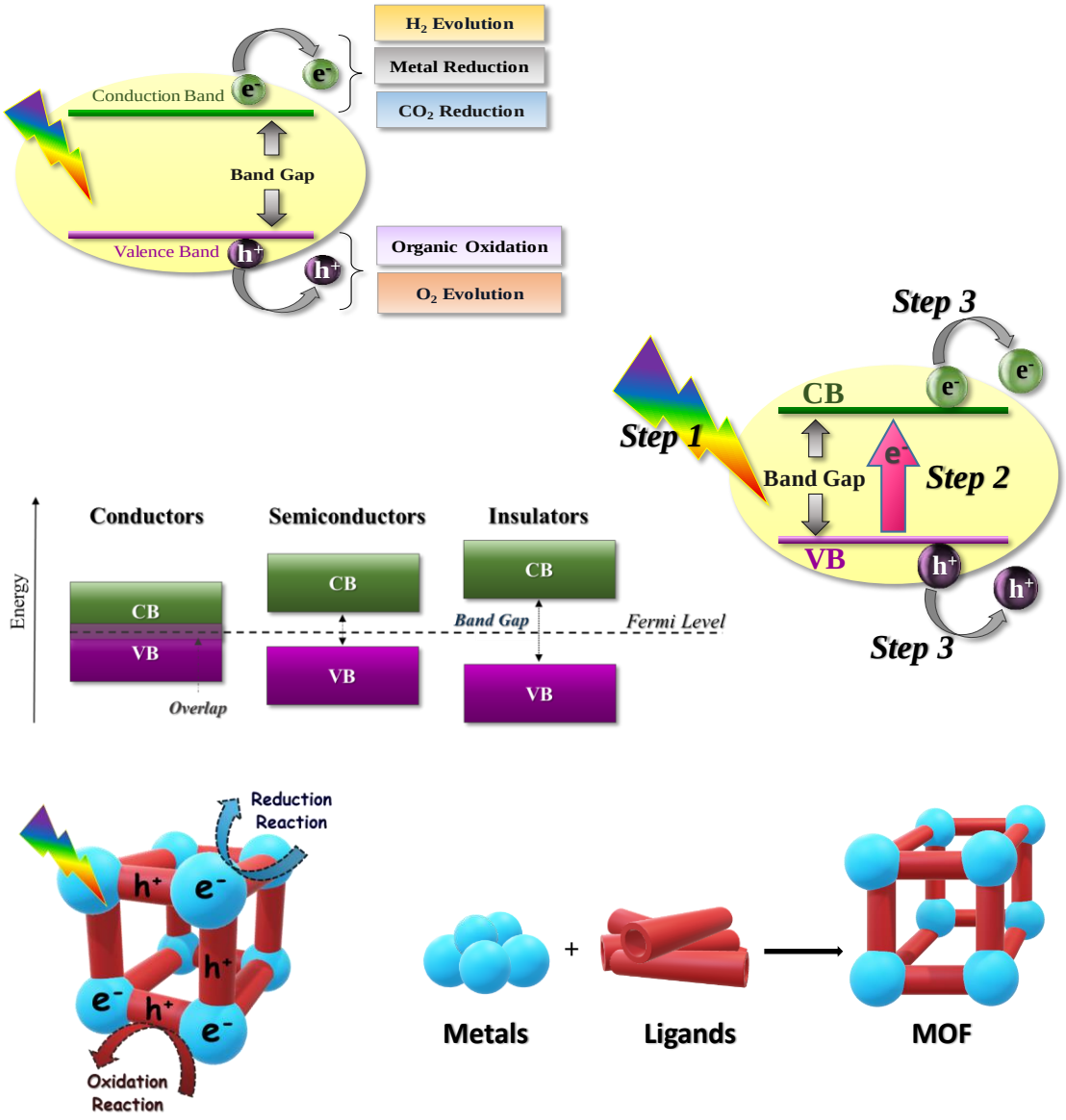

S. Kampouri's contribution: writing the manuscript and construction of figures

1.1 Introduction to Photocatalysis

Figure 1.1: *Images illustrating current environmental problems: growing air and water pollution, aridity, climate change, wildfires. Credits to Markus Spiske, Chris LeBoutillier and Leonid Danilov from Pexels.*

The images at **Figure 1.1** represent humanity's heritage from the 20th century; the increasingly growing environmental pollution and water scarcity, abused natural resources, climate change and extensive deforestation. These major problems are consequences of our society's activities and are associated with the industrial rise, the increasing growth of population and an economy relying on the exploitation of fossil fuels. Thus, it is our urgent obligation to develop sustainable strategies to mitigate these environmental problems. Among renewable energy technologies, a promising approach lies in the use of energy from light to excite a material that can enable different redox reactions. This broad field is known as photocatalysis. Each potential redox reaction that can occur represents an individual photocatalytic field. More specifically, the major photocatalytic fields that have been extensively studied include water splitting (reduction: H_2 production, oxidation: O_2 production), carbon dioxide (CO_2) reduction, synthesis of molecules, oxidation of organic pollutants, metal reduction and disinfection through the inactivation of pathogenic microorganisms, such as viruses, bacteria and protozoa (**Figure 1.2**).[2]

Photocatalytic water splitting into H_2 and O_2 constitutes a field of significant importance, since H_2 is regarded as an ideal replacement of fossil fuels, allowing for an energy cycle free of greenhouse gasses.[3] The fundamental principles in this field will be thoroughly described in chapter 1.3. Another major field in photocatalysis includes the light-driven oxidation of organic substances, which can be used to either achieve full degradation of hazardous organic contaminants or to synthesize useful

organic molecules. The increasing amounts of wastewater and high toxicity of several organic substances in streams have prompted extensive research in this field.[4] Photocatalytic reduction of metal ions is another efficient approach to alleviate water pollution induced by inorganic pollutants and is based on the fact that the toxicity of a given metal is highly correlated with its oxidation state. This photocatalytic field serves to transform such metals to a more environmentally benign form (e.g. Cr^{VI} to Cr^{III}) or to reduce them to their elemental form and remove it for safe disposal.[5] Last, considering that CO_2 represents the most common greenhouse gas contributing to global warming, the field of CO_2 photocatalytic reduction into useful chemicals (e.g. methane, methanol, formaldehyde, formic acid, and others) is regarded as a promising technology to avoid further increase in the concentration of CO_2 in the atmosphere.[6] In principle, this photocatalytic process involves the reduction of CO_2 along with the oxidation of water, which leads to the production of solar fuels.[7]

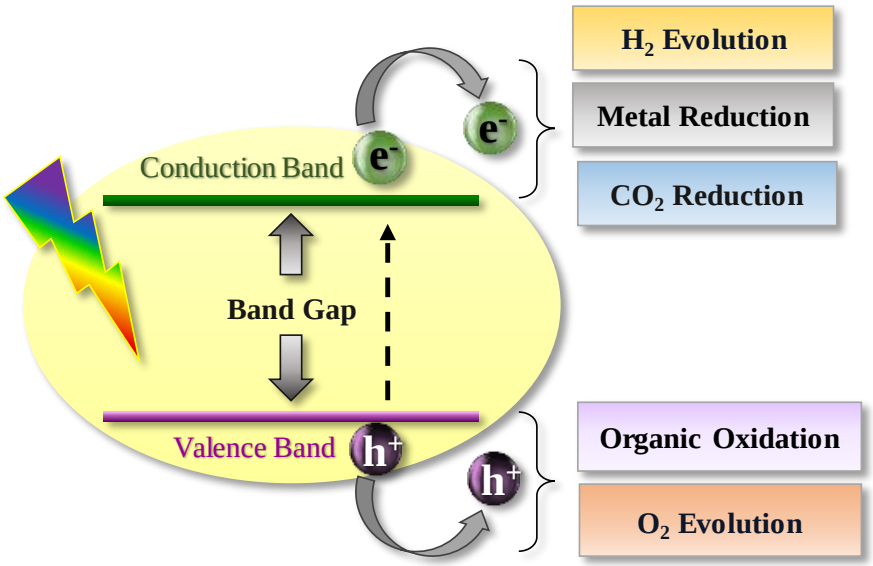

Figure 1.2: *Major photocatalytic fields.*

1.2 Fundamental Principles of Photocatalysis

One of the milestones in the photocatalysis field constitutes the exploration of titanium dioxide (TiO_2) for light-induced water splitting, reported in 1972 by Fujishima and Honda.[8] Since then, immense research efforts in photocatalysis has focused on TiO_2 and other semiconducting materials.[9] In contrast to conductors, where the valence and conduction bands (VB and CB, respectively) overlap, a given semiconducting material is characterized by a VB and CB that are separated by a band gap (**Figure 1.3**A). In this case, the band gap is significantly smaller than that of insulating materials (within the energy range of UV, visible or infrared light) and thus, when sufficient light energy is employed,

electron-hole pairs can be generated. The main requirement for this process to occur is that the photons' energy should be equal to or higher than the band gap energy of a given semiconductor. Subsequently, the photogenerated charge carriers will be transferred to the surface of the photocatalyst where redox reactions can be initiated. Conclusively, the major steps in every photocatalytic reaction involve *i.* the light harvesting by the photocatalyst *ii.* the charge separation and transportation to the surface of the photocatalyst, followed by *iii.* the redox reactions (**Figure 1.3**B). The overall equilibrium of the kinetics and thermodynamics of these three distinct steps governs the photocatalytic performance of a light-active material.

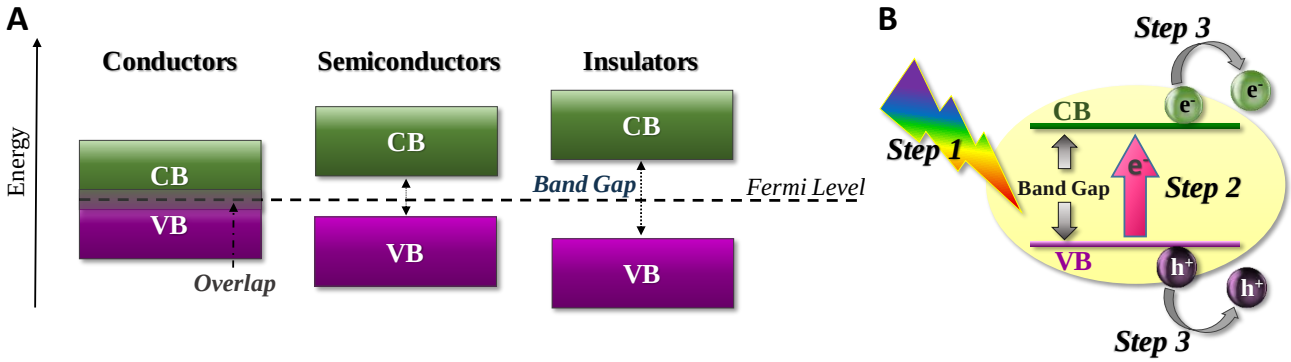

Figure 1.3: *(A) Band gap diagram of conductors, semiconductors and insulators. (B) Schematic illustration of major photocatalytic steps. Step 1: Light absorption, Step 2: Generation of electron-hole pairs and their migration to the surface of the photocatalyst and Step 3: Surface redox reactions.*

1.2.1 First Major Photocatalytic Step: Light harvesting

Regarding the first step of light absorption, it is highly important not only for the material to exhibit enhanced light absorption (high value of absorbance coefficient), but also to harvest light with specific energy. The ultimate goal in the development of new technologies is to utilize energy from renewable sources such as the sun, wind and wave power. Thus, in the field of photocatalysis it is of crucial importance to harvest the abundant solar energy. The power of the solar energy incident on the Earth's surface is around 1000 W m^{-2}. Should all this energy be exploited, it could completely cover the global energy demand.[10] The solar spectra at sea level is comprised of around 43% visible and 53% infrared light. UV light, on the other hand, accounts for only 4% of the solar radiation (**Figure 1.4**). While it is known that the most stable semiconductors are characterized by wide band gaps, materials with narrow band gaps, which are capable of absorbing light in the visible or infrared region, are highly desirable.

Numerous research studies have been devoted to the development of strategies in order to enhance or extend the absorption of materials (photocatalysts) in the visible region of the solar spectrum.

Approaches to achieve this include the utilization of dyes as photosensitizers,[11] doping a given semiconductor with metal or non-metal ions,[12] utilizing plasmonic nanoparticles for surface plasmon resonance,[13] or coupling with narrow band gap semiconductors for the formation of heterojunctions (**Figure 1.5**).[14]

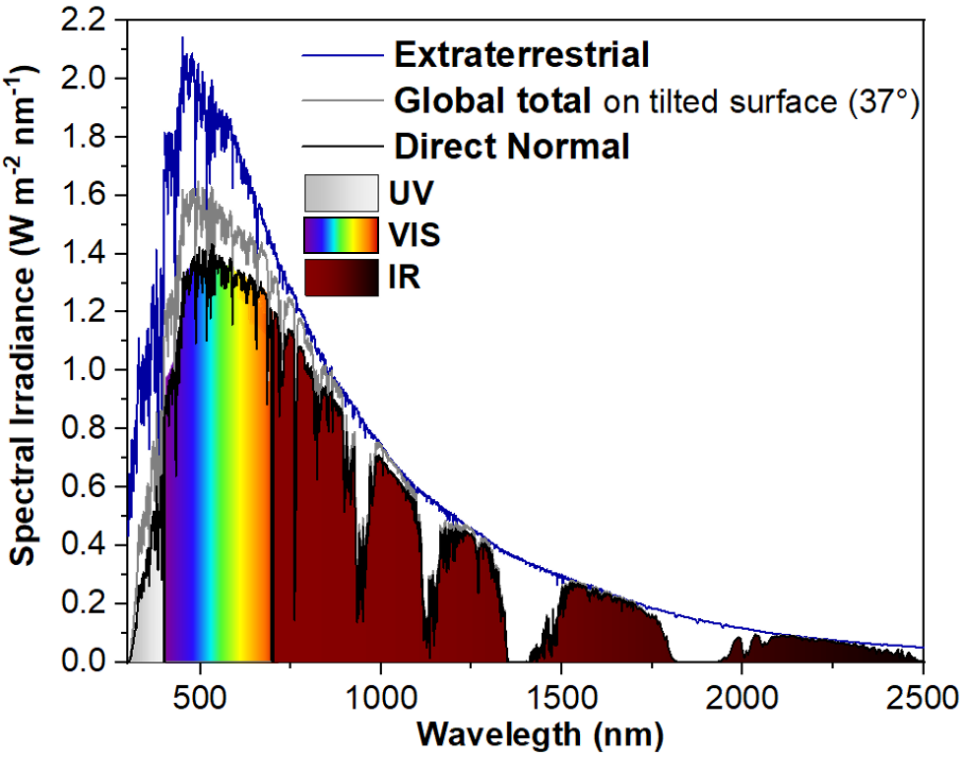

Figure 1.4: *Soral irradiance spectra (G-173). Blue, gray and black lines represent the extraterrestrial, the global total on 37° sun-facing tilted surface and the direct normal spectral irradiance, respectively. The ultraviolet (UV), visible (Vis) and infrared (IR) regions are highlighted. Data taken from the American Society for Testing and Materials (ASTM).*[15]

1.2.2 Second Major Photocatalytic Step: Charge Separation and Migration

As mentioned above, the second step in a photocatalytic reaction involves the separation and migration of the photogenerated charge carriers, which is of significant importance. A photocatalyst with a large visible-light absorption does not guarantee photocatalytic efficiency. The excited state lifetime of the photocatalyst should be long enough for the photogenerated charge carriers to be transported to the surface of the material and, subsequently, to initiate a chemical reaction. High electron-hole recombination rates within the photocatalysts can explain why many photocatalytic reactions demonstrate low efficiencies. Improvement of this second step has attracted intense research interest, with numerous successful strategies being reported, including the design of high crystalline

photocatalysts with less grain boundaries or other defects,[16] the formation of heterojunctions (**Figure 1.5**),[17] or incorporation of co-catalysts to inhibit the undesired electron-hole recombination, by withdrawing the generated charges.[18] Moreover, modification of the optical and electronic properties of a photocatalyst by following the aforementioned approaches could also result in enhanced charge separation efficiency, in addition to improving the first step of light harvesting.[19]

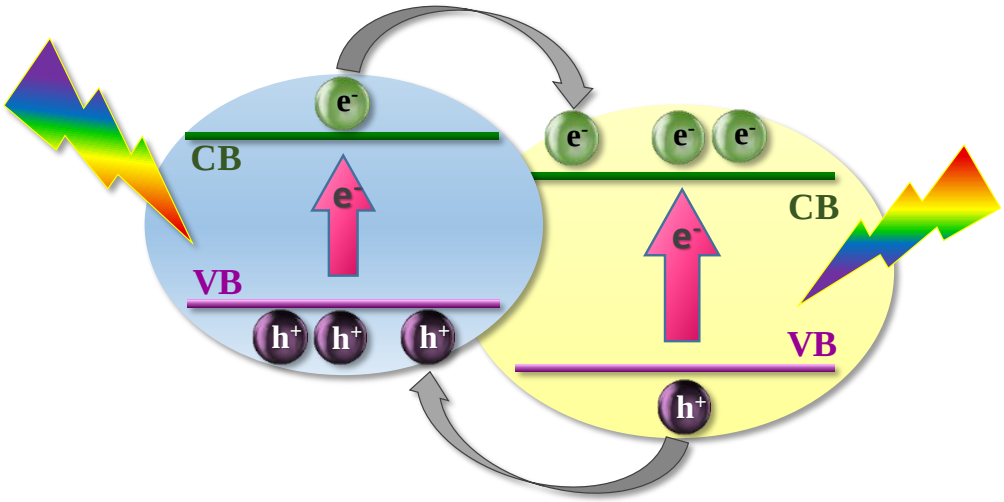

Figure 1.5: *Spatial separation of the photogenerated charge carriers within a type II heterojunction with a staggered gap.*

1.2.3 Third Major Photocatalytic Step: Catalytic Redox Reaction

The third step of the photocatalytic reaction has been rather neglected in terms of scientific attention, as compared to the previous two steps. This final step can be significantly promoted by inclusion of catalytic active sites, such as the co-catalysts. Co-catalysts are frequently incorporated in photocatalytic systems, since they play a key role in inhibiting the undesired electron hole recombination and reducing the activation energy of a given reaction. An appropriate co-catalyst should exhibit thermodynamic compatibility with the photocatalyst, high intrinsic catalytic activity for a given reaction, and affinity with the reactants. For example, in the case of the H_2 evolution reaction, the free energy of H_2 adsorption, ΔG_H, is highly correlated with the catalytic activity of a co-catalyst and thus is considered as a descriptor for evaluating co-catalysts for this reaction.[20] In principle, such co-catalysts should be characterized by a ΔG_H value close to zero, exhibiting adequate interactions with H_{ads} but avoiding H_{ads} being too strongly bound to the co-catalyst (**Figure 1.6**). There have been few recent reviews summarizing the advances in improving this final step through the incorporation of catalytic active sites.[21]

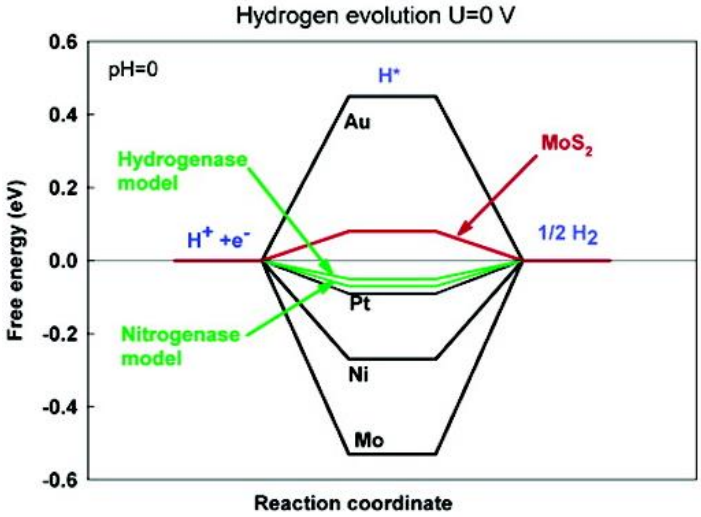

Figure 1.6*: Calculated free energy diagram for H_2 evolution at a potential U = 0 relative to the standard H_2 electrode at pH = 0. Reprinted with permission from Ref 20. Copyright 2005 American Chemical Society.*

1.3 Photocatalytic Hydrogen Evolution

The continuously growing energy consumption, along with severe environmental problems caused by the utilization of fossil fuels, have induced immense research efforts directed toward the development of an alternative energy "path", free of pollutants or greenhouse gases, such as N_2O and CO_2.[22] H_2 is considered a clean fuel and a sustainable energy carrier, since it can be produced from natural sources (e.g. water, biomass), it stores high mass-specific energy density, and it only produces water as result of its combustion.[23] Currently, most of the industrially produced H_2 is derived from fuel-based processes; more specifically steam methane reforming and coal gasification. These H_2 production methods however, contribute to the global warming, since CO_2 is also generated as a by-product in high quantities.[24] Interestingly, 5% of the industrially produced H_2 is generated through water electrolysis, which can be a sustainable process when the electricity used is generated by renewable resources (e.g. solar, wind, hydropower). That being said, the high cost of this technique has hindered its broad industrialization.[25]

As mentioned above, H_2 can also be directly generated through photochemical water splitting. Over the last few decades, photocatalytic H_2 evolution has been widely studied, and, solar-driven photocatalysis is regarded as an ideal method to sustainably produce H_2.[26] Pure water splitting involves two half reactions of H_2 and O_2 generation. For this process to occur, it is necessary that the highest level of a material's VB is more positive than the water oxidation level (1.23 eV versus NHE, normal hydrogen electrode), while the lowest level of the CB should be more negative than the H_2 evolution

potential (0 eV vs NHE, **Figure 1.7**). Therefore, the minimum band gap for a suitable water splitting photocatalyst should be 1.23 eV. It should be mentioned that the water oxidation half reaction involves the transfer of four electrons and is more energetically demanding than the water reduction process (minimum potential of 1.23 V per electron transfer).[27] In addition, since the Gibbs energy for overall water splitting is positive ($\Delta G>0$), it is challenging to avoid the back reaction.[28] Consequently, the oxidation half-reaction represents the bottleneck of overall water splitting. Thus, sacrificial electron donors are usually employed, obstructing the O_2 evolution reaction, to promote the H_2 generation.[29]

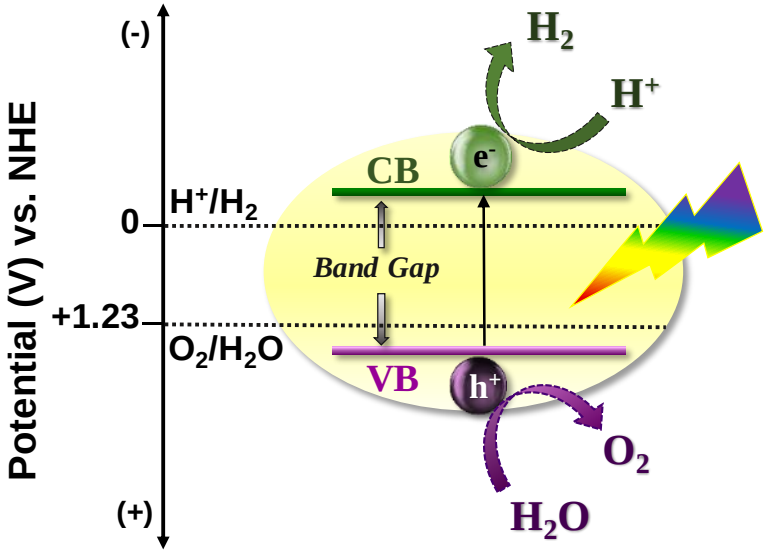

Figure 1.7: *Energy diagrams of photocatalytic water splitting relative to NHE, at pH = 0, with the H_2 evolution and O_2 evolution reactions redox potentials.*

On the other hand, the H_2 evolution half reaction involves two electrons and can be expressed through three possible steps. The first step is well established and known as the Volmer step, whereby in acidic media a proton reacts with an electron to form atomic hydrogen adsorbed on the surface of the photocatalyst ($H^+ + e^- \rightarrow H_{ads}$) or in an alkaline environment, a water molecule reacts with an electron to form atomic hydrogen and also hydroxide ($H_2O + e^- \rightarrow H_{ads} + OH^-$). The second part of this reaction can involve the Heyrovsky step as well as the Tafel step. According to the Heyrovsky step, the adsorbed atomic hydrogen will react with an electron and either a proton to form H_2 in acidic media ($H_{ads} + H^+ + e^- \rightarrow H_2$), or with a water molecule to form H_2 and hydroxide anions in alkaline media ($H_{ads} + H_2O + e^- \rightarrow H_2 + OH^-$). The Tafel step is the same in both acidic and alkaline environments and involves the combination of two adsorbed atomic hydrogens to form H_2 ($H_{ads} + H_{ads} \rightarrow H_2$).

In addition to the photocatalyst, the following auxiliary components can assist a photocatalytic H_2 evolution system (**Figure 1.8**):

i) Co-catalysts are employed in most cases to promote the photocatalytic activity. After the photoexcitation of the photocatalyst, the presence of both electrons and holes in the material can result in the recombination of these charge carriers. This phenomenon is highly correlated with the excited state lifetime of the photocatalyst and is the key reason why the efficiencies of such reactions can be low. The co-catalysts can significantly increase the H_2 evolution reaction yield, since they serve a two-fold purpose, inhibiting the undesired recombination of the photo-generated charge carries and reducing the activation energy for the H_2 evolution reaction.[21a] There are innumerable examples of noble metal-based (e.g. Pt, Pd, Au),[30] transition-metal-based (e.g. Co, Ni, MoS_2, Ni_2P, CoP, CuO),[31] nanocarbon-based (e.g. graphene, carbon nanotubes)[32] and molecular-based (e.g. cobaloximes, $Mo_3S_{13}^{2-}$)[33] co-catalysts. Among them, Pt is considered the paradigm of efficient co-catalysts for H_2 production due to its low overpotential for this reaction and the suitable Fermi level for withdrawing the photoexcited electrons.[34]

ii) Photosensitizers can also be utilized to extend or enhance the light absorption of the photocatalyst in the visible region (44% of the solar energy), through electron transfer from their antibonding to the CB of the photocatalyst. Typical examples of photosensitizers are organic dyes, such as eosin Y,[35] $[Ru(bpy)_3]^{2+}$,[36] or porphyrins.[37]

iii) Reagents such as electron acceptors (e.g. methyl viologen cation, MV^{2+})[38] or sacrificial electron donors (triethylamine, triethanolamine, ethanol, methanol) can be used to either mediate the transfer of the photogenerated electrons or balance the H_2 evolution half reaction, respectively. In particular, electron donors are regularly used since they can remarkably enhance the photocatalytic performance.

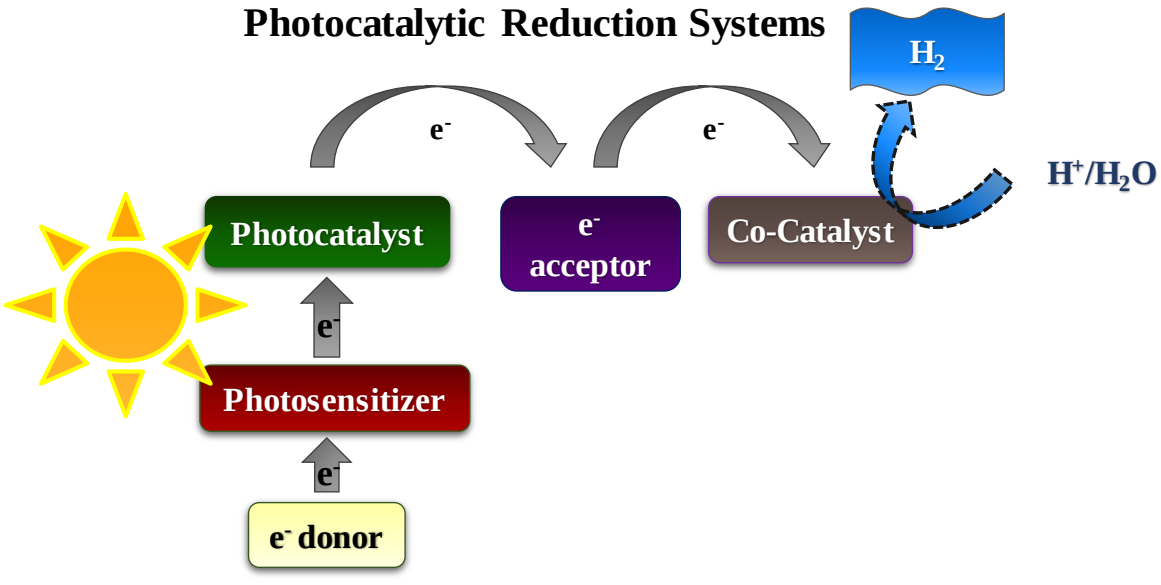

Figure 1.8: *Schematic illustration of the possible constituents of a photocatalytic H_2 evolution system.*

1.4 Photocatalytic Oxidation of Organic Compounds

Although industrial development has engendered countless advancements in technology, amenities in lifestyle and rise in the economy, it has also inflicted extended deterioration of the environment. One of the most critical environmental problems faced over the last century is water pollution, mainly caused by human activities. Textile or food processing industries, pharmaceutical companies, agricultural activities, and power plants are some of the main sources of hazardous contaminants. Wastewater contains a variety of organic pollutants, such as organic dyes, phenols, fertilizers and hydrocarbons, which can cause incontrovertible environmental problems.[39] A large fraction of these contaminants is mutagenic, carcinogenic, or toxic and their presence poses significant risks for public health.[40] In addition, the vast majority of these organic substances can damage aquatic ecosystems and inhibit the exchange of O_2 in water.[41] Moreover, severe water scarcity is projected to impact a quarter of the world's population within the next few years.[42] Thus, increasing generation of wastewater along with the water shortage projected in the near future has provoked the urgent development of methodologies that can offer effective decontamination of water so as to enable an efficient recycling of wastewater.

So far, conventional water treatment methods (e.g. coagulation, sedimentation, filtration, adsorption) have been characterized by high operating costs, as well as the fact that they can generate other undesired hazardous by-products, or they cannot fully degrade the targeted organic pollutants.[43] Another option to decompose these organic substances from water is through advanced oxidation processes (AOPs), which are based on the generation of strongly oxidizing radical species (e.g. $^{\bullet}OH$) that can efficiently and non-selectively destruct even the most resistant organic species.[4a] The AOPs include a range of techniques, such as wet, electrochemical or super critical water oxidation[44], ozonation,[45] hydrogen peroxide-based methods,[46] and photolysis. In particular, heterogeneous photocatalytic oxidation is a promising approach that can lead to complete degradation of a wide range of hazardous organic substances into easily biodegradable compounds or less toxic molecules, by utilizing light.

It is widely known that *i.* the holes (h^+), *ii.* the hydroxyl radicals ($^{\bullet}OH$) and *iii.* the superoxide radicals ($O_2^{\bullet-}$) are the three main active species involved in photocatalytic oxidation processes (**Figure 1.9**).[47] As mentioned above, upon irradiation of a photocatalyst, generation of excited high-energy states of electron and hole pairs occurs. The hole in the VB is a powerful oxidizing agent that can react either directly with organic molecules and successfully oxidize them to less hazardous products such as CO_2 and H_2O, or it can react with water to generate highly reactive hydroxyl radicals ($^{\bullet}OH$) (equation 1).

Moreover, the promoted electron in the CB (e^-) can initiate oxygen ionosorption by reacting with O_2 to form an anion superoxide radical ($O_2^{\bullet-}$) (equation 2). The latter can further react with hydrogen cations (H^+) and be protonated to the hydroperoxyl radical ($HOO^\bullet$), which acts as an e^- scavenger, being reduced to HOO^-, elongating the lifetime of the excited state and subsequently being protonated to hydrogen peroxide (H_2O_2).[4a]

$$h^+ + H_2O \rightarrow {}^\bullet OH + H^+ \qquad \text{(equation 1)}$$

$$e^- + O_2 \rightarrow O_2^{\bullet-} \qquad \text{(equation 2)}$$

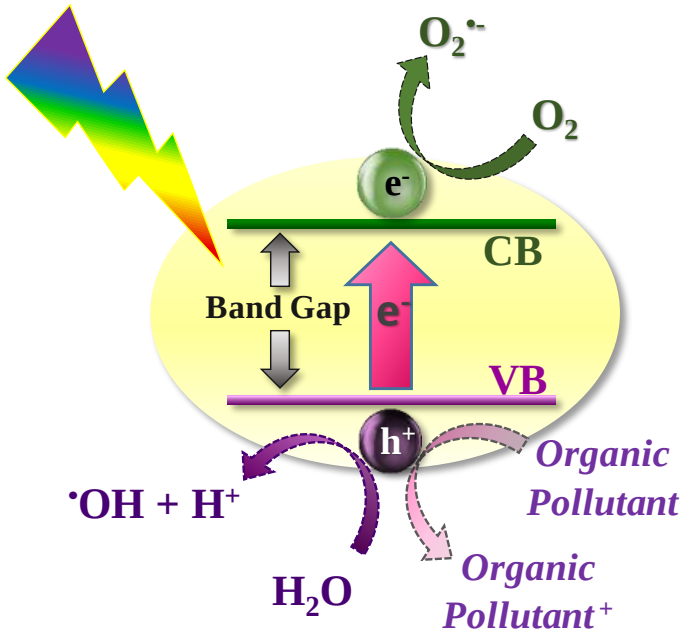

Figure 1.9: *Schematic representation of the photoexcitation of a photocatalyst in the presence of organic pollutants. The mechanism for the generation of anion superoxide and hydroxyl radicals, as well as that for the direct organic pollutant's oxidation is also illustrated.*

Titanium dioxide (TiO_2) has been considered a very promising photocatalyst for the mineralization of wastewater as well, and has thus been extensively studied.[48] However, its incapability of operating under visible light restricts its utilization in practical applications. Therefore, immense research endeavours have focused on extending its absorption into the visible light region.[49]

In contrast with photocatalytic H_2 evolution systems, photocatalytic organic degradation systems are usually less complicated as they usually consist of less components. In the majority of examples reported in the literature, only a photocatalyst is used to harvest the light. It should be mentioned that the photocatalytic oxidation of organic substances is commonly performed under aerated conditions, where O_2 acts as an electron scavenger, capturing the photogenerated electrons and being transformed

to superoxide radicals, which can promote the degradation process. Furthermore, additional electron scavengers are often included, such as H_2O_2, persulfate (PS), and peroxymonosulfate (PMS), to further suppress the electron-hole pair recombination, thus enhancing the photodegradation efficiency.[50] In contrast to the photocatalytic H_2 evolution field, co-catalysts are not as frequently used for this application.[47, 51]

In the field of photocatalytic degradation of organic substances, parameters such as the pH of the solution and the initial concentration of the pollutant can strongly influence the photocatalytic efficiency.[52] In particular, variations in the pH can have a profound impact on the photocatalytic degradation rate, since it is a critical parameter for the adsorption of a targeted compound on the surface of the photocatalyst. This is of paramount importance, especially when the photocatalyst is amphoteric (e.g. TiO_2) and consequently, the charge of its surface is pH-dependent.[53] Therefore, it is crucial that these parameters are varied and optimized to obtain legitimate and comparable results.

1.5 Dual-Functional Photocatalysis

Dual-functional photocatalysis constitutes a hybrid field where different photocatalytic fields are combined for a two-fold purpose. In particular, the photocatalytic generation of H_2 coupled with the simultaneous photocatalytic oxidation of organic substances has attracted radically increasing research interest over the last few years.[54] This field can be divided in two subcategories depending on the nature and target of the oxidation process. Both of these categories involve the photocatalytic generation of H_2 from water (as the main source) coupled with either the degradation of organic pollutants or the transformation of organic substances into value added products (**Figure 1.10**).

The utilization of organic substrates for H_2 evolution through photocatalysis was introduced in the late ‘70s and early ‘80s,[55] when the conversion of carbohydrates to H_2 was explored, commonly known as photoreforming.[56] Similar to dual-functional photocatalysis, photoreforming focuses on the production of H_2 by utilizing organic substrates. However, in photoreforming, the sacrificial organic molecules to be oxidized are not necessarily hazardous substances and can be useful carbohydrates, such as methane and ethanol.[57] In addition, in the field of dual-purpose photocatalysis, the H_2 should be mainly derived from the water reduction reaction. For example, earlier this year, Zhang *et al.* reported the photocatalytic dehydrogenation of benzyl alcohol for the simultaneous H_2 and benzaldehyde production using a Ni-decorated $Zn_{0.5}Cd_{0.5}S$ photocatalytic system.[58] However, in this work, the authors attributed the H_2 generation to its extraction from benzyl alcohol and thus, it cannot be considered a paradigm of dual-functional photocatalytic activity. Consequently, although these two

fields can overlap, only a fraction of studies in the photoreforming field can be considered dual-functional photocatalysis, which is when either the targeted organic molecules are pollutants or when the aim of the oxidation is the synthesis of value-added products (e.g., aldehydes, furoic acid or imine).

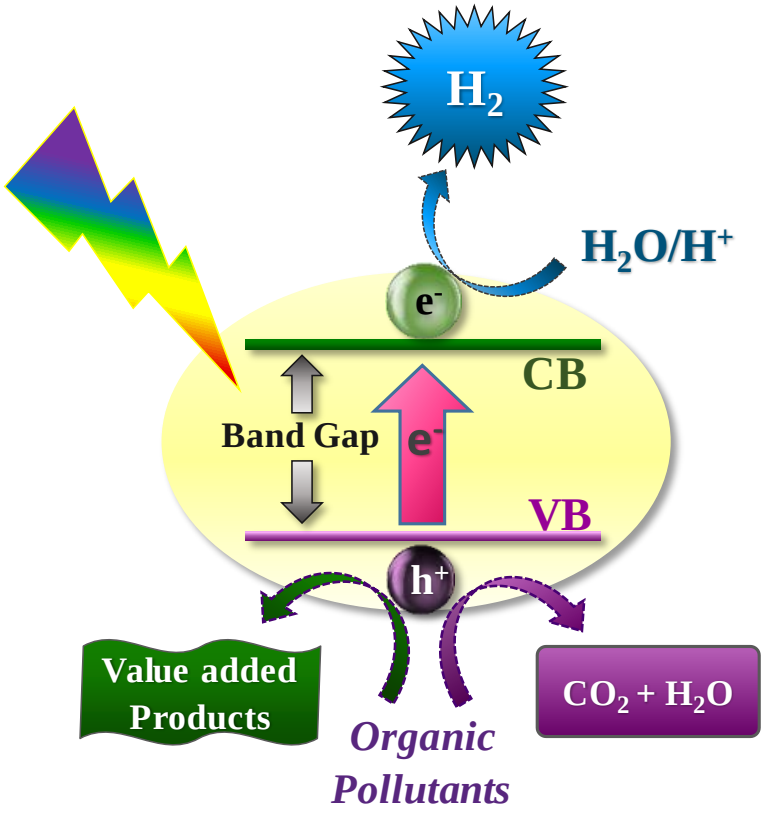

Figure 1.10: *Schematic representation of the mechanism for dual-functional photocatalysis for H_2 generation coupled with oxidation of organic pollutants to either achieve full degradation of hazardous organic contaminants or to synthesize useful organic molecules.*

Even though H_2 evolution and organic oxidation have been studied separately in photocatalytic systems,[59] their integration in a single process is relatively new. The basic principles of the individual photocatalytic fields are combined, generating new mechanistic aspects and criteria for the selection of appropriate dual-functional photocatalysts. Desired characteristics of a dual-purpose photocatalytic system include those applied in general photocatalysis, comprising low cost, extended solar light absorption, prolonged excited state lifetime and high electron-hole separation efficiency. In addition, a dual-purpose photocatalyst for H_2 production coupled with organic oxidation should have VB and CB with suitable energy and be capable of oxidizing the organic molecules with holes as the dominant active species and with the electrons being transferred to water molecules or protons. Since O_2 is a good electron scavenger, almost every study in the field is carried out under anoxic conditions.

1.6 Metal-Organic Frameworks for Photocatalysis

Metal-organic frameworks (MOFs) represent an interesting type of porous, crystalline materials, that can be self-assembled through the coordination of organic linkers with metal ions/clusters (**Figure 1.11**).[60] A wide variety of MOF structures has been reported since the term 'metal-organic-frameworks' was first conceived by Yaghi in 1995 [61]. Owing to their modular nature, large porosity and high surface area (up to 7000 m^2/g),[62] MOFs are considered promising candidates for a variety of applications, such as gas storage and separation, magnetic materials, chemical sensing, catalysis, and biomedicine. [63]

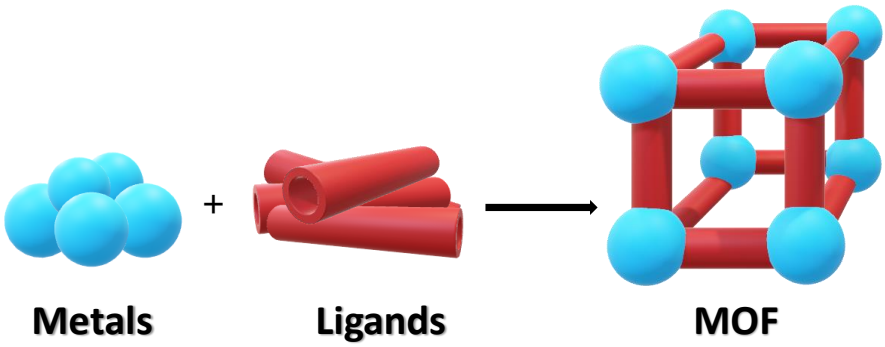

Figure 1.11: *Schematic representation of MOFs' constituents*.

The understanding and elucidation of the main optical and vibrational properties of MOF-5 represent one of the milestones in the field, paving the way for MOFs' implementation in light-related applications.[64] In fact, MOFs have burst onto the light-driven catalysis field only a decade ago,[65] and have since been considered promising candidates for photocatalytic applications, including H_2 evolution, organic pollutants degradation, CO_2 and metal ions reduction.[66] On the basis of a strict definition, MOFs cannot be regarded as semiconductors, which is the traditional type of materials for light-driven catalytic applications.[16a, 67] However, they can exhibit a semiconductor-like behavior upon irradiation, deriving from their optically active ligands and their electronic interactions with the metal nodes. Upon illumination of a light-responsive MOF, an electron will be excited from the highest occupied crystalline orbitals (HOCOs) to the lowest unoccupied crystalline orbitals (LUCOs), analogous to the VB and CB in the band theory of solids, or the bonding and antibonding orbitals in the molecular orbital theory.[1]

The main factor triggering MOFs' exploration in photocatalytic applications lies in the limitations of the traditional materials (photocatalysts) that have been predominantly employed in this technology.[3] Especially for solar-driven photocatalysis, the bottleneck of such technologies is related to the

shortcomings of the traditional semiconductor photocatalysts. More specifically, typical wide band-gap semiconductors (i.e., TiO_2) suffer from limited sunlight harvesting, while the ones characterized by narrow band-gap (i.e., a-Fe_2O_3, $BiVO_4$, CdS) demonstrate high charge carrier recombination, poor surface kinetics or instability.[67-68]

MOFs are endowed with extremely high structural versatility, which allows a level of tunability of the optical, electronic and catalytic properties.[69] By carefully selecting light-absorbing linkers and catalytically active metals with comparable energy of their frontier orbitals, one can design numerous MOFs that would be excellent candidates for photocatalytic applications. Therefore, the tremendous scientific attention received by MOFs in the general catalysis field can be anticipated, considering that one can target and tune the desired features of a MOF through careful choice of ligand and metal. In other words, MOFs offer the exciting possibility to combine the advantages of homogeneous catalysts – such as high tunability – with those of heterogeneous catalysts; robustness and insolubility.

1.6.1 MOFs stability under water splitting conditions

Water stability is a crucial property for many materials to be industrially applicable, since water is abundant in the preparation, storage, transportation and application processes. Especially when it comes to water splitting, it is indispensable for the MOFs to demonstrate stability under aqueous conditions, as well as being resistant to acidic or basic conditions (e.g. water reduction in the presence of sacrificial donors).[70] The robustness of a given MOF toward water depends on the strength of the bonds between the metal and the oxygen or nitrogen atoms from the ligand comprising it. Unfortunately, due to the lability of ligand-metal bonds, a considerable amount of reported MOFs are sensitive to water content, which results in their gradual decomposition when the environment contains moisture. [71]

Water stable MOFs by definition are classified as those that do not exhibit structural breakdown under exposure to water content. In order to determine if a MOF structure remains stable in a water stability test, we can compare some of their typical characteristics such as crystallinity (powder X-ray diffraction) or structural porosity (gas adsorption capacity) between the pristine and post-exposure to water samples. During the last few years, plenty water-stable MOFs has been reported, mainly due to the improved understanding toward MOF structural stability in water. These water stable MOFs could be categorized into three groups: *i.* metal carboxylate frameworks consisting of high-valence metal ions (e.g. Ti^{4+} Fe^{3+}, Cr^{3+}, and Zr^{4+}), such as the Ti-based MIL-125,[72] the Cr-based MIL-101[73] and the Zr-based UIO-66,[74] *ii.* metal azolate frameworks containing nitrogen-donor ligands, such as the MAF

(metal azolate frameworks) series of materials developed by Chen's group,[75] *iii.* MOFs functionalized by hydrophobic pore surfaces or with blocked metal ions, such as CALF-25.[76] These MOFs are likely to retain their structure under the exhaustive water splitting conditions.

1.6.2 MOFs' Optical Response

One of the key advantages of MOFs is their tunable optical properties deriving from the rational design through careful choice of the ligand and metal comprising it. The overall optical behavior of a MOF is governed by the optical properties of the metals and ligands composing it, and their interactions. Similar energy of the ligands' and metals' frontier orbitals and spatial overlap between them can give rise to charge transfer between those two constituents and a smaller optical gap of the MOF comprising them, allowing for light absorption in the visible and infrared, which are the dominant regions of the solar spectrum. Charge transfer between those two components can occur either from the ligand's orbitals to those of the metal (Ligand to Metal Charge Transfer, LMCT) or vice versa (Metal to Ligand Charge Transfer, MLCT). On the other hand, limited or no energetic and spatial overlap of the linkers' and metals' orbitals results in the light harvesting properties of the MOF being similar to those of the individual free ligand and metal comprising it.[77] The presence or absence of such electronic interactions between the ligand and metal of a given MOF can be explored through UV-Vis absorption spectroscopy, while electron paramagnetic resonance (EPR) could be a useful tool to shed light into the charge transfer mechanism (LMCH or MLCT), through observation of the potential change in the oxidation state of the metal.

As mentioned before, MOFs have the ability to behave as semiconductors, with their electrons being excited from their VB (or HOCOs) to their CB (or LUCOs) upon exposure to light with appropriate energy. However, a great number of MOFs exhibit light absorption only in the UV-region, while undoubtedly one of the main challenges in photocatalysis lies in the ability of the photocatalyst to exploit sunlight. Several approaches have been investigated in order to tackle this issue, including the utilization of light absorbing organic and metal-organic chromophores as building units for the synthesis of MOFs,[78] doping different photosensitizers into the cavities of MOFs, [79] or linker functionalization with electron donating functional groups, such as $-NH_2$ or -OH.[80]

1.6.3 MOF-based Photocatalytic Systems for Water reduction

Similar to the traditional semiconductor photocatalysis field, MOF-based photocatalytic system for the H_2 evolution reaction can consist of several components in addition to the MOF, which is the main

component and typically acts as an antenna harvesting light. So far, electron donors are always used in such systems, since to our knowledge, currently there are no reports of MOF photocatalysts splitting pure water into H_2 and O_2, and these substances are used to avoid the water oxidation reaction. Recently, Ziao e*t al.* reported a Cd-based MOF photocatalyst, Cd-TPAPy – comprised of 1,3,6,8-tetrakis(p-benzoic acid)pyrene (H_4TBAPy) as the ligand – that is capable of catalyzing both the water reduction and oxidation reaction with the assistance of Pt or CoPi as co-catalysts.[81] However, the authors did not investigate the photocatalytic activity of Cd-TPAPy for both the water reduction and oxidation reactions simultaneously, but explored these two reactions separately, using a sacrificial electron donor (triethanolamine, TEOA) and an electron scavenger ($AgNO_3$) for the H_2 and O_2 production, respectively (**Figure 1.12**).

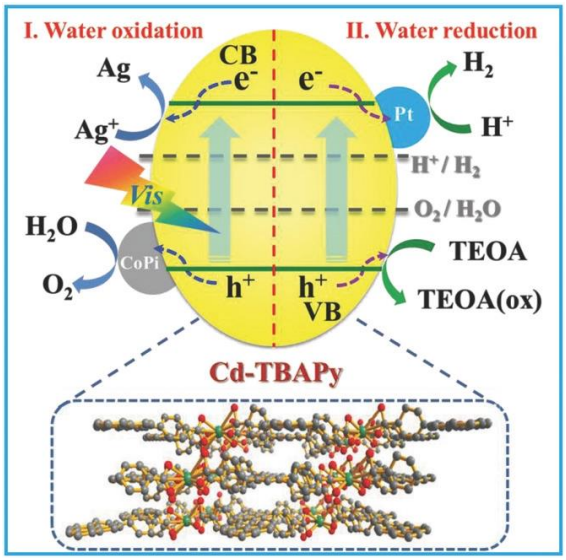

Figure 1.12: *Schematic illustration of the proposed mechanism for photocatalytic H_2 and O_2 evolution over Cd-TBAPy. Reprinted with permission from Ref. 81 Copyright © 2018 John Wiley and Sons.*

In addition to electron donors, another type of sacrificial reagent that could be used is a redox shuttle, mediating the electron transfer from the photocatalyst to the co-catalyst. However, their utilization is far less frequent compared to electron donors. In this context, Fateeva *et al*. designed and investigated a MOF-based on porphyrin linkers and aluminum (known as AlPMOF), using ethylenediaminetetraacetic acid (EDTA) as the electron donor, Pt nanoparticles as the co-catalyst, with and without methyl viologen (MV) as the electron mediator.[82] AlPMOF represents one of the very early examples of MOF photocatalysts and demonstrates visible-light absorption similar to its porphyrin ligand. Although this system exhibited adequate photocatalytic activity, the actual rate of hydrogen production was lower when MV was present, which was attributed to diffusion limitations of MV in the pores of the MOF.

Dyes can also be incorporated in MOF-based photocatalytic systems for water reduction, acting as photosensitizers. Similar to the dye sensitized solar cells in which a ruthenium-based dye is typically adsorbed on the surface of TiO_2,[83] in MOF photocatalytic systems, upon illumination the dye absorbs light – ideally in the region where the MOF is incapable of absorbing. Then, the photoexcited electron is transferred from the antibonding orbitals of the dye to the LUCOs/CB of the MOF from which it can be involved in the reduction reaction process. Interestingly, in MOF-based systems, the dye molecules can be adsorbed not only on the exterior surface of the MOF but also within its pores, increasing the amount of dye molecules able to electronically interact with the MOF. Dyes are often used in such systems, especially in the cases where the MOF absorbs light only in the UV region. A typical example of UV-active MOF photocatalysts is the Zr-based UIO-66, synthesized by Cavka *et al.* at the University of Oslo.[74] Considering that UIO-66 represents one of the most stable photocatalysts for this type of materials, there are several photocatalytic studies in the literature showing that UIO-66 can be assisted by dyes (e.g., Rhodamine B[84] and Erythrosin B)[79a] for the absorption of light in the visible region. More specifically, He *et al.* explored the photocatalytic activity of UIO-66 with Pt as the co-catalyst, TEOA as the electron donor, with and without Rhodamine B as the photosensitizer. Under visible light irradiation – in which UIO-66 is mainly inactive – the Pt/UIO-66 photocatalytic system demonstrated 30-fold greater activity when Rhodamine B was used (116 versus 3.9 μmol g^{-1} h^{-1} with and without Rhodamine B, respectively). The proposed mechanism is illustrated at **Figure 1.13** and involves electron transfer first, from the antibonding orbitals of Rhodamine B to the LUCOs/CB (denoted as LUMO at **Figure 1.13**) of UIO-66 and subsequently electron migration to the Pt NPs, where protons are reduced to H_2.

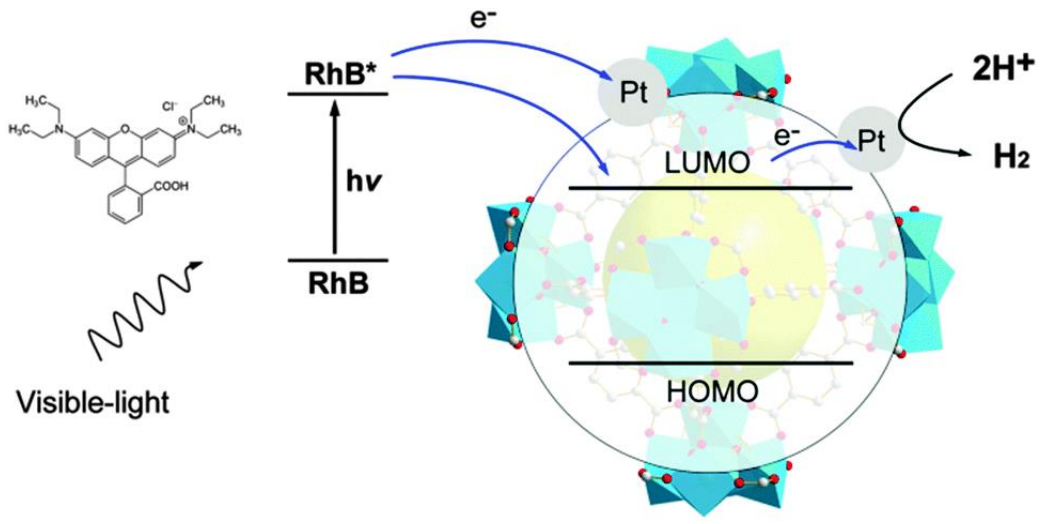

Figure 1.13: *Schematic representation of proposed mechanism for photocatalytic H_2 generation over Rhodamine B (RhB) sensitized Pt/UiO-66 under visible-light. Reproduced from Ref. 84 with permission from The Royal Society of Chemistry.*

Another important component frequently used in MOF-based photocatalytic systems is the co-catalyst, in order to inhibit the undesired electron-hole recombination and offer catalytic active sites for the reaction to occur. So far, the vast majority of MOF photocatalysts reported are combined with expensive noble metal nanoparticles, such Pt.[85] Due to their high porosity, MOFs offer the possibility to incorporate the co-catalysts within their cavities. In this context, Xiao *et al.* investigated the impact of the co-catalyst's location relative to the MOF photocatalyst, on the overall activity of the system.[85a] More specifically, they supported Pt nanoparticles either inside the porous assemblies of UIO-66-NH_2 or on its surface (**Figure 1.14**). The group showed that encapsulating the Pt co-catalysts within the pores of UIO-66-NH_2 results in higher photocatalytic efficiency of 257.38 (versus 50.26 μmol g^{-1} h^{-1} for UIO-66-NH_2 with Pt nanoparticles simply deposited on the surface). This enhancement of the photocatalytic activity was attributed to the shorter electron-transport paths between the co-catalyst and the photocatalysts, further promoting the charge separation efficiency.

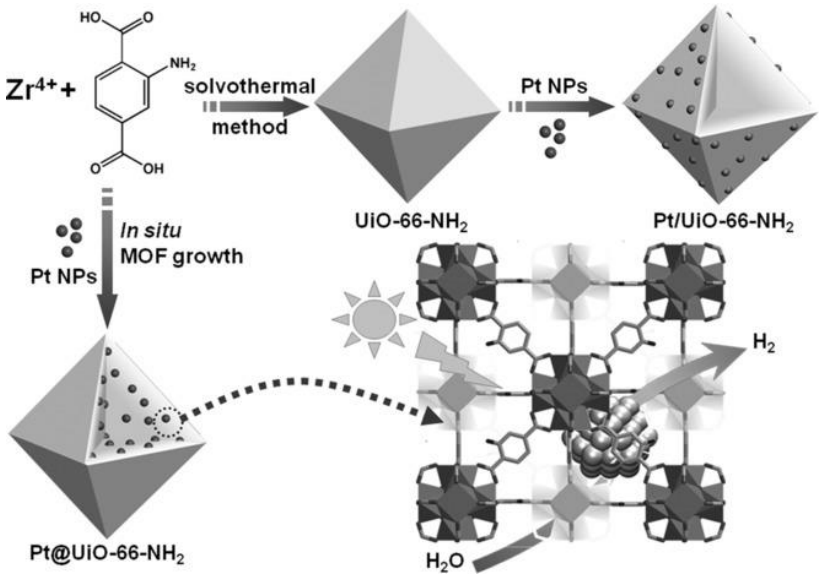

Figure 1.14: *Schematic representation of the synthesis procedure of UiO-66-NH_2 with encapsulated Pt NPs (Pt@UiO-66-NH_2) and of Pt NPs deposited on the exterior surface of the MOF (Pt/UiO-66-NH_2), with the mechanism for photocatalytic H_2 production over Pt@UiO-66-NH_2 being highlighted. Reprinted with permission from Ref. 85a Copyright © 2016 John Wiley and Sons.*

Summarizing, these extra components typically incorporated in MOF-based photocatalytic systems for H_2 evolution, are significantly increasing the overall cost and complexity of such systems. Furthermore, some of these components – such as dyes and electron donors – can be toxic and hazardous (e.g., Rhodamine B, triethylamine, TEOA and methanol). To overcome these disadvantages, several challenging issues need to be tackled. First, MOFs that exhibit strong and extensive light absorption must be developed to avoid the use of dyes as photosensitizers. Second,

abundant photocatalysts that exhibit high electron-hole separation efficiencies or noble-metal-free cocatalysts are highly desired materials and, hence, research efforts should focus on this aspect. Finally, the incorporation of highly toxic or expensive sacrificial electron donors can be avoided by either developing photocatalysts capable of splitting water into H_2 and O_2 or able to perform dual-functional photocatalysis, for simultaneous production of H_2 and oxidation of targeted organic compounds (e.g., degradation of organic contaminants or synthesis of useful chemicals).

1.7 Objectives of this Thesis

In line with the scientific endeavors to optimize and extend the range of materials used for photocatalytic applications, the main objective of this thesis lies in the optimization of MOF-based photocatalytic systems. In an ideal case, the photocatalyst should demonstrate extended solar light absorption, high electron-hole separation and migration efficiency, and high catalytic activity. In fact, these desired features are correlated to the three major photocatalytic steps (as explained in **Chapter 1.2**). It is thus the main focus of this thesis to improve the photocatalytic activity of MOF-based photocatalytic systems, by exploring and promoting these three major steps of *i.* light harvesting, *ii.* charge separation and transport and *iii.* catalytic redox reactions. More specifically, **Chapter 2** highlights how using abundant co-catalysts can modify the last two photocatalytic steps of charge separation and catalytic reaction, and thus significantly improve the photocatalytic activity and lower the cost of MOF-based systems. In **Chapter 3**, first, the influence of different electron donors on the activity of the abundant MOF-based system described in the previous chapter is investigated. The second part of **Chapter 3** shows that the overall cost and sustainability of such systems can be further improved by replacing the electron donors with organic contaminants, performing dual-functional photocatalysis for concurrent H_2 production and pollutants degradation. **Chapter 4** describes a strategy to promote the first and second photocatalytic steps of light absorption and charge separation, which lies in the design of MOF/MOF heterojunctions. This strategy exploits the advantages of MOFs as photocatalysts in their maximum potential (e.g. high tunability of the optoelectronic and catalytic properties), and simultaneously tackle their common challenges (e.g. high charge recombination rates and susceptibility to photocorrosion). Finally, **Chapter 5** focuses on an alternative use of MOFs in the photocatalysis field, where the MOF is used as a precursor for the synthesis of more active semiconductor photocatalysts with interesting morphology.

Chapter 2 Variation of Abundant Co-catalysts in a Metal-Organic Framework Photocatalytic System

Parts of this chapter are based on published works:

'*Photocatalytic Hydrogen Generation from a Visible-Light Responsive Metal-organic framework system: the impact of nickel phosphide nanoparticles*'

S. Kampouri, T. N. Nguyen, C. P. Ireland, B. Valizadeh, F. M. Ebrahim, G. Capano, D. Ongari, A. Mace, N. Guijarro, K. Sivula, A. Sienkiewicz, L. Forró, B. Smit, K. C. Stylianou,

J. Mater. Chem. A, 2018, 6, 2476 - 2481

Ref. 86 – Reproduced by permission of The Royal Society of Chemistry

and

'Concurrent Photocatalytic Hydrogen Generation and Dye Degradation Using MIL-125-NH_2 under Visible Light Irradiation'

S. Kampouri, T. N. Nguyen, M. Spodaryk, R. G. Palgrave, A. Züttel, B. Smit, K. C. Stylianou,

Adv. Funct. Mater., 2018, 28, 1806368

Reprinted in adapted versions with permission from Ref. 87 Copyright © 2018 John Wiley and Sons

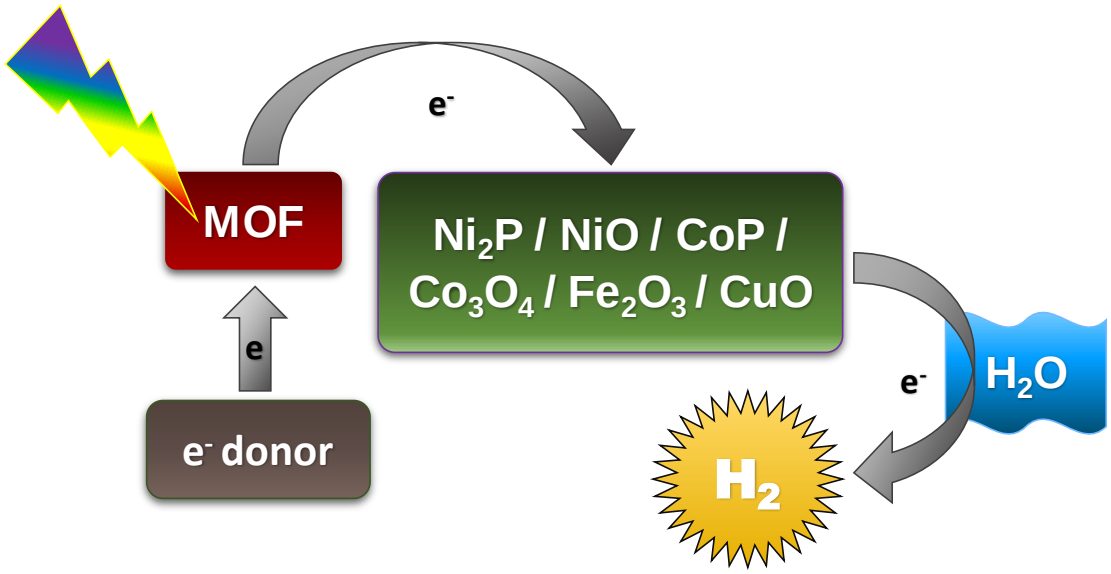

S. Kampouri's contribution: Conceiving the project's idea, synthesis of materials, characterization (powder X-ray diffraction, UV-Vis absorption and photoluminescence spectroscopy, nitrogen sorption isotherms, Fourier-transform infrared measurements), designing and performing experiments (photocatalytic experiments, quantum yield calculations), writing text and constructing figures.

2.1 Introduction

Several MOF-based photocatalytic systems have been tested for visible-light driven H_2 production; most of them are based on reductive metal ions, such as Ti^{IV} and Zr^{IV} and visible-light-active ligands that can harvest solar light and convert it into H_2.[88] Recently, Cu^{I} or Cu^{II}-based MOFs were found to be good candidates for the photocatalytic water reduction reaction under UV/vis or visible irradiation.[89] Despite the great promise of MOFs toward water splitting, the majority of these MOF-based systems demonstrate very low apparent quantum yields and still utilize expensive noble-metal-based co-catalysts, such as Pt nanoparticles (NPs).[90] The broad utilization of Pt NPs as co-catalysts – especially with MOF-based systems – lies in their low overpotential for the H_2 evolution reaction, their suitable Fermi level for withdrawing photoexcited electrons and their facile preparation.[34a] However, their incorporation does not guarantee the best photocatalytic performance, while with dwindling supplies of precious metals it is crucial to eliminate their utilization.

Although very few examples have been reported in the literature, the synergy between MOFs and co-catalysts is proven to be a key factor for the photocatalytic performance of the system, as different hydrogen generation rates and quantum yields are observed when the same MOF is used.[91] Key factors for achieving optimal synergy include energetic alignment and kinetic compatibility between the MOF photocatalyst and the co-catalyst, so as to ensure high electron transfer rates. Consequently, there is a need to investigate the activity of earth-abundant co-catalysts – as alternatives to noble metals – and explore their interactions with a given MOF. It is worth noting that since the number of potential earth-abundant metal oxides or phosphides is essentially limitless, it should be possible to boost the H_2 generation performance of a MOF-based photocatalytic system by simply choosing the appropriate co-catalyst.

This chapter describes the investigation of different transition metal-based co-catalysts with MIL-125-NH_2. MIL-125 is the first titanium-based MOF reported, consisting of a titanium-oxo cluster and terephthalate (BDC) as the organic linker.[72] Replacing this linker with 2-aminoterphthalate (NH_2-BDC) results in the same structure (MIL-125-NH_2), but with visible light absorption as opposed to the UV offered by MIL-125,[92] making it a promising photocatalyst.[93] Variation of the co-catalysts alters the second and third major photocatalytic steps of charge separation and catalytic reaction, which can significantly promote the overall activity of the MIL-125-NH_2-based photocatalytic system. Indeed, all the co-catalysts (Ni_2P, NiO, CoP, Co_3O_4, Fe_2O_3, CuO and Pt nanoparticles) investigated were found to significantly improve the activity of MIL-125-NH_2, with the Ni_2P/MIL-125-NH_2 system demonstrating the highest catalytic activity.

2.2 Synthesis and Characterization

$MIL\text{-}125\text{-}NH_2$ was synthesised based on a reported procedure (see section S2.1, Appendix)[94] and subsequently characterised by means of powder X-ray diffraction (PXRD), nitrogen adsorption-desorption isotherms, scanning electron microscopy (SEM) and UV-vis absorption spectroscopy. The PXRD pattern of the bulk $MIL\text{-}125\text{-}NH_2$ is in great agreement with the pattern derived from the single-crystal structure and the nitrogen isotherms revealed the microporous nature of the $MIL\text{-}125\text{-}NH_2$, with a BET surface area of ~1200 $m^2\ g^{-1}$ (**Figure 2.1**A, B). The $MIL\text{-}125\text{-}NH_2$ crystals display a circular-disc-type morphology with a mean particle size of around 800 nm, as illustrated by the SEM images (**Figure 2.1**C). The UV-vis absorbance spectrum of the free ligand $NH_2\text{-}H_2BDC$ and the Kubelka-Munk representation of the UV-vis diffuse reflectance spectrum of $MIL\text{-}125\text{-}NH_2$ (**Figure 2.1**D), indicate that the latter exhibits a red shift. This red shift leads to a strong absorption in the 330-500 nm range and is ascribed to the ligand-to-metal charge transfer (LMCT).[86]

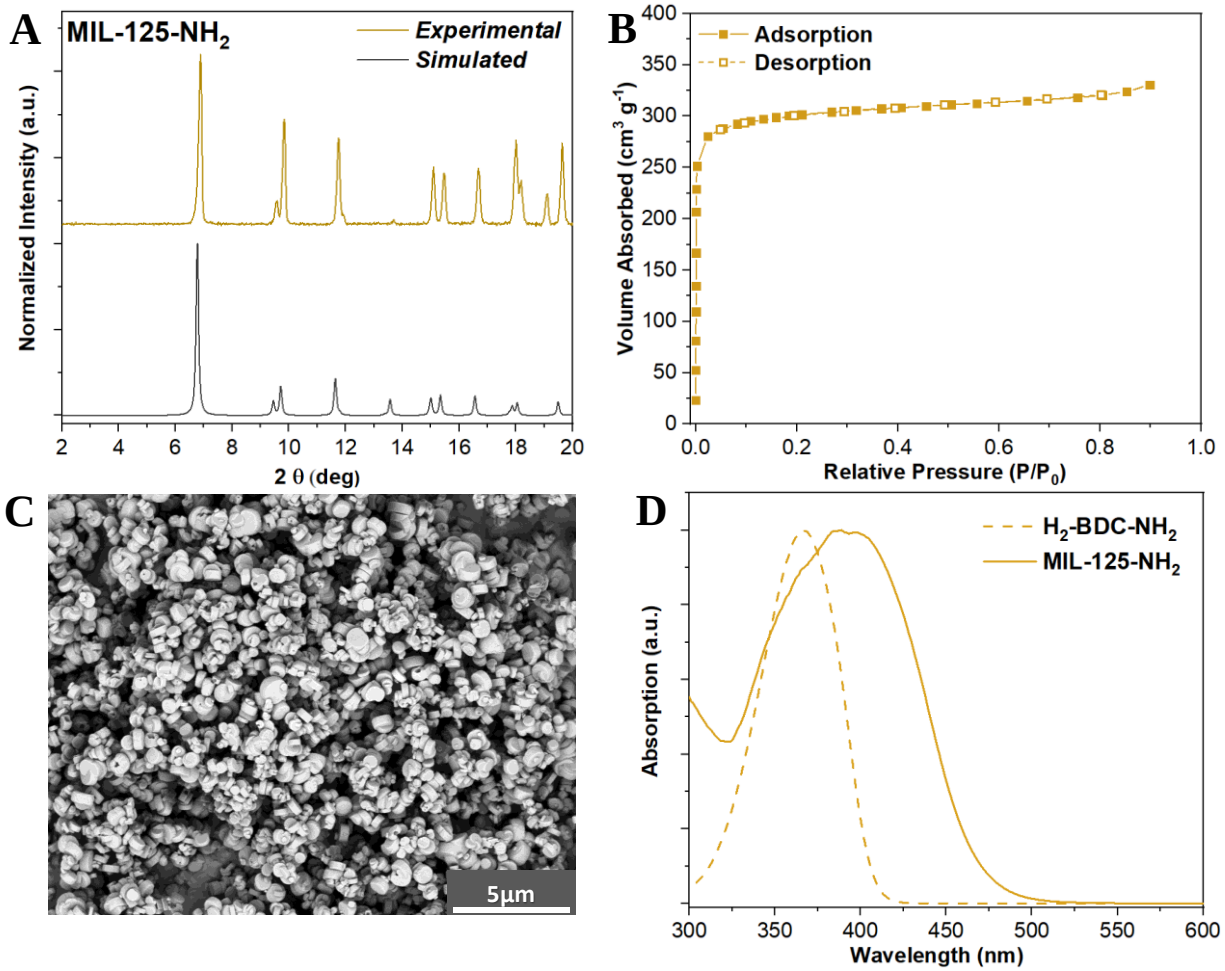

Figure 2.1: (*A) PXRD patterns, (B) N_2 adsorption-desorption isotherm and (C) SEM image of the as-synthesized $MIL\text{-}125\text{-}NH_2$. (D) UV-Vis absorbance of free ligand $H_2BDC\text{-}NH_2$ and Kubelka-Munk representation of diffuse reflectance of $MIL\text{-}125\text{-}NH_2$.*

A range of transition metal phosphide and oxide co-catalysts (Ni_2P, NiO, CoP, Co_3O_4, Fe_2O_3 and CuO) was selected, based on their availability and low cost compared to noble-metal nanoparticles, which are commonly used in photocatalytic water splitting.[90a] The selected co-catalysts were synthesised based on a MOF-derived technique (**Figure 2.2**).[95] When this synthetic method is used, the self-sacrificing MOF acts as a structure directing template allowing for a more rational preparation of NPs.[96] Specifically, the use of MOFs as precursors can lead to the generation of nano-sized materials, with higher specific surface areas, thermal stability and catalytic activity.[97] For example, Yu *et al.* developed an efficient electrocatalyst through an easy and scalable one-pot thermal treatment of bimetallic zeolitic imidazolate frameworks (ZIFs).[98] For more information about the synthetic protocols employed see section S2.1 in the Appendix.

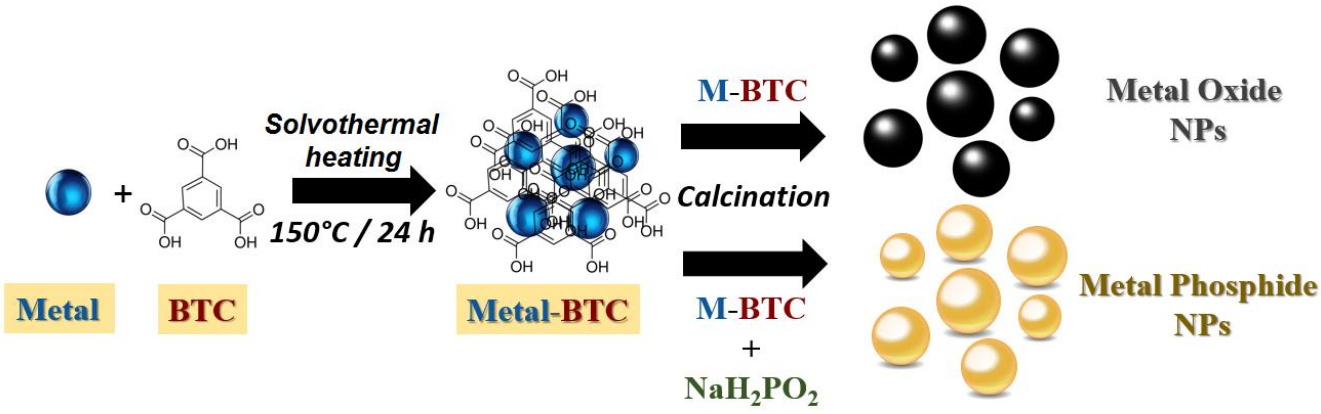

Figure 2.2: *Schematic illustration of the synthetic procedure employed for the generation of transition metal oxide and phosphide NPs.*

The formation, phase purity and morphology of the MOF-derived NPs were explored through PXRD, nitrogen sorption isotherms and transmission electron microscopy (TEM). The PXRD patterns of the as-synthesised NiO, Ni_2P, Co_3O_4, CoP, Fe_2O_3 and CuO NPs are in good agreement with the simulated and previously reported patterns (**Figure 2.3**).[99] The TEM images revealed the morphology and size of these NPs; the NiO, Ni_2P, Co_3O_4, and CuO NPs illustrate a spherical shape with a mean size of 10 - 20 nm, whereas Fe_2O_3 NPs demonstrate a size of 200 nm (**Figure 2.4**). The dimensions of the rod-shaped CoP NPs are approximately 20 nm x 6 nm, which is in agreement with previous reports of MOF-derived CoP NPs.[100]

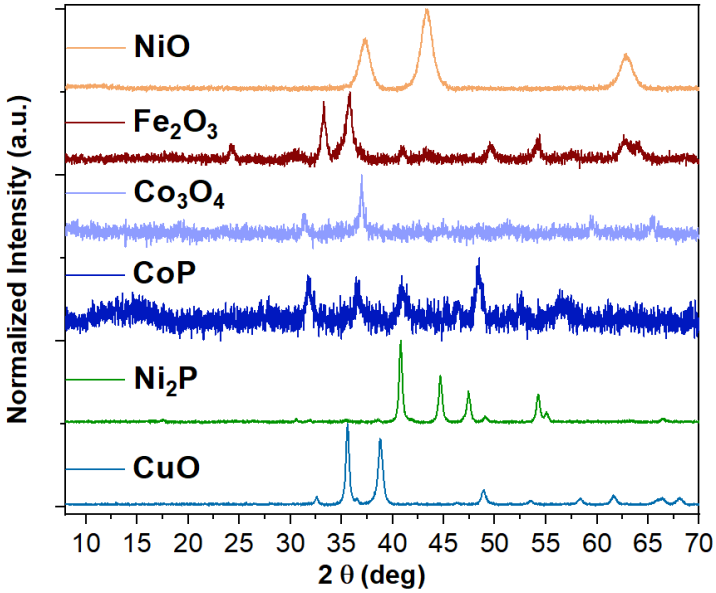

Figure 2.3: *PXRD patterns of MOF-derived NiO, Fe_2O_3, Co_3O_4, CoP, Ni_2P and CuO NPs.*

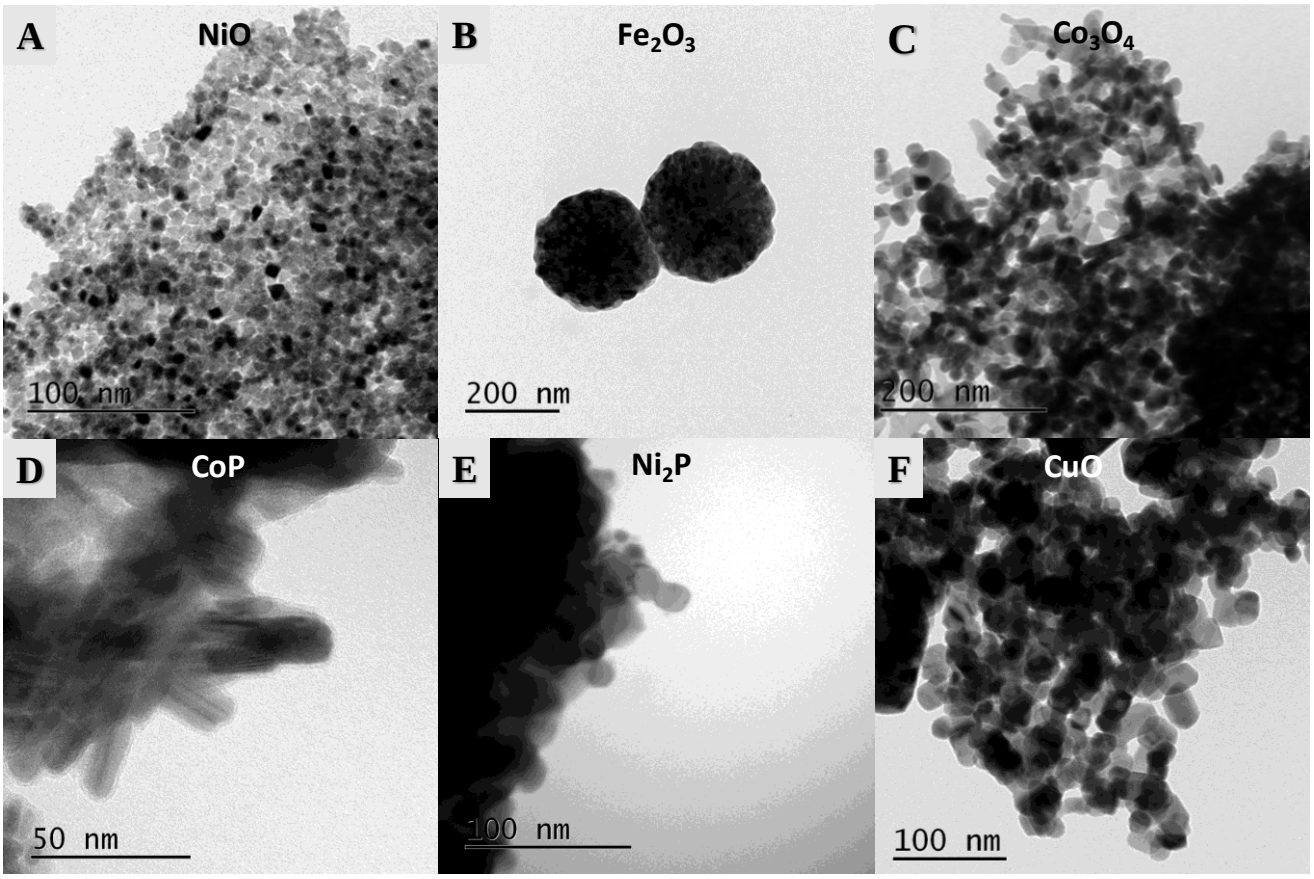

Figure 2.4: *High-resolution TEM images of: (A) NiO, (B) Fe_2O_3, (C) Co_3O_4, (D) CoP, (E) Ni_2P and (F) CuO NPs.*

2.3 Photocatalytic Activity

In order to assess the photocatalytic performance of the different co-catalyst/MIL-125-NH_2 systems, the crystalline powder of MIL-125-NH_2 was physically mixed with varying amounts of the co-catalyst NPs. Such simple incorporation of the co-catalyst (physical mixture) is advantageous, considering that complicated steps are prevented (e.g. photodeposition[90a, 101] or encapsulation[102]) and the loaded amounts of the co-catalysts are highly controllable and reproducible. The ratio between the co-catalyst and the MIL-125-NH_2 amount is crucial, since there is a volcano-type trend between the added amount of a given co-catalyst and the photocatalytic activity of a system. In principle, the addition of the co-catalyst increases the production of H_2, since these NPs play a key role in facilitating the electron-hole separation within the MIL-125-NH_2 (Figure S.2). However, further increase in the amount of the co-catalyst decreases the photocatalytic performance of the system. This is attributed to the fact that an excess amount of the co-catalyst leads to restricted penetration of the incident light in the photocatalytic solution, and can hinder the contact between MIL-125-NH_2 and the electron donor.[21a]

The photocatalytic solution used for these experiments includes acetonitrile (CH_3CN), triethylamine (TEA) as the electron donor and water in a volumetric ratio of 79: 16: 5 v/v/v, respectively. The optimal amounts of each co-catalyst (i.e., the amount that produced the highest H_2 evolution rate) varies within the range of 7.9 - 10.2 wt.% (Figure S.2). Interestingly, as illustrated in **Figure 2.5**, the optimised Ni_2P/MIL-125-NH_2 photocatalytic system displays the highest hydrogen evolution rate of 1230 μmol h^{-1} g^{-1} (over 8 h), followed by NiO/MIL-125-NH_2, which exhibits a rate of 1084 μmol h^{-1} g^{-1}. The performances of the Co_3O_4/MIL-125-NH_2 and CoP/MIL-125-NH_2 systems are comparable. The optimised Fe_2O_3/MIL-125-NH_2 system exhibits a H_2 evolution rate of 435 μmol h^{-1} g^{-1}, followed by the CuO/MIL-125-NH_2 system which demonstrates the lowest rate of 139 μmol h^{-1} g^{-1}. It is worth mentioning that when only the co-catalysts were subjected to photocatalytic test, only traces of H_2 were detected (Table S.1). Likewise, without any co-catalysts, MIL-125-NH_2 exhibits a very low H_2 evolution rate of 51.2 μmol h^{-1} g^{-1}.The significantly inferior performance of solely the MIL-125-NH_2 highlights that the incorporation of the co-catalysts in the system remarkably promotes the H_2 evolution rate.

Inspired by these results, we wanted to evaluate the efficiency of the best performing Ni_2P/MIL-125-NH_2 using a metric based on the incident radiation. For that, we calculated the apparent quantum yield (AQY) at 450 nm through Ferrioxalate actinometry (see section S2.3, Appendix).[103] Ni_2P/MIL-125-NH_2 demonstrates an AQY value of 6.6 %, which is among the highest reported efficiencies for MOFs[69b, 90b, 104] and comparable to leading photocatalysts (Table S.2).[105]

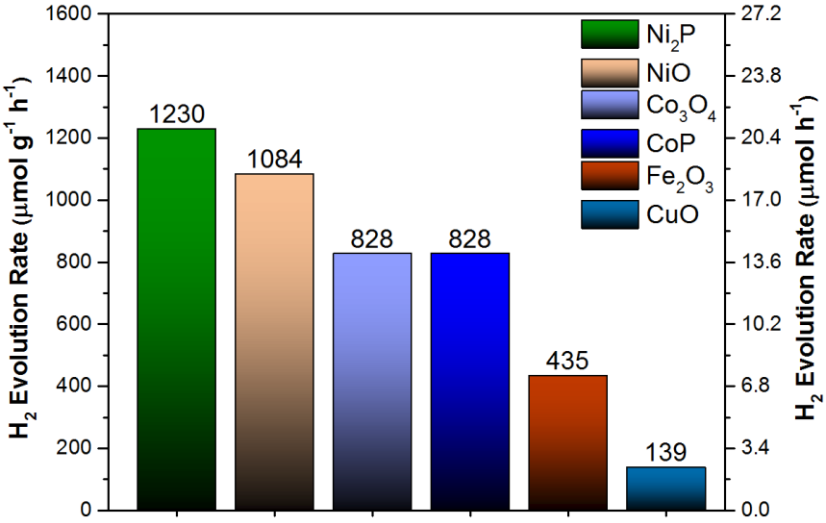

Figure 2.5: *Comparison of H_2 evolution rates (with respect to MIL-125-NH_2) of 9.2 wt.% Ni_2P/MIL-125-NH_2, 8.6 wt.% NiO/MIL-125-NH_2, 7.9 wt.% Co_3O_4/MIL-125-NH_2, 8.8 wt.% CoP/MIL-125-NH_2, 10.2 wt.% Fe_2O_3/MIL-125-NH_2 and 7.9 wt.% CuO/MIL-125-NH_2 under visible light irradiation for 8 hours.*

After the photocatalytic test the stability of MIL-125-NH_2 and co-catalysts was confirmed by means of PXRD, X-ray photoelectron spectroscopy (XPS), SEM, Energy-dispersive X-ray spectroscopy (EDX) and N_2 sorption isotherms (for more information see section S2.4 in the Appendix). Recycling experiments for three consecutive cycles of 12 hours were performed on both Ni_2P/MIL-125-NH_2 and NiO/MIL-125-NH_2 systems. The results showed that the photocatalytic activity of both systems is stable throughout the cycles (**Figure 2.6**), while PXRD experiments confirm that their crystallinity is retained (Figure S.8).

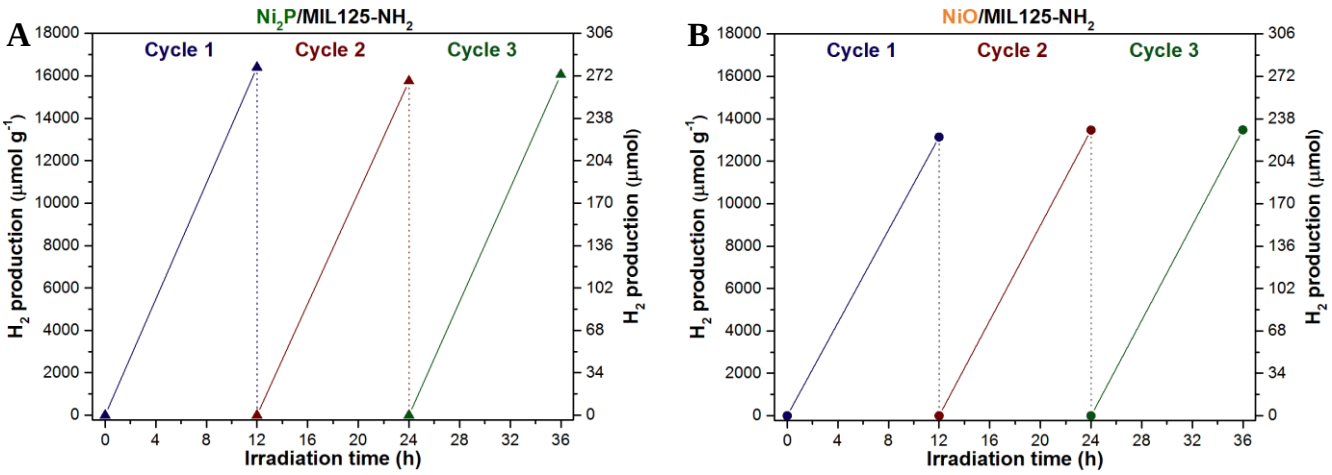

Figure 2.6: *Recycling photocatalytic performance of (A) Ni_2P/MIL-125-NH_2 and (B) NiO/MIL-125-NH_2 for 3 consecutive cycles.*

2.4 Mechanism

In order to obtain insights into the charge separation efficiency and the synergy between the MIL-125-NH_2 and the different co-catalysts, photoluminescence (PL) and transient PL experiments for each co-catalyst/MIL-125-NH_2 system were performed (**Figure 2.7** and Section S2.5, Appendix). In principle, the addition of the co-catalyst can quench the PL emission of the photocatalyst, since they withdraw the photoexcited electrons and thus prevent the undesired electron-hole recombination. In preparation for the PL experiments, MIL-125-NH_2 was mixed with different amounts of co-catalyst NPs and the mixtures were subsequently suspended in the photocatalytic solution. To assess how efficiently each co-catalyst inhibits the electron-hole recombination, the emission quenching was quantified by integrating the PL curves of the MIL-125-NH_2 and the samples with the optimal amount of each co-catalyst, $PL_{co\text{-}cats}/PL_{MOF}$ (**Table 1**). The charge separation efficiency follows the order: $Ni_2P > CoP \approx Co_3O_4 > Fe_2O_3 > CuO > NiO$. The PL results are consistent with the photocatalytic performance (H_2 generation rates) of each system, apart from the NiO/MIL-125-NH_2 system. As can be seen in **Figure 2.7**, the NiO NPs are less efficient at attracting the photogenerated electrons, yet this system exhibits one of the highest photocatalytic H_2 generation rates.

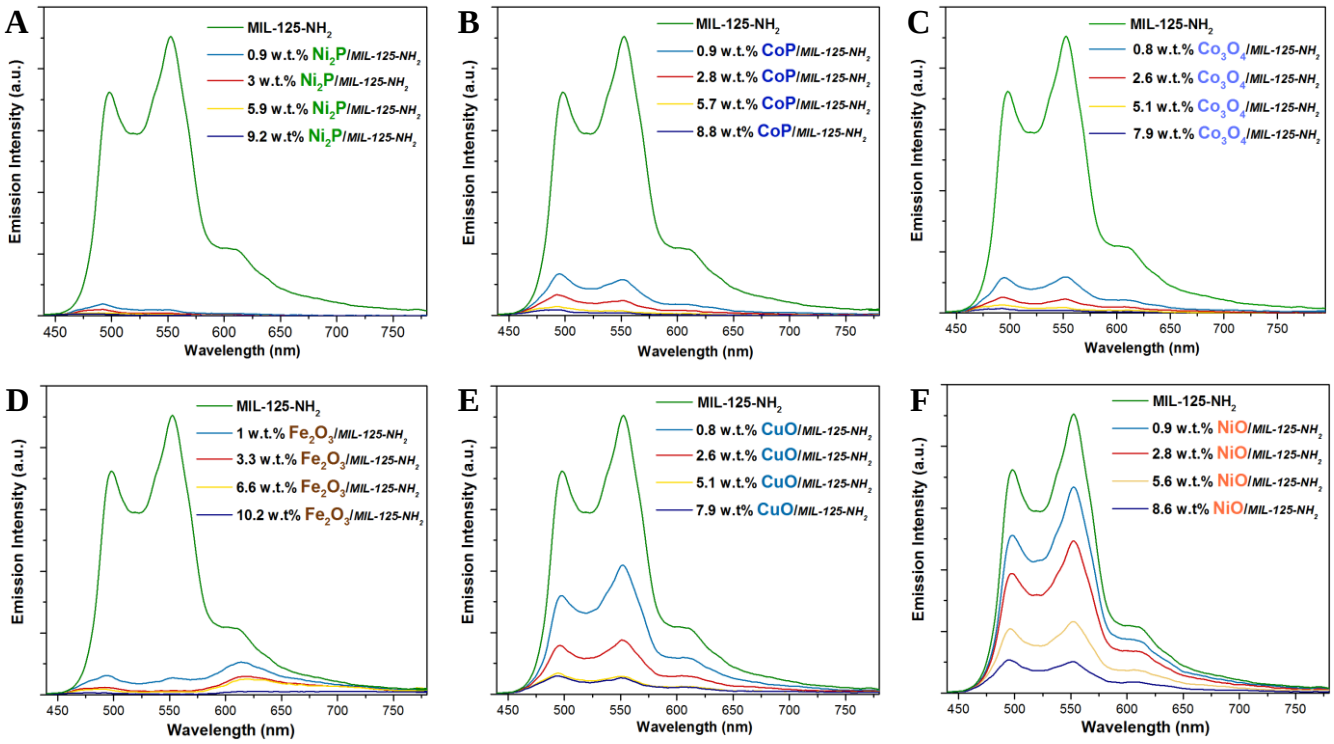

Figure 2.7: *PL spectra of the suspensions of MIL-125-NH_2 with different amounts of: (A) Ni_2P, (B) CoP, (C) Co_3O_4, (D) Fe_2O_3, (E) CuO and (F) NiO. The excitation wavelength was 420 nm.*

Table 1: *Photoluminescent emission quench ($PL_{co\text{-}cat}/PL_{MOF}$) and current density for different co-catalysts.*

Co-catalyst	Ni_2P	CoP	Co_3O_4	Fe_2O_3	CuO	NiO
$PL_{co\text{-}cat.}$ / PL_{MOF}, %	0.7	2.6	2.5	6	17.2	28.8
Current Density, mA cm^{-2} *at -0.9 V versus* Ag/Ag^+	-0.07	–	–	–	–	-0.22

In order to gain a better understanding of the discrepancy between the PL results and the photocatalytic H_2 generation rate of the NiO/MIL-125-NH_2 system, electrochemical measurements were performed (cyclic voltammetry, CV and linear scan voltammetry, LSV). The intrinsic activity of NiO in catalysing the H_2 evolution reaction was determined and compared with that of Ni_2P NPs. The intrinsic catalytic activities of the co-catalysts were compared in terms of current density. To ensure that the conditions of the electrochemical experiments are comparable to those applied in photocatalysis, a solution containing acetonitrile and water (90:10) was used, with 0.1 M tetrabutylammonium perchlorate (TBAP), to ensure the availability of conductive ions in the electrolyte. It was established that the current density (intrinsic catalytic activity) of NiO NPs is notably higher than that of the Ni_2P NPs (i.e., -0.22 and -0.07 mA cm^{-2} for NiO and Ni_2P, respectively at -0.9 V versus Ag/Ag^+), compensating for the inferior performance of the former in withdrawing electrons (**Table 1** and Figure S.11). Hence, the good photocatalytic activity of the NiO/MIL-125-NH_2 system with respect to H_2 generation can be attributed to the superior intrinsic activity of NiO in catalysing the reduction of protons/H_2O to H_2. For more information about the electrochemical measurements see section S2.6 in the Appendix.

2.5 Comparison of Ni_2P to Pt

In order to compare the performance of Ni_2P/MIL-125-NH_2 with that of Pt/MIL-125-NH_2, we synthesized "naked" Pt NPs[106] with a size of ~19 nm (for more information, see section S2.7 in the Appendix). We then mixed them with MIL-125-NH_2 and investigated the performance of this system under the same conditions that were used for Ni_2P/MIL-125-NH_2. The amount of Pt NPs was varied and the optimum Pt/MIL-125-NH_2 system produces H_2 with a maximum evolution rate of 646 μmol g^{-1} h^{-1}, which is almost half of that demonstrated by the noble-metal-free Ni_2P/MIL-125-NH_2 system (**Figure 2.8**).

The effectiveness of charge separation with the Pt/MIL-125-NH_2 system was studied by PL emission spectroscopy. **Figure 2.9**A compares the PL spectra of MIL-125-NH_2 with various amounts of Pt NPs and the corresponding amounts of Ni_2P NPs. It is apparent that the overall PL quenching with the Ni_2P/MIL-125-NH_2 system is more drastic than that of Pt/MIL-125-NH_2, while the optimized amount of Pt NPs (2 wt.%, in terms of photocatalytic activity) does not induce complete quenching of the PL emission, which is the case for the optimized 9.2 wt.% Ni_2P/MIL-125-NH_2 system. In order to gain further insights into the charge separation efficiency, photochemical chronoamperometry measurements were carried out (**Figure 2.9**B) and showed that upon illumination both Ni_2P/MIL-125-NH_2 and Pt/MIL-125-NH_2 exhibit comparable initial photocurrents at the early stage, but the photocurrent in the presence of Pt NPs decays faster over time. These results are in agreement with those obtained through PL spectroscopy and suggest that the charge recombination in Pt/MIL-125-NH_2 is more pronounced and faster than in the Ni_2P/MIL-125-NH_2 system.

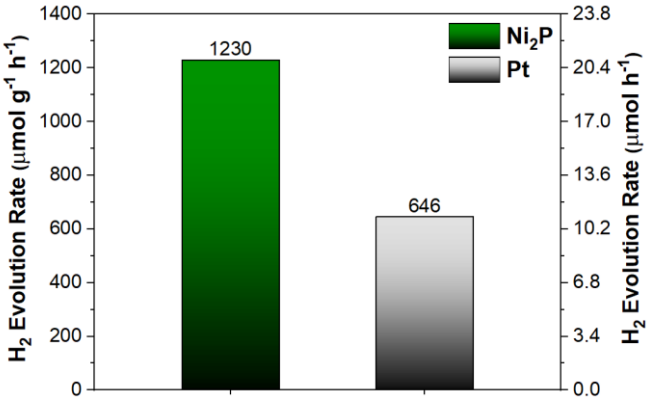

Figure 2.8: *Comparison of the photocatalytic activity of MIL-125-NH_2 with optimized amounts of Ni_2P (green) and Pt (gray) NPs as co-catalysts.*

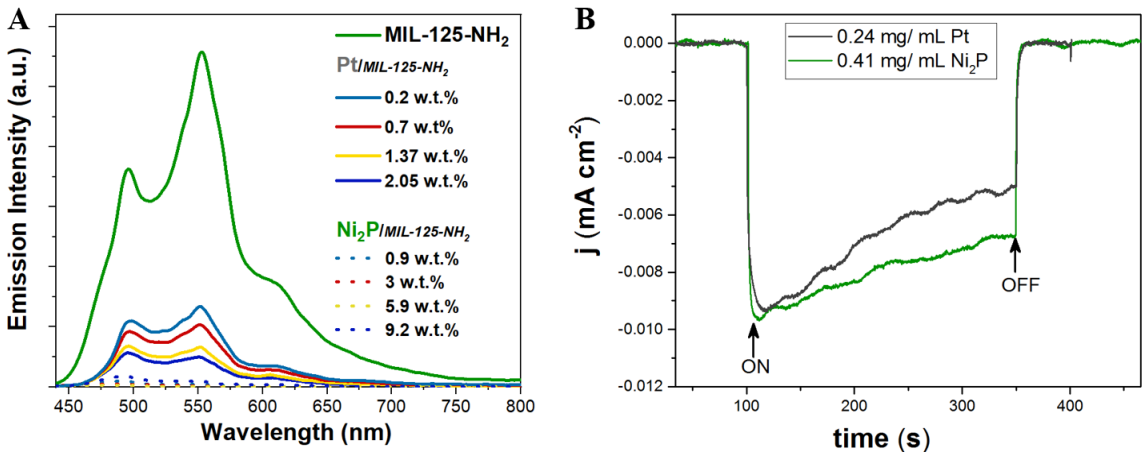

Figure 2.9: *(A) Comparison of the PL spectra of MIL-125-NH_2 with and without various amounts of Pt NPs (solid lines) and the corresponding amounts of Ni_2P NPs (dotted lines). Excitation at 420 nm. (B) Photocurrent responses of MIL-125-NH_2 with the optimized amounts of Ni_2P (9.2 wt.%, green) and Pt (2.05 wt.%, black).*

2.6 Summary and Conclusions

There are relatively few examples of noble metal-free MIL-125-NH_2-based photocatalytic systems explored toward the H_2 evolution reaction. The majority of the investigated systems in this study outperform other systems based on MIL-125-NH_2 with noble metal co-catalysts – such as Pt and Au NPs,[69b, 90a, 107] as well as with abundant co-catalysts (e.g., Co-dioxime-diimine).[69b] More detailed comparison between the best performing Ni_2P/MIL-125-NH_2 with other MOF-based systems in the literature can be found in section S2.9 in the appendix.

From this study it is apparent that the photocatalytic performance of a system is not only influenced by the individual performance of the MOF (in terms of light absorption and charge separation within the structure) or the co-catalyst (in terms of intrinsic catalytic activity), but is also highly determined by the synergy between these two components. The last step of H_2 formation and desorption is associated solely with the intrinsic catalytic activity of the co-catalyst. However, despite the importance of high intrinsic activity, the last step cannot take place if there is not sufficient electron transfer from the MOF to the co-catalyst.

The literature contains many examples of visible light-active MOFs whose photocatalytic activity could be substantially improved by carefully selecting an appropriate co-catalyst.[86, 90, 108] The criteria for the co-catalyst selection should relate mainly to its synergy with the photocatalyst, rather than to its intrinsic catalytic activity. The target of this strategy is to achieve efficient interactions between the two components, ensuring efficient migration of electrons from the MOF to the co-catalyst. Transition metal phosphides and oxides have emerged as promising co-catalysts for the H_2 evolution reaction and their use in MOF-based photocatalytic systems can lead to performances similar to those achieved by traditional semiconductors.

Chapter 3 Variation of Electron-Donors and Dual-Functional Photocatalysis

Parts of this chapter are based on published work:

'Concurrent Photocatalytic Hydrogen Generation and Dye Degradation Using MIL-125-NH_2 under Visible Light Irradiation'

S. Kampouri, T. N. Nguyen, M. Spodaryk, R. G. Palgrave, A. Züttel, B. Smit, K. C. Stylianou,
Adv. Funct. Mater., 2018, 28, 1806368

Reprinted in adapted versions with permission from Ref. 87 Copyright © 2018 John Wiley and Sons

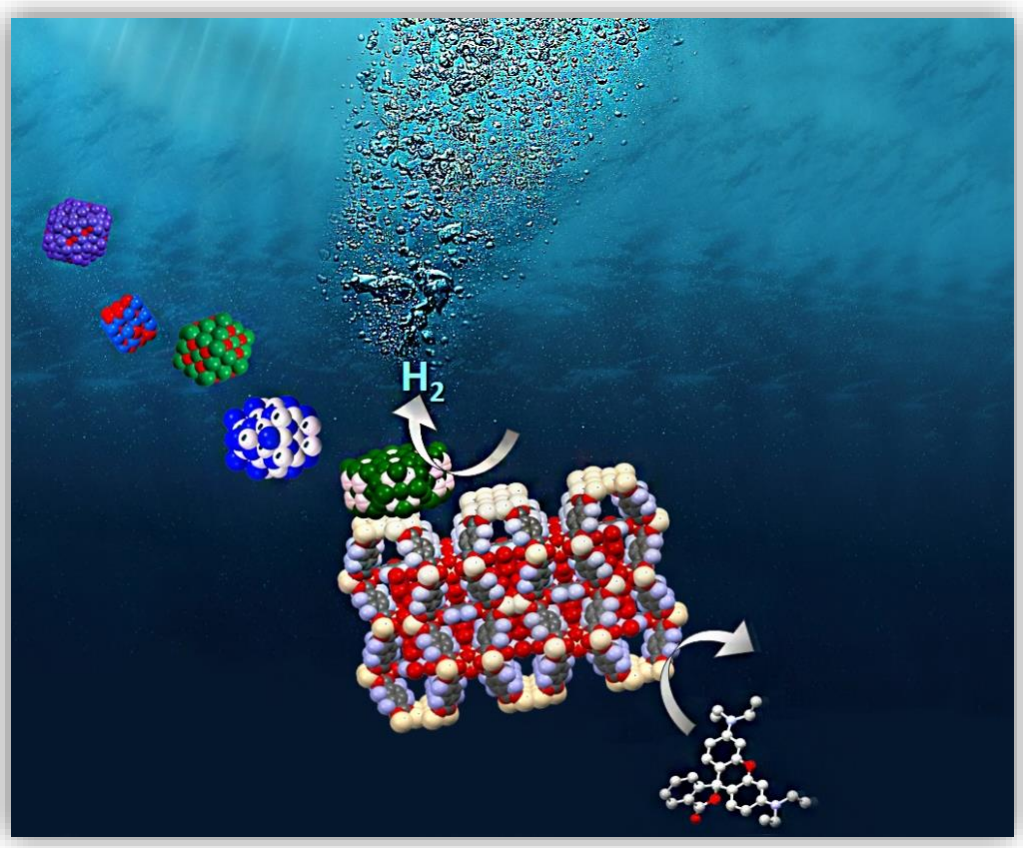

S. Kampouri's contribution: Conceiving the project's idea, synthesis of materials, characterization (powder X-ray diffraction, UV-Vis absorbance spectroscopy), designing and performing experiments (photocatalytic experiments, trapping experiments of active species), writing text and constructing figures.

3.1 Introduction

Similar to semiconductor photocatalysis, in the field of MOFs, sacrificial agents are frequently employed. In particular sacrificial electron donors are always employed with MOF-based photocatalytic systems for the H_2 evolution reaction. As previously mentioned, electron donors are used to scavenge the photogenerated holes, preventing the thermodynamically more demanding O_2 production reaction, thus boosting the H_2 generation.[109] In principle, an efficient electron donor should exhibit thermodynamic adequacy with the photocatalyst, irreversible transformation into inert molecules and fast kinetics of oxidation.[29b] Depending on individual photocatalytic systems, other potentially desirable characteristics for electron donors include stability across a certain pH range, diffusion into the pores of the photocatalyst, and being used in high concentrations without causing any degradation or collapse to the other components present in the system (e.g. photocatalyst, co-catalyst).

Currently, many of the substances used as electron donors are toxic and hazardous (e.g., TEA, TEOA, methanol) or an energy resource themselves (e.g. methanol and ethanol) and their introduction increases the cost of the photocatalytic system.[27, 110] Optimizing the activity and abundancy of the MIL-125-NH_2-based photocatalytic system in the previous chapter prompted us to focus on another important factor inhibiting the real-life application of such systems, which is the utilization of electron donors. In this chapter, first the photocatalytic performance of the Ni_2P/MIL-125-NH_2 system with different typical examples of electron donors is explored. Then, in an attempt to address the limitations related to the utilization of electron donors, an organic pollutant (Rhodamine B) is used as a replacement of typical electron donors. Considering that the active species for the H_2 evolution reaction (e^-) can be complementary to those for the organic pollutant's degradation reaction (h^+), our proof-of-concept approach envisions dual-functional photocatalysis for the simultaneous production of hydrogen and pollutant degradation using the Ni_2P/MIL-125-NH_2 system, under visible light radiation. It should be mentioned here that to date, there are relatively few reports of systems combining the photocatalytic hydrogen evolution with the degradation of organic compounds, with the UV-active semiconductors (e.g. TiO_2) being the most studied materials.[111]

3.2 Variation of Electron-Donors

In this section, I describe the photocatalytic performance of the Ni_2P/MIL-125-NH_2 system with different sacrificial reagents as electron donors. In addition to TEA, four other commonly used electron-donors were investigated; L-ascorbic acid (H_2A), methanol (MeOH), ethanol (EtOH), and TEOA.[88a, 112] The amount of water was kept constant at 5% v/v in all examined photocatalytic solutions. For more information about the different photocatalytic solutions explored see section S3.1 in the Appendix.

As shown at **Figure 3.1**A, varying the electron donors has a profound impact on the H_2 production rate. Using TEA and TEOA promotes the H_2 generation, however the H_2 evolution rate in the case of TEOA is ~6 times lower than that when TEA is employed (215 vs. 1230 μmol h^{-1} g^{-1}). When EtOH or MeOH is used, the Ni_2P/MIL-125-NH_2 system exhibits remarkably inferior activity, with H_2 evolution rates of only 38 and 26 μmol h^{-1} g^{-1} for EtOH and MeOH, respectively. When L-ascorbic acid is introduced as the electron donor, no H_2 evolution is observed. Both Ni_2P and MIL-125-NH_2 retain their stability after all these photocatalytic tests (**Figure 3.1**B). The inactivity of L-ascorbic acid can be associated with the fact that the photocatalytic solution contains significant amount of acetonitrile, which is a much less polar solvent than water and therefore can inhibit the dissociation of H_2A into HA^- and the subsequent oxidation of HA^- to $HA^{\bullet}$ as in aqueous media. EtOH and MeOH are weaker bases than TEA and TEOA, which may explain why they are less effective electron donors.

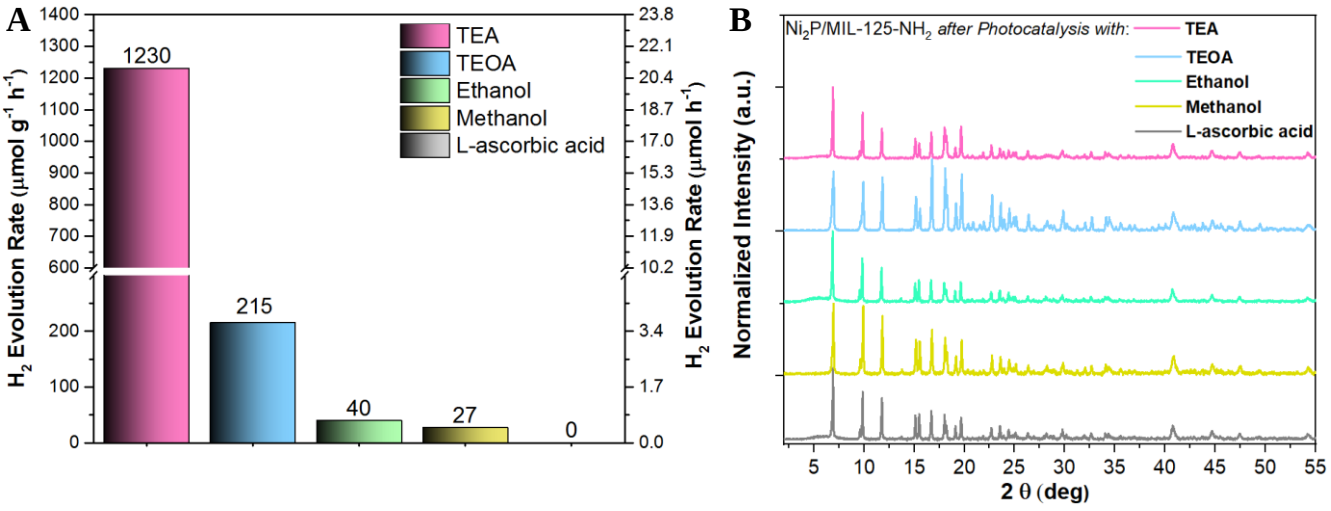

Figure 3.1: *(A) Comparison of H_2 evolution rates of Ni_2P/MIL-125-NH_2 with different electron donors, under visible light irradiation for 8 h, (B) PXRD patterns of 9.2 wt.% Ni_2P/MIL-125-NH_2 after the photocatalytic test with different electron donors.*

Generally, in every photocatalytic reaction the electron transfer processes should be faster than the charge recombination. Furthermore, since the same number of electrons and holes are to be used, the rate of the oxidation reaction of the electron donors should be sufficiently high so as not to slow down the water reduction process. It appears that the oxidation of EtOH and MeOH is not adequate within the Ni_2P/MIL-125-NH_2 system, leading to the inferior performance of these photocatalytic systems. Finally, the higher H_2 evolution rate of the photocatalytic system with TEA compared to that with TEOA can be attributed to the difference in the concentrations used (TEA: 7.2 M, TEOA: 0.01 M, Table S.3). This effect can also be observed from the electrochemical measurements (CV) of TEA and TEOA at these concentrations. More specifically, when scanned toward positive potential, the current density of the anodic peak with TEA (onset at 1.4 V vs. Ag/Ag^+) is an order of magnitude higher than that of TEOA (and the other electron donors). In principle, the current density should be proportional to the rate of oxidation and the concentration of the electron donors. This indicates that even if the oxidation of TEA and TEOA occurs at comparable rates, the ability to use a much higher concentration of TEA with the Ni_2P/MIL-125-NH_2 system is important for the efficiency of the electron donation process. It is worth noting that we attempted to increase the concentration of TEOA in the photocatalytic system, but this led to the partial or complete degradation of MIL-125-NH_2. For more information about the electrochemical experiments, see section S3.1.1 in the Appendix.

3.3 Dual-Functional Photocatalytic Activity

As the above results demonstrate, using electron donors can favourably influence the performance of a photocatalytic system toward the H_2 evolution reaction. Nevertheless, incorporating electron donors into a photocatalytic system can induce toxicity (in the case of TEA, TEOA, and MeOH) and increase the cost of the system. In an attempt to address these limitations and provide a proof-of-concept for an alternative approach, we explored a system in which the electron donor was replaced by a typical organic pollutant, envisioning H_2 generation coupled with water remediation.

As mentioned previously, the main active species required for pollutants oxidation can be complementary to those needed for the photocatalytic H_2 evolution reaction. However, the challenge of combining these two reactions lies in the fact that the photocatalytic H_2 production is unlikely to occur in aerated conditions, since O_2 acts as an electron scavenger, whereas the photocatalytic oxidation of organic pollutants is significantly promoted in the presence of O_2. Hence, the photocatalyst should be capable of degrading the organic pollutant with the holes being the dominant active species and the electrons being transferred to protons (H^+) or water molecules to generate H_2.

This idea of dual-functional photocatalysis was explored by using the optimized 9.2 wt.% Ni_2P/MIL-125-NH_2 system and Rhodamine B (RhB) as a representative of organic pollutants in wastewater. RhB is a hazardous dye widely used in the cosmetic, textile, paint and plastic industry,[113] and its photocatalytic degradation has been extensively studied with MOFs.[114] RhB is toxic and its presence in water can result in teratogenic and carcinogenic effects on public health.[66c, 115]

The RhB concentration was varied in the CH_3CN-based solution with water, in order to identify the favourable conditions for H_2 production. As illustrated in **Figure 3.2**A, when the dye concentration initially increases, the H_2 evolution rate is promoted, indicating that more RhB molecules are available to interact with the photoexcited holes. Further increase in RhB concentration causes a decrease in the amount of H_2 generated, since a portion of the incident light is inhibited from approaching the MIL-125-NH_2. The H_2 evolution rate reaches a maximum value of 335 μmol h^{-1} g^{-1} at a RhB concentration of 1.2 ppm in the photocatalytic solution (0.02 mg in 17 mL). The H_2 evolution rate is lower when RhB is used as an electron donor than when TEA is used. This is in accordance with the basicity of these substances and the fact that the TEA concentration used is significantly higher than that of RhB. In addition, the smaller size of the TEA molecules could allow them for more efficient diffusion through the porous assemblies of MIL-125-NH_2, and thus provide more effective electron donation. The overall advantage of using RhB as an electron donor relies on the significant benefit of dual-functional photocatalysis.

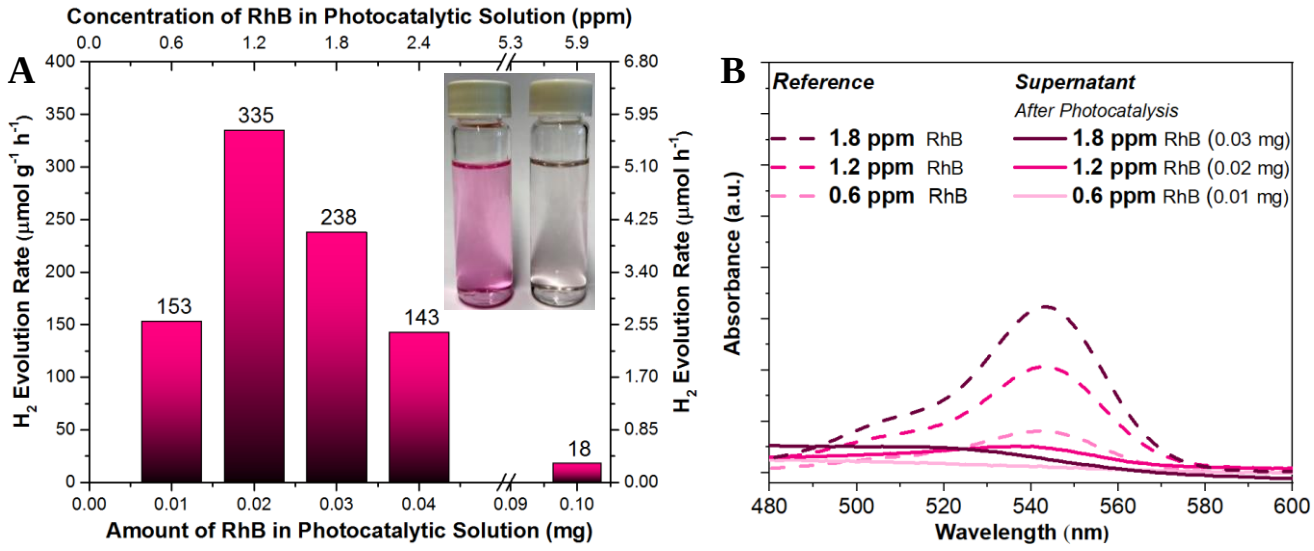

Figure 3.2: *(A) Photocatalytic H_2 evolution rates of Ni_2P/MIL-125-NH_2 in 17 mL of photocatalytic solutions with different concentrations of RhB, under visible light irradiation for 8 h. Inset: photograph showing the difference in the color of the photocatalytic solution before and after the photocatalytic test, with initial RhB concentration of 1.2 ppm. (B) UV-Vis spectra of reference samples and supernatants after the photocatalytic RhB decolorization process.*

After the photocatalytic test, the RhB concentration was monitored for the three best performing solutions (initial RhB concentration of 0.6, 1.2 and 1.8 ppm, **Figure 3.2**B). For this purpose, the UV-Vis absorbance spectra of the supernatants after the photocatalytic test were collected. With an initial RhB concentration of 0.6 ppm, the dye is completely degraded and with concentration of 1.2-1.8 ppm, the dye concentration substantially decreases. Control experiments were performed to confirm that RhB was photodegraded and not absorbed by MIL-125-NH_2. The Ni_2P/MIL-125-NH_2 system was immersed in 1.2 ppm RhB solution and kept in the dark for 24 h. The supernatant was then collected and subjected to UV-vis absorbance spectroscopy. Interestingly, there is no notable difference between the RhB concentrations before and after this test (**Figure 3.3**A). Moreover, when 1.2 ppm RhB solution was irradiated in the absence of MIL-125-NH_2, there was no change in the dye concentration, confirming that no self-photolysis of RhB occurs (**Figure 3.3**B). These results indicate that RhB is indeed involved in the photocatalytic process for H_2 evolution.

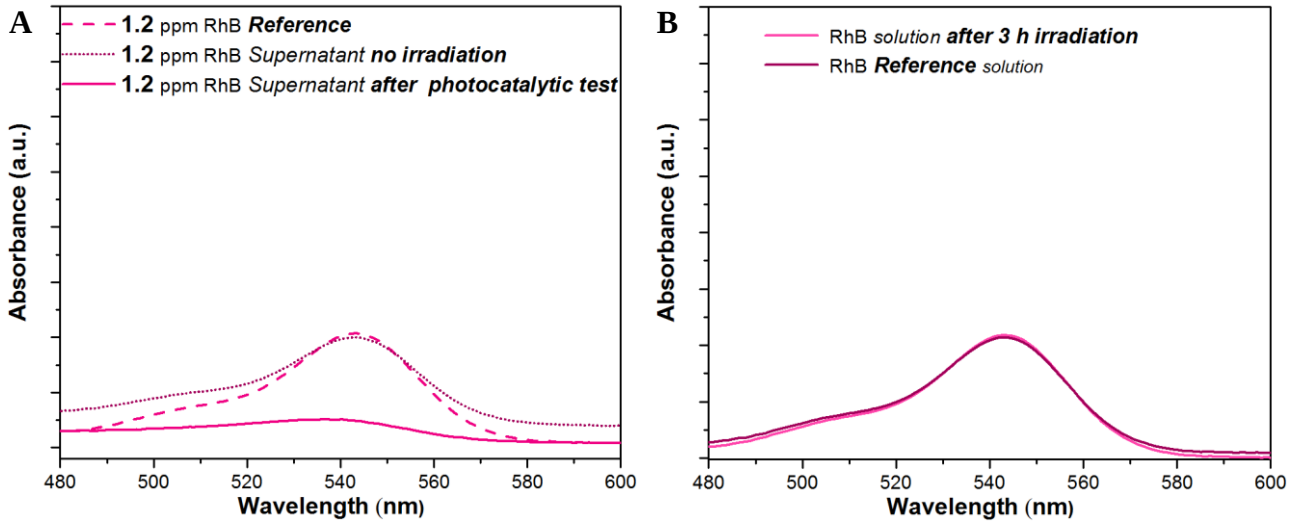

Figure 3.3: *Control experiments: (A) UV-vis spectra of 1.2 ppm RhB solution (reference), the supernatant of the same solution combined with Ni_2P/MIL-125-NH_2 after 24 h in the dark and after the photocatalytic test. (B) UV-Vis spectra of 1.2 ppm RhB solution (reference) and same solution after 3 h irradiation with visible light.*

To provide further confirmation of the role of RhB and elucidate the photocatalytic mechanism, trapping experiments of active species were carried out using the optimal RhB concentration (1.2 ppm, 2.5 μM) and 0.01 M tert-Butanol as •OH radical scavenger or 0.01 M TEOA as hole scavenger (more information in section S3.2, Appendix). As displayed in **Figure 3.4**, the addition of TEOA and tert-Butanol leads to 11.2 % and 18.7 % decrease in the RhB concentration, respectively. This confirms that both the holes and •OH radicals are involved in this process, with the former being the more dominant species. These results further prove that RhB acts as a sacrificial electron donor, scavenging the photoexcited holes and promoting the H_2 generation, which leads to its decomposition, as

demonstrated by UV-Vis spectroscopy. After all the photocatalytic experiments, the stability of the samples was verified by means of PXRD (Figures S18 and S19, Appendix). For more information about the control experiments see section S3.2 in the Appendix.

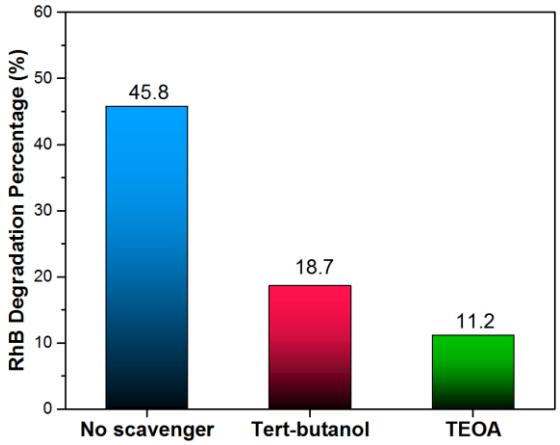

Figure 3.4: *The impact of the incorporation of TEOA as hole scavenger and tert-butanol as •OH radical scavenger on the RhB degradation rate after 3 h photocatalytic test.*

3.4 Summary and Conclusions

In summary, variation of the electron donors highlights their significant influence on the overall photocatalytic performance toward the hydrogen evolution reaction. When TEA is used, the Ni_2P/MIL-125-NH_2 demonstrates significantly higher H_2 evolution rates, which can be associated with the higher basicity of TEA, its compatibility with MIL-125-NH_2 (in terms of MIL-125-NH_2 being stable in high concentrations of TEA) and the fast kinetics of the TEA oxidation process.

Drawing on these insights, we then integrated the photocatalytic H_2 evolution and degradation of the organic dye RhB in a single process using the Ni_2P/MIL-125-NH_2 system under deaerated conditions. This dual-functional photocatalytic system generates H_2 at a relatively high rate and the organic dye – acting as an electron-donor – is degraded under visible-light irradiation. Although the dual-functional photocatalysis field is in its infancy, there are several scientific studies focused on the simultaneous photocatalytic H_2 production and organic pollutants degradation.[1] However, the majority of these studies are based on wide-band-gap semiconductors (i.e., TiO_2), restricting the profitable irradiation to only 4% of the solar spectrum that constitutes the UV region.[116] For example, Cho *et al.* and Kim *et al.* recently investigated the concept of dual-functional photocatalysis for H_2 production with simultaneous degradation of 4-chlorophenol and urea or urine.[111] These photocatalytic systems however are based on UV-active semiconductors such as $SrTiO_3$ and TiO_2, and noble metals NPs (e.g.

Rh, Pt) as co-catalysts. In our work, the Ni_2P/MIL-125-NH_2 photocatalytic system operates under visible light irradiation – a dominant region of the solar spectrum – and is free of noble metals. To the best of our knowledge this is the first example of a dual-functional MOF-based photocatalytic system able to simultaneously produce H_2 and degrade organic pollutants under visible light irradiation. This study showcases the great potential of MOFs in photocatalytic applications and paves the way for the generation of new visible light-active and water-stable MOF-photocatalysts that can accomplish simultaneous water remediation as well as H_2 generation.

Chapter 4 Design of MOF/MOF Heterojunctions

Parts of this chapter are based on submitted manuscript:

'*Development of a MOF/MOF Heterojunction for Enhanced Photocatalytic Performance*'

S. Kampouri, F. M. Ebrahim, M. Fumanal, P. A. Schouwink, B. Smit,* Christopher P. Ireland* and K. C. Stylianou*

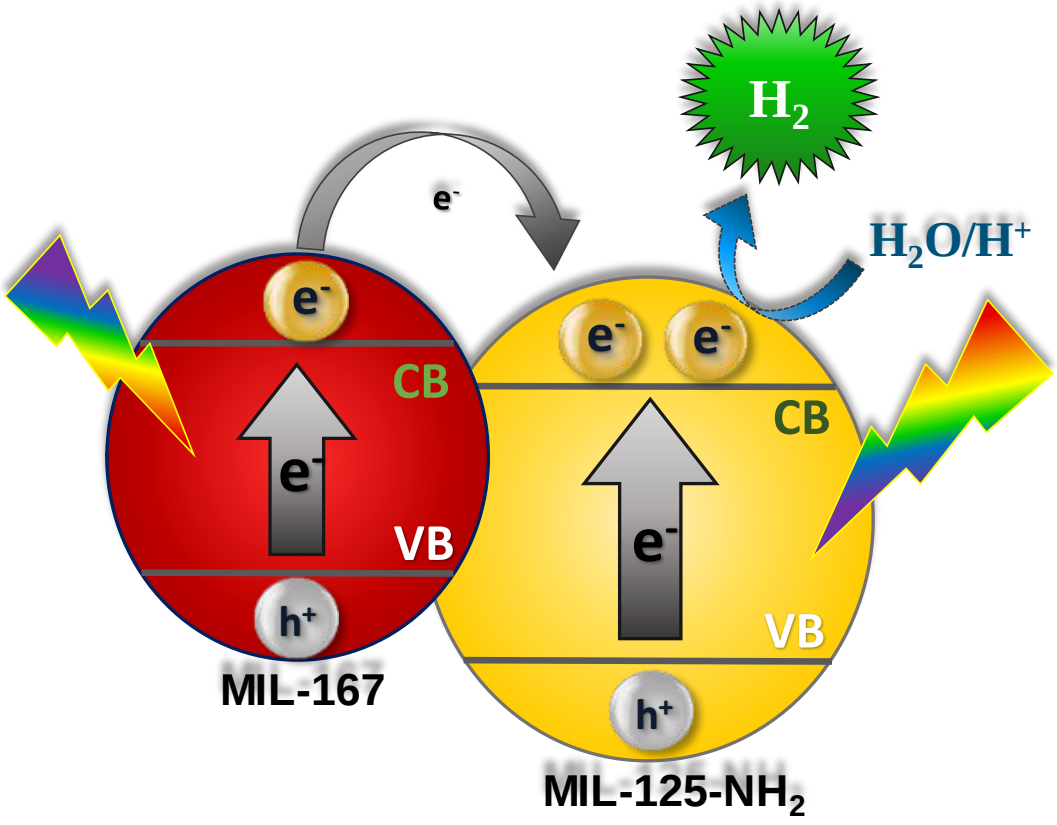

S. Kampouri's contribution: Conceiving the project's idea, synthesis of materials, characterization (powder X-ray diffraction, UV-Vis absorption, steady-state and transient photoluminescence spectroscopy, nitrogen sorption isotherms, scanning electron microscopy), designing and performing experiments (photocatalytic experiments, quantum yield calculations), writing text and constructing figures.

4.1 Introduction

As mentioned above, only a minor fraction of photons in sunlight corresponds to the UV region; the vast majority being in the visible and infrared regions. Considering the importance of exploiting the abundant solar energy, light-active materials with narrow band gap (< 2.95 eV), capable of absorbing a large part of the spectrum that composes sunlight, are highly desired. Besides light harvesting (first major photocatalytic step), the separation of the photogenerated charge carriers and their efficient migration (second major photocatalytic step) are additional important factors that define the overall photocatalytic activity of a system.[20] This is the main reason why the majority of photocatalytic systems utilize metal-based nanoparticles or molecular complexes as co-catalysts that can inhibit the undesired electron-hole recombination.[21a, 30b] In semiconductor photocatalysis, an alternative strategy to optimize the optical, electronic and catalytic properties is to combine different materials in a form of a heterojunction.[117] By carefully matching materials with different band gaps, absorption of a wider region of light can be achieved.[118] In addition, depending on the position of the conduction and valence band of the materials that are combined, the photogenerated electrons can be spatially separated from the holes, which can decrease the probability of the undesired charge carrier recombination (e.g. type II heterojunction of staggered gap, **Figure 4.1**).

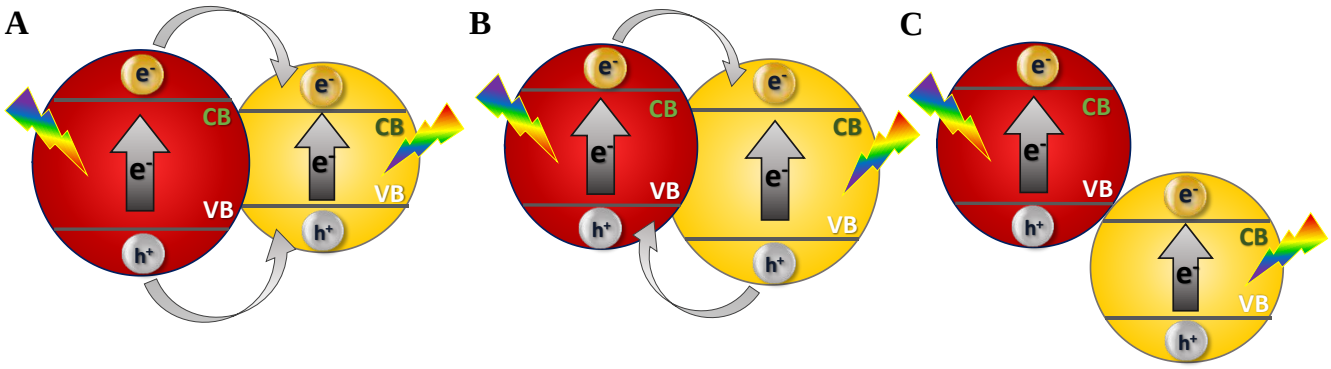

Figure 4.1: *Schematic representation of three different types of heterojunctions: (A) type I, with straddling gap (B) type II with staggered gap and (C) type III with broken gap.*

Similar to semiconductor photocatalysis, also in the field of MOF photocatalysis, one of the main challenges is to develop a system that has both a narrow band gap as well as sufficient charge separation efficiency. Inspired by semiconductor systems, in this chapter, we explored the strategy of combining different MOFs to form a MOF/MOF heterojunction for photocatalysis. Heterojunctions with MOFs recently started to be explored, with the majority of studies focusing on combining MOFs with either semiconductors or COFs (covalent-organic frameworks).[92b, 119] Recently, synthetic protocols for the design of MOF/MOF core-shell/satellite architectures have been reported.[120]

However, the synthesis of MOF-on-MOF structures does not guarantee the formation of a heterojunction, with the latter involving electronic interactions that alter the optoelectronic properties of the hybrid materials. In the ideal case, fully optimized MOF/MOF heterojunctions should demonstrate extended solar-light harvesting properties, high charge separation efficiency, enhanced catalytic activity and high porosity (allowing for facile diffusion of the photocatalytic solution). Understanding and elucidating the impact of the altered optoelectronic properties of MOF/MOF heterojunctions on the photocatalytic activity – although neglected – is of key importance for the strategic design of highly active MOF-based photocatalysts. Development of such a photocatalytic system would eliminate the necessity of additional expensive components, such as co-catalysts and/or dyes as photosensitizers.

This chapter describes the implementation of this strategy to improve the activity of the well-studied MIL-125-NH_2. To select an optimum component to form a heterojunction, we need a MOF with complementary light harvesting properties to those of MIL-125-NH_2. As MIL-125-NH_2 absorbs light early in the visible (< 500 nm), we need a MOF with more extended visible-light absorption. A promising candidate is MIL-167, also a stable Ti-based MOF, which shows immense light absorption in the extended visible (up to ~700 nm).[121] By combining these two MOFs, we envisioned enhanced photocatalytic activity driven by light energy harvested from almost the whole visible region.

4.2 Synthesis and Characterization

The synthetic protocols of the individual MOF components MIL-125-NH_2 and MIL-167 are based on reported procedures and are described in sections S2.1 and S4.1 in the Appendix.[86, 121] For the synthesis of the MIL-167/MIL-125-NH_2 materials, we developed a strategy in which we use the MIL-167 crystals as additional nucleation centers for the growth of MIL-125-NH_2 (**Figure 4.2**). As anticipated based on the thermogravimetric analysis (TGA) profile (Figure S.22, Appendix), MIL-167 retains its structural integrity throughout the heating process, thus its amount was varied resulting in the synthesis of several MIL-167/MIL-125-NH_2 hybrid materials, with different ratios between their MOF components (Figure S23, Appendix). SEM images show that the large crystals of MIL-167 (~ 60 μm) are homogeneously covered by the significantly smaller crystals of MIL-125-NH_2 (~ 300 nm, **Figure 4.3**). More SEM images as well as more details about the characterization of the samples can be found in Section S4.2, in the Appendix.

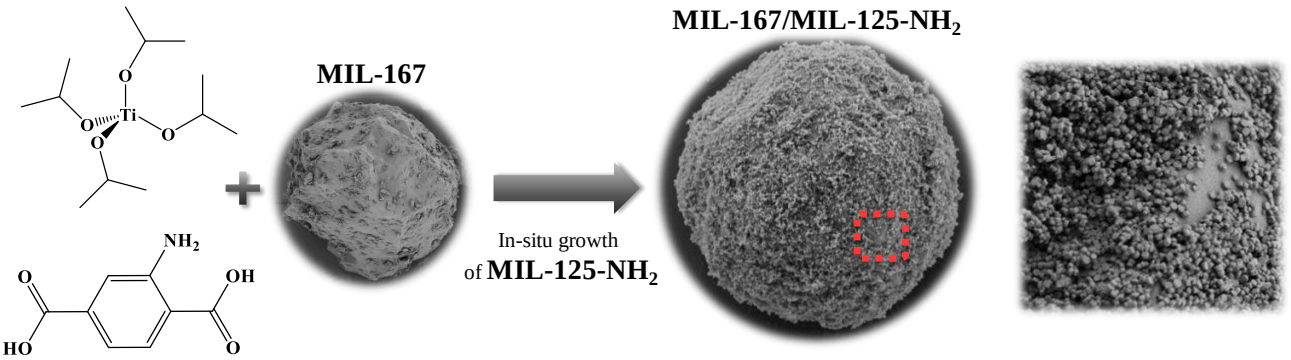

Figure 4.2: *Schematic representation of the synthetic protocol of the MIL-167/MIL-125-NH₂ heterojunction. MIL-125-NH₂ is synthesized in the presence of MIL-167 crystals.*

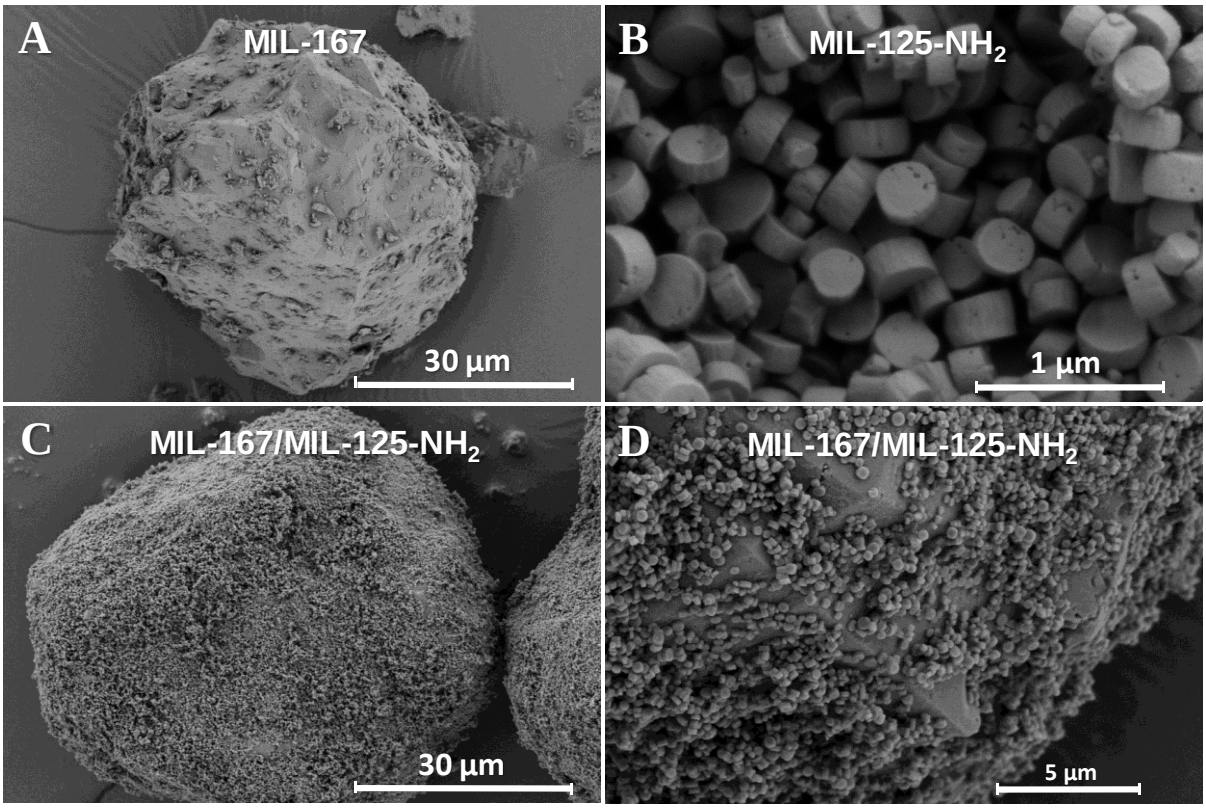

Figure 4.3: *SEM images of (A) MIL-167, (B) MIL-125-NH₂, (C) and (D) MIL-167/MIL-125-NH₂, with different magnification.*

4.3 Photocatalytic Activity

The photocatalytic activities of three different MIL-167/MIL-125-NH₂ materials with 3, 8, and 13 wt.% of MIL-167 were investigated toward the H_2 evolution reaction. For this purpose, the samples were irradiated under visible light (≥420 nm), with TEA as the electron donor and without the assistance of any co-catalysts (see Section S3 for more details). As shown in **Figure 4.4**, the MIL-

167/MIL-125-NH_2 materials significantly outperform their constituent components MIL-167 and MIL-125-NH_2. In fact, MIL-167 produces only traces of H_2, while the best-performing 8 wt.% MIL-167/MIL-125-NH_2 outperforms MIL-125-NH_2 by a factor of almost ten. As a comparison, the photocatalytic activities of the analogous physical mixtures of MIL-125-NH_2 and MIL-167 were investigated. The physical mixtures (with the same MIL-167:MIL-125-NH_2 ratios) exhibit inferior photocatalytic activities, ranging from 30 to 50 μmol h^{-1} g^{-1}, attributed to the activity of solely the MIL-125-NH_2 component. After the photocatalytic experiments, the stability of the samples was verified by means of PXRD and N_2 sorption isotherms (Figure S26). Furthermore, recycling experiments revealed that the MIL-167/MIL-125-NH_2 heterojunctions consistently produce hydrogen for more than 36 h (Figure S27), while no significant oxidation of the MOFs' linkers was observed after the cycles (Table S5).

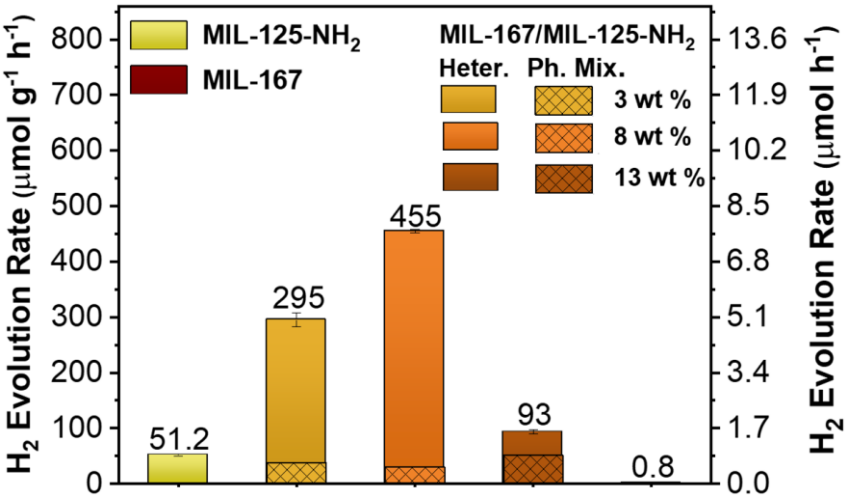

Figure 4.4: *Photocatalytic performance of MIL-125-NH_2 (yellow), MIL-167 (red), 3 wt.% (light orange), 8 wt.% (orange), and 13 wt.% (dark orange) MIL-167/MIL-125-NH_2. The heterojunctions are represented with solid fill, while the corresponding physical mixtures with patterned fill.*

4.4 Mechanism

To understand this performance increase, we carried out a combined experimental and computational study to explore the optoelectronic properties of these materials. One of the aims of creating a heterojunction is to extend the visible-light absorption of MIL-125-NH_2. **Figure 4.5**A demonstrates that indeed the MIL-167/MIL-125-NH_2 materials exhibit an extended light absorption in the region from 500 to 750 nm. As with the photocatalytic experiments we use only visible-light ($\lambda \geq 420$ nm), this enhancement has a significant effect on the number of photons absorbed. To determine the formation of a heterojunction and its type, we carried out PL spectroscopy by suspending the different

samples in acetonitrile. **Figure 4.5**B compares the PL emission of the heterojunction materials with that of MIL-125-NH_2, MIL-167 and their analogous physical mixtures. In the MIL-125- NH_2 emission spectrum, we observe three dominant peaks at around 470, 490 and 550 nm. In this region, MIL-167 weakly emits and shows no clear emission peaks. The MIL-167/MIL-125-NH_2 materials, exhibit more similar PL emission to that of MIL-125-NH_2. However, with the MIL-167/MIL-125-NH_2 materials, the weaker emission peak of MIL-125-NH_2 at 470 nm is significantly intensified. The magnitude of this intensification depends on the amount of MIL-167 in the samples. This increase in intensity indicates that within MIL-167/MIL-125-NH_2 there are now more electrons in the conduction band (or LUCOs) of MIL-125-NH_2 that when they recombine with the hole, they intensify the emission peak at 470 nm. As these electrons can only come from the CB of MIL-167, its CB should be higher in energy than that of MIL-125-NH_2 and the MOFs should exhibit good electronic contact.

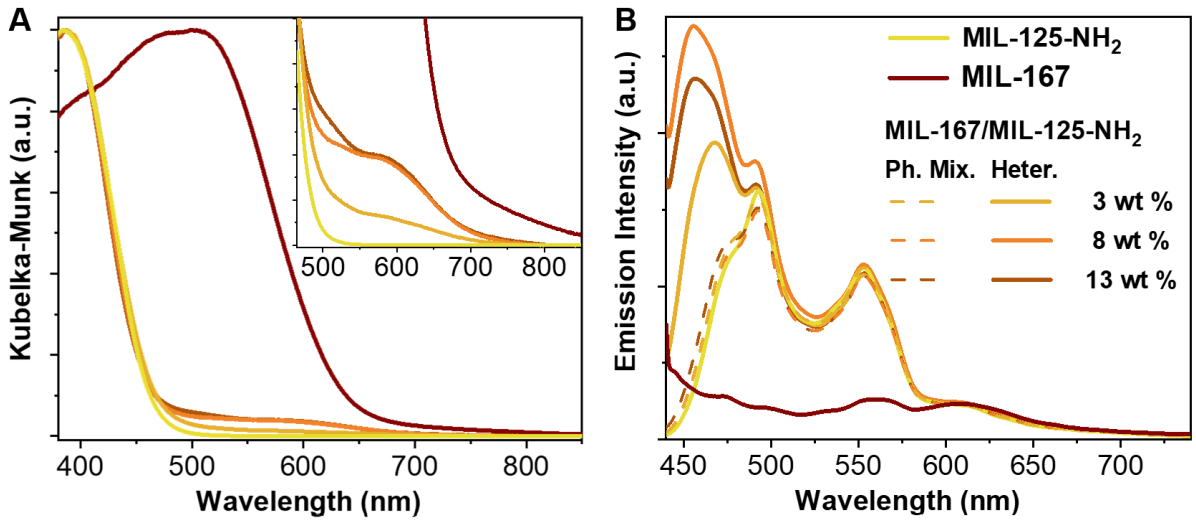

Figure 4.5: *(A) UV-vis absorption spectra and (B) PL emission of MIL-125-NH_2 (yellow), MIL-167 (red), MIL-167/MIL-125-NH_2 heterojunctions (solid lines, mustard: 3 wt.%, orange: 8 wt.% and dark orange 13 wt.%) and corresponding physical mixtures (dotted lines, mustard: 3 wt.%, orange: 8 wt.% and dark orange: 13 wt.%). The excitation wavelength was 420 nm.*

However, this is not the case for the physical mixtures of MIL-167 and MIL-125-NH_2, which demonstrate similar emission to that of MIL-125-NH_2. The absence of the intensified MIL-125-NH_2 emission peaks with the physical mixtures, manifests the lack of interactions between the two MOF crystals when they are physically mixed. This can be correlated with their different morphology compared to the heterojunction materials, as the MIL-125-NH_2 crystals are randomly aggregated on small regions of the MIL-167 crystals (**Figure 4.6**). These results demonstrate that the synthetic method of growing MIL-125-NH_2 in the presence of MIL-167 results in the formation of a heterojunction.

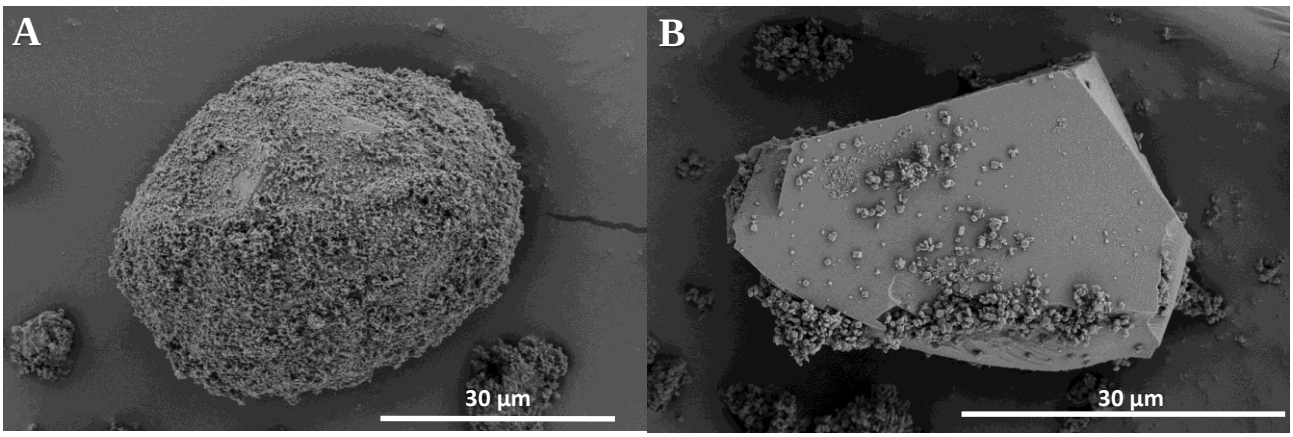

Figure 4.6: *SEM images comparing the morphology of (A) the 8 wt.% MIL-167/MIL-125-NH₂ heterojunction sample with that of (B) its analogous physical mixture of MIL-167 and MIL-125-NH₂.*

To further confirm these results and determine the relative positions of the valence bands (or HOCOs) of MIL-167 and MIL-125-NH_2, density functional theory (DFT) calculations were used (for details, see section S4.4.1, Appendix). **Figure 4.7**A illustrates the positions of the VBs and CBs of both MOFs, with respect to the vacuum level. The calculations reveal that the CB of MIL-167 is 0.6 eV above the CB of MIL-125-NH_2, which is in nice agreement with the PL results. As the VB of MIL-167 is above that of MIL-125-NH_2, the MIL-167/MIL-125-NH_2 materials demonstrate the characteristics of a type II heterojunction; staggered gap (**Figure 4.7**B). In this heterojunction, MIL-167 is the photosensitizer (harvesting light in the extended visible region where MIL-125-NH_2 is incapable) and MIL-125-NH_2 is the (photo)catalyst.

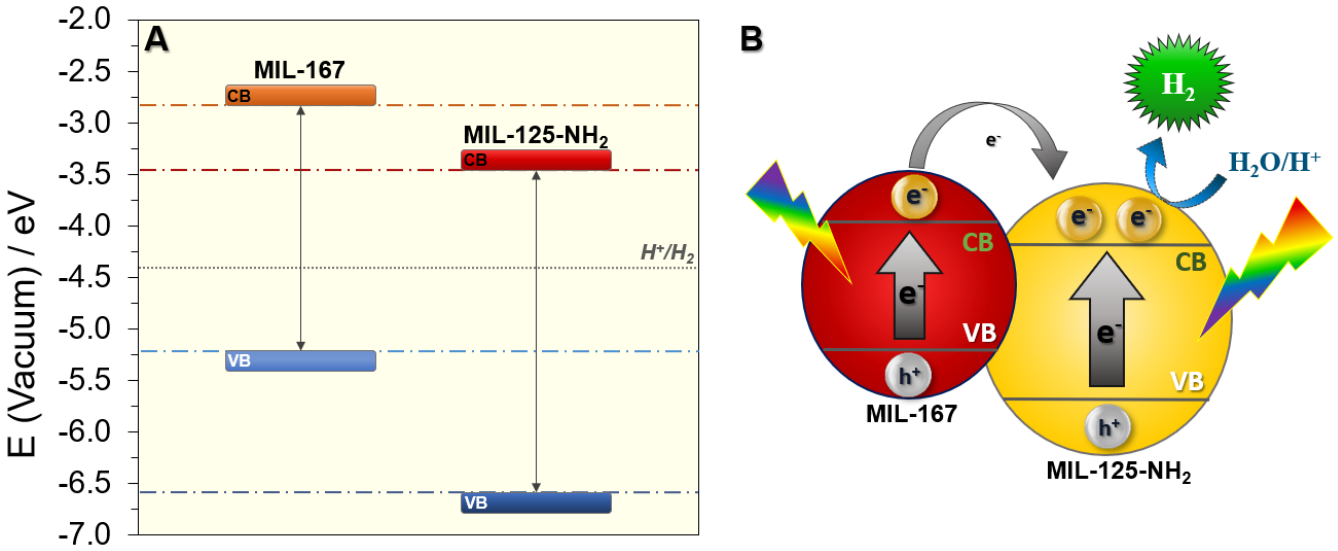

Figure 4.7: *(A) Computed electronic band alignment relative to the vacuum level of MIL-167 and MIL-125-NH₂. (B) Schematic representation of a type II heterojunction with MIL-167 and MIL-125-NH₂.*

To further prove the photosensitization effect by the MIL-167 counterpart, we performed a new photocatalytic test, irradiating the MIL-167/MIL-125-NH_2 heterojunction with wavelength higher than 515 nm. Although MIL-125-NH_2 slightly absorbs in this region ($\lambda \geq 515$nm), the MIL-167/MIL-125-NH_2 heterojunction is photocatalytically active, producing significantly higher amounts of hydrogen compared to that of MIL-125-NH_2 (197 versus 5 μmol g^{-1}, for MIL-167/MIL-125-NH_2 and MIL-125-NH_2, respectively, after 8 h irradiation). These results further highlight the substantial improvement of the MIL-125-NH_2 photocatalyst by combining it with MIL-167, and the extended light absorption properties of the MIL-167/MIL-125-NH_2 heterojunctions. Furthermore, the apparent quantum yields (AQY) of the MIL-167/MIL-125-NH_2 heterojunction were calculated at 450 and 500 nm (see section S4.4.2, Appendix).[103] The AQYs were 2.5 % and 0.7 %, at 450 and 500 nm, respectively, which are high values for this type of materials and comparable to semiconductor photocatalysts (Table S6).[84, 105b, 122] These results are in line with the light absorption properties, as both MOF counterparts of the heterojunction absorb photons at 450 nm. However, at 500 nm, it is mainly the MIL-167 counterpart that absorbs photons, thus the AQY at this wavelength is lower, but further confirms the photosensitization effect.

Having a type II heterojunction is necessary but not sufficient for enhanced photocatalytic activity. It is also important to ensure that the long lifetime (3 - 5 μs) of the electrons in MIL-125-NH_2 is not influenced negatively by the formation of the heterojunction. Sufficiently long lifetimes are required for an electron to be able to be involved in other processes (i.e. electron transfer within the heterojunction or to protons/water molecules) before recombining with the hole. Transient PL spectroscopy experiments reveal that the lifetime associated with the main PL emission peaks of MIL-125-NH_2, displayed in **Figure 4.5**B, is not influenced by the formation of the heterojunctions (for details see section S.4.4.3, Appendix).

The photocatalytic performance shows an optimum activity with the 8 wt.% MIL-167/MIL-125-NH_2 sample (**Figure 4.4**). This volcano type trend between the photocatalytic performance and the amount of MIL-167 in the heterojunctions can be associated with different competing mechanisms taking place. MIL-125-NH_2 is photosensitized further in the visible region by MIL-167 (**Figure 4.5**A). However, the bulky large crystals of MIL-167 can compete with MIL-125-NH_2 in the absorption of photons with higher energy (corresponding to less than 500 nm) and in excess amounts they could also act as recombination centers. In the case of 8 wt.% MIL-167/MIL-125-NH_2, optimum interactions between the two MOFs occur, thus resulting in superior photocatalytic activity. This is further supported by the PL data, where the emission peak of MIL-125-NH_2 at ~ 470 nm is the most intensified

for the 8 wt.% MIL-167/MIL-125-NH_2, compared to the other heterojunction materials, revealing a higher density of electrons being transferred from MIL-167 to MIL-125-NH_2.

4.5 Heterojunction with UIO-66-NH_2 and MIL-125-NH_2

With the aim of successfully applying the developed methodology with other materials, we synthesized UIO-66-NH_2/MIL-125-NH_2 heterojunctions, following a similar synthetic and characterization protocol (see section S4.5, Appendix). DFT calculations show that the energetic positions of the UIO-66-NH_2 CB and VB are higher than those of MIL-125-NH_2, which is also in agreement with the literature (**Figure 4.8**A).[123] We can thus expect a type II heterojunction, but now with comparable band gaps of the individual MOF components. This is not ideal as none of the MOF components can photosensitize the other. Indeed, the UV-vis spectra of the different samples demonstrate that increasing the amount of UIO-66-NH_2 in the UIO-66-NH_2/MIL-125-NH_2 materials, results in an increasing small blue-shift (from around 500 nm for MIL-125-NH_2 to a maximum of 450 nm for UIO-66-NH_2), attributed to the slightly smaller visible-light absorption of UIO-66-NH_2 (**Figure 4.8**B).

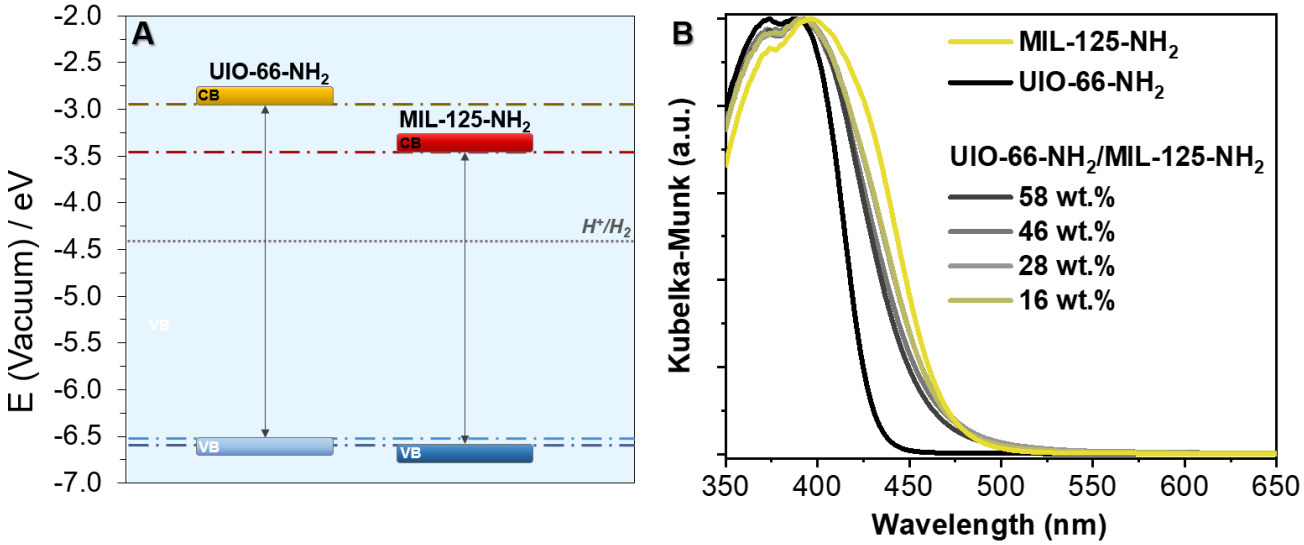

Figure 4.8: *(A) Computed electronic band alignment relative to the vacuum level of UIO-66-NH_2 and MIL-125-NH_2. (B) UV-vis absorption spectra of MIL-125-NH_2 (yellow), UIO-66-NH_2 (black) and UIO-66-NH_2/MIL-125-NH_2 materials (dark-light gray).*

As expected, the photocatalytic experiments shown in **Figure 4.9**A, illustrate that there is no enhancement in the photocatalytic activity. On the contrary, increasing the amount of UIO-66-NH_2 has a negative impact on the H_2 evolution, which attains a minimum value of 0.8 μmol h^{-1} g^{-1}, when only UIO-66-NH_2 is irradiated. It is noteworthy that a heterojunction is still formed in this system, as manifested by the PL experiments. The PL spectra of the UIO-66-NH_2/MIL-125-NH_2 materials follow

a similar trend to that of the MIL-167/MIL-125-NH_2 heterojunctions; the weak emission peak of MIL-125-NH_2 located at around 470 nm, and generally the entire emission is significantly intensified with increasing amounts of UIO-66-NH_2 in the heterojunction materials (**Figure 4.9**B). These results indicate that, upon irradiation, photoexcited electrons are transferred from the CB of UIO-66-NH_2 to that of MIL-125-NH_2, enhancing the intensity of the MIL-125- NH_2 emission. However, due to their comparable light absorption, photons with appropriate energy reaching the heterojunction can now either excite an electron within MIL-125-NH_2 or UIO-66-NH_2. This competition is not beneficial for photocatalysis, as it increases the number of possible charge recombination pathways.

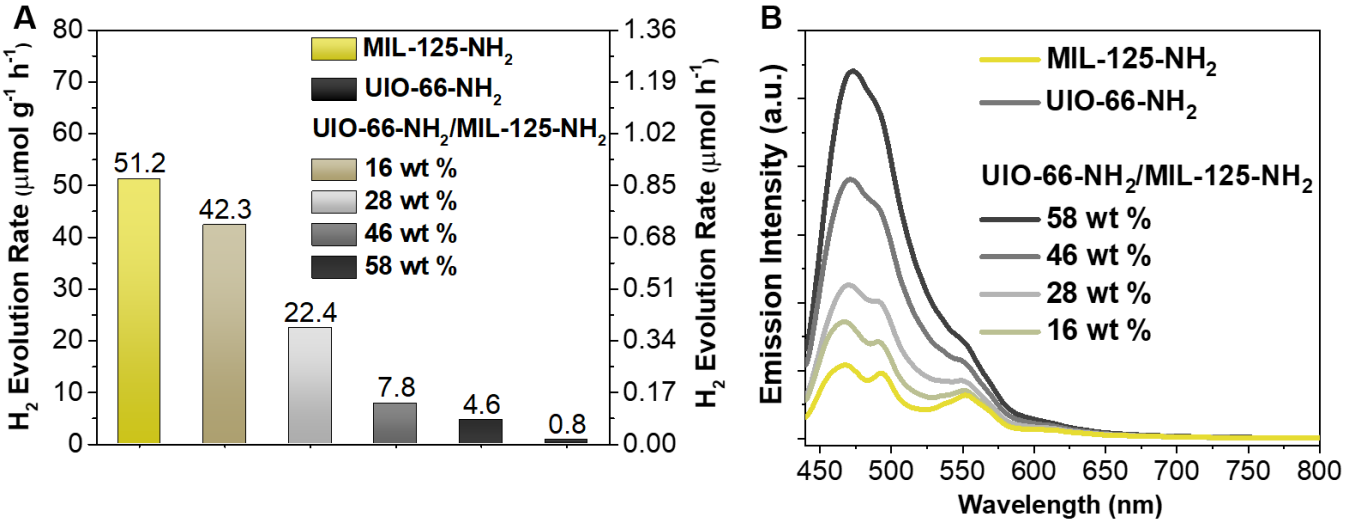

Figure 4.9: *(A) Photocatalytic performance and (B) PL spectra of MIL-125-NH_2 (yellow), UIO-66-NH_2 (black) and UIO-66-NH_2/MIL-125-NH_2 heterojunctions (dark-light gray).*

4.6 Summary and Conclusions

Summarizing, this chapter describes a strategy to improve the photocatalytic activity of MOF-based systems, through the construction of MOF/MOF heterojunctions. As a proof-of-concept, MIL-125-NH_2 was synthesized in the presence of either MIL-167 or UIO-66-NH_2 crystals. The MIL-167/MIL-125-NH_2 heterojunction materials exhibit significantly greater photocatalytic performance, which is attributed to the charge spatial separation and the extended visible-light absorption. Combined experimental and computational efforts demonstrate that MIL-167/MIL-125-NH_2 is a type II heterojunction with a staggered gap, where MIL-167 acts as the photosensitizer and MIL-125-NH_2 withdraws the electrons and acts as the photo(catalyst). The inferior activity of another type II heterojunction with UIO-66-NH_2 and MIL-125-NH_2 (UIO-66-NH_2/MIL-125-NH_2) highlights the importance of selecting appropriate MOFs for this strategy, exhibiting complementary light absorption

properties and suitable band alignment. Future efforts should focus on further elucidating the mechanism of this novel type of heterojunctions and exploring the impact of the morphological characteristics on the photocatalytic activity.

Chapter 5 MOF-derived Titanium Dioxide for Photocatalysis; The Impact of the Templated Morphology

Parts of this chapter are based on published work:

'Mixed-Phase MOF-Derived Titanium Dioxide for Photocatalytic Hydrogen Evolution: The Impact of the Templated Morphology'

S. Kampouri, C. P. Ireland, B. Valizadeh, E. Oveisi, P. A. Schouwink, M. Mensi, K. C. Stylianou, ACS Appl. Energy Mater. 2018, 1, 11, 6541-6548

Reprinted in adapted version with permission from Ref.124 Copyright © 2018 American Chemical Society

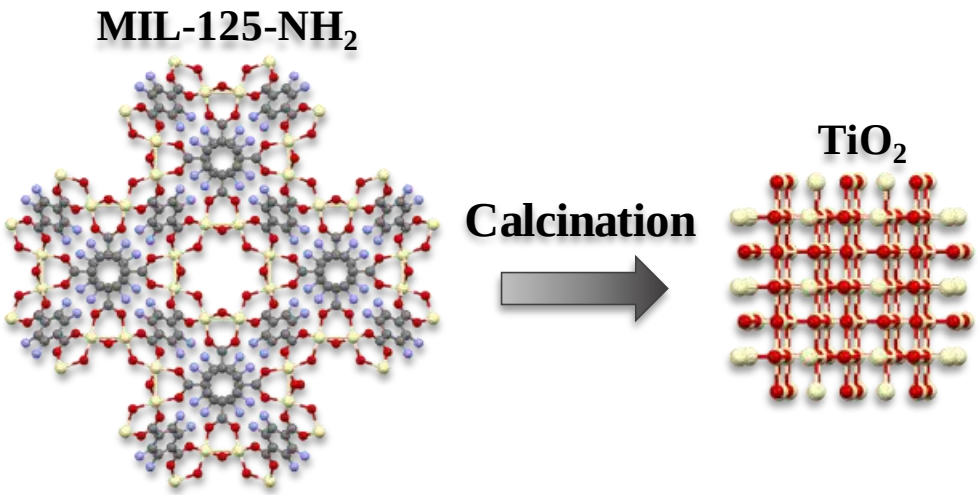

S. Kampouri contributed in conceiving the project's idea, the synthesis of materials, characterization (powder X-ray diffraction, UV-Vis absorption, photoluminescence spectroscopy, nitrogen sorption isotherms, scanning electron microscopy), designing and performing experiments (photocatalytic experiments), writing text and constructing figures.

5.1 Introduction

Titanium dioxide (TiO_2) was the first material investigated for the photocatalytic splitting of water,[8, 125] and despite its very limited solar light absorption (UV-active), it is still considered a promising photocatalyst, due to its chemical and thermal stability, non-toxicity, high reactivity and low cost.[126] Although tremendous research efforts have focused on the use of TiO_2 nanoparticles in a variety of photocatalytic applications (water splitting, water remediation, CO_2 reduction),[127] the impact of the shape and morphology of TiO_2 NPs on their activity, as well as the interplay between the two most common phases of TiO_2 (rutile and anatase) remain questionable.

The low temperature TiO_2 anatase phase is generally recognized as a better catalyst toward the H_2 evolution reaction. This is attributed to its high surface reactivity, meaning that a higher concentration of active sites is present compared to the TiO_2 rutile phase.[128] Nevertheless, the more thermodynamically stable TiO_2 rutile phase has a smaller band gap implying that a higher proportion of early visible light can be absorbed, thus careful engineering of TiO_2 rutile phase particles can lead to enhanced photocatalytic performance.[129] On the other hand, materials based on mixed TiO_2 rutile and anatase phases have demonstrated superior photocatalytic performance in comparison with the single phase TiO_2.[130] P25 Degussa, a mixed phase commercial TiO_2 is widely used as a standard material for photocatalysis and was studied by Bickley in 1990 to ascertain its success compared to a single phase TiO_2.[130a] The conclusion was that the excellent electronic contact between the two phases allowed enhanced electron-hole separation.

Subsequent literature has both agreed[130b, 130c] and disputed[130d] these findings and specifically the morphology of the phases' interface and the interactions between them. However, ample evidence has been provided through both experimental and computational approaches to prove that there is indeed a synergy between the anatase and rutile phases, allowing more efficient electron-hole separation.[130e] A general understanding has therefore been developed that TiO_2 materials with the anatase and rutile phases in a 3:1 ratio can outperform comparably formed single phase TiO_2. The different structural arrangement of TiO_2 anatase and rutile phases affords distinct phase electronic structures. As conclusively demonstrated by Scanlon *et al.*,[131] close electronic contact between the two phases allows electrons on rutile TiO_2 to irreversibly be transferred to the complementary TiO_2 anatase phase, with this synergy promoting the electron-hole separation efficiency.

In order to engineer the electronic contact between the two TiO_2 phases, several synthetic techniques have been utilized; approaches of physically mixing anatase and rutile TiO_2 have been attempted, but mixing does not allow the two phases to sufficiently interact with each other and achieve this

synergy.[132] Synthetic efforts on mixed phase TiO_2 have employed the sol-gel route, hydro/solvo-thermal method, electrodeposition, direct oxidation method or chemical vapor deposition.[133] Many of these techniques, however, lack of control, are impractical or may not provide highly active and stable TiO_2 NPs.

While MOFs themselves hold great potential for catalytic applications, limitations related to their thermal and chemical stability under harsh conditions (e.g., in highly acidic/basic media or high temperatures, > 400 ^oC) have recently triggered their utilization as precursors for the preparation of very stable metal oxides with high catalytic activities.[95, 97, 99, 134] More specifically, the MOF-mediated synthesis involves the use of MOFs as crystalline self-sacrificing templates, in order to tailor the shape, composition, surface area and stability of the resulting materials.[135] Calcination of MOFs in air leads to the partial or complete burning of the organic ligands and formation of highly active metal-oxide NPs, while carbonization at high temperatures under inert conditions can result in a carbon matrix encapsulating the metal phase (NPs).[136]

Among the Ti^{IV}-based MOFs, MIL-125-NH_2 was recently utilized as a precursor for the synthesis of TiO_2 decorated with either palladium or gold NPs for photocatalytic applications, such as CO_2 reduction and hydrogen evolution.[137] The employment of expensive noble metal NPs as co-catalysts was necessary to enhance the otherwise inadequate photocatalytic performance of TiO_2, attributed to high electron-hole recombination rates. Although these studies provided important insights, there is still a need to better understand the impact of templated MOF-derived TiO_2 rutile and anatase phases, and the effect of the morphology on the synergy between the two phases in photocatalysis.

In this chapter, the photocatalytic performance of TiO_2 prepared using the MIL-125-NH_2 as a starting material is primarily investigated. By calcining MIL-125-NH_2 over a range of temperatures, the ratio of the anatase and rutile phases can be controlled and optimized for the photocatalytic H_2 evolution reaction. For comparison, TiO_2 synthesized from precipitated amorphous titanium hydroxide and MIL-167-derived TiO_2 was prepared. Interestingly, the photocatalytic activity of the best-performing mixed-phase MIL-125-NH_2-derived TiO_2 is higher than all the other TiO_2 samples, including the commercially available P25 Degussa. Morphological studies reveal the unique nature of the templated MIL-125-NH_2-derived TiO_2 with nanosized anatase and rutile NPs forced into effective contact with each other, leading to an efficient electron-hole separation. This work highlights the role of effective interactions of TiO_2 anatase and rutile phases in a template and offers an intriguing outline for the development of efficient photocatalysts.

5.2 Synthesis and Characterization

Prior to the MOF-mediated synthesis of TiO_2, TGA of MIL-125-NH_2 was carried out. **Figure 5.1A** shows the TGA profile of MIL-125-NH_2. Two major weight losses are observed from 30 to ~200 °C, owed to the removal of guest molecules from the pores of MIL-125-NH_2, and from 360 to 600 °C related to the structural collapse of MIL-125-NH_2. The final product obtained after heating MIL-125-NH_2 at 600 °C corresponds to the remaining metal oxide, TiO_2, as confirmed by PXRD.

Acquiring a clear perception regarding the thermally-induced structural collapse of the MIL-125-NH_2, allowed us to continue with the synthesis of MOF-derived TiO_2 at selected temperatures (400 - 800 °C) under air (see section S5.1, Appendix). As can be seen in **Figure 5.1**B, calcination at different temperatures yields TiO_2 with differing ratios between the TiO_2 anatase and rutile phases. The anatase to rutile transformation is reconstructive, meaning that it involves the breaking of chemical bonds. The transformation temperature itself can vary depending on the starting material particle size, shape and volume and experimental factors such as atmosphere, heating rate and sample container. Reported temperatures for the TiO_2 anatase to rutile transformation vary from 400 to 1200°C.[138] Presently, heating the MIL-125-NH_2 crystals up to 400 °C leads to the formation of pure TiO_2 anatase phase. Increasing the temperature to 500°C induces the formation of the rutile phase (giving rise to a mixed phase TiO_2), which gradually becomes the dominant phase at 800 °C. Here, the anatase to rutile phase transformation is at the lower end of the range of temperatures reported for this transformation.[139 140]

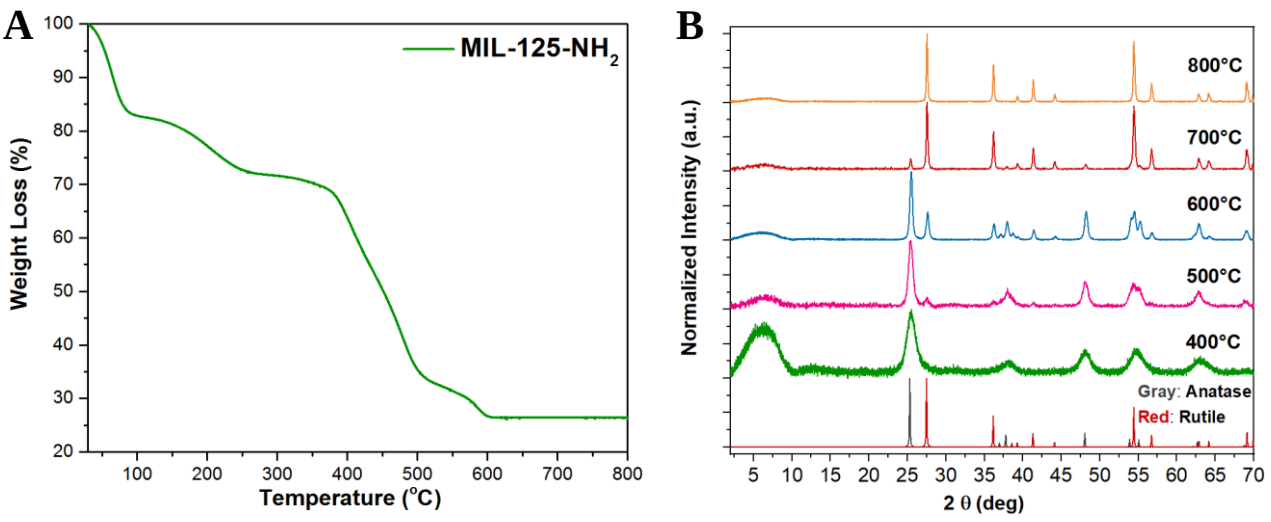

Figure 5.1: *(A) TGA curve of MIL-125-NH_2 obtained under airflow with a heating rate of 5 °C min^{-1}. (B) PXRD patterns of the as-synthesized MIL-125-NH_2-derived TiO_2.*

Further insights into the specific crystallization process can be gained from a variable temperature (VT) PXRD experiment, where MIL-125-NH_2 enclosed in a quartz capillary was heated from 30 to 800 °C (**Figure 5.2**A). Although direct comparison of ex-situ and in-situ experiments is not applicable (due to the crystallization process being rather complex and related to heating rate, dwell time and volume of the heating vessel), the in-situ VT PXRD experiment offers an insight into the TiO_2 anatase and rutile phase formation. Upon heating, the PXRD patterns show that the Bragg reflections of MIL-125-NH_2 are eliminated due to decomposition, leading to an amorphous powder. Upon further heating, initial formation of the TiO_2 anatase phase is observed as a broad hump at 25.2 ° 2θ, at furnace temperature of 560 °C. The peak width (Full width half maximum: FWHM 1.73 2θ) manifests a lack of crystallinity which can be indicative of defects and a small domain size (**Figure 5.2**B). This poor crystallinity may be related to the removal of the organic ligand which disrupts the crystallization process at the initial stages of TiO_2 formation. Interestingly, further heating to 660°C reveals the formation of a more crystalline TiO_2 rutile phase with a FWHM of 0.31 2θ. The integral intensity of the TiO_2 anatase Bragg peak remains constant during initial rutile formation, suggesting that the initial formation results from the same matrix as anatase. Both phases co-exist before the TiO_2 rutile phase becomes the dominant phase at 785 °C. The TiO_2 anatase and rutile phase composition, and the average domain size were quantified by Rietveld refinement from the as-prepared TiO_2 samples (**Table 2**). It is found that the domain size for both TiO_2 anatase and rutile phases is comparable at the same temperature, and increases with temperature.

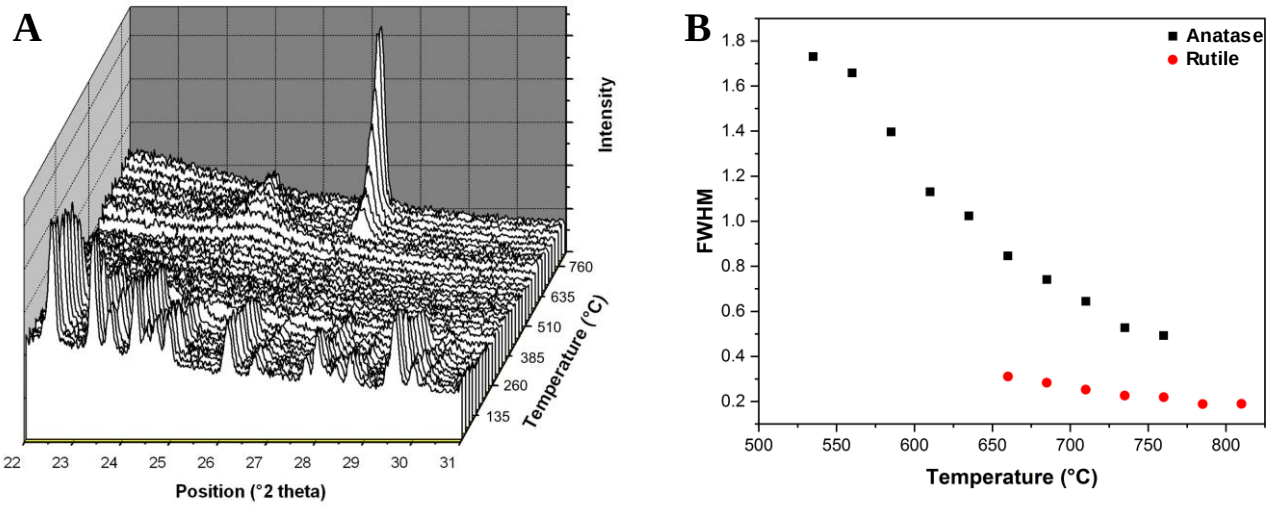

Figure 5.2: *(A) Variable temperature PXRD patterns of MIL-125-NH_2 heated up to 810 °C and (B) Full Width Half Maximum (FWHM) values of the TiO_2 anatase and rutile peaks derived from the variable temperature PXRD patterns of MIL-125-NH_2.*

Table 2: *PXRD-derived data revealing the size and composition of TiO_2 synthesized using MIL-125-NH_2 and TiH_4O_4 as precursors.*

	MIL-125-NH_2-derived TiO_2					TiH_4O_4-derived TiO_2				
Synthesis Temp. (°C)	400	500	600	700	800	400	500	600	700	800
Anatase (w.t. %)	98	87	66	11	-	100	100	100	92	20
Rutile (w.t. %)	2	13	34	89	100	-	-	-	8	80
Size Anatase (nm)	5.7	11	22	44	-	13	17	26	43	56
Size Rutile (nm)	5.9	12	25	47	61	-	-	-	87	87

To serve as a reference, different pure and mixed phase TiO_2 were also obtained by calcining (400 - 800 °C) precipitated amorphous titanium hydroxide (TiH_4O_4) as a starting material (see section S5.1, Appendix). The TGA profile of the TiH_4O_4 shows a weight loss up to 450 °C, related to the removal of hydroxide, coordinated water and/or organic residues derived from the titanium isopropoxide (**Figure 5.3**A). Upon calcination, the TiO_2 anatase to rutile phase transformation starts at 700 °C and above this temperature, the TiO_2 rutile phase becomes dominant (Figure 1d). VT PXRD experiments collected on TiH_4O_4, using the same protocol used with MIL-125-NH_2 revealed that the formation of TiO_2 anatase phase begins at a significantly lower temperature than the MIL-125-NH_2-derived TiO_2, with peaks of anatase identified as low as 180°C (**Figure 5.3**B, C). Interestingly, the qualitative trend of domain-sizes of anatase and rutile is inversed between MIL-125-NH_2 and TiH_4O_4-derived samples, with initial rutile formation from TiH_4O_4 showing a much larger FWHM than from MIL-125-NH_2 (**Figure 5.3**D). This suggests that nucleation and growth proceeds through different mechanisms, which is likely related to the topological differences between a pre-existing framework/matrix of Ti-O polyhedral in TiH_4O_4 as opposed to discrete Ti-O clusters separated by the organic ligands in MIL-125-NH_2. Furthermore, the ex-situ determined domain size of the TiO_2 anatase phase is significantly greater than that of the MIL-125-NH_2-derived material, with the FWHM only 0.73 2θ, implying a much higher degree of crystallinity. This improved crystallinity delays the formation of the rutile phase to 710 °C. [138]

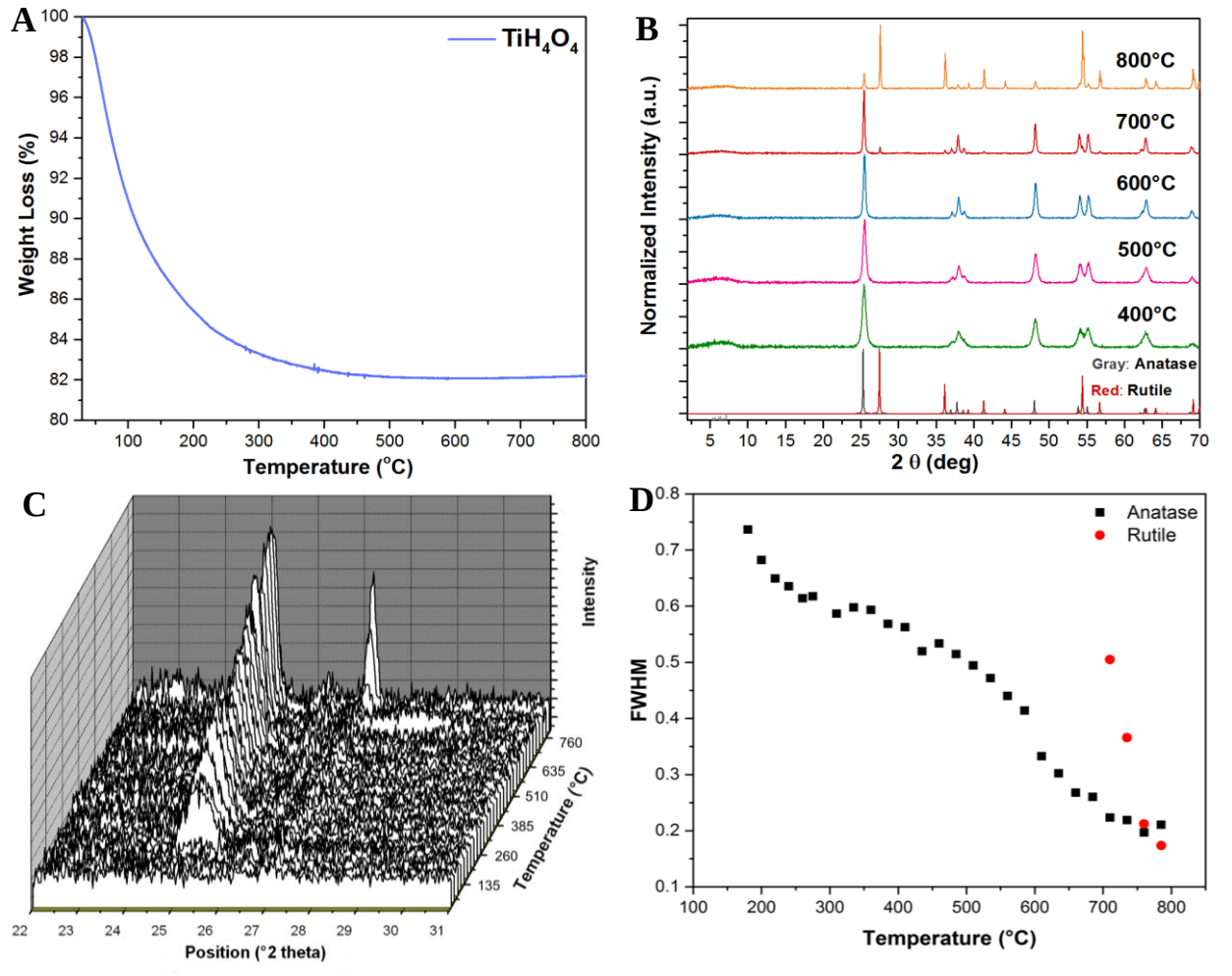

Figure 5.3: *(A) TGA curve of precipitated TiH_4O_4 obtained under airflow with a heating rate of 5 °C min^{-1}. (B) PXRD patterns of TiH_4O_4-derived TiO_2. (C) Variable temperature PXRD patterns of TiH_4O_4 heated up to 810 °C. (D) FWHM values of the TiO_2 anatase and rutile peaks derived from the variable temperature PXRD patterns of amorphous titanium hydroxide (TiH_4O_4).*

Figure 5.4 displays the Kubelka-Munk representation of the UV-vis diffuse reflectance spectra of TiO_2 synthesized from MIL-125-NH_2 and TiH_4O_4 as precursors. The spectra of both families are in agreement with the literature,[141] with the presence of rutile – which has a smaller band gap – causing a red shift in the light absorption edge compared to phase pure anatase TiO_2. In the case of the MIL-125-NH_2-derived TiO_2 synthesized through calcination at 400 °C, there is an extended light absorbance in the visible region, which is attributed to the residual carbon from the MIL-125-NH_2 covering the surface of TiO_2 and is in agreement with the TGA data (**Figure 5.1**A).

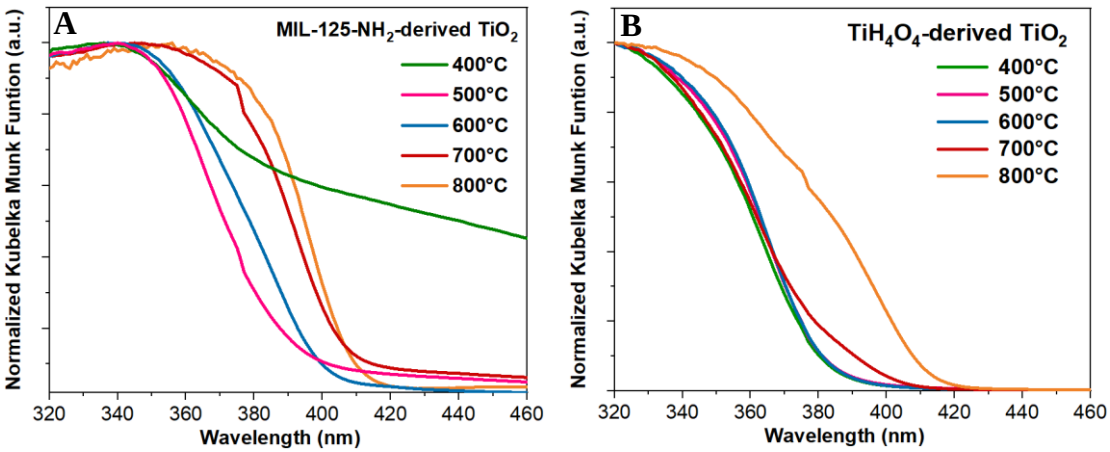

Figure 5.4: *Kubelka-Munk representation of the UV-Vis diffuse Rrflectance of (A) MIL-125-NH_2-derived and (B) TiH_4O_4-derived TiO_2.*

The morphologies of MIL-125-NH_2- and TiH_4O_4-derived TiO_2 were investigated through SEM and TEM. As can be seen in **Figure 5.5**, the well-defined crystal shape of MIL-125-NH_2 is retained during heating. It is found that the MIL-125-NH_2-derived TiO_2 exhibits a cuboid shape with round corners and its size is significantly reduced compared to the MIL-125-NH_2 crystals (0.5 - 2 μm, **Figure 5.5**A). The size reduction is associated with the high calcination temperature and subsequently to the removal of the guest-molecules and organic ligand in MIL-125-NH_2. TEM images show that the crystal-templates consisted of nanosized TiO_2 NPs (**Figure 5.6**). This is further confirmed by dark-field TEM, where the incident electron beam is tilted so that only the reflections of specific diffracting crystallographic planes contribute to image formation (Figures S32 and S33). Depending on the diffraction angle, TiO_2 NPs of specific crystallographic orientation are illuminated in the dark-field image, confirming the multi-particle nature of the crystal-template. The co-existence of both TiO_2 rutile and anatase phases produced at 600 °C was additionally proven by selected area electron diffraction (SAED) pattern measurements (Figure 3c). The observed diffraction pattern is comparable with Bikley's seminal work on P25, with the many nanosized TiO_2 particles diffracting to give Debye-Scherrer rings.[130a] These rings can be indexed to both TiO_2 anatase and rutile phases, confirming the multiphase nature of this material (**Figure 5.6**C).

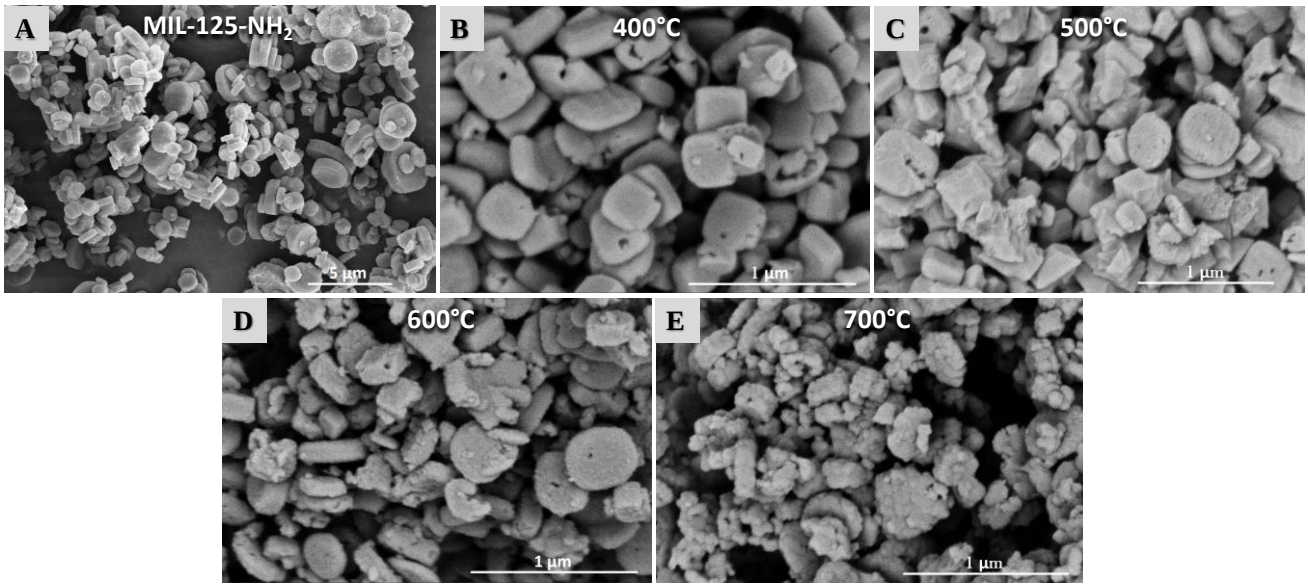

Figure 5.5: *SEM images of (A) MIL-125-NH_2 and MIL-125-NH_2-derived TiO_2 samples synthesized at (B) 400 °C, (C) 500 °C, (D) 600 °C and (E) 700 °C for 1 h. The images are of the same magnification except that of MIL-125-NH_2, which is of 5 times less magnification in order to display the morphology of the larger MOF crystals.*

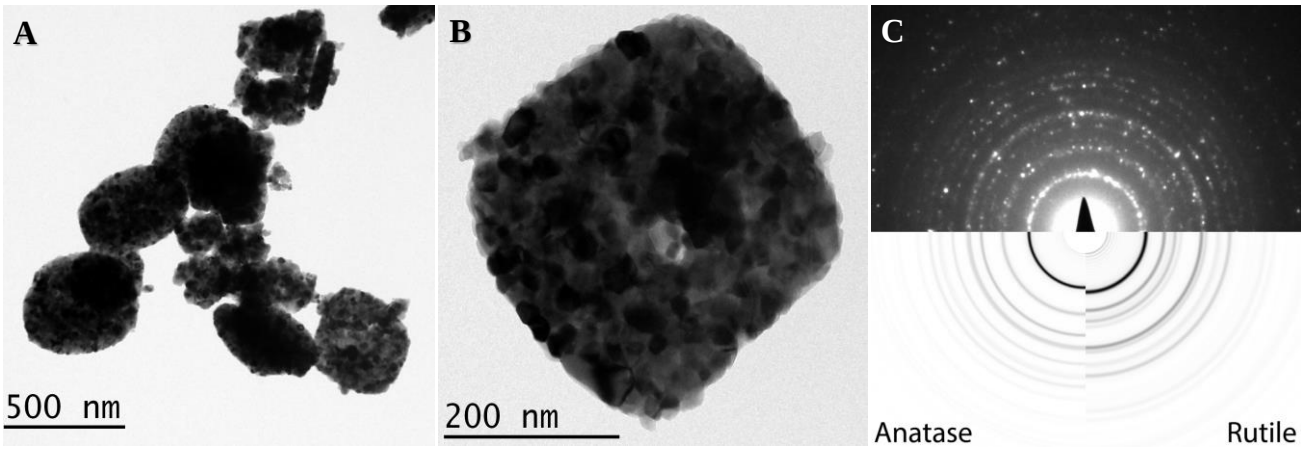

Figure 5.6: *(A) and (B) Bright-field TEM images, and (C) selected area electron diffraction pattern of MIL-125-NH_2-derived TiO_2 synthesized through calcination at 600°C for 1 h. Simulated electron diffraction patterns of anatase and rutile phases (ring sampling diffraction planes) are shown at the down part of image (C).*

In contrast to the MIL-125-NH_2-derived TiO_2, the morphology of TiH_4O_4-derived TiO_2 resembles disordered arrangement of bulk aggregates (**Figure 5.7**), typical of precipitated and co-precipitated metal oxide NPs and reminiscent of P25 TiO_2 NPs.[142] Further morphological characterization can be found in section S5.2.2 in the Appendix. The differing morphology of the MIL-125-NH_2- and TiH_4O_4-derived TiO_2 offer up an intriguing question of how this could affect the synergy between the TiO_2 anatase and rutile phases.

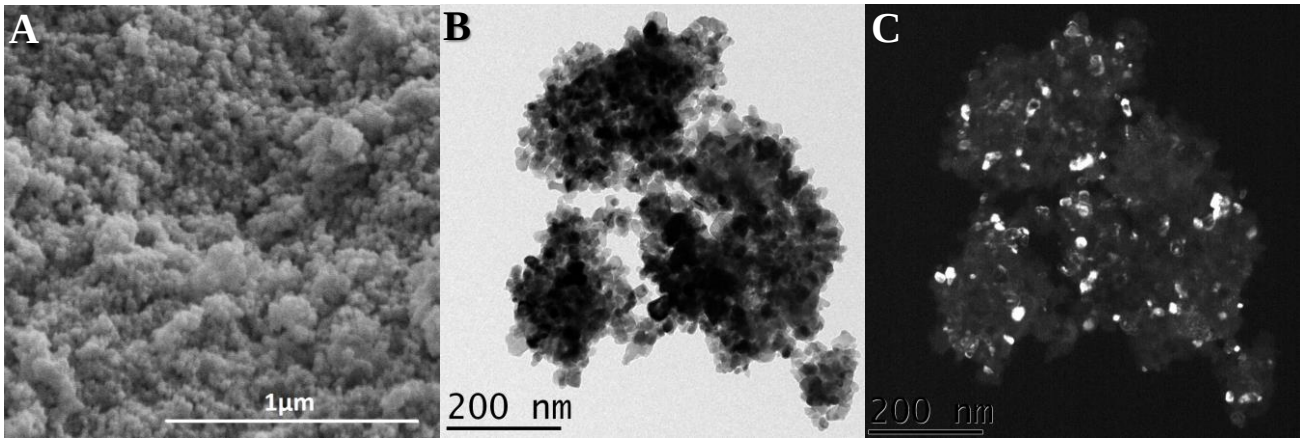

Figure 5.7: *(A) SEM, (B) bright-field TEM and (C) dark-field TEM images of the TiH_4O_4-derived TiO_2 sample synthesized at 500 °C.*

5.3 Photocatalytic Activity

After characterization, the performance of the MIL-125-NH_2-derived TiO_2 NPs was investigated toward the photocatalytic H_2 evolution reaction, with MeOH used as the sacrificial electron donor (20 v/v%) in the absence of co-catalyst, under UV-Vis light radiation. As shown in **Figure 5.8**A, the ratio between the TiO_2 anatase and rutile phases was found to have a profound impact on the photocatalytic performance. More specifically, increasing the rutile phases induces a volcano type trend with respect to the H_2 evolution rate. The sample with a composition of 66 w.t.% TiO_2 anatase and 34 w.t.% TiO_2 rutile (synthesized through calcination of MIL-125-NH_2 at 600°C) exhibits the highest H_2 evolution rate of 1394 μmol h^{-1} g^{-1}. Materials with higher amounts of TiO_2 rutile phase exhibit inferior photocatalytic performance and the H_2 evolution rate for the TiO_2 with composition of 11 w.t.% TiO_2 anatase, 89 w.t.% TiO_2 rutile is 372 μmol h^{-1} g^{-1}. The same trend between the activity and the ratio between the TiO_2 anatase and rutile phases is observed for the TiH_4O_4-derived TiO_2, with the 92 w.t% anatase and 8 w.t.% rutile TiO_2 exhibiting the best photocatalytic performance, with a H_2 evolution rate of 259 μmol h^{-1} g^{-1} (**Figure 5.8**A).

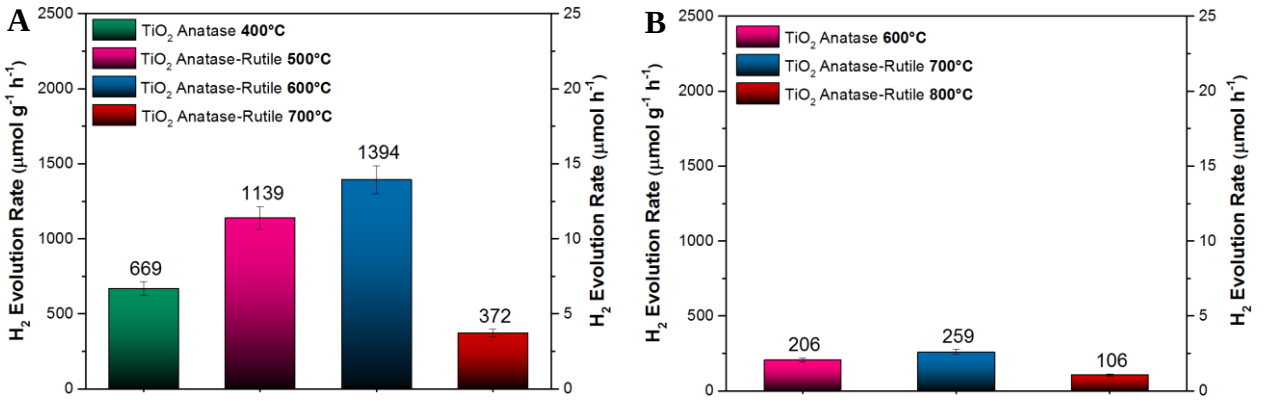

Figure 5.8: *Comparison of H_2 evolution rates of (A) MIL-125-NH_2-derived TiO_2 samples synthesized at different temperatures and B) TiH_4O_4-derived TiO_2 samples synthesized at 600°C (anatase), 700°C (anatase-rutile) and 800°C (anatase-rutile).*

The higher photoactivity of the mixed-phase TiO_2 (66 w.t.% TiO_2 anatase and 34 w.t.% TiO_2 rutile) as compared to phase pure TiO_2 anatase or rutile phase is thought to be owed to the synergistic effect between the two polymorphs, allowing for a more efficient charge carrier separation, provided that the two phases are in good electronic contact. The photogenerated electrons flow from the TiO_2 rutile to the TiO_2 anatase phase, which finally catalyzes the H_2 evolution reaction.[131] Recycling experiments were carried out for the best performing TiO_2 for three consecutive cycles. The photostability and the morphology of the MIL-125-NH_2-derived TiO_2 are fully preserved, with consistent H_2 rates produced over 3 cycles (**Figure 5.9**). The SEM images of TiO_2 after photocatalysis demonstrate that the templated morphology of the material is conserved, and PXRD shows no loss of crystallinity with the same TiO_2 anatase-rutile phase composition (Figure S.36).

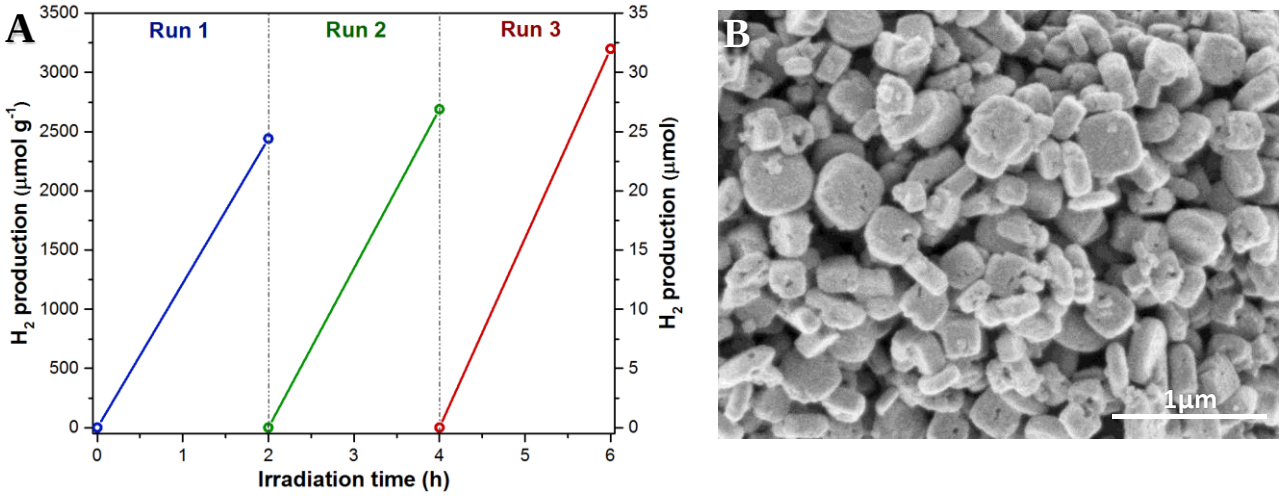

Figure 5.9: *(A) Recycling photocatalytic experiments and (B) SEM image of MIL-125-NH_2-derived TiO_2 (with optimum TiO_2 anatase to rutile ratio of 66:34) after recycling experiments.*

5.4 Comparison of MIL-125-NH_2-derived TiO_2 to other TiO_2 Samples

Intrigued by these results, the photocatalytic activities of two additional TiO_2 samples consisting of both the TiO_2 anatase and rutile phases were explored; the commercial P25 Degussa TiO_2 (with anatase-rutile phases in a composition of approximately 70:30)[142] and another MOF-derived TiO_2 using MIL-167 as the precursor.[121] **Figure 5.10**A illustrates that the MIL-167-derived TiO_2 NPs were successfully synthesized through calcination of the precursor at 600 °C for 1 h in air (for more information, see section S1.2 in the Appendix). Under these conditions, a mixed phase TiO_2 with composition of TiO_2 75 w.t.% anatase and 25 w.t.% rutile was prepared (Table S9). SEM images (**Figure 5.10**B, C) show that the morphology of MIL-167-derived TiO_2 is based upon irregularly shaped aggregates with a large size of 5-20 μm. Despite the use of a crystalline MOF as precursor, the morphology of MIL-167-derived TiO_2 is more comparable with that of the TiH_4O_4-derived TiO_2 rather than that of the MIL-125-NH_2 derived TiO_2. TEM images indicate that the size of the MIL-167-derived TiO_2 NPs is 30-40 nm, significantly larger than the TiO_2 NPs derived from MIL-125-NH_2 (**Figure 5.11**A).

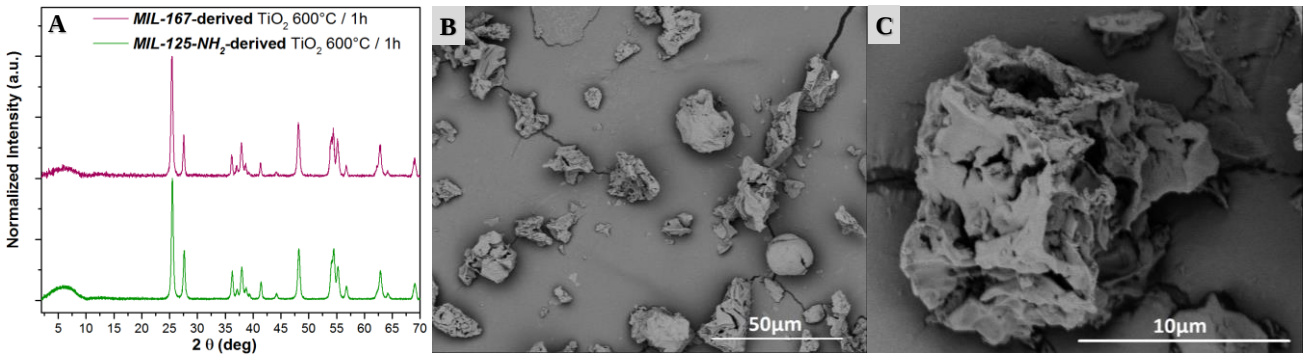

Figure 5.10: *(A) PXRD patterns of the MIL-167- and MIL-125-NH_2- derived TiO_2, synthesized through calcination at 600°C. SEM images of MIL-167-derived TiO_2 at (B) smaller and (C) larger magnification.*

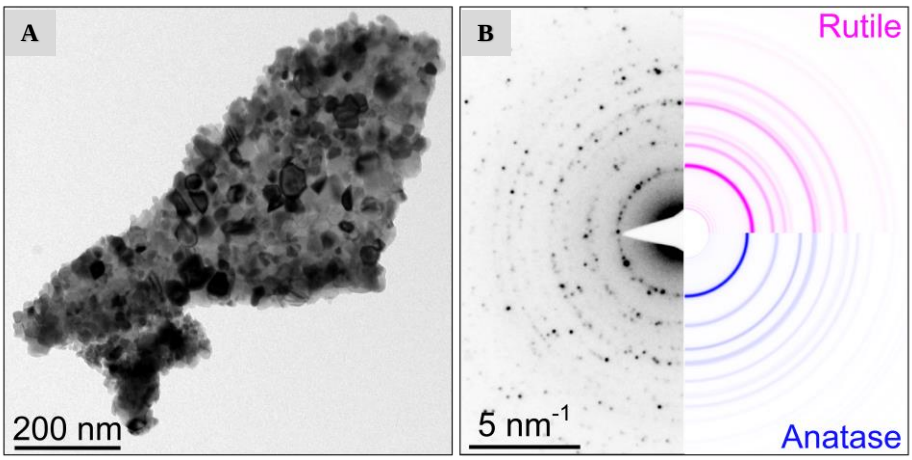

Figure 5.11: *(A) TEM image and (B) selected area electron diffraction pattern of MIL-167-derived TiO_2.*

The photocatalytic performance of the different mixed phase TiO_2 is shown in **Figure 5.12**A. The best MIL-125-NH_2-derived TiO_2 outperforms all the other TiO_2 samples, including the commercially available P25 Degussa.[130a] This is despite the relatively higher BET surface area of P25 Degussa compared to the other TiO_2 samples (**Figure 5.13**A). More specifically, the P25 Degussa TiO_2 exhibited a H_2 evolution rate of 624 μmol h^{-1} g^{-1}, followed by the MIL-167-derived sample with a rate of 274 μmol h^{-1} g^{-1}, which is comparable to that achieved by the TiH_4O_4-derived TiO_2 (259 μmol h^{-1} g^{-1}). For the best performing MIL-125-NH_2-derived TiO_2 and P25 Degussa, the dependence of the H_2 evolution rate on the concentration of photocatalyst in solution was further explored and found that the MIL-125-NH_2-derived TiO_2 reaches a higher plateau than that of the P25 Degussa TiO_2 (Figure S38). This implies that the required amount of MIL-125-NH_2-derived TiO_2 photocatalyst is lower, indicative of a well dispersed sample in solution.[143] The Kubelka-Munk representation of the UV-vis diffuse reflectance spectra of the examined samples is illustrated in **Figure 5.13**A. The indirect band gap for each of the materials was extrapolated from the linear section of the Tauc plot for an indirect bandgap. It can be seen that the indirect band gap is similar for all samples; 2.96 eV for MIL-125-NH_2-derived and MIL-167-derived TiO_2, 2.98 eV for TiH_4O_4-derived and 3.08 eV for P25 Degussa.

The superior photocatalytic performance of the MIL-125-NH_2-derived TiO_2 NPs over the other TiO_2 samples can be attributed to the morphology differences observed in SEM and TEM images (**Figure 5.12**B). The fact that the precursors in MOF-mediated syntheses are themselves well-defined crystals allows the resulting templated TiO_2 NPs to retain an exceptional close contact throughout the calcination and transformation process. These findings highlight that the TiO_2 anatase to rutile phase ratio is not the only predominant factor determining the photocatalytic performance, since excellent electronic contact between the two TiO_2 phases is a prerequisite for successful electron-hole separation and thus high photocatalytic activity.

Qualitatively, this is supported by an observation from the photocatalysis experiments, where the MIL-125-NH_2-derived TiO_2 suspension retained its white color throughout the photocatalytic test, in contrast to TiO_4H_4-, MIL-167-derived TiO_2 and P25, which obtained a blue hue (Inset at **Figure 5.12**A). The blue color is attributed to the presence of Ti^{III} in the TiO_2, indicative of inefficient electron transport from the TiO_2 NPs to the water molecules or protons, in contrast to MIL-125-NH_2-derived TiO_2, where no Ti^{III} was observed, indicating superior electron transport and water reduction.

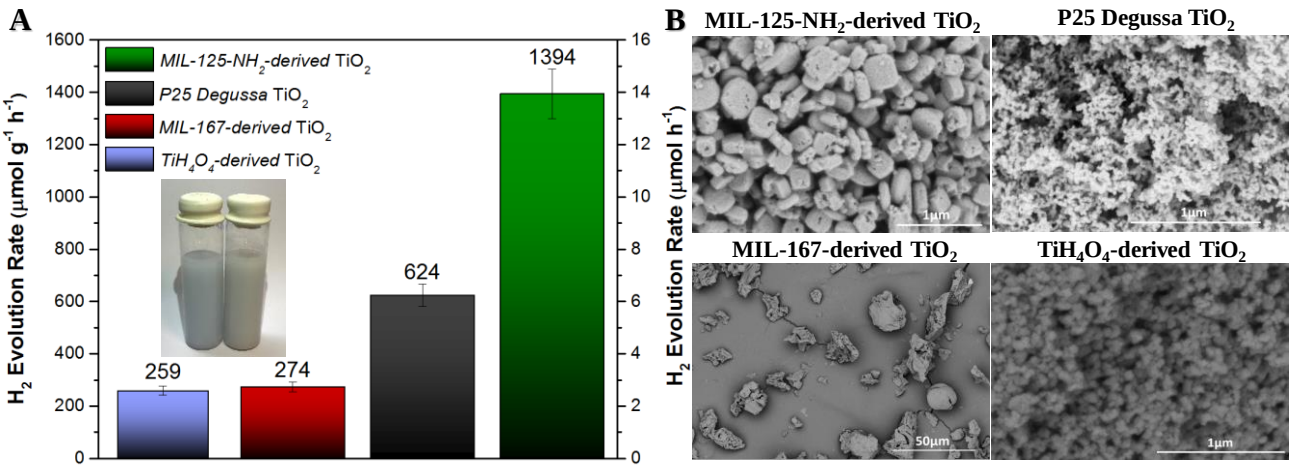

Figure 5.12: *(A) Comparison of photocatalytic activity and (B) SEM images of the MIL-125-NH_2- derived, MIL-167- derived, TiH_4O_4-derived TiO_2 and P25 Degussa. Inset: Photograph of the light-blue-colored P25 Degussa (left) and the MIL-125-NH_2-derived TiO_2 (right), after the photocatalytic test.*

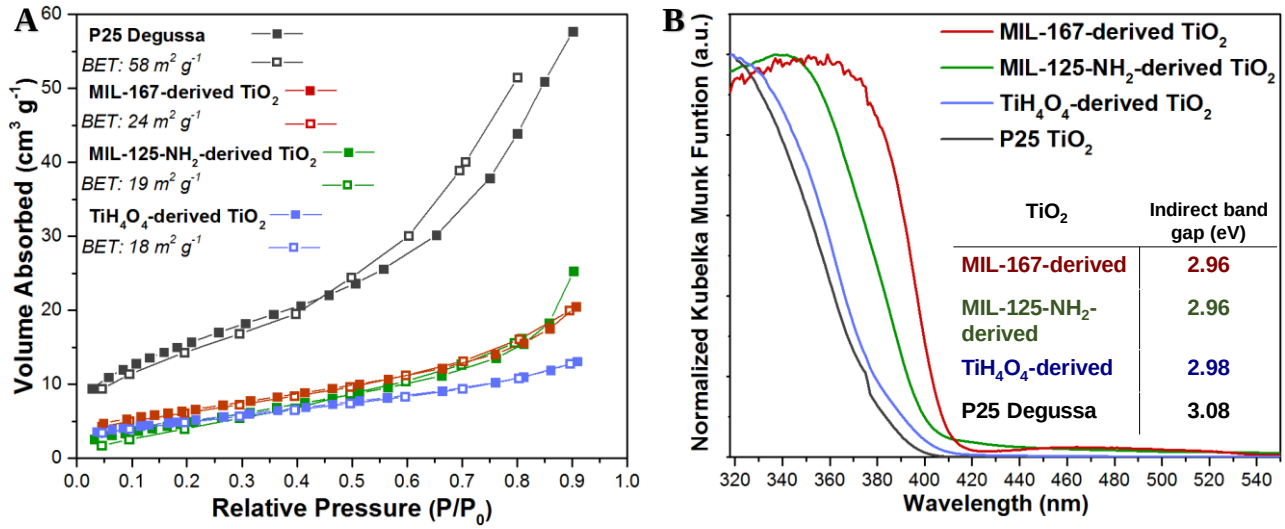

Figure 5.13: *(A) N_2 sorption isotherms for the best performing MIL-125-NH_2-derived, TiH_4O_4-derived, MIL-167-derived and P25 Degussa TiO_2 and corresponding BET surface areas. (B) Kubelka-Munk representation of UV-Vis diffuse reflectance of MIL-167-derived, MIL-125-NH_2-derived, TiH_4O_4-derived TiO_2 and P25 Degussa. Inset: band gap values for each of the materials, extrapolated from the linear section of the Tauc plot for an indirect bandgap.*

To further study this, PL experiments were performed to follow the irradiative recombination of the photo-excited charge carriers in the different TiO_2 samples and thus to gain further insights into the charge separation efficiency (Figure S39). In principle, the electron-hole recombination can occur through different pathways, including irradiative recombination through trap states, in addition to the irradiative band gap emission, which is less observed with TiO_2 – being an indirect band gap

semiconductor.[144] For comparison reasons, the irradiative recombination of photogenerated charge carriers was quantified by integrating the PL emission curves of the different TiO_2 samples (**Table 3**). The PL emission follows the order: MIL-167-derived TiO_2 > TiH_4O_4-derived TiO_2 > P25 Degussa > MIL-125-NH_2-derived TiO_2. The PL results exhibit a comparable trend with the photocatalytic results. The MIL-125-NH_2-derived TiO_2 (best-performing photocatalyst) demonstrates the lowest PL emission, followed by the P25, which is the second best-performing photocatalyst.

Table 3: *Integration of the PL emission curves of MIL-167-derived, TiH_4O_4-derived, MIL-125-NH_2-derived TiO_2 and P25 Degussa.*

MIL-167-derived TiO_2 (a.u. 10^7)	TiH_4O_4-derived TiO_2 (a.u. 10^7)	P25 Degussa (a.u 10^7)	MIL-125-derived TiO_2 (a.u. 10^7)
7.6	4	1.7	0.93

5.5 Summary and Conclusions

In summary, this chapter describes a synthetic method in which MIL-125-NH_2 crystals are used as a precursor for the preparation of TiO_2 NPs composed of pure or mixed rutile and anatase phases. The crystals of MIL-125-NH_2 act as a template for the synthesis of TiO_2 and the templated mixed-phase TiO_2 (with anatase to rutile composition of 66:34) produces a H_2 rate of 1394 μmol h^{-1} g^{-1}, without the assistance of any co-catalysts. The optimum MIL-125-NH_2-derived TiO_2 notably outperforms the commercial P25 Degussa, the conventionally synthesized TiH_4O_4- and the MIL-167-derived TiO_2. Two major aspects explain the high photocatalytic activity of the MIL-125-NH_2-derived TiO_2: *i.* the unique morphology that facilitates the constrained contact of NPs between the TiO_2 anatase and rutile phases and *ii.* the distribution of the TiO_2 anatase and rutile phases within the MIL-125-NH_2-derived template. These factors combine to result in an enhanced synergistic effect, which significantly suppresses the undesired electron-hole recombination. Our study highlights that high charge separation efficiency can be morphologically-induced within TiO_2 by using crystalline starting materials.

Chapter 6 Conclusions and Outlook

In line with the scientific endeavors to optimize and extend the range of materials used for photocatalytic applications, over the past few years, the relatively new application of MOFs in photocatalysis has received considerably increasing scientific attention. When this field was in its infancy, most of the scientific studies demonstrated activities far from the state-of-the-art or lacked advanced characterization techniques for the evaluation of the MOF photocatalysts. However, since then, MOFs in photocatalysis have come a long way. Recent studies show high activities and involve sophisticated optoelectronic characterization techniques. In addition, the scientific focus in this field has been slowly shifted toward MOFs' adaptation for 'real-world' applications, in terms of lower-cost and potential scale-up.

In line with these intense scientific efforts, the research activity described in this thesis contributed in the general advancement of the MOFs photocatalysis field, by favorably altering their properties associated with light absorption, charge separation and catalysis, which constitute the three major photocatalytic steps. Gaining insights into how established strategies for traditional photocatalysts can impact MOFs' properties gave rise to noble-metal-free MOF-based systems with significantly improved photocatalytic activities. These scientific efforts led to diminishing the gap between academic research and industry, highlighting the great potential of MOFs as photocatalysts and bringing this field a step closer to viability as a real-life application. However, there is still a lot of room for improvement in order for this type of photocatalytic systems to become industrialized.

In general, MOFs' synthetic protocols can involve the utilization of environmentally hazardous or expensive solvents, as well as result in low yields. These factors complicate the commercialization of MOFs. Therefore, optimizing the MOF's synthetic protocols in terms of sustainability, cost and yields of products is crucial for the advancement of the general field. In particular for MOFs in photocatalysis, there is also a need for novel materials with high intrinsic properties (optoelectronic and catalytic properties) that can be further optimized through the aforementioned strategies described in this thesis. Furthermore, considering the fact that water stability is a crucial property – especially for photocatalytic applications – future work should be directed toward improving the stability of MOFs. This way the utilization of organic solvents in the photocatalytic solution could be avoided, and thus photocatalytic hydrogen production could be achieved in pure water. Last but not least, the form (suspensions) and size of the materials used in photocatalysis (e.g. nanoparticles) can be challenging for scale-up and applicability. To tackle these last challenging issues, research efforts should be devoted to incorporating these materials within a device (i.e., PEC device).

Appendix

S1 Experimental

S1.1 Materials and General Methods

2-aminobenzene-1,4-dicarboxylic acid (NH_2-H_2BDC, 99%), 2,5-dihydroxyterephtalic acid (H_4DHBDC, 98%), titanium isopropoxide ($Ti(OCH(CH_3)_2)_4$, 97%), nickel nitrate hexahydrate ($Ni(NO_3)_2{\cdot}6H_2O$, 99.999% trace metal basis), cobalt nitrate hexahydrate ($Co(NO_3)_2 \cdot 6H_2O$, 99.999% trace metal basis), copper nitrate trihydrate ($Cu(NO_3)_2 \cdot 3H_2O$, ≥ 99%), iron nitrate nonahydrate ($Fe(NO_3)_3{\cdot}9H_2O$, ≥ 99.95% trace metals basis), chloroplatinic acid hexahydrate ($H_2PtCl_6 \cdot 6H_2O$, ACS reagent, ≥ 37.50% Pt basis), Zirconium(IV) Chloride (≥ 99.9% trace metals basis), anhydrous N,N-dimethylformamide (DMF; $(CH_3)_2NCHO$, 99.8%), anhydrous methanol (CH_3OH, 99.8%), N,N-diethylformamide (DEF, 99%), ethanol (EtOH, reagent grade), acetonitrile (CH_3CN, ≥ 99.5), sodium hypophosphite (NaH_2PO_2, ≥ 99%), isopropanol ($(CH_3)_2CHOH$, ≥ 98%), triethylamine (TEA, ≥ 99%), triethanolamine (TEOA, reagent grade, 98%), tetrabutylammonium perchlorate (TBAP, ≥ 99.0%, for electrochemical analysis), Rhodamine B (analytical standard) and tert-Butanol (≥ 99.0%, ACS reagent) were purchased from Sigma Aldrich. Benzene-1,3,5-tricarboxylic acid ($C_6H_3(COOH)_3$, H_3BTC, > 98.0%) was purchased from TCI. N,N-dimethylformamide (DMF, ≥ 99.5%) and Methanol (MeOH, ≥ 99.9%) were purchased form Carl Roth and Fisher scientific, respectively.

S1.2 Characterization

Powder X-ray Diffraction (PXRD) data were typically collected on a Bruker D8 Advance diffractometer at ambient temperature using monochromated Cu Kα radiation (λ= 1.5418 Å), with a 2θ step size of 0.02° and a 2θ range of 2 to 70°. The Al_2O_3 NIST standard SRM1976b was used for size analysis. Reported phase composition and domain sizes were determined by Rietveld refinement using Topas, the latter are based on integral breadths in an isotropic size approximation.

Nitrogen adsorption-desorption isotherms were collected using a BEL-SORP mini (BEL Japan, Inc.) at 77 K. Prior to data collection, the samples were degassed at 423 K for 12 h. The BET surface areas were estimated from the amount of N_2 adsorbed at 77 K using the BET (Brunauer-Emmett-Teller) equilibrium equation.

High-resolution transmission electron microscopy (HR-TEM) images of the co-catalysts were collected on FEI Tecnai G2 Spirit Twin instrument, equipped with a 80-120 kV LaB6 gun.

Scanning electron microscopy (SEM) images and **energy dispersive X-ray** maps (EDX) were collected on FEI Teneo instrument, equipped with an energy dispersive X-ray detector (XFlash Silicon drift detector). Prior imaging, the samples were deposited on a carbon tape and were coated with a ~7 nm thick Iridium layer. **TEM** images were collected on a FEI Tecnai Osiris instrument.

UV-Vis absorbance and diffuse reflectance spectra were obtained with a PerkinElmer UV-Vis Spectrometer. For the UV-Vis absorbance, 1 cm optical path length quartz cuvettes were used. The diffuse reflectance was collected by depositing the powders within quartz slides and the Kubelka-Munk function was applied to the raw data in order to eliminate scattering.

Steadt-State Photoluminescence (PL) spectra were measured with a Fluorescence Spectrometer LS 55 (PerkinElmer). For the MOF-based photocatalytic systems, the excitation wavelength was 420 nm and the experiments were performed using either suspensions of 17 mg of MIL-125-NH_2 with different amounts of each co-catalyst in 2.5 mL of the photocatalytic solution (co-catalysts/MIL-125-NH_2 project) or 3.5 mg of the MOFs in 3.5 mL of either acetonitrile or the photocatalytic solution (MOF/MOF heterojunctions project). For the TiO_2-based photocatalytic systems, the excitation wavelength was 340 nm and the experiments were performed on suspensions of 0.45 mg of TiO_2 in 3 mL of the photocatalytic solution (20 v/v % MeOH and water). In all cases, the PL spectra were acquired using chemical-resistant, 1 cm optical path length, quartz cuvettes.

Time-Resolved photoluminescence performed with a LP980 laser flash spectrometer (Edinburgh Instruments). The samples were excited by 5 ns laser pulses at $\lambda = 420$ nm (nanosecond tunable Ekspla NT340 laser with 5 Hz repetition rate). In a typical experiment, 0.35 mg of the investigated materials was dispersed in 3.5 mL of acetonitrile. The suspension was sonicated for ~30 min and then placed in a 1 cm path-length quartz cuvette.

X-ray photoelectron spectroscopy (XPS) was carried out using a Thermo Fisher Scientific Theta Probe spectrometer, with a base pressure of 5×10^{-10} mbar and utilizing monochromated Al K alpha radiation (1486.6 eV). The analysis area was defined by the X-ray spot size which was 400 mm. Photoelectron kinetic energy was measured using a hemispherical analyser operated in constant analyser energy (CAE) mode with a pass energy of 50 eV for high resolution spectra and 200 eV for survey spectra. The electron lens axis is 50° from the sample normal, and photoelectrons are accepted over an angular range of 60°. A 2D position sensitive detector was used. A dual beam (electron and Ar ion) charge compensation device was used to prevent charging of the sample surface.

Fourier-transform infrared spectroscopy (FTIR) measurements were carried out with the Spectrum Two FTIR spectrometer (PerkinElmer).

Electrochemical experiments were conducted in a standard three-electrode electrochemical cell, using Autolab 302N (Metrohm). Pt wire was used as counter electrode and the reference electrode was Ag/Ag^+ with 0.01M $AgNO_3$ and 0.1 M TB-AP in acetonitrile (ALS Japan). The amount of electrolyte used in a typical experiment was approximately 50 mL.

Inductively coupled plasma optical emission spectrometry (ICP-OES) measurements were performed using a NexIon 350 (Perkin Elmer) spectrometer.

Thermogravimetric analyses (TGA) was carried out with a standard TG-DTA analyzer under air atmosphere, at a heating rate of 5 °C/min for all measurements.

Variable Temperature (VT) Powder X-ray Diffraction data was collected on a Bruker D8 Advance diffractometer equipped with a LynxeyeXE detector using non-monochromated Cu Kα radiation. The sample was packed in a capillary and placed in a furnace, where it was heated at 30 °C min-1 to set temperatures at 25 ° C intervals. Data was collected in the 2θ range 22 to 31°, with a 0.02° step size.

CHN elemental analysis was performed on a Thermo Scientific Flash 2000 Organic Elemental Analyzer.

S1.3 Photocatalysis

The photocatalytic experiments with all the MOF-based systems were carried out using a 25 mL Pyrex glass reactor, under continuously visible light irradiation using a 300 W Xe lamp equipped with a UV cut-off filter ($\lambda \geq 420$ nm, **Figure S.1**). In a typical experiment, 17.0 mg of the MOF photocatalysts were mixed with different amounts of each co-catalyst and were suspended in 17.0 ml of a photocatalytic solution consisting of acetonitrile, deionized water and a given electron donor. For the experiments with the different co-catalyst/MIL-125-NH_2 systems and the MOF/MOF heterojunctions, the electron donor used was TEA (Conditions: 2.8 mL TEA in 0.8 mL H_2O and 13.4 mL CH_3CN). Subsequently, the suspensions were purged with nitrogen for 20 min under gentle stirring (to remove dissolved oxygen) and sonicated for 20 min. The amount of hydrogen produced was determined by abstracting 200 μL of the gaseous product from the head space of the reactor and analyzing it by means of gas chromatography (PerkinElmer Clarus 480 GC, equipped with a thermal conductivity detector and a molecular sieve 5 A column, with N_2 as the carrier gas). When TiO_2 was explored as photocatalyst, similar procedure was followed, apart from the facts that 10 mg of the photocatalysts were suspended in a photocatalytic solution comprised of water and MeOH (20 v/v%) as the electron donor, while the samples were irradiated with UV-Vis light (no cut-off filter).

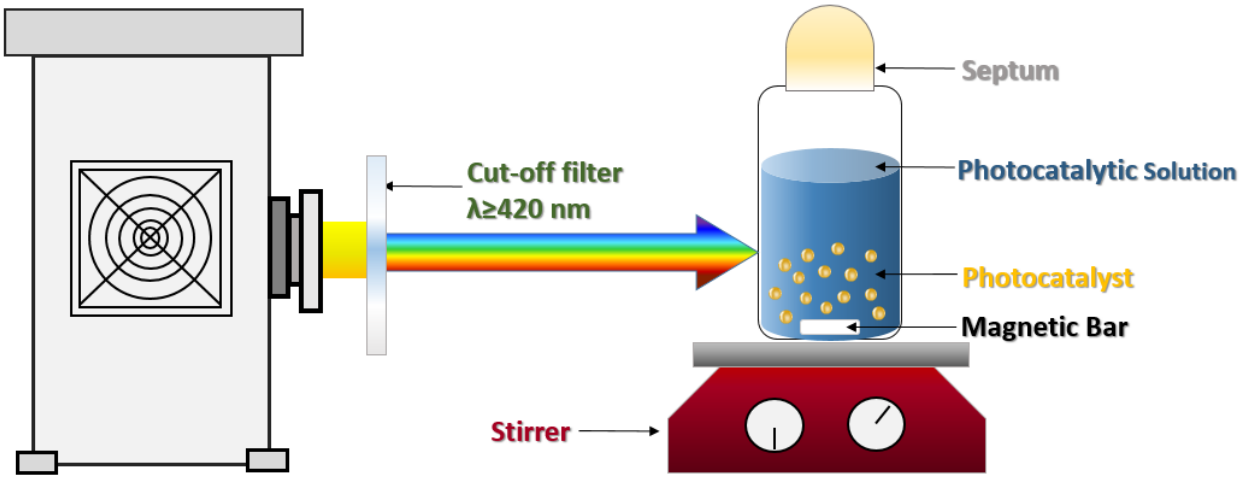

Figure S.1: *Schematic illustration of the photocatalytic set-up used.*

S2 Supporting Information for Chapter 2: Variation of Co-catalysts

S2.1 Synthetic Procedures

Synthesis of MIL-125-NH_2

The MOF was synthesized by following a reported procedure.[94] 0.286 g of NH_2-H_2BDC was dissolved in a mixture of 4.0 mL anhydrous DMF and 1.0 mL anhydrous MeOH. 0.286 mL of titanium isopropoxide was added in the mixture, which was sonicated for 30 min and then heated up to 120 °C for 72h. The obtained product was washed several times with DMF and MeOH.

Prior to photocatalytic testing, the MIL-125-NH_2 was subjected to a washing protocol, in order to remove uncoordinated free ligand and exchange the solvents within the pores of the MOF. The washing procedure involved the immersion of 500 mg of the as-synthesized MIL-125-NH_2 in 25 mL of DMF for 12 h and after centrifugation, the product was twice submerged in 25 mL of MeOH for 12 h. Subsequently, the sample was dried at 70 °C and then suspended in 0.5 L of the photocatalytic solvent mixture of acetonitrile (CH_3CN), TEA and deionized water. The suspension was stirred overnight under nitrogen atmosphere and finally washed with 100 mL of acetone.

Synthesis of co-catalysts

Ni_2P nanoparticles (NPs) were synthesized based on a reported procedure.[145] First, the Ni-BTC MOF was synthesized by mixing 0.255 g of $Ni(NO_3)_2 \cdot 6H_2O$ and 0.102 g H_3BTC in 14.0 mL in MeOH; the suspension was then heated for 24 h at 150 ºC in a Teflon liner inserted in a stainless steel autoclave. The obtained solid was washed several times with MeOH and then dried under vacuum at 60 °C. In a typical preparation of Ni_2P NPs, 0.10 g of the as-prepared Ni−BTC and 0.30 g of NaH_2PO_2 were mixed together, loaded into a ceramic crucible, and heated to 275 °C for 2 h in a furnace. After cooling to room temperature, the product was washed with water and EtOH and dried at 75 °C for 12 h.

CoP NPs were synthesized following similar procedure to that of Ni_2P, except that $Co(NO_3)_2 \cdot 6H_2O$ (0.255 mg) was used instead of $Ni(NO_3)_2 \cdot 6H_2O$, for the preparation of the Co-BTC powder.

NiO and **Co_3O_4** NPs were prepared by loading 0.1 g of the as-synthesized Ni-BTC and Co-BTC powders, respectively into a ceramic crucible and heated up to 375 °C for 2 h in a furnace. After cooling to room temperature, the product was washed with water and EtOH and dried at 75 °C for 12 h.

CuO NPs were prepared similar to NiO and Co_3O_4, except that $Cu(NO_3)_2 \cdot 3H_2O$ was used as the metal source for the synthesis of the Cu-BTC powder.

Fe_2O_3 NPs were synthesized similar to NiO and Co_3O_4 NPs, however in this case the precursor Fe-BTC powder was prepared by dissolving 0.51 g of $Fe(NO_3)_3 \cdot 9H_2O$ and 0.102 g H_3BTC in MeOH.

Pt NPs were synthesized based on a reported procedure.[106] More specifically, 119.5 μL of $H_2PtCl_6 \cdot 6H_2O$ was added in 16 mL aqueous solution with 0.2 M acetic acid concentration. The solution was sonicated for 5 min and then put into a Teflon-lined autoclave and heated up to 180 °C for 2 h. After cooling to room temperature, the product was washed with EtOH and dried at 60 °C for 12 h.

S2.2 Photocatalytic Experiments

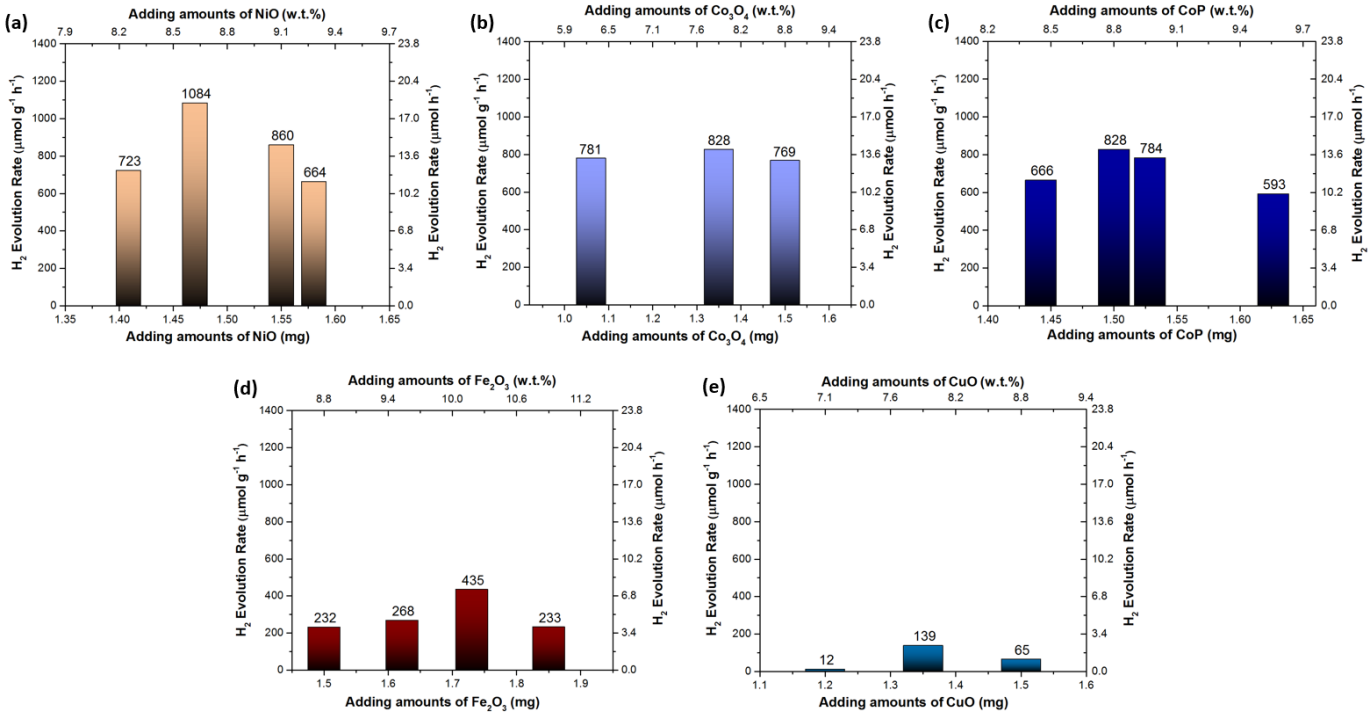

Figure S.2: *Photocatalytic H_2 evolution rates of MIL-125-NH_2 (17.0 mg) against different adding amounts of (a) NiO, (b) Co_3O_4, (c) CoP, (d) Fe_2O_3 and (e) CuO NPs under visible light irradiation for 8 h.*

Table S.1: *Photocatalytic experiments carried out under irradiation of each co-catalyst for 14 h.*

	Ni_2P	NiO	Co_3O_4	CoP	Fe_2O_3	CuO
Hydrogen evolved in 14 h (μmol)	0	0.4	0	0.3	0	0

S2.3 Calculation of Apparent Quantum Yield

Moles of photons emitted by the xenon lamp

The moles of photons emitted by the xenon lamp at 400 nm was calculated by means of **Ferrioxalate actinometry**: [146] Stock solutions were prepared using Millipore water:

0.40 M Iron (III) stock solution (**1**) was prepared by dissolving 4.025 g iron(III) nitrate nonahydrate ($Fe(NO_3)_3 \cdot 9H_2O$) in 20.0 mL of water. This was acidified with 1.375 mL sulfuric acid (H_2SO_4), and filled up to 25 mL with additional water.

1.20 M Di-potassium oxalate stock solution (2) was prepared by adding 4.975 g di-potassium oxalate monohydrate ($K_2C_2O_4$) to 25.0 mL of water.

Phenanthroline/buffer solution (3) was prepared by dissolving 0.025g anhydrous 1,10-phenanthroline ($C_{12}H_8N_2$) and 5.625g sodium acetate trihydrate ($NaCH_3COO \cdot 3H_2O$) in 20.0 mL of water. 1.22 mL sulfuric acid (H_2SO_4) was added and the solution was filled up to 25.0 mL with additional water.

The reaction solution was prepared by adding 1.7 mL of solution (**1**) and 1.7 mL of solution (**2**) with 30.6 mL of water in the dark. After stirring, 17. mL of the solution was transferred into a reactor (reactor **A**) which was irradiated by a 300 W Xe lamp equipped with a monochromatic filter (450 nm) for 46 min, while the remaining 17 mL was kept in the dark (reactor **B**). 0.5 mL of sample from reactor (A) was extracted, then added in 1.0 mL of solution (**3**) and made up to 5.0 mL with water. 0.5 mL of sample from reactor B was treated the same. UV-Vis absorbance (400-600 nm) was recorded for both samples, with the difference in absorbance between the two recorded at 510 nm. The moles of Fe^{2+} were calculated by using the formula: $\mathbf{n_{Fe(II)} = \frac{V_1\, V_3\, A}{10^3\, V_2\, L\, \varepsilon}}$

$\mathbf{V_1}$: irradiation volume, $\mathbf{V_2}$: sample taken, $\mathbf{V_3}$: final volume, **L**: optical path-length, **ΔA**: absorbance difference at 510 nm, **ε**: absorbance coefficient.

From this, the number of photons per min was calculated using the formula: $\mathbf{\frac{n_{photons}}{min} = \frac{n_{Fe(II)}}{\Phi_\lambda\, t\, F}}$

Φ_λ: Quantum yield for iron production at wavelength λ, t: time, F: mean fraction of light absorbed

Calculation: $\mathbf{n_{Fe(II)} = \frac{V_1\, V_3\, \Delta A}{10^3\, V_2\, L\, \varepsilon}}$

Where:

V_1: irradiation volume (17.0 mL), **V_2**: sample taken (0.5 mL), **V_3**: final volume (5.0 mL), **L**: optical pathlength (1.0 cm), **ΔA**: absorbance difference at 510 nm: **ΔA_1**= 0.870758, **ΔA_2**= 0.892268, **ε**: molar extinction coefficient (11100 L mol^{-1} cm^{-1})

Moles of Iron(II):

1st measurement $n_{Fe(II)} = 1.36654\ 10^{-5}$

2nd measurement $n_{Fe(II)} = 1.33359\ 10^{-5}$

$$\frac{\mathbf{n_{photons}}}{\mathbf{min}} = \frac{\mathbf{n_{Fe(II)}}}{\mathbf{\Phi_\lambda\ t\ F}}$$

Φ_λ: Quantum yield for iron production = 1.11 at ~450 nm

t: time = 46 min

F: mean fraction of light absorbed = 1

$$\frac{\mathbf{\bar{n}_{photons}}}{\mathbf{min}} = \mathbf{5.1713\ 10^{-7}}$$

Moles of hydrogen generated under 400 nm and 450 nm radiation

The amount of hydrogen generated under 400 nm radiation was carried out using the same reaction mixture and set-up as the photocatalytic experiments with the exception of using 450 nm band pass filter with the xenon lamp. Amount of H_2 for Ni_2P/MIL-125-NH_2: 2.0937 10^{-6} mol in 240 min (4 h).

Apparent quantum yield (AQY) determination

The apparent quantum yield was calculated by using the following formula: $\mathrm{AQY}(\%) = \frac{2\frac{\mathrm{N\ H_2}}{\mathrm{min}}}{\frac{\mathrm{N\ photons}}{\mathrm{min}}} 100$

Where $\frac{N\ H_2}{min}$ = number of hydrogen molecules evolved per minute and $\frac{N\ photons}{min}$ = number of incident photons per minute.

Calculation:

- **Ni_2P/MIL-125-NH_2**:

AQY = 6.6 % at 400 nm

S2.4 Stability

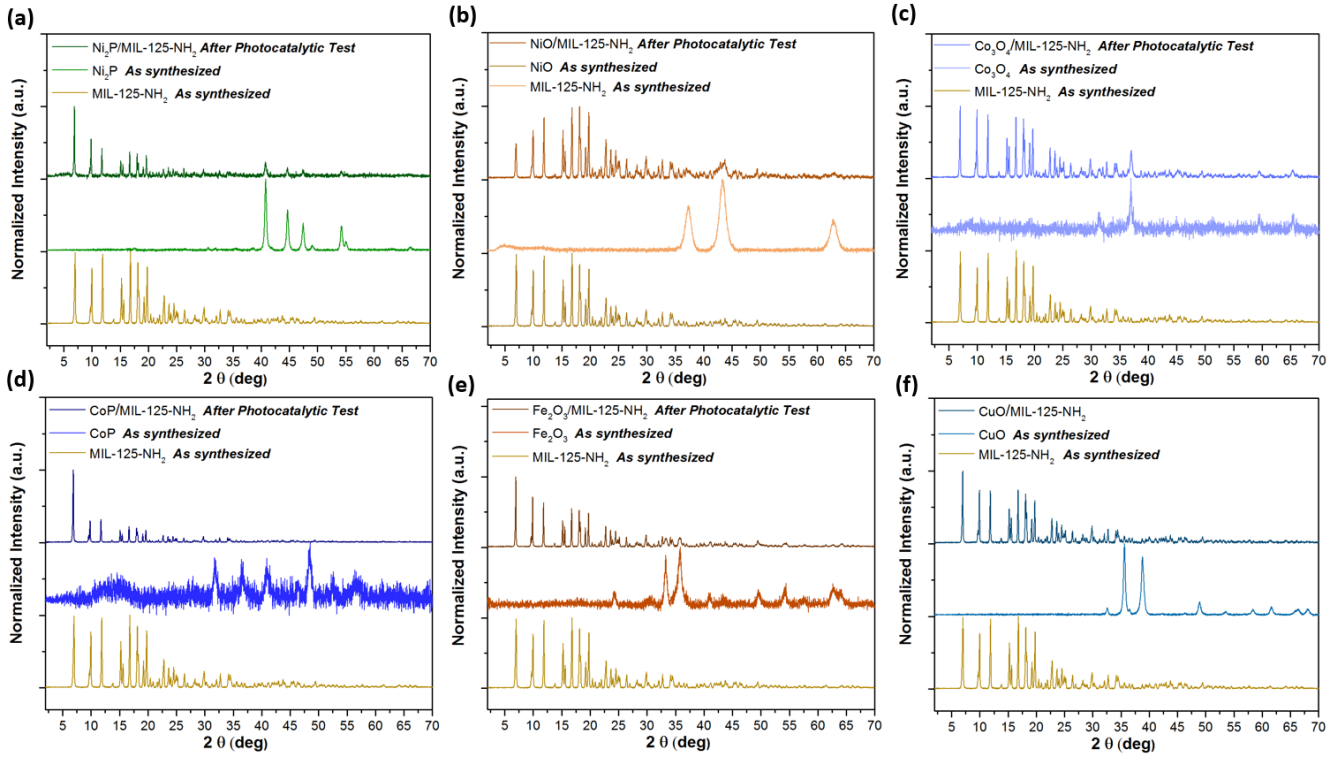

Figure S.3: *PXRD patterns of the as-synthesized MIL-125-NH$_2$ and the different co-catalysts, and the co-catalyst/MIL-125-NH$_2$ systems after the photocatalytic test.*

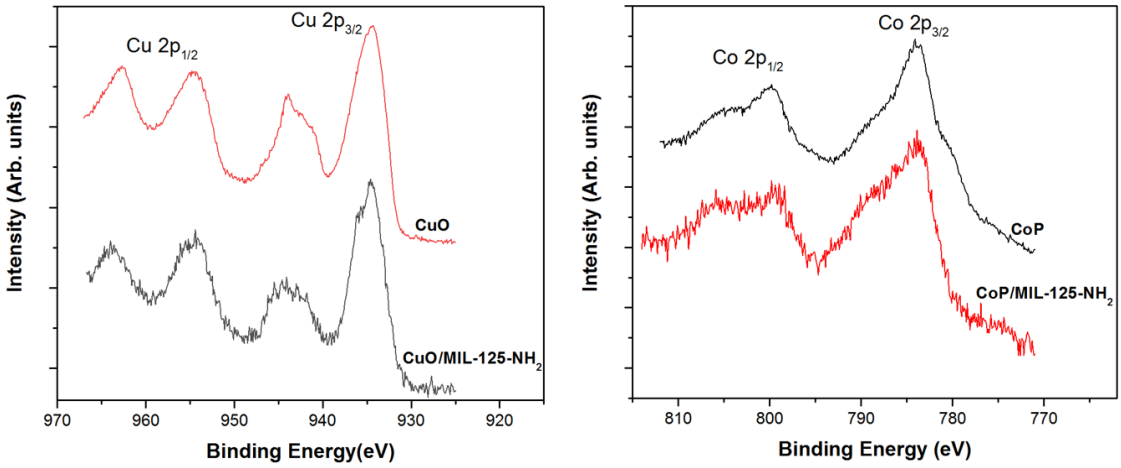

Figure S.4: *XPS data on the CuO/MIL-125-NH$_2$ (left) and CoP/MIL-125-NH$_2$ system (right) after photocatalysis, confirming that the co-catalysts are stable.*

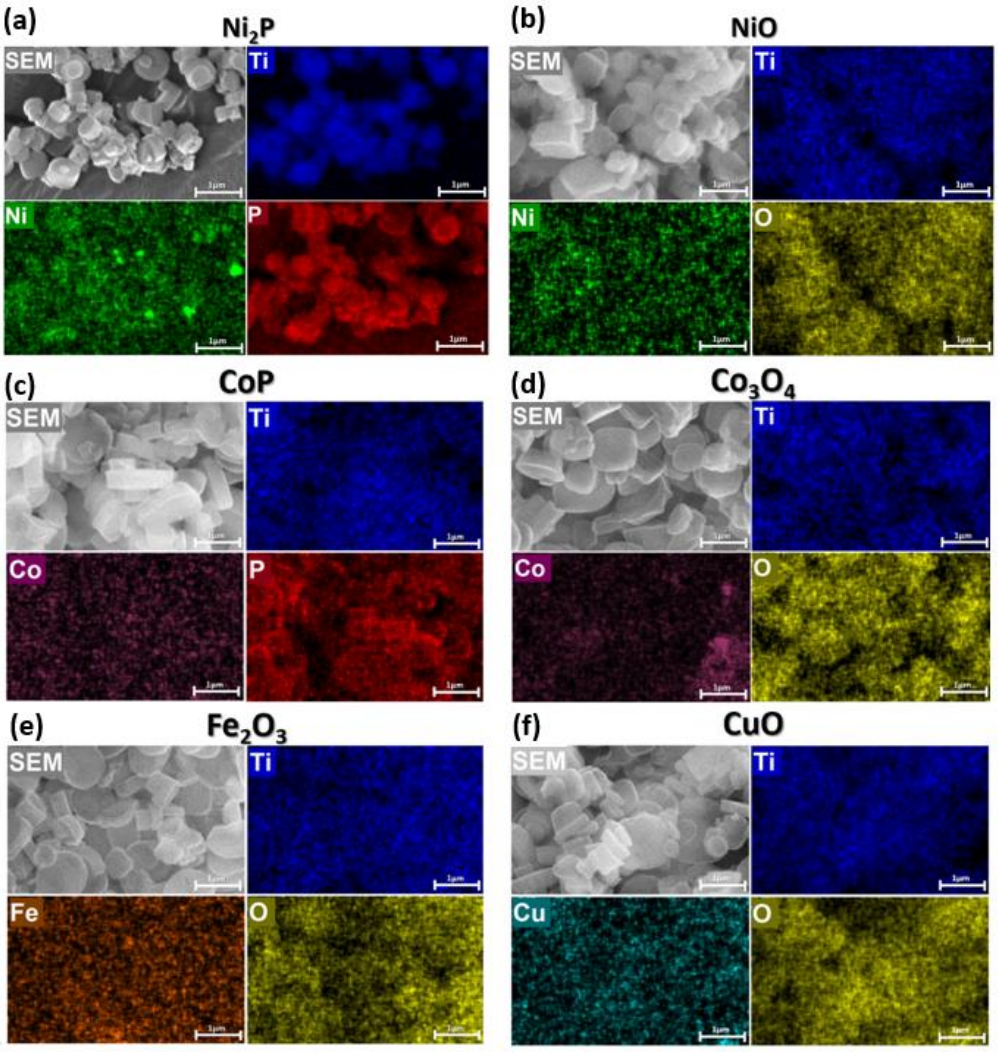

Figure S.5: *(a) SEM images after photocatalytic test and corresponding EDX elemental analysis for (a) Ni_2P/MIL-125-NH_2 (b) NiO/MIL-125-NH_2, (c) CoP/MIL-125-NH_2, (d) Co_3O_4/MIL-125-NH_2, (e) Fe_2O_3/MIL-125-NH_2 and (f) CuO/MIL-125-NH_2. Scale bar: 1 μm.*

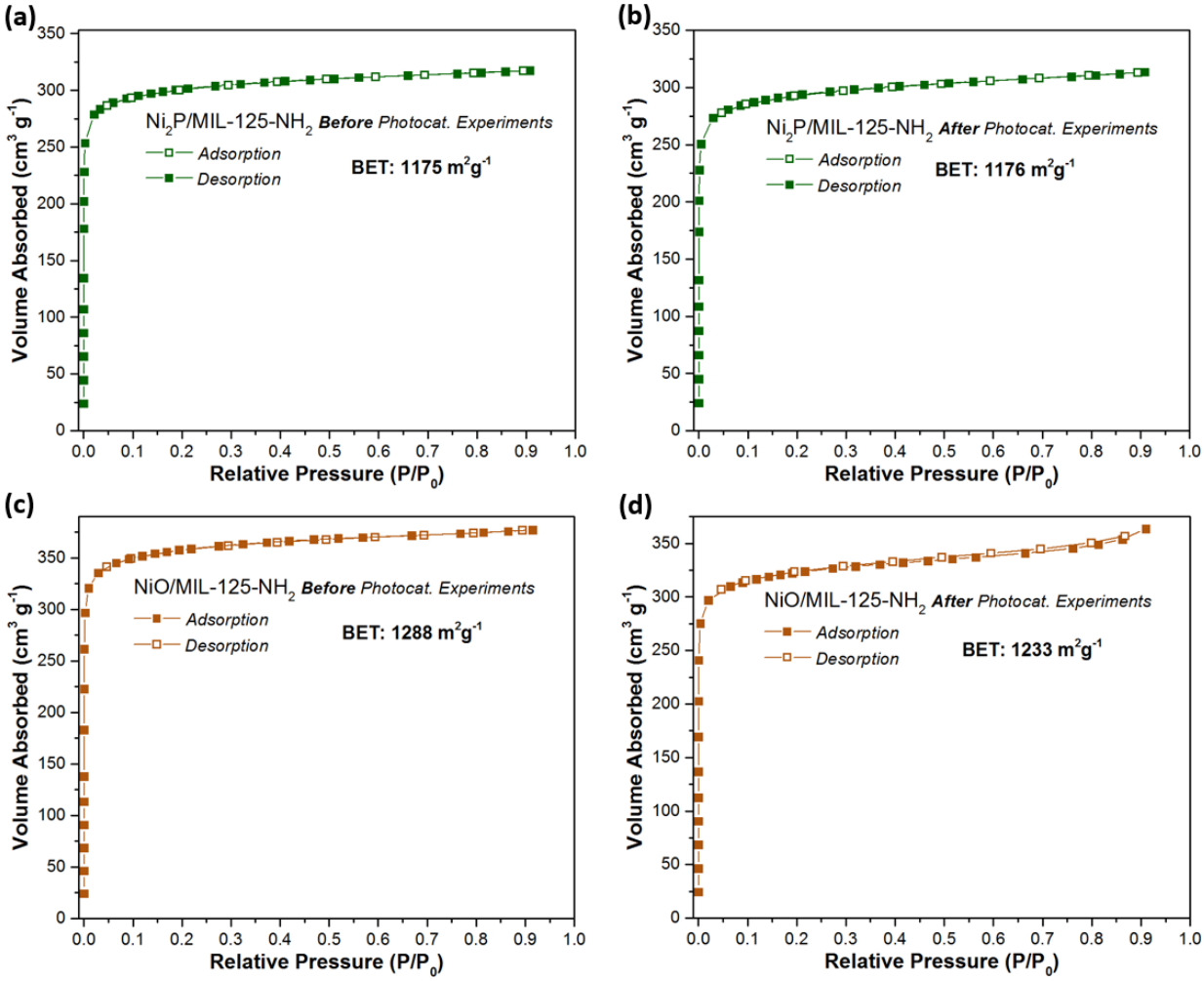

Figure S.6: *N_2 adsorption-desorption isotherms of Ni_2P/MIL-125-NH_2 (green) (a) before (with a calculated BET surface area of 1175 m^2 g^{-1}) and (b) after the photocatalytic experiments (with a calculated BET surface area of 1176 m^2 g^{-1}). N_2 adsorption-desorption isotherms of NiO/MIL-125-NH_2 (orange), (c) before (with a calculated BET surface area of 1288 m^2 g^{-1}) and (d) after the photocatalytic experiments (with a calculated BET surface area of 1233 m^2 g^{-1}).*

Figure S.3 shows that the MIL-125-NH_2, NiO, Co_3O_4, Fe_2O_3 and Ni_2P NPs retained their crystallinity after the photocatalytic water reduction reaction. XPS measurements were carried out for the CuO/MIL-125-NH_2 and CoP/MIL-125-NH_2 systems, since the characteristic Bragg reflections of CuO and CoP NPs were not apparent in the PXRD patterns due to their low concentration and crystallinity compared to the amount of MIL-125-NH_2 used (Figure S.4). The Cu and Co 2p peaks were characteristic of Cu(II) and Co(III) respectively, and showed no significant change after the photocatalytic test. The SEM mapping images of each co-catalyst/MIL-125-NH_2 system confirmed that all the compositional elements of each system are present after the photocatalytic test (Figure S.5). Furthermore, the N_2 adsorption-desorption isotherms collected on the best-performing Ni_2P/MIL-125-NH_2 and NiO/MIL-125-NH_2 systems before and after the photocatalytic experiments showed

comparable BET surface areas, demonstrating the retention of the porous structure of MIL125-NH_2 (Figure S.6).

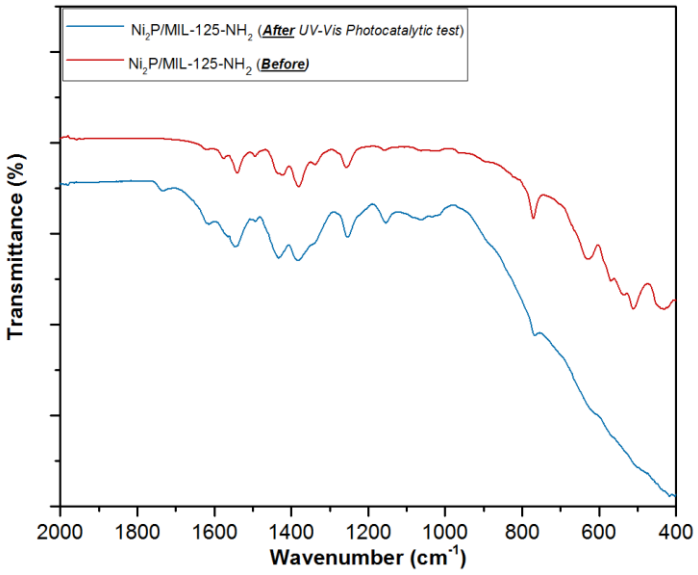

Figure S.7: *FTIR spectra of Ni_2P/MIL-125-NH_2 before (red) and after (blue) photocatalytic test.*

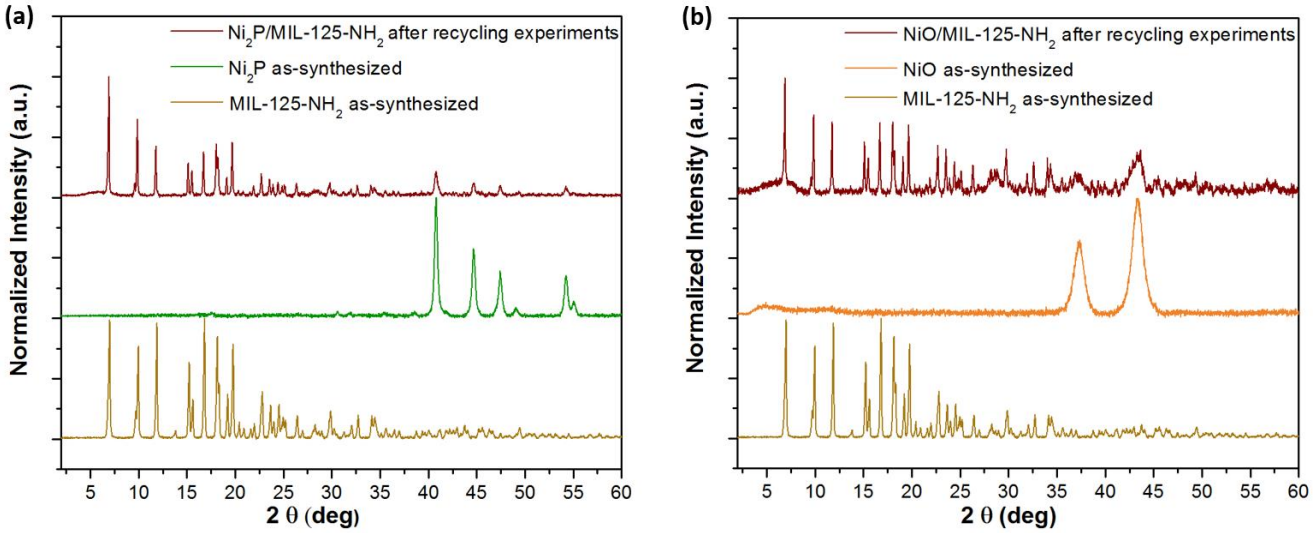

Figure S.8: *PXRD patterns of (a) Ni_2P/MIL-125-NH_2 and (b) NiO/MIL-125-NH_2.*

S2.5 Photoluminescence spectroscopy

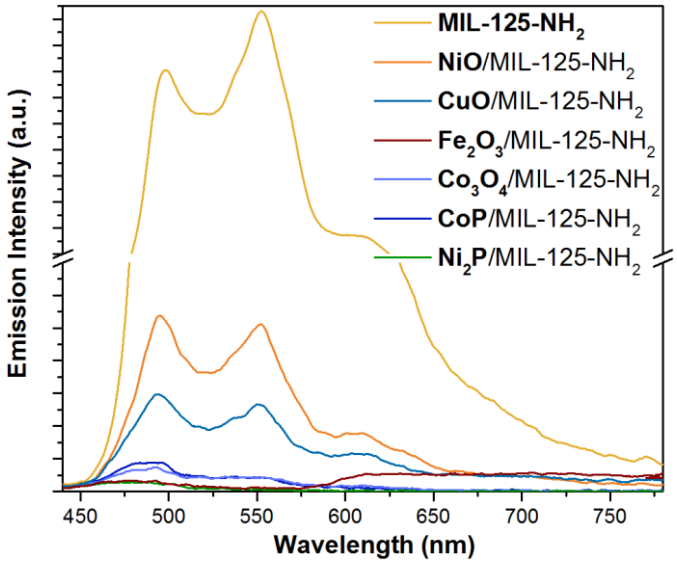

Figure S.9: *PL spectra of the MIL-125-NH₂ and the suspensions of MIL-125-NH₂ with the optimized amounts of: NiO (orange), CuO (blue), Fe₂O₃ (red), Co₃O₄ (violet) CoP (navy blue) and Ni₂P (green, optimized for photocatalytic hydrogen evolution). The co-catalyst-induced quenching of the PL follows the descending order of Ni₂P > CoP ≈ Co₃O₄ > Fe₂O₃ > CuO > NiO. The excitation wavelength was 420 nm.*

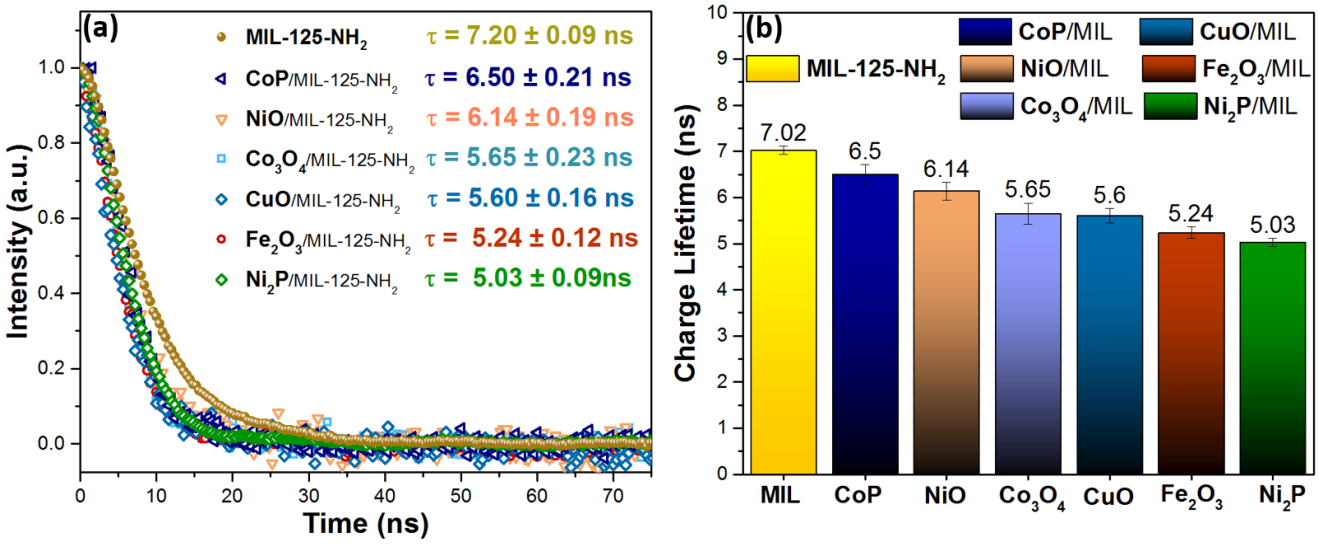

Figure S.10: *(a) Time Resolved PL decay curves and (b) lifetime of MIL-125-NH₂ and MIL-125-NH₂ with different co-catalysts. The excitation wavelength was 420 nm. Since the lifetimes of the co-catalyst/MIL-125-NH₂ systems were not highly different from each other, drawing further conclusions based on these results might be inconclusive.*

S2.6 Electrochemical experiments with co-catalysts

The intrinsic catalytic activity of Ni_2P and NiO in acetonitrile and water (90:10), with 0.1M tetrabuthylammonium perchlorate (TBAP, ensuring the availability of conductive ions) have been explored. This investigation was conducted by means of cyclic voltammetry (CV) at 50 mV s^{-1} scan rate and by linear scan voltammetry (LSV) at 1 mV s^{-1} in a standard 3-electrode electrochemical cell. The suspension containing the co-catalysts was prepared by mixing 10 mg of each co-catalyst with 1 mL solution of EtOH and water (2:1) and 20 μL of Nafion (5 wt.%). The suspension was deposited as a thin film on a polished glassy carbon electrode with diameter of 3 mm (S= 0.07065 cm^2), which was used as a working electrode. The loading of each co-catalyst was 0.7 mg cm^{-2}. Pt wire was used as counter electrode, while Ag/Ag^+ with 0.01 M $AgNO_3$ and 0.1 M TBAP in acetonitrile (ALS Japan) was used as reference electrode.

Prior the LSV measurement, the CV of the electrode with the co-catalysts was obtained in a non-aqueous electrolyte with 0.1 M TBAP. Subsequently, the electrode was transferred to the cell with water-containing electrolyte and the CV at 50 mV s^{-1} was measured again in order to define the hydrogen evolution reaction (HER) region (-0.7 V to -1.2 V). This potential window was selected to perform further investigation of the intrinsic catalytic activity of the co-catalysts. In order to compare the intrinsic catalytic activity of Ni_2P and NiO, the current densities were collected under similar conditions to those applied for the photocatalytic test.

It was established that the current density (intrinsic catalytic activity toward HER) of the examined Ni_2P is lower than that of the NiO co-catalyst. For example, at -0.9 V versus Ag/Ag^+, the current density of the Ni_2P and NiO co-catalysts is -0.07 and -0.22 mA cm^{-2}, respectively.

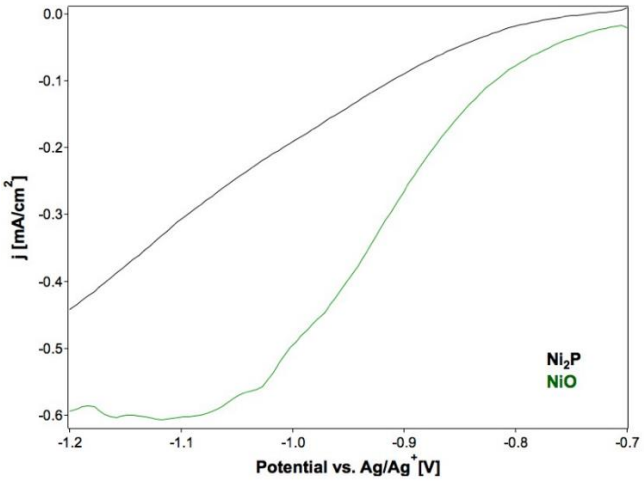

Figure S.11: *Cathodic polarization curves of the electrodes with Ni_2P and NiO NPs obtained by linear scan voltammetry.*

S2.7 Pt NPs as co-catalysts with MIL-125-NH_2

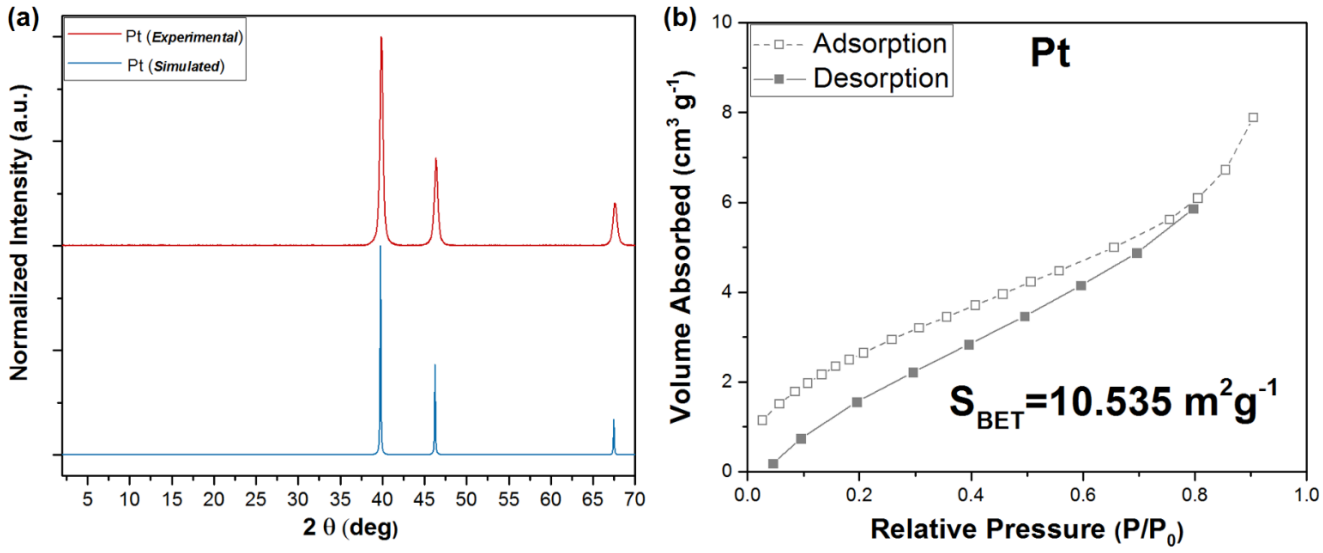

Figure S.12: *(a) PXRD patterns of the simulated (blue) and as-synthesized (red) Pt NPs. (b) N_2 adsorption-desorption isotherm of Ni_2P NPs.*

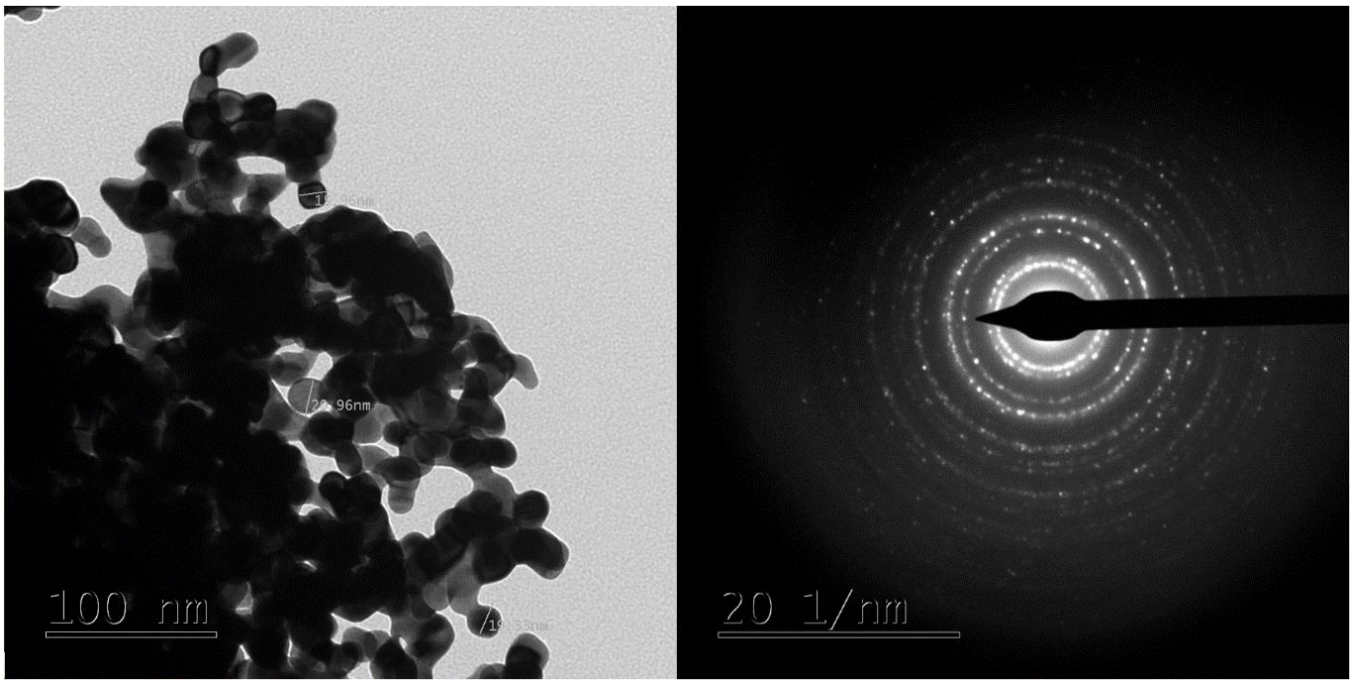

Figure S.13: *(a) TEM image and (b) electron diffraction pattern of Pt NPs. The size of Pt NPs is estimated to be around 20-30 nm.*

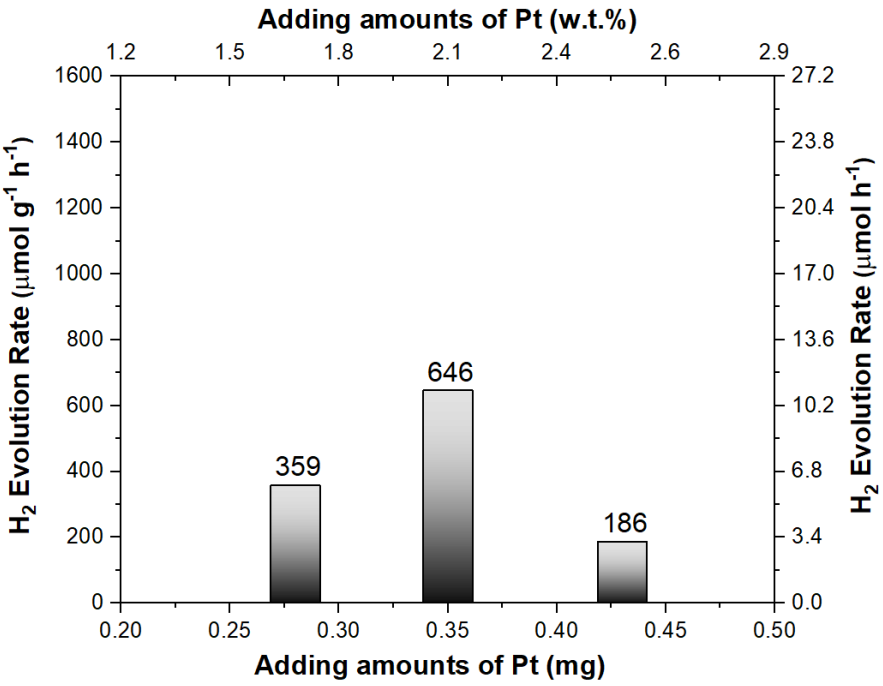

Figure S.14: *H_2 evolution rate of 17.0 mg MIL-125-NH_2 against different adding amounts of Pt NPs.*

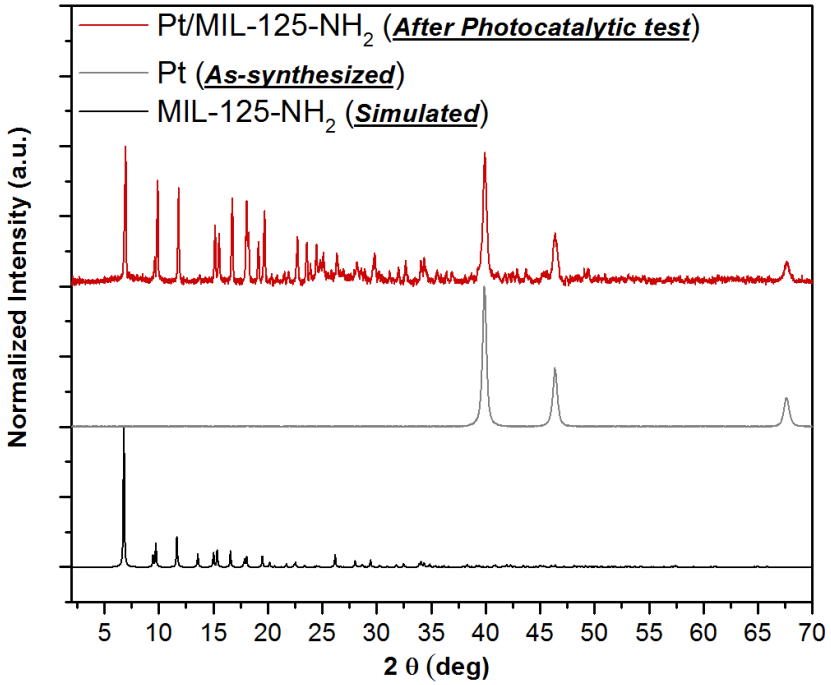

Figure S.15: *PXRD patterns of MIL-125-NH_2 simulated (dark gray), Pt NPs as-synthesized (light gray) and 2 (± 0.4) wt.% Pt/MIL-125-NH_2 after photocatalytic test.*

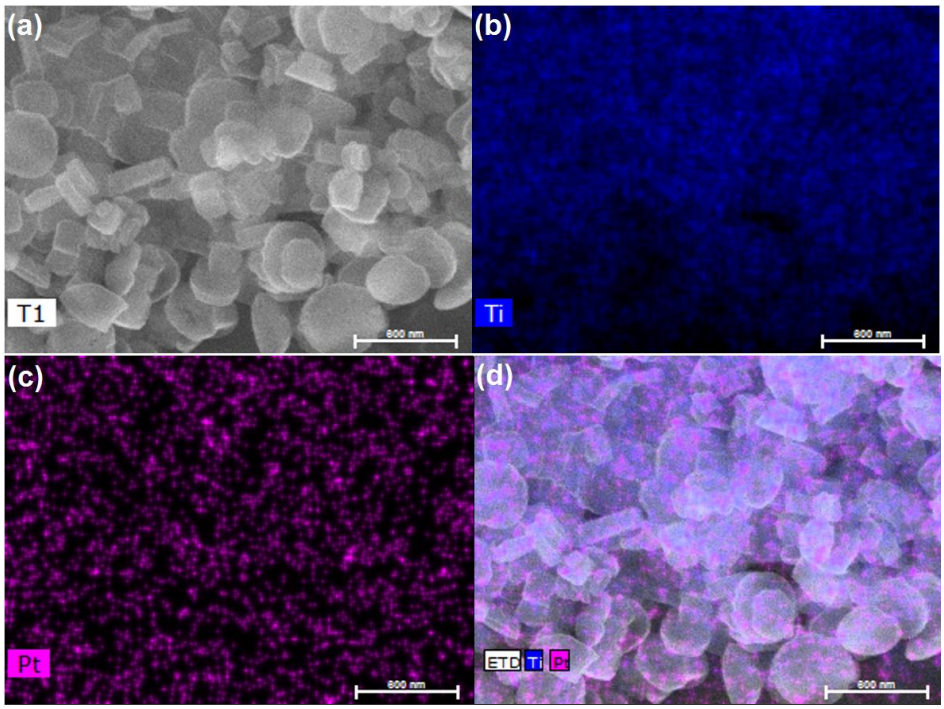

Figure S.16: *(a) SEM image of 2 (± 0.4) wt.% Pt/MIL-125-NH₂ after photocatalytic testing, and corresponding EDX maps of (b) Titanium, (c) Pt and (d) both Ti and Pt.*

S2.8 Comparison of Ni_2P/MIL-125-NH_2 with other studies in the literature

Table S.2: *Comparison of Ni_2P/MIL-125-NH_2 with other MOF-based hydrogen generation photocatalytic systems.*

Photocatalyst	**Co-catalyst**	**Light Source** λ (nm)	**H_2 Evolution Rate** *with respect to the MOF*	**QY**	**Ref.**
MIL-125- NH_2 (Ti)	Pt NPs photodeposited	≥ 420	*333 μmol h^{-1} g^{-1}		[147]
Uio-66-NH_2 (Zr/Ti)	Pt NPs	≥ 420	3.5 mmol mol^{-1} in 5 h		[148]
Ti-MOF-Ru(tpy)₂	Pt NPs	≥ 420	*100-200 μmol h^{-1} g^{-1}	**AQY: 0.2** % at 500 nm	[88d]
MIL-125-NH_2 (Ti)	Pt NPs photodeposited	≥ 420	*525 μmol h^{-1} g^{-1}		[149]
Al-PMOF	Pt NPs	≥ 420	200 μmol g^{-1} h^{-1}		[82]

Uio-66 (Zr)	2.87 wt.% Pt	≥ 380	257.38 μmol h^{-1} g^{-1}		[122]
MIL-125(Ti)	Pt	≥ 320	*155 μmol h^{-1} g^{-1}		[150]
MIL-100 (Fe)	0.8 wt.% Pt photodeposited	≥ 420	109 μmol h^{-1} g^{-1}		[85b]
MOF-253 (Al)	Pt complex	≥ 420	100 μmol h^{-1}	**QE**: 1.63% at 440 nm	[151]
$[Cu(enMe)_2]_4[PNb_{12}O_{40}(VO)_6](OH)_5\ 6H_2O$	0.75% Pt	Hg lamp	43.86 μmol g^{-1} h^{-1}		[152]
$[Gd_2(abtc)(H_2O)_2(OH)_2]\ 2H_2O$	1.5 w.t.% Ag	Xe lamp	* 212 μmol h^{-1} g^{-1}		[122]
$Zr_6(\mu_3\text{-}O)_4(\mu_3\text{-}OH)_4(bpdc)_{5.94}(L1)_{0.06}$	Pt NPs photodeposited	≥ 420	3400 turnovers after 48hrs	**AQY:** 3 x 10^{-4} % at 440 nm	[153]
UiO-66 (Zr)	Pt NPs in sol	Xe doped mercury	2.4 ml in 3hrs	**QY**: 0.1% at 370 nm	[154]
UiO-66-NH2 (Zr)	Pt NPs in sol	Xe doped mercury	2.8 ml in 3hrs	**QY**: 3.5% at 370 nm	[154]
UiO-66 (Zr) + Rhodamine B	Pt NPs on MOF	≥ 420	116 μmol h^{-1} g^{-1}		[84]
Uio-66 (Zr) + Erythrosin B	0.5 w.t.% Pt (photo-deposited)	≥ 420	*444 μmol h^{-1} g^{-1}		[79a]
$Cu(RSH)(H_2O)]_n$ + Eosin Y (1D-polymer)	N/A	≥ 420	7880 μmol g^{-1} h^{-1}		[155]
[Fe-Fe]@ZrPF	[FeFe} based complex	≥ 420	3.5 μmol h^{-1} in 120 min		[156]
UiO-66 Fe-Fe + $Ru(bpy)_3$	Fe-Fe	Blue LED 470 nm	* 280 μmol h^{-1} g^{-1}		[157]
POM@UiO-67	POM	≥ 400	699 μmol h^{-1} g^{-1} wrt POM		[158]
MIL-125-NH_2 (Ti)	Co(III)-oxime	≥ 408	*~637 μmol h^{-1} g^{-1}	**AQY:** 0.5 %	[33a]
MIL-125-NH_2 (Ti)	Nickel(II) Species	≤ 360	*6693 μmol h^{-1} g^{-1}		[91b]
Cu-I-bpy		UV-light Irradiation	7090 μmol h^{-1} g^{-1}		[89a]

$[Cu^{I}Cu^{II}_2(DCTP)_2]NO_3 \cdot 1.5DMF_n$	H_2PtCl_6	320-780 nm	*32 μmol h^{-1} g^{-1}		[89b]
MIL-125-NH_2	Ni_2P NPs	Xe lamp ≥ 420	1230 μmol h^{-1} g^{-1}	**AQY:** 6.6 %	This work [86]

** = calculated μmol h^{-1} g^{-1}*

Unless otherwise stated, H_2 rate in respect of MOF

S3 Supporting Information for Chapter 3: Variation of Electron-Donors and Dual-Functional Photocatalysis

S3.1 Variation of electron donors

Table S.3: *Concentration of each electron-donor within the photocatalytic solution (with acetonitrile and water). The selection of these specific concentrations was based on other scientific studies with MOF-based photocatalytic systems in the literature.*[88a, 91a, 112] *The amount of water was kept constant at ~5 v/v% in all the examined photocatalytic solutions.*

	TEA	TEOA	MeOH	EtOH	L-ascorbic acid
Concentration (v/v%)	16	-	36.3	36.3	-
Concentration (M)	7.2	0.01	24.7	17.1	0.1

S3.1.1 Electrochemical experiments

The oxidation/reduction behavior of five sacrificial agents: EtOH, MeOH, TEA, TEOA and L-ascorbic acid in a non-aqueous solution of acetonitrile with 0.1 M tetrabuthylammonium perchlorate (TBAP) has been explored. This investigation was conducted by means of cyclic voltammetry at different scan rates in a standard three-electrode electrochemical cell, using the Bipotentiostatat 2325 (ALS Japan). Pt wires were used as working and counter electrodes and Ag/Ag^+ with 0.01 M $AgNO_3$ and 0.1M TBAP in acetonitrile (ALS Japan) was used as reference electrode. The amount of electrolyte used in a typical experiment was approximately 55 mL. Prior to the investigation of the electrolyte with sacrificial reagents, the blank electrolyte (0.1 M TBAP in acetonitrile) was tested in order to define any possible influence from it. Two oxidation peaks are observed with current densities of less than 0.1 mA cm^{-2} at -0.57 V and 0.625 V (Figure S17a).

The electrolyte with TEA shows an order of magnitude higher current density at the oxidation peak (~40 mA cm^{-2} at scan rates of 50 and 20 mV s^{-1}, ~12 mA cm^{-2} at scan rate of 5 mV s^{-1}), than the other compounds in electrolyte. However, due to higher currents the two-step oxidation observed in the case of TEA, transformed into one wide peak with maximum at 1.4 V (Figure S17b). The electrolyte with TEOA shows two oxidation peaks at 0.797 V and 1.073 V (scan rate: 50 mV s^{-1}), which can be associated with the two following steps: 1) positively charged aminyl radical is formed (at 0.797 V),

which 2) directly reacts with the TEOA and forms iminium species (at 1.073 V).[29b] The range of the obtained current densities is between 1.2 to 2 mA cm^{-2} (Figure S17c).

The electrolytes with EtOH (Figure S17d) and MeOH (Figure S17e) show one small oxidation peak at: 1.88 V and 0.963 V (scan rate: 50 mV s^{-1}), respectively. The current density of the oxidation peaks is 0.8 and 1.61 mA cm^{-2}, for EtOH and MeOH, respectively. According to Han et. Al.,[159] there are two kinds of protons in the ethanol molecule. One is bonded to the oxygen atom and the other bonded to the carbon atom. If the proton bonded to the oxygen atom is firstly oxidized, then the first reaction step is: $CH_3CH_2OH \rightarrow [CH_3CH_2O]_{ad} + H^+ + e^-$

If the proton bonded to the carbon atom is firstly oxidized, then the first reaction step should be: $CH_3CH_2OH \rightarrow [CH_3CHOH]_{ad} + H^+ + e^-$

It cannot be concluded which one of the two reaction pathways is right and thus the observed peak for EtOH corresponds to one of the above-mentioned reactions. Similar mechanism is assumed for MeOH.

L-ascorbic acid exhibits 2 oxidation and 2 reduction peaks at all scan rates (Figure S17f). While the small peak could be the reducible artefact from acetonitrile, the highest peak at 1.1 V corresponds to the oxidation of ascorbic acid. It has a corresponding reduction peak at -0.8 V ($C_6H_8O_6 \rightarrow C_6H_6O_6 + 2H^+ + 2e^-$). The maximum current density of 1.8 mA cm^{-2} was observed at a scan rate of 100 mV s^{-1}

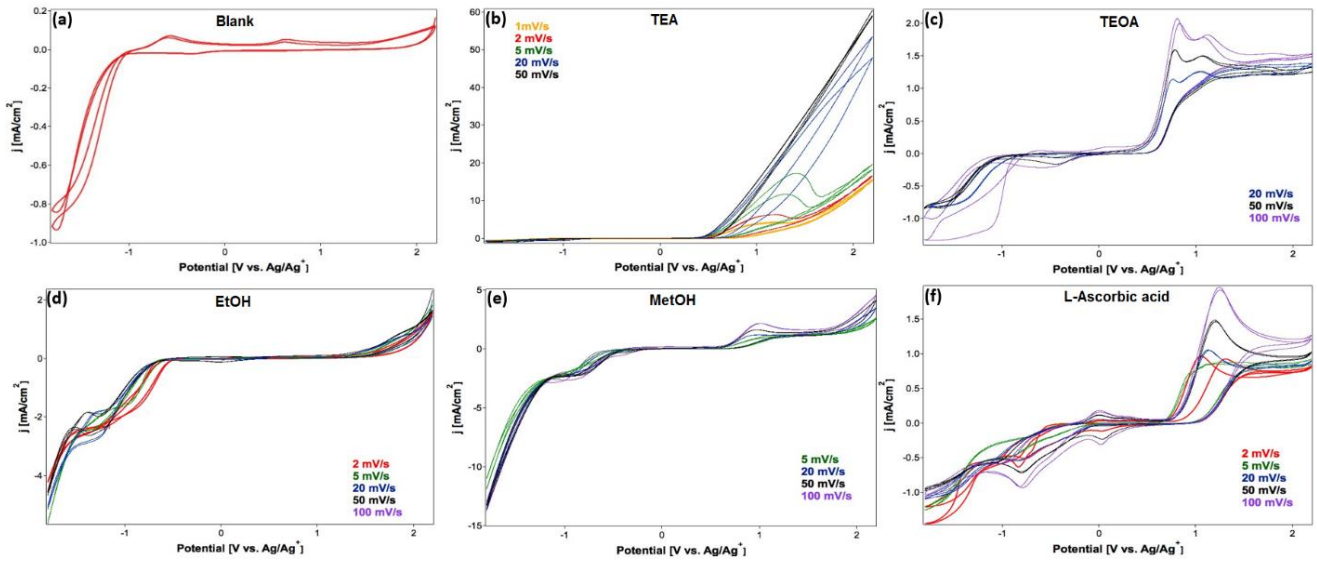

Figure S.17: *Cyclic voltammograms of (a) blank electrolyte (0.1 M TBAP in acetonitrile) at 20 mV s^{-1}, (b) TEA, (c) TEOA, (d) EtOH, (e) MeOH and (f) L-ascorbic acid in the same solution.*

S3.2 Photocatalytic Hydrogen evolution coupled with Rhodamine B degradation

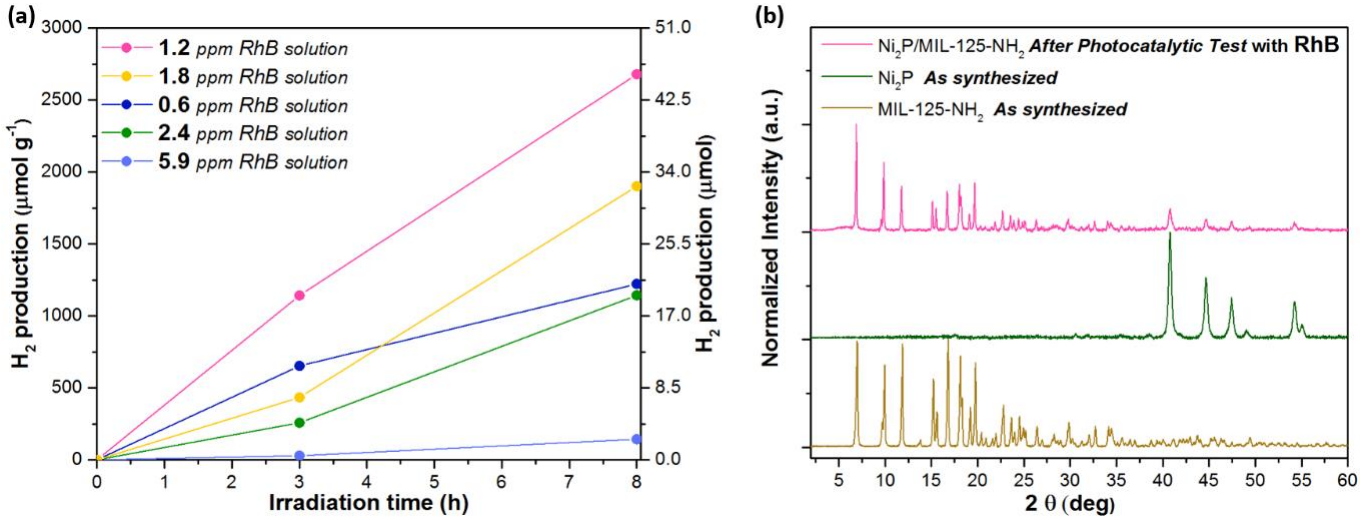

Figure S.18: *(a) Photocatalytic H_2 production of Ni_2P/MIL-125-NH_2 in aqueous acetonitrile solution with variant concentrations of Rhodamine B (RhB), (b) PXRD patterns of the as-synthesized MIL-125-NH_2 and Ni_2P, and the Ni_2P/MIL-125-NH_2 after the photocatalytic test in 17 mL solution with 0.02 mg of RhB (1.2 ppm).*

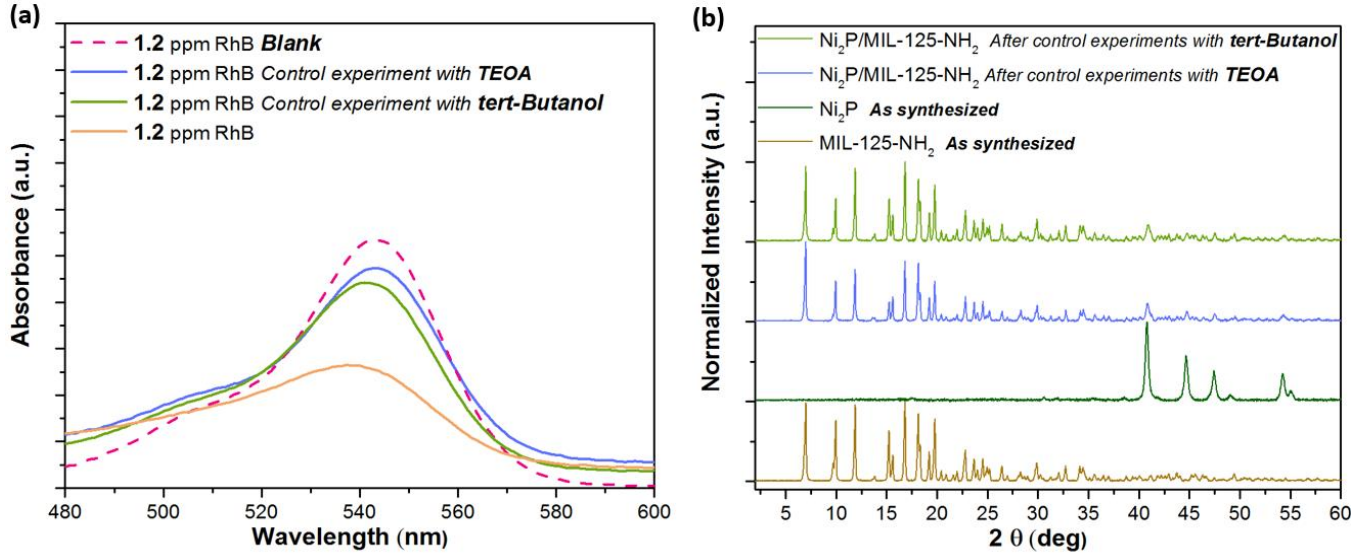

Figure S.19: *(a) Trapping experiments of active species: UV-Vis spectra of 1.2 ppm RhB solution (blank) and supernatants after photocatalytic test of the same solution with 0.01 M TEOA (e^- scavenger), 0.01 M tert-butanol (•OH radical scavenger) and no scavenger, and (b) corresponding PXRD patterns. The duration of the photocatalytic tests was 3 h.*

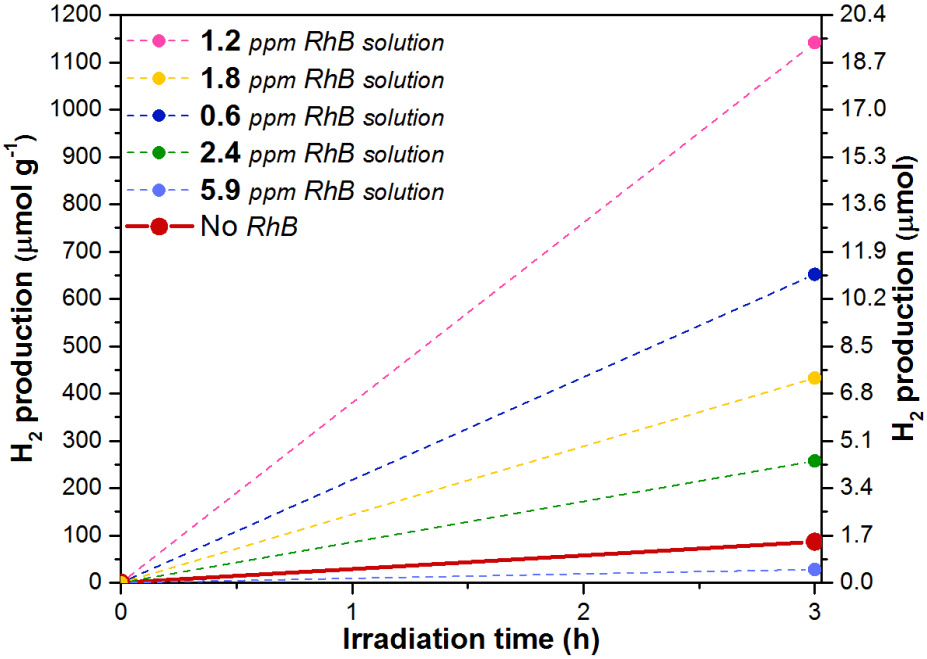

Figure S.20: *Control experiment: H_2 evolution of Ni_2P/MIL-125-NH_2 in an aqueous acetonitrile solution, without any RhB or other electron donors, after 3 h visible light irradiation (solid red line). This result was compared with the photocatalytic performance of Ni_2P/MIL-125-NH_2 in aqueous acetonitrile solution with variant concentration of RhB (dashed lines).*

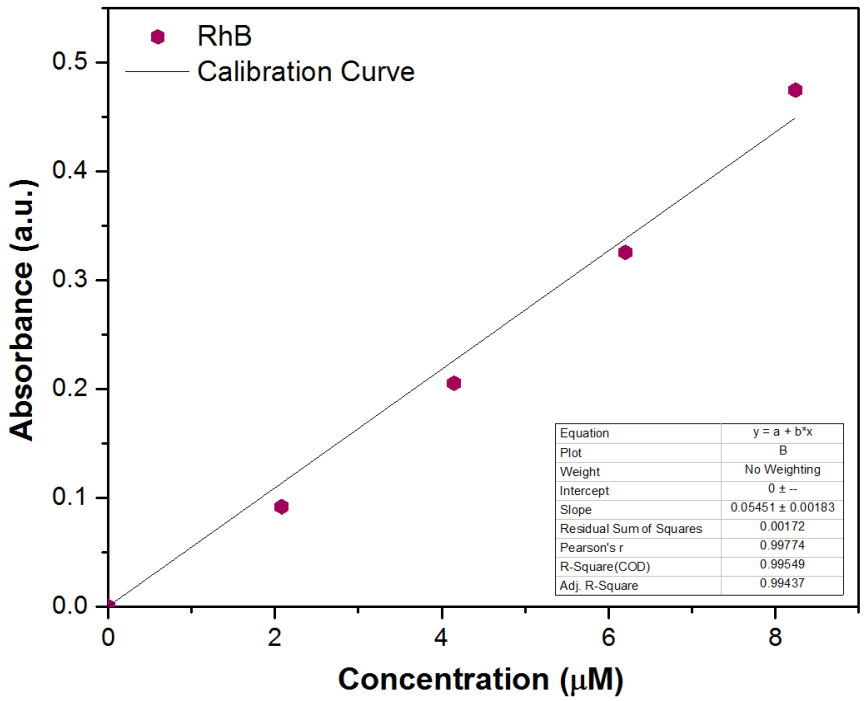

Figure S.21: *Calibration curve of RhB in acetonitrile solution with water (5 v/v% H_2O). Absorbance peak at 543 nm.*

S4 Supporting Information for Chapter 4: Construction of MOF/MOF Heterojunctions

S4.1 Synthetic Procedures

Synthesis of MIL-167

MIL-167 was synthesized based on reported procedures, [121] as follows:
The linker H_4DOBDC (1.585 g) was dissolved in 2.2 mL DEF and 2.2 mL MeOH. After stirring of the mixture for few minutes, 0.592 mL of titanium isopropoxide was added. Then, the suspension was placed in a Teflon liner and were heated up to 180 °C for 24h. The obtained dark red powder was first washed several times with DEF then it was stirred overnight in MeOH and the next day it was washed several times with MeOH. Finally, the obtained powder was dried at 60 °C for ~5 h.

Synthesis of MIL-167/MIL-125-NH_2

The MIL-167/MIL-125-NH_2 samples were synthesized following similar procedure to that of MIL-125-NH_2, except that various amounts of MIL-167 (5-110 mg) were introduced in the MIL-125-NH_2-precursor solution, prior to heating.

S4.2 Characterization

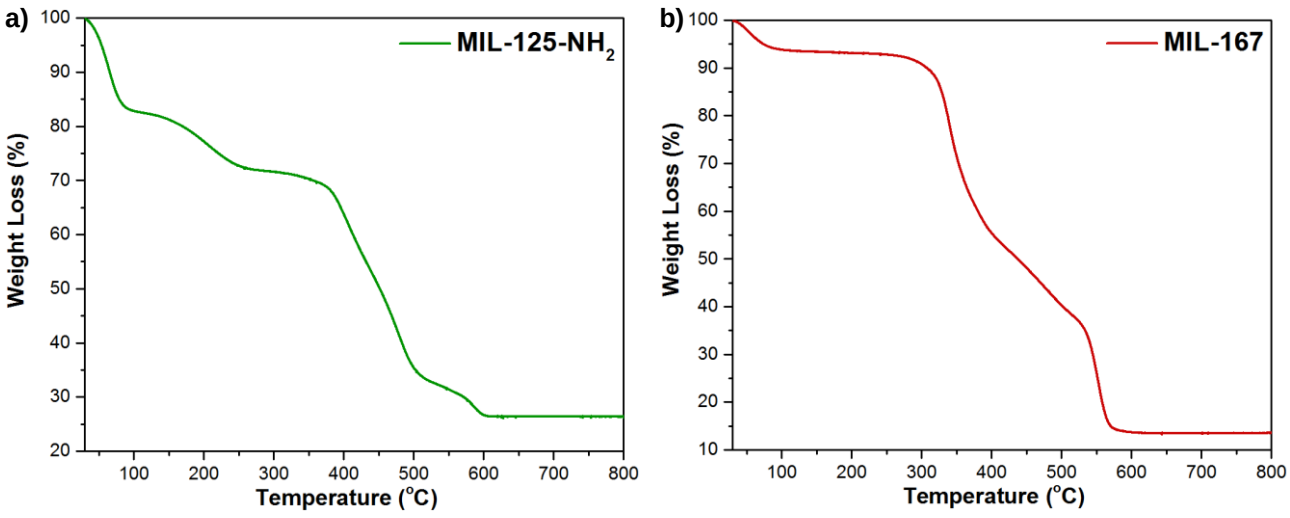

Figure S.22: *TGA curve of a) MIL-125-NH_2 and b) MIL-167 obtained under airflow with a heating rate of 5 °C min^{-1}.*

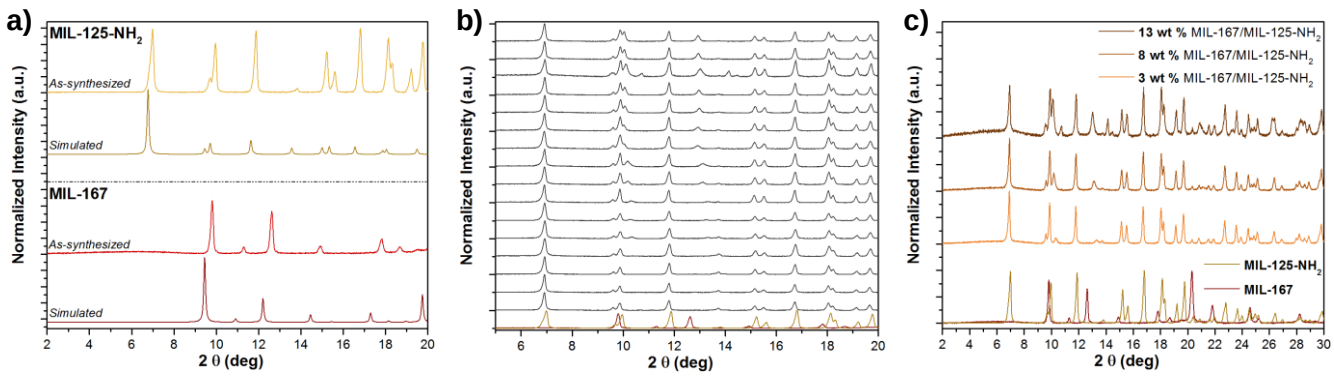

Figure S.23: *PXRD patterns of a) the as-synthesized (light colors) and simulated (dark colors) MIL-125-NH₂ (yellow) and MIL-167 (red), b) MIL-125-NH₂ synthesized in the presence of increasing amounts of MIL-167 (5 - 100 mg, increasing toward the top of the figure) and c) MIL-125-NH₂ synthesized in the presence of 20, 40 and 60 mg of MIL-167.*

Table S.4: *X-ray diffraction-derived data (measurements in 0.4 mm borosilicate glass capillaries).*

Synthesis of MIL-125-NH₂ in:	MIL-125-NH₂ composition (wt.%)	MIL-167 composition (wt.%)
20 mg MIL-167	97	3
40 mg MIL-167	92	8
60 mg MIL-167	87	13

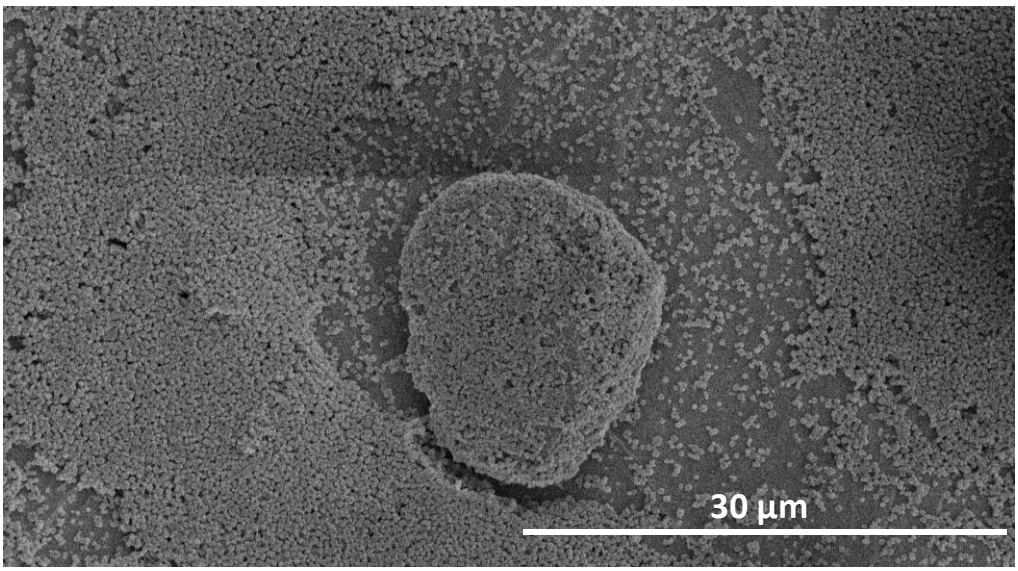

Figure S.24: *SEM image of MIL-167/MIL-125-NH₂ heterojunction sample. In this case, prior to microscopy the samples were added in a MeOH solution, sonicated and then drop-casted on the SEM holder, which was allowed to dry.*

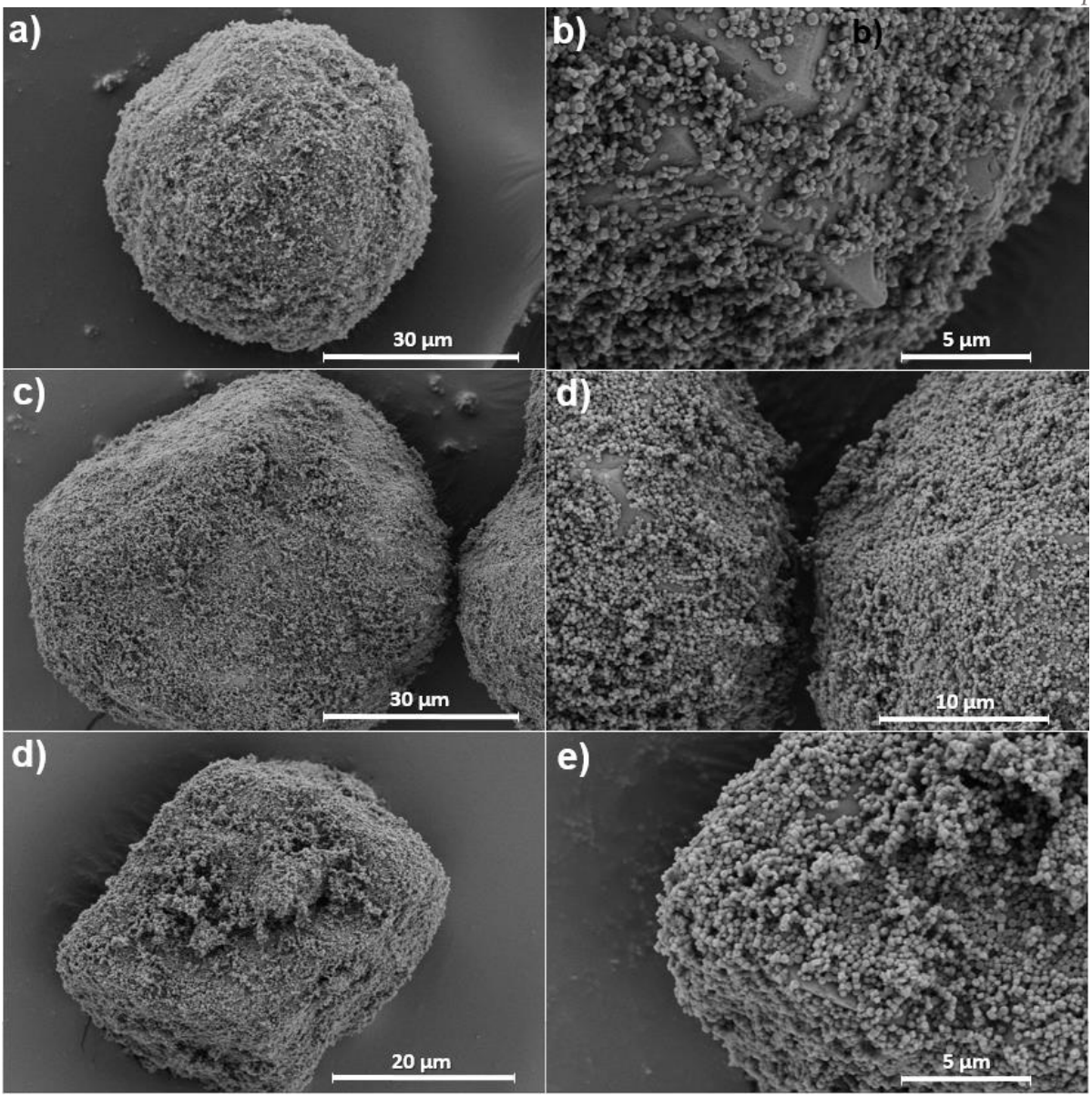

Figure S. 25: *SEM images of a), b): 3 wt.% MIL-167/MIL-125-NH_2, c), d): 8 wt.% MIL-167/MIL-125-NH_2 and d), e) 13 wt.% MIL-167/MIL-125-NH_2, with different magnification. The samples were prepared by spreading a small amount of the MIL-167/MIL-125-NH_2 dry powder on a carbon type SEM holder and then blowing the it with N_2 to remove excess material.*

MIL-125-NH_2 crystals demonstrate a cylindrical disc type of morphology with an approximate diameter of 400 nm. On the other hand, MIL-167 crystals are spheres of significant greater size, with their diameter approximated at 30-60 μm. The notable difference between the morphology of these two MOFs, allows the visual distinguishing of MIL-167 and MIL-125-NH_2 within the heterojunction samples (Figures S24 and S25). It is thus apparent that the bulky spherical crystals of MIL-167 are covered by the significantly smaller crystals of MIL-125-NH_2, with the latter being also spread around MIL-167 at Figure S24.

S4.3 Stability

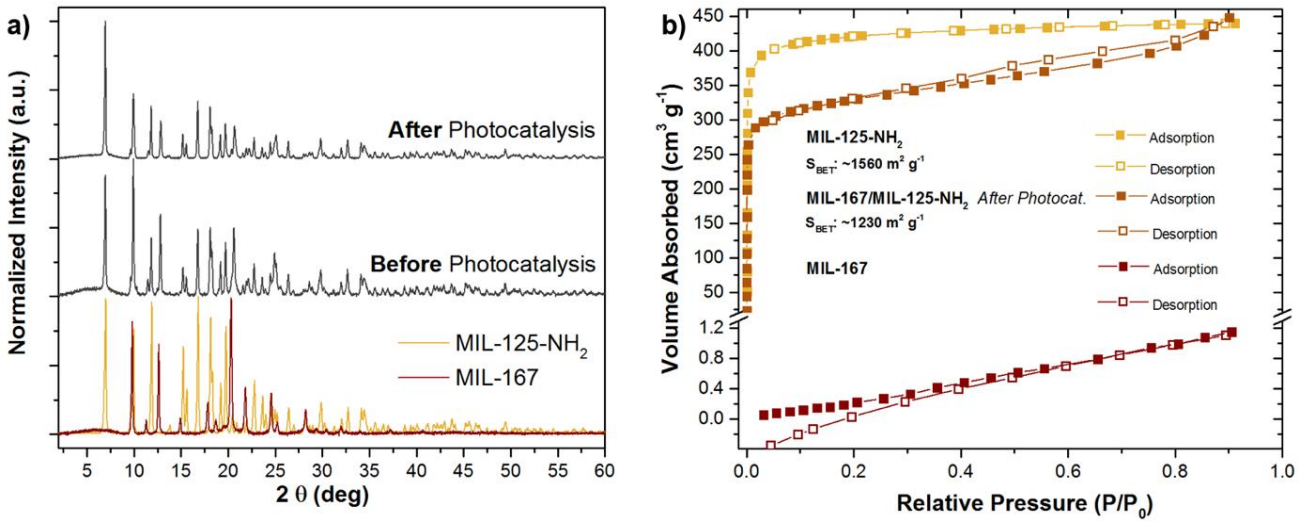

Figure S.26: *a) PXRD patterns of 8 wt.% MIL-167/MIL-125-NH₂ before and after photocatalysis, and b) N₂ sorption isotherms of the as-synthesized MIL-125-NH₂ and MIL-167, and 8 wt.% MIL-167/MIL-125-NH₂ after photocatalysis. The BET (Brunauer-Emmett-Teller) surface area of the 8 wt.% MIL-167/MIL-125-NH₂ is smaller than that of the as-synthesized MIL-125-NH₂ (1230 versus 1560 m^2 g^{-1}), which is associated with the presence of the non-porous MIL-167, contributing to the overall mass of the sample.*

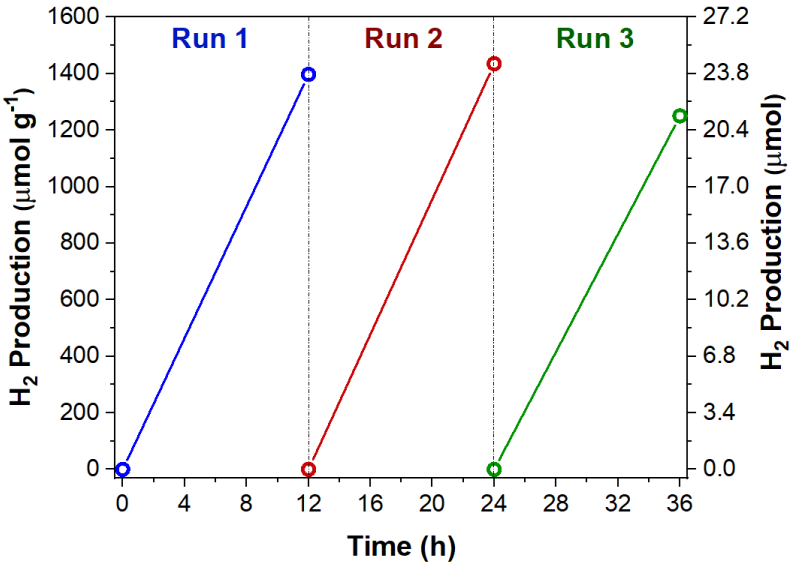

Figure S.27: *Photocatalytic recycling experiments of MIL-167/MIL-125-NH₂ for three consecutive cycles of 12 h each. MIL-167/MIL-125-NH₂ consistently produces hydrogen for more than 36 h.*

Table S.5: *Inductively coupled plasma mass spectrometry (ICPMS) results. Concentration of Ti ions in the MIL-167/MIL-125-NH_2 suspensions before and in the supernatant after 36 hours irradiation. A negligible concentration of Ti ions (0.2 % of the initial concentration) is present in the supernatant after the recycling experiments, showing that there is no significant oxidation of the MOFs' linkers.*

	(1 mg mL^{-1}) MIL-167/MIL-125-NH_2 suspension before photocatalysis	Supernatant after 36 hours photocatalysis
Ti ions Concentration (ppm)	42.5	0.09

S4.4 Mechanism

S4.4.1 Density Functional Theory Calculations

DFT calculations were performed using the CP2K computational chemistry package. The atomic coordinates and cell parameters were optimized using the PBE functional with D3 dispersion correction.[160,161] The Goedecker-Teter-Hutter pseudopotentials were used with a cut-off of 450 Ry,[162] and DZVP-MOLOPT basis set for H, C, O and N atoms and TZVP-MOLOPT basis set for Ti atoms.[163] The initial structure of MIL-125-NH_2 was built from the experimental one by means of adding -NH_2 groups. In the case of MIL-167, the solvent and counterions were removed and 32 -$[HN(CH_3)_3]^+$ cations were added in order to neutralize the unit cell. After ground state relaxation of MIL-125-NH_2 and MIL-167 crystals at PBE level, ground state calculations were performed with PBE0 functional. Auxiliary Density Matrix Method (ADMM) was used in order to reduce the computational cost, pFIT3 was used for H, C, O and N atoms and cFIT11 for Ti atoms.[164] Following the methodology previously reported by Walsh and coworkers,[165] the electrostatic potential average in the pore of the material was taken as analogous to the vacuum level and the PBE0 Kohn-Sham energy levels were aligned relative to this potential:

$$\varepsilon_{KS}^{absolute} = \varepsilon_{KS} - \Phi_{av}$$

Then, the highest occupied eigenvalue was taken as the ionization potential (IP), and the electron affinity (EA) from the difference between the IP and the computed bang gap E_g:

$$EA = IP - E_g$$

S4.4.2 Calculation of Apparent Quantum Yield

Moles of photons emitted by the xenon lamp

For the AQY calculations a similar procedure to that described in section S.24 was followed. First the three following stock solutions were prepared (as described in section S.24): 0.40 M iron (III) stock solution (**1**), 1.20 M di-potassium oxalate stock solution (**2**) and phenanthroline/buffer solution (**3**). Then, the reaction solution was prepared by adding 1.70 mL of solution (**1**) and 1.70 mL of solution (**2**) with 30.6 mL of water in the dark. After stirring, 17.0 mL of the solution was transferred into a reactor (reactor **A**) which was irradiated by a 300 W Xe lamp equipped with a monochromatic filter (450 or 500 nm) for 25 min, while the remaining 17 mL was kept in the dark (reactor **B**). 0.1 mL of sample from reactor **A** was extracted, and added 0.2 mL of solution (**3**), and made up to 5.0 mL with water. 0.1 mL of sample from reactor **B** was treated the same. UV-Vis absorbance (400-600 nm) was recorded for both samples, with the difference in absorbance between the two recorded at 510 nm. The moles of Fe^{2+} were calculated by using the formula: $n_{Fe(II)} = \frac{V_1\, V_3\, \Delta A}{10^3\, V_2\, L\, \varepsilon}$, as follows:

V_1: irradiation volume (17.0 mL),

V_2: sample taken (0.1mL),

V_3: final volume (5.0 mL),

L: optical pathlength (1.0 cm),

ΔA absorbance difference at 510 nm:

- At 450 nm irradiation: **ΔA_1**= 0.75837, **ΔA_2**= 0.75531
- At 500 nm irradiation: **ΔA_1**= 0.76362, **ΔA_2**=0.72065

ε: molar extinction coefficient (11100 L mol^{-1} cm^{-1})

- **Moles of iron(II) at 450 nm irradiation**:

1st measurement $n_{Fe(II)} = 5.8074\ 10^{-5}$

2nd measurement $n_{Fe(II)} = 5.7839\ 10^{-5}$

- **A Moles of iron(II) at 500 nm irradiation**:

1st measurement $n_{Fe(II)} = 5.8475\ 10^{-5}$

2nd measurement $n_{Fe(II)} = 5.5185\ 10^{-5}$

From this, the number of photons per min was calculated using the formula $\frac{n_{photons}}{min} = \frac{n_{Fe(II)}}{\Phi_\lambda\, t\, F}$, as follows:

Φ_λ: Quantum yield for iron production at wavelength λ (1.11 at ~450 nm and 0.86 at ~500 nm)

t: time (25 min)

F: mean fraction of light absorbed = 1

- **At 450 nm:** $\frac{\mathbf{n_{photons}}}{\mathbf{min}} = \mathbf{2.08851\ 10^{-6}}$
- **At 500 nm:** $\frac{\mathbf{\bar{n}_{photons}}}{\mathbf{min}} = \mathbf{2.64326\ 10^{-6}}$

Moles of hydrogen generated under 450 nm and 500 nm radiation

The amount of hydrogen generated by MIL-167/MIL-125-NH_2 under 450 or 500 nm radiation was carried out using the same reaction mixture and set-up as the photocatalytic experiments (Figure S6) with the exception of using a 450 nm or 500 nm band pass filter with the xenon lamp.

- Amount of H_2 at **450 nm**: 6.34382 10^{-6} mol in 240 min (4 h)
- Amount of H_2 at **500 nm**: 4.66284 10^{-6} mol in 480 min (8 h)

Apparent quantum yield determination

The apparent quantum yield (AQY) was calculated by using the following formula: $\mathrm{AQY}(\%) = \frac{2\frac{\mathrm{N\,H_2}}{\mathrm{min}}}{\frac{\mathrm{N\ photons}}{\mathrm{min}}} 100$, where $\frac{N\,H_2}{min}$ = number of hydrogen molecules evolved per minute and $\frac{N\ photons}{min}$ = number of incident photons per minute. Thus, **AQY** = **2.53 %** and **0.74 %** at **450** and **500 nm**, respectively.

Table S.6: *Comparison of the AQY values at wavelengths corresponding to the visible range (λ ≥ 420 nm) of different photocatalytic systems in the literature.*

MOF-based System	**AQY**	**Wavelength**	**Ref.**
Pt/UiO-66 (Zr)	0.25 %	420 nm	112
Pt/CdS/UiO-66 (Zr)	1.2 %	420 nm	112
Pt/$Zr_6(\mu_3\text{-}O)_4(\mu_3\text{-}OH)_4(bpdc)_{5.94}(L1)_{0.06}$	5.6 x 10^{-4} %	440 nm	85c
Pt/MIL-125-NH_2 (Ti)	1.3 %	450 nm	107b
This Work	2.5 %	450 nm	
Ni_2P/MIL-125-NH_2	6.6 %	450 nm	86
Pt/MIL-125-NH_2 (Ti)	0.3 %	500 nm	107b
Pt/Ti-MOF-Ru(tpy)$_2$	0.2 %	500 nm	88d
This Work	0.7 %	500 nm	
Pt/Al-PMOF	0.1 %	-	82
Other Systems			
Ni_2P/TiO_2	0.9%	400 nm	86
MoS_2/CdS	7.3 %	420 nm	166
Ni/CdS	11.2%	450 nm	167
Ni/CdS	5.9 %	520 nm	167

S4.4.3 Transient Photoluminescence Spectroscopy

The fluorescence lifetimes of our samples were collected through time-resolved PL, performed with a LP980 laser flash spectrometer (Edinburgh Instruments). The samples were excited by 5 ns laser pulses at λ = 420 nm (nanosecond tunable Ekspla NT340 laser with 5 Hz repetition rate) and the lifetimes were recorded at different wavelengths (460, 490 and 550nm) based on the PL emission peaks of the samples (Figure 3B). In a typical experiment, 0.35 mg of MIL-125-NH_2, MIL-167 or MIL-167/MIL-125-NH_2 was dispersed in 3.5 mL of acetonitrile. The suspension was sonicated for ~30 min and then placed in a 1 cm path-length quartz cuvette. The transient PL spectroscopy data were fitted to a monoexponential decay to determine the lifetimes.

Table S.7: *Comparison of the lifetimes of MIL-125-NH_2, 8 wt.% MIL-167/MIL-125-NH_2 and MIL-167, recorded at different wavelengths based on the PL emission peaks of the samples.*

	Lifetimes (μs)		
	460 nm	490 nm	550 nm
MIL-125-NH_2	5.364 ± 0.009	4.650 ± 0.013	3.113 ± 0.017
8 wt.% MIL-167/MIL-125-NH_2	5.273 ± 0.011	3.676 ± 0.028	3.259 ± 0.017
MIL-167	-	0.721 ± 0.018	0.532 ± 0.007

S4.5 UIO-66-NH_2/MIL-125-NH_2 Heterojunctions

S4.5.1 Synthetic Protocol

Synthesis of UIO-66-NH_2

UIO-66-NH_2 was synthesized by slightly modifying a reported procedure,[74] as follows:
First, two stock solutions were synthesized. The first one by dissolving 0.240 g of the linker NH_2-H_2BDC in 20 mL DMF and the second one by dissolving 0.320 g of zirconium (IV) chloride in 20 mL DMF. After sonicating the mixtures for sufficient time (in order for the linker or metal salt to be dissolved in the solvent), 2 mL of each solution was added in 10 mL vials and were heated up to120 ^{o}C for 48 h. The obtained light-yellow solids were first washed several times with DMF, then stirred overnight in MeOH and the next day they were washed several times with MeOH. Finally, the obtained powder was dried at 60 °C for ~5 h.

Synthesis of UIO-66-NH_2/MIL-125-NH_2

The UIO-66-NH_2/MIL-125-NH_2 samples were synthesized following similar procedure to that of the MIL-167/MIL-125-NH_2 except that 10, 20, 40 or 60 mg of UIO-66-NH_2 were introduced in the MIL-125-NH_2-precursor solution (instead of MIL-167), prior to heating.

S4.5.2 Powder X-ray Diffraction

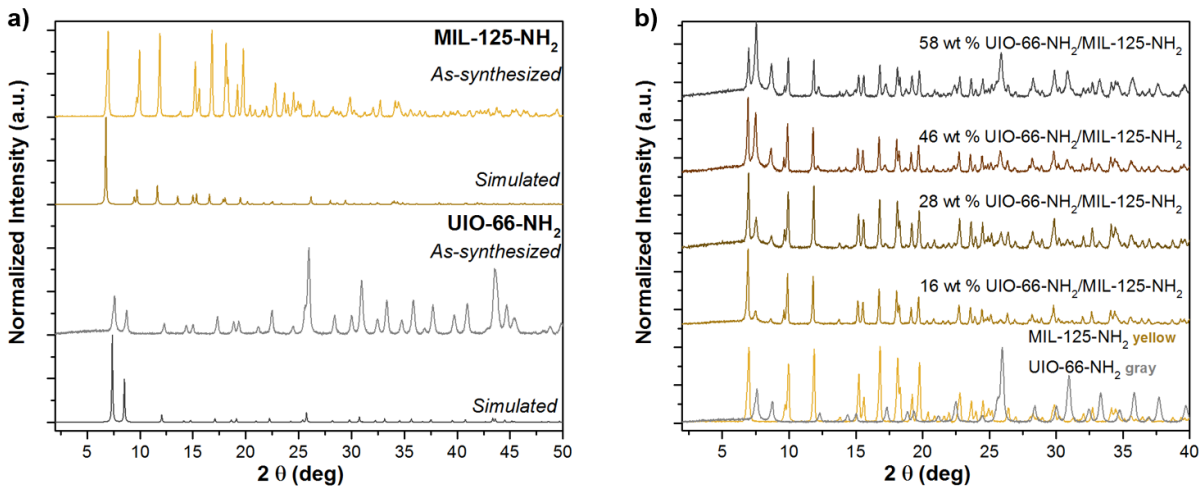

Figure S.28: *PXRD patterns of a) the as-synthesized (light colors) and simulated (dark colors) MIL-125-NH_2 (yellow) and UIO-66-NH_2 (gray), and b) MIL-125-NH_2 synthesized in the presence of 10, 20, 40 and 60 mg of UIO-66-NH_2.*

Table S. 8: *X-ray diffraction-derived data (measurements in 0.4 mm borosilicate glass capillaries).*

Synthesis of MIL-125-NH_2 in:	MIL-125-NH_2 composition (wt.%)	Uio-66-NH_2 composition (wt.%)
10 mg UIO-66-NH_2	84	16
20 mg UIO-66-NH_2	72	28
40 mg UIO-66-NH_2	54	46
60 mg UIO-66-NH_2	42	58

S4.5.3 Scanning Electron Microscopy

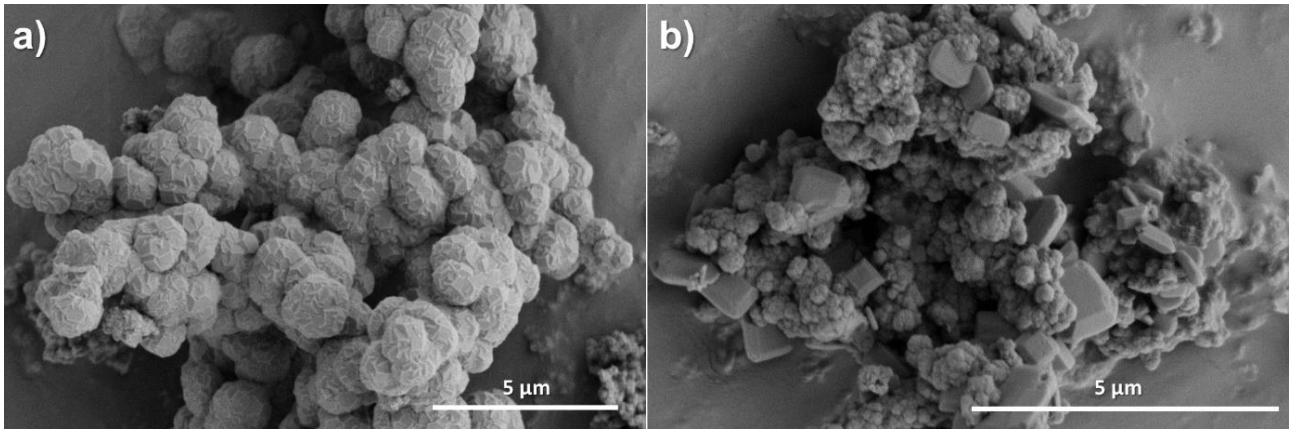

Figure S.29: *a) SEM image of UIO-66-NH_2 and b) 58 wt.% UIO-66-NH_2/MIL-125-NH_2.*

S4.5.4 Stability

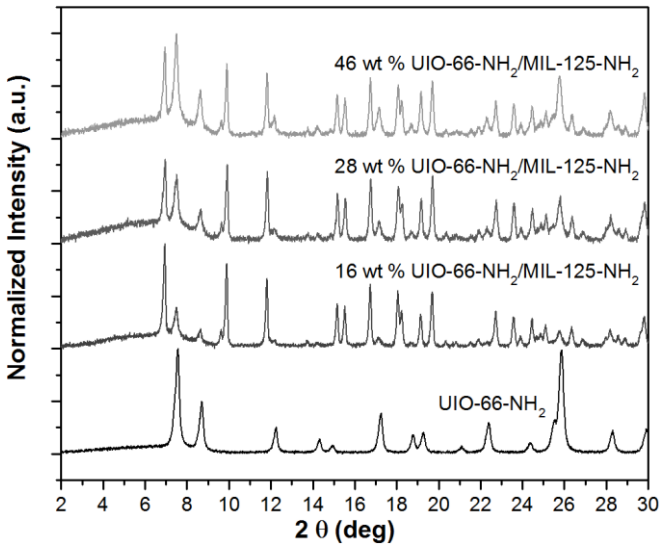

Figure S.30: *PXRD patterns of UIO-66-NH_2, 16 wt.%, 28 wt.% and 46 wt.% UIO-66-NH_2/MIL-125-NH_2 after photocatalysis.*

S5 Supporting Information for Chapter 5: MOF-derived TiO_2 for Photocatalysis

S5.1 Synthetic Procedures

Synthesis of MIL-125-NH_2-derived TiO_2

In a typical preparation, 200 mg of the as-synthesized MIL-125-NH_2 powder was placed in a ceramic crucible covered with foil and calcined for 1 h at either 400 °C, 500 °C, 600 °C, 700 °C or 800 °C. The obtained product was washed several times with EtOH and water, and then dried at 75 °C for 12 h.

Synthesis of precipitated TiH_4O_4-derived TiO_2

The TiH_4O_4-derived TiO_2 was synthesized following a similar procedure to a reported one.[168] 5 mL of titanium isopropoxide were mixed with 15 mL isopropanol. The solution was slowly added in 250 mL millipore water, under vigorous stirring. The precipitated titanium hydroxide (TiH_4O_4) solid was filtered with 400 mL of distilled water and then dried for 3 h at 120 °C. The obtained powder was put in a ceramic crucible covered with foil and calcined for 1 h at either 400 °C, 500 °C, 600 °C, 700 °C or 800 °C. The resulting white powders were washed several times with EtOH and water, and then dried at 75 °C for 12 h.

Synthesis of MIL-167-derived TiO_2

MIL-167-derived TiO_2 was synthesized following similar procedure to that of MIL-125-NH_2-derived TiO_2, except that 200 mg of the MIL-167 was used instead of MIL-125-NH_2 and the sample was heated up to 600 °C for 1 h.

S5.2 Characterization

S5.2.1 X-ray Photoelectron Spectroscopy

X-ray photoelectron spectroscopy (XPS) was performed, to analyze the surface of the mixed phase material. XPS revealed a titanium 2p peak at a binding energy of 458.5 eV. Each TiO_2 rutile and anatase phase has a distinct binding energy separated by 0.4 eV, allowing us to quantify the composition of both phases on the surface of TiO_2.[131] From the fitting, the TiO_2 anatase and rutile phase composition of the MIL-125-NH_2-derived TiO_2 at 600 ° C is 15:85 (Figure S31a) indicating a higher rutile content on the surface compared to the bulk (66:34). This higher surface rutile content is also the case with the TiH_4O_4-derived TiO_2 (Figure S31b). This analysis is consistent with the thermal

heating process involved, whereby the surface of the particle is where the initial transformation between anatase and rutile takes place.

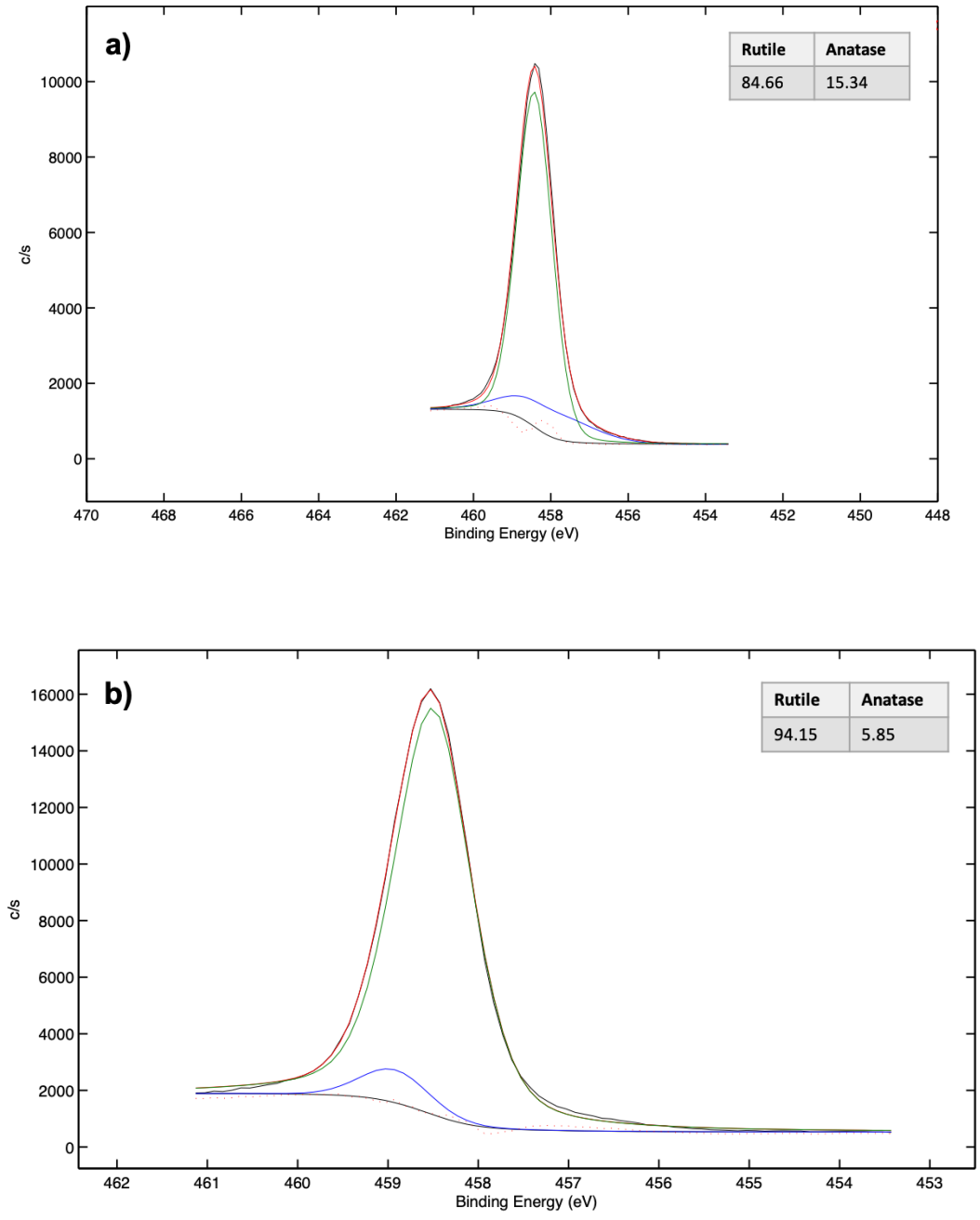

Figure S.31: *XPS showing the Ti 2p binding energy of a) the best performing MIL-125-NH_2-derived TiO_2 sample (synthesized at 600 °C) and b) the best performing TiH_4O_4 sample (synthesized at 700 °C). Included is the fitting for the TiO_2 anatase and rutile phase, determined using 2 Voigt functions; insert is the relative area of the fits related to each line.*

S5.2.2 Transmission and Scanning Electron Microscopy

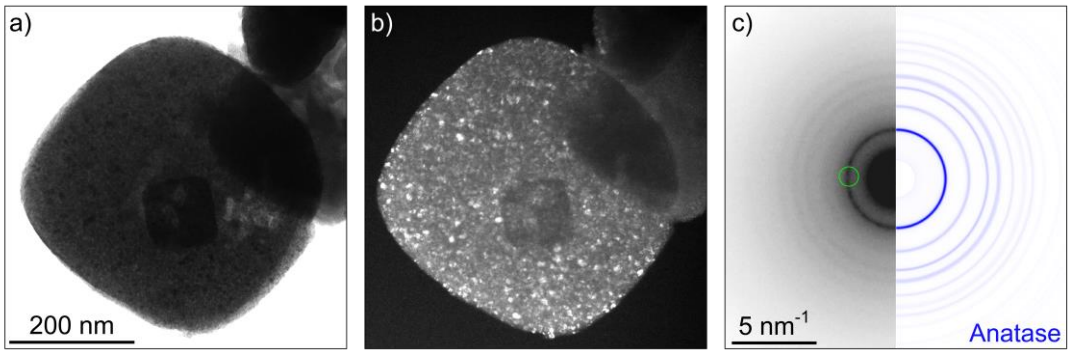

Figure S.32: *a) Bright-field and b) dark-field TEM images of MIL-125-NH_2-derived TiO_2 synthesized through calcination at 400°C for 1 h. c) Selected Area Electron Diffraction (SAED) pattern. Dark-field TEM image was acquired from the reflections shown by a circle on the SAED pattern.*

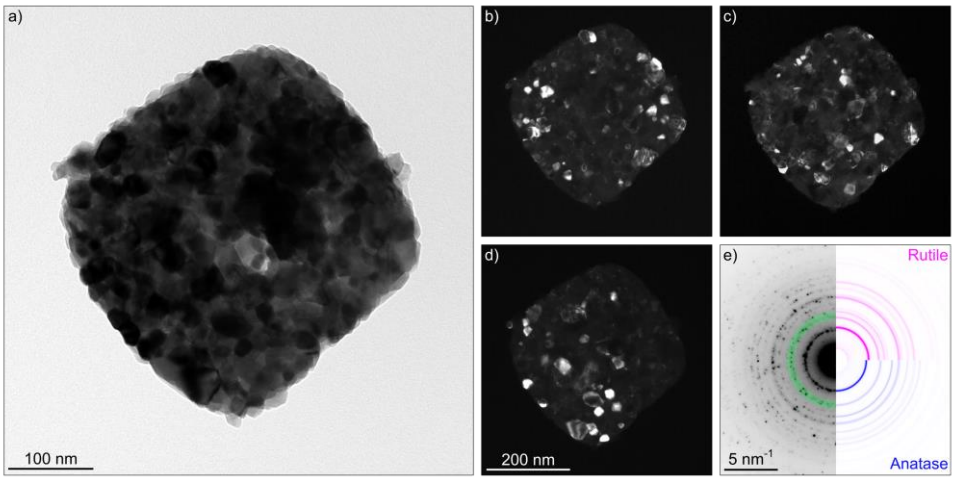

Figure S.33: *a) Bright-field and b), c), d) dark-field TEM images of MIL-125-NH_2-derived TiO_2 synthesized through calcination at 600°C for 1 h. e) SAED pattern. For the acquisition of the dark-field images, the incident electrons beam is tilted so that only reflections of specific diffracting crystallographic planes contribute to image formation. Depending on the angle of diffraction, specific nano-sized particles are illuminated, manifesting the multi-particle nature of the template. Dark-field TEM images correspond to the diffracting planes shown by a green circle in the SAED pattern.*

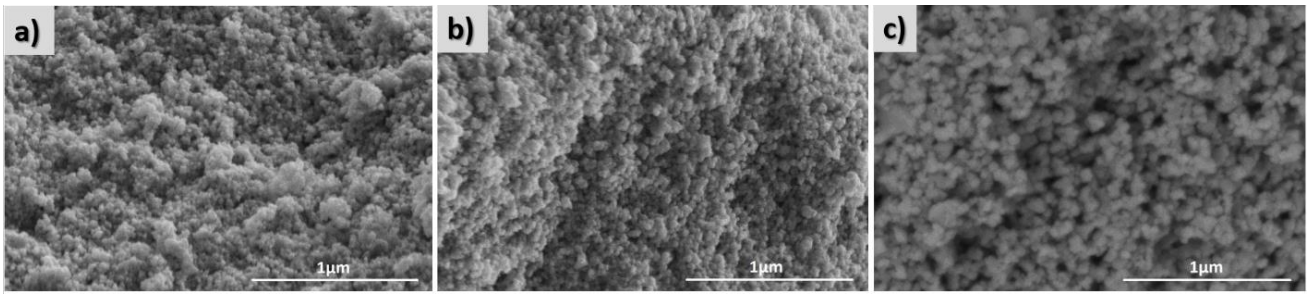

Figure S.34: *SEM image of the TiH_4O_4-derived TiO_2 samples synthesized at a) 500 °C, b) 600 °C and c) 700 °C for 1 h. The images are of the same magnification.*

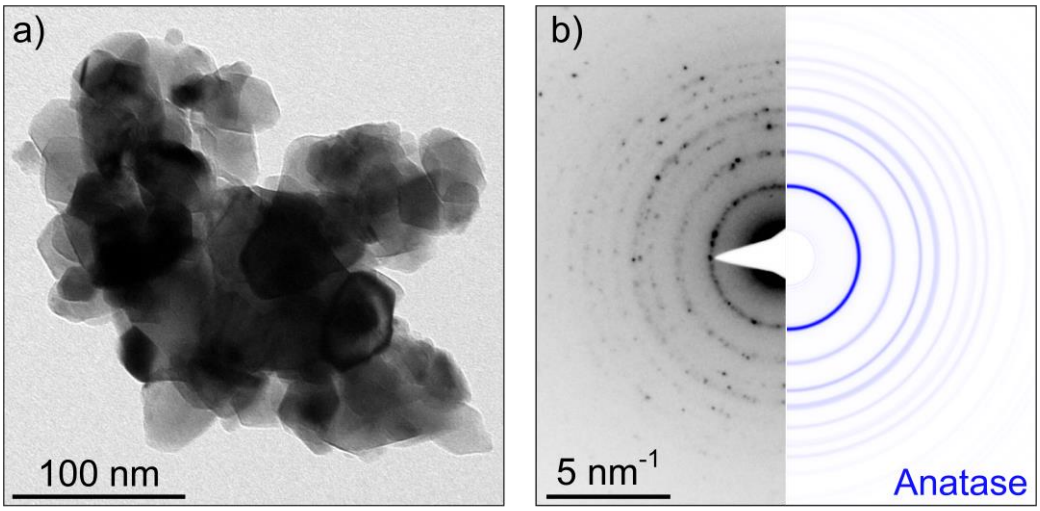

Figure S.35: *a) Bright-field TEM image and b) SAED pattern of TiH_4O_4-derived TiO_2 synthesized through calcination at 500°C for 1 h.*

S5.2.1 PXRD after Recycling Experiments

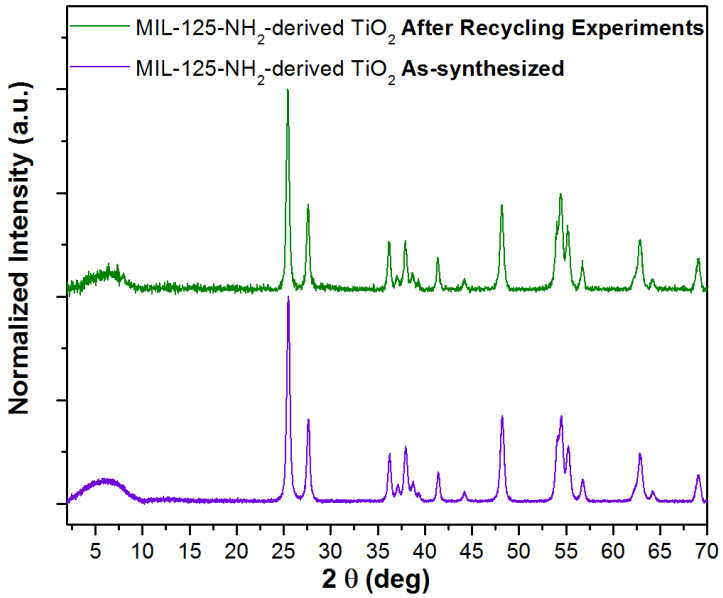

Figure S.36: *PXRD pattern of MIL-125-NH_2- derived TiO_2 (with optimum TiO_2 anatase to rutile ratio of 66:34) before and after recycling experiments.*

S5.2.3 TGA of MIL-167-derived TiO_2

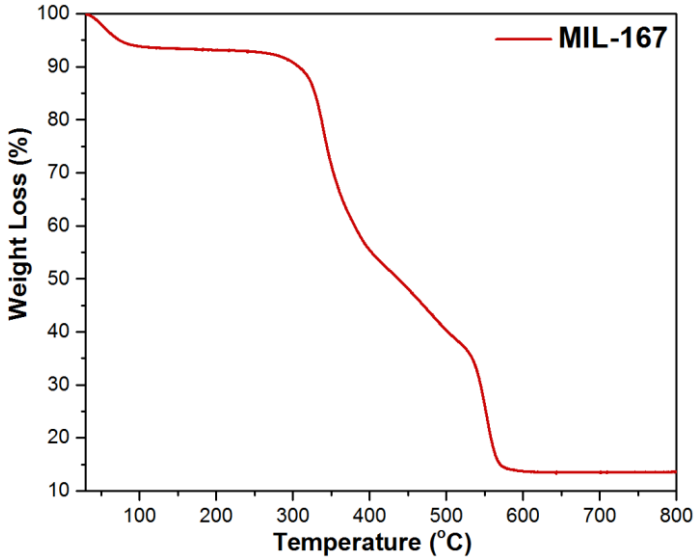

Figure S.37: *TGA curve of MIL-167 obtained under airflow with a heating rate of 5 °C min^{-1}.*

Table S. 9: *X-ray diffraction-derived data.*

	Anatase (w.t. %)	Rutile (w.t. %)	Size Anatase (nm)	Size Rutile (nm)
MIL-167-derived TiO_2	74.5(6)	25.5(8)	22	33
P25 Degussa TiO_2	88.3(3)	11.7(8)	20	34

S.5.3 Comparison of MIL-125-NH_2-derived TiO_2 to other TiO_2 samples

S5.3.1 Dependence of the Photocatalytic Activity on the Concentration of Photocatalyst

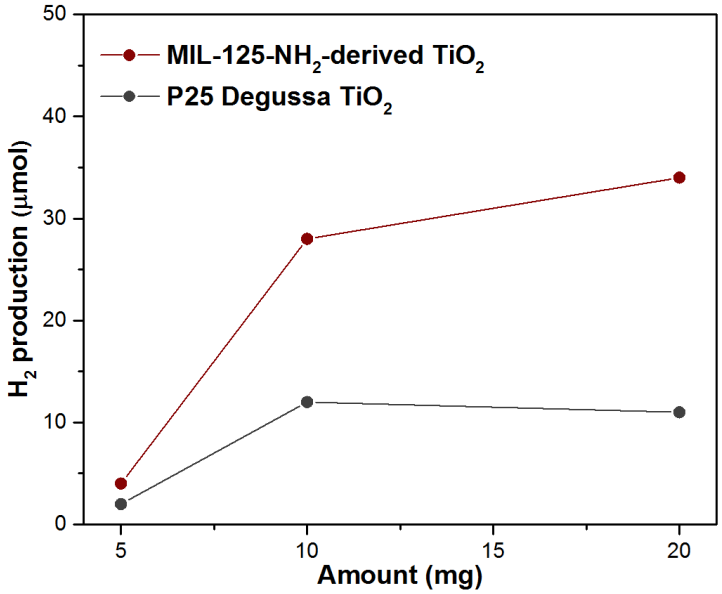

Figure S.38: *Dependence of the H_2 evolution on the concentration of photocatalyst in solution, for the best-performing MIL-125-NH_2-derived and P25 Degussa TiO_2.*

S5.3.2 Photoluminescence Spectroscopy

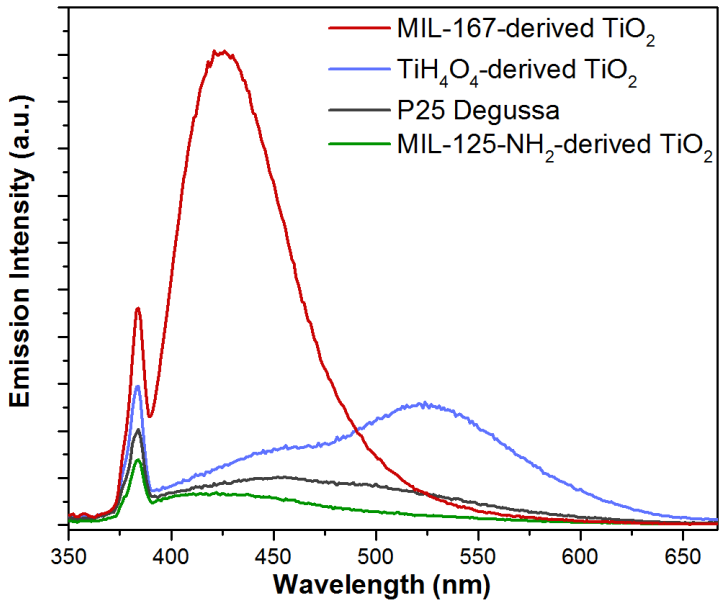

Figure S.39: *PL spectra of the MIL-167-derived, TiH_4O_4-derived, MIL-125-NH_2-derived TiO_2 and P25 Degussa. The excitation wavelength was at 340 nm.*

S5.3.3 Elemental Analysis

Table S.10: *Elemental analysis for the best performing MIL-125-NH_2-derived TiO_2 sample (synthesized at 600 °C). A small amount of carbon, traces of hydrogen and no nitrogen were observed.*

	Nitrogen (%)	Carbon (%)	Hydrogen (%)
MIL-125-NH_2-derived TiO_2	0	1.154	0.138

References

1. Kampouri, S.; Stylianou, K. C., Dual-Functional Photocatalysis for Simultaneous Hydrogen Production and Oxidation of Organic Substances. *ACS Catalysis* **2019,** *9*, 4247-4270.
2. a) Augugliaro, V.; Camera-Roda, G.; Loddo, V.; Palmisano, G.; Palmisano, L.; Soria, J.; Yurdakal, S., Heterogeneous Photocatalysis and Photoelectrocatalysis: From Unselective Abatement of Noxious Species to Selective Production of High-Value Chemicals. *J. Phys. Chem. Lett.* **2015,** *6*, 1968-1981; b) Linsebigler, A. L.; Lu, G.; Yates, J. T., Photocatalysis on TiO2 Surfaces: Principles, Mechanisms, and Selected Results. *Chem. Rev.* **1995,** *95*, 735-758; c) Nie, L.; Zhang, Q., Recent progress in crystalline metal chalcogenides as efficient photocatalysts for organic pollutant degradation. *Inorganic Chemistry Frontiers* **2017,** *4*, 1953-1962; d) Wenderich, K.; Mul, G., Methods, Mechanism, and Applications of Photodeposition in Photocatalysis: A Review. *Chem. Rev.* **2016,** *116*, 14587-14619; e) Dalrymple, O. K.; Stefanakos, E.; Trotz, M. A.; Goswami, D. Y., A review of the mechanisms and modeling of photocatalytic disinfection. *Appl. Catal., B* **2010,** *98*, 27-38; f) Mills, A.; LeHunte, S., An overview of semiconductor photocatalysis. *J. Photoch. Photobio. A* **1997,** *108*, 1-35.
3. Ahmad, H.; Kamarudin, S. K.; Minggu, L. J.; Kassim, M., Hydrogen from photo-catalytic water splitting process: A review. *RENEW. SUST. ENERG. REV.* **2015,** *43*, 599-610.
4. a) Gaya, U. I.; Abdullah, A. H., Heterogeneous photocatalytic degradation of organic contaminants over titanium dioxide: A review of fundamentals, progress and problems. *J. Photoc. Photobio. C* **2008,** *9*, 1-12; b) Ali, I.; Asim, M.; Khan, T. A., Low cost adsorbents for the removal of organic pollutants from wastewater. *J. Environ. Manage.* **2012,** *113*, 170-183.
5. a) Kabra, K.; Chaudhary, R.; Sawhney, R. L., Solar photocatalytic removal of metal ions from industrial wastewater. *Environmental Progress* **2008,** *27*, 487-495; b) Kabra, K.; Chaudhary, R.; Sawhney, R. L., Treatment of Hazardous Organic and Inorganic Compounds through Aqueous-Phase Photocatalysis: A Review. *Ind. Eng. Chem. Res.* **2004,** *43*, 7683-7696; c) Li, M.; Gou, H.; Al-Ogaidi, I.; Wu, N., Nanostructured Sensors for Detection of Heavy Metals: A Review. *ACS Sustain. Chem. Eng.* **2013,** *1*, 713-723.
6. Low, J.; Cheng, B.; Yu, J., Surface modification and enhanced photocatalytic CO2 reduction performance of TiO2: a review. *Appl. Surf. Sci.* **2017,** *392*, 658-686.
7. Shehzad, N.; Tahir, M.; Johari, K.; Murugesan, T.; Hussain, M., A critical review on TiO2 based photocatalytic CO2 reduction system: Strategies to improve efficiency. *Journal of CO2 Utilization* **2018,** *26*, 98-122.
8. a) Schrauzer, G. N.; Guth, T. D., Photolysis of Water and Photoreduction of Nitrogen on Titanium-Dioxide. *J. Am. Chem. Soc.* **1977,** *99*, 7189-7193; b) Fujishima, A.; Honda, K., Electrochemical Photolysis of Water at a Semiconductor Electrode. *Nature* **1972,** *238*, 37-38.
9. Mills, A.; Le Hunte, S., An overview of semiconductor photocatalysis. *Journal of Photochemistry and Photobiology A: Chemistry* **1997,** *108*, 1-35.
10. Osterloh, F. E., Inorganic Materials as Catalysts for Photochemical Splitting of Water. *Chemistry of Materials* **2008,** *20*, 35-54.
11. a) Zhang, X.; Peng, T.; Song, S., Recent advances in dye-sensitized semiconductor systems for photocatalytic hydrogen production. *J. Mater. Chem. A* **2016,** *4*, 2365-2402; b) Pan, J.; Shao, X.; Xu, X.; Zhong, J.; Hu, J.; Ma, L., Organic Dye Molecules Sensitization-Enhanced Photocatalytic Water-Splitting Activity of MoS2 from First-Principles Calculations. *J. Phys. Chem. C* **2020,** *124*, 6580-6587; c) Jo, M.; Choi, S.; Jo, J. H.; Kim, S.-Y.; Kim, P. S.; Kim, C. H.; Son, H.-J.; Pac, C.; Kang, S. O., Utility of Squaraine Dyes for Dye-Sensitized Photocatalysis on Water or Carbon Dioxide Reduction. *ACS Omega* **2019,** *4*, 14272-14283; d) Chowdhury, P.; Gomaa, H.; Ray, A. K., Dye-Sensitized Photocatalyst: A Breakthrough in Green Energy and Environmental Detoxification. In *Sustainable Nanotechnology and the Environment: Advances and Achievements*, American Chemical Society: 2013; Vol. 1124, pp 231-266.
12. a) Stavrinadis, A.; Pelli Cresi, J. S.; d'Acapito, F.; Magén, C.; Boscherini, F.; Konstantatos, G., Aliovalent Doping in Colloidal Quantum Dots and Its Manifestation on Their Optical Properties: Surface Attachment versus Structural Incorporation. *Chem. Mater.* **2016,** *28*, 5384-5393; b) Watanabe, K.; Iwase, A.; Nozawa, S.; Adachi, S.-i.; Kudo, A., Effects of Coapplication of Rh-Doping and Ag-Substitution on the Band Structure of Li2TiO3 and the Photocatalytic Property. *ACS Sustain. Chem. Eng.* **2019,** *7*, 9881-9887; c) Shen, S.; Wang, Q., Rational Tuning the Optical Properties of Metal Sulfide Nanocrystals and Their Applications. *Chem. Mater.* **2013,** *25*, 1166-1178.
13. a) Shaik, F.; Peer, I.; Jain, P. K.; Amirav, L., Plasmon-Enhanced Multicarrier Photocatalysis. *Nano Lett.* **2018,** *18*, 4370-4376; b) Choi, K. M.; Kim, D.; Rungtaweevoranit, B.; Trickett, C. A.; Barmanbek, J. T. D.; Alshammari, A. S.; Yang, P.; Yaghi, O. M., Plasmon-Enhanced Photocatalytic CO2 Conversion within Metal–Organic Frameworks under Visible Light. *J. Am. Chem. Soc.* **2017,** *139*, 356-362; c) Zhao, M.; Chen, P., Exploring Plasmonic Photocatalysis via Single-Molecule Reaction Imaging. *Nano Letters* **2020**; d) Torimoto, T.; Horibe, H.; Kameyama, T.; Okazaki, K.-i.; Ikeda, S.; Matsumura, M.; Ishikawa, A.; Ishihara, H., Plasmon-Enhanced

Photocatalytic Activity of Cadmium Sulfide Nanoparticle Immobilized on Silica-Coated Gold Particles. *J. Phys. Chem. Lett.* **2011,** *2*, 2057-2062.
14. a) Huang, H.; Li, D.; Lin, Q.; Shao, Y.; Chen, W.; Hu, Y.; Chen, Y.; Fu, X., Efficient Photocatalytic Activity of PZT/TiO2 Heterojunction under Visible Light Irradiation. *J. Phys. Chem. C* **2009,** *113*, 14264-14269; b) Liu, B.; Yin, D.; Zhao, F.; Khaing, K. K.; Chen, T.; Wu, C.; Deng, L.; Li, L.; Huang, K.; Zhang, Y., Construction of a Novel Z-Scheme Heterojunction with Molecular Grafted Carbon Nitride Nanosheets and V2O5 for Highly Efficient Photocatalysis. *J. Phys. Chem. C* **2019,** *123*, 4193-4203; c) Lu, Y.; Liu, X.-L.; He, L.; Zhang, Y.-X.; Hu, Z.-Y.; Tian, G.; Cheng, X.; Wu, S.-M.; Li, Y.-Z.; Yang, X.-H.; Wang, L.-Y.; Liu, J.-W.; Janiak, C.; Chang, G.-G.; Li, W.-H.; Van Tendeloo, G.; Yang, X.-Y.; Su, B.-L., Spatial Heterojunction in Nanostructured TiO2 and Its Cascade Effect for Efficient Photocatalysis. *Nano Letters* **2020**.
15. Reference Air Mass 1.5 (ASTM) G-173 Solar Spectra https://www.nrel.gov/grid/solar-resource/spectra-am1.5.html.
16. a) Yanagida, S.; Yoshiya, M.; Shiragami, T.; Pac, C.; Mori, H.; Fujita, H., Semiconductor photocatalysis. I. Quantitative photoreduction of aliphatic ketones to alcohols using defect-free zinc sulfide quantum crystallites. *J. Phys. Chem.* **1990,** *94*, 3104-3111; b) Fang, Z.; Weng, S.; Ye, X.; Feng, W.; Zheng, Z.; Lu, M.; Lin, S.; Fu, X.; Liu, P., Defect Engineering and Phase Junction Architecture of Wide-Bandgap ZnS for Conflicting Visible Light Activity in Photocatalytic H2 Evolution. *ACS Appl. Mater. Interfaces* **2015,** *7*, 13915-13924; c) Huang, H.; Zhou, C.; Jiao, X.; Yuan, H.; Zhao, J.; He, C.; Hofkens, J.; Roeffaers, M. B. J.; Long, J.; Steele, J. A., Subsurface Defect Engineering in Single-Unit-Cell Bi2WO6 Monolayers Boosts Solar-Driven Photocatalytic Performance. *ACS Catal.* **2020,** *10*, 1439-1443.
17. a) Cho, Y.; Kim, S.; Park, B.; Lee, C.-L.; Kim, J. K.; Lee, K.-S.; Choi, I. Y.; Kim, J. K.; Zhang, K.; Oh, S. H.; Park, J. H., Multiple Heterojunction in Single Titanium Dioxide Nanoparticles for Novel Metal-Free Photocatalysis. *Nano Lett.* **2018,** *18*, 4257-4262; b) Teranishi, T.; Sakamoto, M., Charge Separation in Type-II Semiconductor Heterodimers. *J. Phys. Chem. Lett.* **2013,** *4*, 2867-2873; c) Gong, H.; Li, Z.; Chen, Z.; Liu, Q.; Song, M.; Huang, C., NiSe/Cd0.5Zn0.5S Composite Nanoparticles for Use in p–n Heterojunction-Based Photocatalysts for Solar Energy Harvesting. *ACS Applied Nano Materials* **2020,** *3*, 3665-3674.
18. a) Zhao, L.; Ye, F.; Wang, D.; Cai, X.; Meng, C.; Xie, H.; Zhang, J.; Bai, S., Lattice Engineering on Metal Cocatalysts for Enhanced Photocatalytic Reduction of CO2 into CH4. *Chem. Sus. Chem. 0*; b) Hisatomi, T.; Kubota, J.; Domen, K., Recent advances in semiconductors for photocatalytic and photoelectrochemical water splitting. *Chem. Soc. Rev.* **2014,** *43*, 7520-7535; c) Qi, M.-Y.; Li, Y.-H.; Zhang, F.; Tang, Z.-R.; Xiong, Y.; Xu, Y.-J., Switching Light for Site-Directed Spatial Loading of Cocatalysts onto Heterojunction Photocatalysts with Boosted Redox Catalysis. *ACS Catal.* **2020,** *10*, 3194-3202; d) Wen, T.; Zhang, L.; Schmitt, W., A Mn13-cluster based coordination polymer as a co-catalyst of CdS for enhanced visible-light driven H2 evolution. *Dalton Trans.* **2018,** *47*, 10857-10860.
19. Ola, O.; Maroto-Valer, M. M., Review of material design and reactor engineering on TiO2 photocatalysis for CO2 reduction. *J. Photoc. Photobio. C* **2015,** *24*, 16-42.
20. Hinnemann, B.; Moses, P. G.; Bonde, J.; Jørgensen, K. P.; Nielsen, J. H.; Horch, S.; Chorkendorff, I.; Nørskov, J. K., Biomimetic Hydrogen Evolution: MoS2 Nanoparticles as Catalyst for Hydrogen Evolution. *J. Am. Chem. Soc.* **2005,** *127*, 5308-5309.
21. a) Ran, J.; Zhang, J.; Yu, J.; Jaroniec, M.; Qiao, S. Z., Earth-abundant cocatalysts for semiconductor-based photocatalytic water splitting. *Chem. Soc. Rev.* **2014,** *43*, 7787-7812; b) Bai, S.; Yin, W.; Wang, L.; Li, Z.; Xiong, Y., Surface and interface design in cocatalysts for photocatalytic water splitting and CO2 reduction. *RSC Adv.* **2016,** *6*, 57446-57463; c) Xu, Y.; Xu, R., Nickel-based cocatalysts for photocatalytic hydrogen production. *Appl. Surf. Sci.* **2015,** *351*, 779-793.
22. a) Yentekakis, I. V.; Goula, G.; Kampouri, S.; Betsi-Argyropoulou, I.; Panagiotopoulou, P.; Taylor, M. J.; Kyriakou, G.; Lambert, R. M., Ir-Catalysed Nitrous oxide (N2O) Decomposition: Effect of Ir Particle Size and Metal–Support Interactions. *Catalysis Letters* **2018,** *148*, 341-347; b) Lewis, N. S.; Nocera, D. G., Powering the planet: Chemical challenges in solar energy utilization. *PNAS* **2006,** *103*, 15729-15735.
23. a) Balat, M., Potential importance of hydrogen as a future solution to environmental and transportation problems. *Int. J. Hydrogen Energy* **2008,** *33*, 4013-4029; b) Chaubey, R.; Sahu, S.; James, O. O.; Maity, S., A review on development of industrial processes and emerging techniques for production of hydrogen from renewable and sustainable sources. *Renew. Sust. Energ. Rev.* **2013,** *23*, 443-462.
24. Wang, M.; Wang, Z.; Gong, X.; Guo, Z., The intensification technologies to water electrolysis for hydrogen production – A review. *RENEW. SUST. ENERG. REV.* **2014,** *29*, 573-588.
25. Zou, X.; Zhang, Y., Noble metal-free hydrogen evolution catalysts for water splitting. *Chem. Soc. Rev.* **2015,** *44*, 5148-5180.

26. a) Yuan, Y.-J.; Chen, D.; Yu, Z.-T.; Zou, Z.-G., Cadmium sulfide-based nanomaterials for photocatalytic hydrogen production. *J. Mater. Chem. A* **2018,** *6*, 11606-11630; b) Li, J.; Zhang, L.; Li, J.; An, P.; Hou, Y.; Zhang, J., Nanoconfined Growth of Carbon-Encapsulated Cobalts as Cocatalysts for Photocatalytic Hydrogen Evolution. *ACS Sustain. Chem. Eng.* **2019,** *7*, 14023-14030.
27. Meyer, K.; Ranocchiari, M.; van Bokhoven, J. A., Metal organic frameworks for photo-catalytic water splitting. *Energy Environ. Sci.* **2015,** *8*, 1923-1937.
28. Osterloh, F. E., Photocatalysis versus Photosynthesis: A Sensitivity Analysis of Devices for Solar Energy Conversion and Chemical Transformations. *ACS Energy Letters* **2017,** *2*, 445-453.
29. a) Rajeshwar, K.; Ibanez, J. G., Electrochemical Aspects of Photocatalysis: Application to Detoxification and Disinfection Scenarios. *J. Chem. Educ.* **1995,** *72*, 1044; b) Pellegrin, Y.; Odobel, F., Sacrificial electron donor reagents for solar fuel production. *Comptes Rendus Chimie* **2017,** *20*, 283-295.
30. a) Al-Azri, Z. H. N.; Chen, W.-T.; Chan, A.; Jovic, V.; Ina, T.; Idriss, H.; Waterhouse, G. I. N., The roles of metal co-catalysts and reaction media in photocatalytic hydrogen production: Performance evaluation of M/TiO2 photocatalysts (M=Pd, Pt, Au) in different alcohol–water mixtures. *J. Catal.* **2015,** *329*, 355-367; b) Li, X.; Yu, J.; Jaroniec, M.; Chen, X., Cocatalysts for Selective Photoreduction of CO2 into Solar Fuels. *Chem. Rev.* **2019,** *119*, 3962-4179.
31. a) Tran, P. D.; Xi, L.; Batabyal, S. K.; Wong, L. H.; Barber, J.; Chye Loo, J. S., Enhancing the photocatalytic efficiency of TiO2 nanopowders for H2 production by using non-noble transition metal co-catalysts. *Phys. Chem. Chem. Phys.* **2012,** *14*, 11596-11599; b) Wang, P.; Zhan, S.; Wang, H.; Xia, Y.; Hou, Q.; Zhou, Q.; Li, Y.; Kumar, R. R., Cobalt phosphide nanowires as efficient co-catalyst for photocatalytic hydrogen evolution over Zn0.5Cd0.5S. *Appl. Catal., B* **2018,** *230*, 210-219; c) Bi, W.; Zhang, L.; Sun, Z.; Li, X.; Jin, T.; Wu, X.; Zhang, Q.; Luo, Y.; Wu, C.; Xie, Y., Insight into Electrocatalysts as Co-catalysts in Efficient Photocatalytic Hydrogen Evolution. *ACS Catal.* **2016,** *6*, 4253-4257; d) Lu, K.-Q.; Qi, M.-Y.; Tang, Z.-R.; Xu, Y.-J., Earth-Abundant MoS2 and Cobalt Phosphate Dual Cocatalysts on 1D CdS Nanowires for Boosting Photocatalytic Hydrogen Production. *Langmuir* **2019,** *35*, 11056-11065.
32. a) Thakur, K.; Kandasubramanian, B., Graphene and Graphene Oxide-Based Composites for Removal of Organic Pollutants: A Review. *Journal of Chemical & Engineering Data* **2019,** *64*, 833-867; b) Huang, H.; Pradhan, B.; Hofkens, J.; Roeffaers, M. B. J.; Steele, J. A., Solar-Driven Metal Halide Perovskite Photocatalysis: Design, Stability, and Performance. *ACS Energy Letters* **2020,** *5*, 1107-1123.
33. a) Nasalevich, M. A.; Becker, R.; Ramos-Fernandez, E. V.; Castellanos, S.; Veber, S. L.; Fedin, M. V.; Kapteijn, F.; Reek, J. N.; Van Der Vlugt, J.; Gascon, J., Co@ NH 2-MIL-125 (Ti): cobaloxime-derived metal–organic framework-based composite for light-driven H 2 production. *Energy & Environmental Science* **2015,** *8*, 364-375; b) Dempsey, J. L.; Brunschwig, B. S.; Winkler, J. R.; Gray, H. B., Hydrogen Evolution Catalyzed by Cobaloximes. *Acc. Chem. Res.* **2009,** *42*, 1995-2004; c) Nguyen, T. N.; Kampouri, S.; Valizadeh, B.; Luo, W.; Ongari, D.; Planes, O. M.; Züttel, A.; Smit, B.; Stylianou, K. C., Photocatalytic Hydrogen Generation from a Visible-Light-Responsive Metal–Organic Framework System: Stability versus Activity of Molybdenum Sulfide Cocatalysts. *ACS Appl. Energy Mater.* **2018,** *10*, 30035-30039.
34. a) Wang, D.; Liu, Z.-P.; Yang, W.-M., Revealing the Size Effect of Platinum Cocatalyst for Photocatalytic Hydrogen Evolution on TiO2 Support: A DFT Study. *ACS Catal.* **2018**, 7270-7278; b) Liu, M.; Wang, X.; Liu, J.; Wang, K.; Jin, S.; Tan, B., Palladium as a Superior Cocatalyst to Platinum for Hydrogen Evolution Using Covalent Triazine Frameworks as a Support. *ACS Appl. Energy Mater.* **2020,** *12*, 12774-12782.
35. a) Zhao, J.; Wang, Y.; Zhou, J.; Qi, P.; Li, S.; Zhang, K.; Feng, X.; Wang, B.; Hu, C., A copper(ii)-based MOF film for highly efficient visible-light-driven hydrogen production. *J. Mater. Chem. A* **2016,** *4*, 7174-7177; b) Lynch, P. G.; Richards, H.; Wustholz, K. L., Unraveling the Excited-State Dynamics of Eosin Y Photosensitizers Using Single-Molecule Spectroscopy. *The Journal of Physical Chemistry A* **2019,** *123*, 2592-2600.
36. a) Sun, Y.; Sun, J.; Long, J. R.; Yang, P.; Chang, C. J., Photocatalytic generation of hydrogen from water using a cobalt pentapyridine complex in combination with molecular and semiconductor nanowire photosensitizers. *Chem. Sci.* **2013,** *4*, 118-124; b) Beyene, B. B.; Hung, C.-H., Photocatalytic hydrogen evolution from neutral aqueous solution by a water-soluble cobalt(ii) porphyrin. *Sustainable Energy Fuels* **2018,** *2*, 2036-2043.
37. a) Beyene, B. B.; Hung, C.-H., Photocatalytic hydrogen evolution from neutral aqueous solution by a water-soluble cobalt(ii) porphyrin. *Sustainable Energy Fuels* **2018**; b) Giannoudis, E.; Benazzi, E.; Karlsson, J.; Copley, G.; Panagiotakis, S.; Landrou, G.; Angaridis, P.; Nikolaou, V.; Matthaiaki, C.; Charalambidis, G.; Gibson, E. A.; Coutsolelos, A. G., Photosensitizers for H2 Evolution Based on Charged or Neutral Zn and Sn Porphyrins. *Inorg. Chem.* **2020,** *59*, 1611-1621.
38. a) Gurunathan, K.; Maruthamuthu, P.; Sastri, M. V. C., Photocatalytic hydrogen production by dye-sensitized Pt/SnO2 AND Pt/SnO2/RuO2 in aqueous methyl viologen solution. *Int. J. Hydrog. Energy* **1997,** *22*, 57-62; b) Lu, H.; Hu, R.; Bai, H.; Chen, H.; Lv, F.; Liu, L.; Wang, S.; Tian, H., Efficient Conjugated Polymer–

Methyl Viologen Electron Transfer System for Controlled Photo-Driven Hydrogen Evolution. *ACS Appl. Energy Mater.* **2017,** *9*, 10355-10359; c) Kobosko, S. M.; DuBose, J. T.; Kamat, P. V., Perovskite Photocatalysis. Methyl Viologen Induces Unusually Long-Lived Charge Carrier Separation in CsPbBr3 Nanocrystals. *ACS Energy Letters* **2020,** *5*, 221-223.
39. Shon, H. K.; Vigneswaran, S.; Snyder, S. A., Effluent Organic Matter (EfOM) in Wastewater: Constituents, Effects, and Treatment. *Crit. Rev. Env. Sci. Tec.* **2006,** *36*, 327-374.
40. Deng, W.; Zhao, H.; Pan, F.; Feng, X.; Jung, B.; Abdel-Wahab, A.; Batchelor, B.; Li, Y., Visible-Light-Driven Photocatalytic Degradation of Organic Water Pollutants Promoted by Sulfite Addition. *Environ. Sci. Technol.* **2017,** *51*, 13372-13379.
41. Zeghioud, H.; Khellaf, N.; Djelal, H.; Amrane, A.; Bouhelassa, M., Photocatalytic Reactors Dedicated to the Degradation of Hazardous Organic Pollutants: Kinetics, Mechanistic Aspects, and Design – A Review. *Chem. Eng. Commun.* **2016,** *203*, 1415-1431.
42. Seckler, D.; Barker, R.; Amarasinghe, U., Water Scarcity in the Twenty-first Century. *Int. J. Water Resour. D* **1999,** *15*, 29-42.
43. Pawlowski, L., *Physicochemical Methods for Water and Wastewater Treatment*. Elsevier Science: 1982.
44. a) Bhargava, S. K.; Tardio, J.; Prasad, J.; Föger, K.; Akolekar, D. B.; Grocott, S. C., Wet Oxidation and Catalytic Wet Oxidation. *Ind. Eng. Chem. Res.* **2006,** *45*, 1221-1258; b) Veriansyah, B.; Kim, J.-D.; Lee, J.-C., Supercritical Water Oxidation of Thiodiglycol. *Ind. Eng. Chem. Res.* **2005,** *44*, 9014-9019; c) Martínez-Huitle, C. A.; Rodrigo, M. A.; Sirés, I.; Scialdone, O., Single and Coupled Electrochemical Processes and Reactors for the Abatement of Organic Water Pollutants: A Critical Review. *Chem. Rev.* **2015,** *115*, 13362-13407.
45. a) Cano Quiroz, A.; Barrera-Díaz, C.; Roa-Morales, G.; Balderas Hernández, P.; Romero, R.; Natividad, R., Wastewater Ozonation Catalyzed by Iron. *Ind. Eng. Chem. Res.* **2011,** *50*, 2488-2494; b) Chen, P. N.; Junk, G. A.; Svec, H. J., Reactions of organic pollutants. 1. Ozonation of acenaphthylene and acenaphthene. *Environ. Sci. Technol.* **1979,** *13*, 451-454.
46. a) Zhou, L.; Song, W.; Chen, Z.; Yin, G., Degradation of Organic Pollutants in Wastewater by Bicarbonate-Activated Hydrogen Peroxide with a Supported Cobalt Catalyst. *Environ. Sci. Technol.* **2013,** *47*, 3833-3839; b) Bokare, A. D.; Choi, W., Chromate-Induced Activation of Hydrogen Peroxide for Oxidative Degradation of Aqueous Organic Pollutants. *Environ. Sci. Technol.* **2010,** *44*, 7232-7237.
47. Sha, Z.; Sun, J.; Chan, H. S. O.; Jaenicke, S.; Wu, J., Enhanced Photocatalytic Activity of the AgI/UiO-66(Zr) Composite for Rhodamine B Degradation under Visible-Light Irradiation. *Chem. Phys. Chem.* **2015,** *80*, 1321-1328.
48. a) Mahlambi, M. M.; Ngila, C. J.; Mamba, B. B., Recent developments in environmental photocatalytic degradation of organic pollutants: the case of titanium dioxide nanoparticles—a review. *J. Nanomater.* **2015,** *2015*, 5-5; b) Durán-Álvarez, J. C.; Hernández-Morales, V. A.; Rodríguez-Varela, M.; Guerrero-Araque, D.; Ramirez-Ortega, D.; Castillón, F.; Acevedo-Peña, P.; Zanella, R., Ag2O/TiO2 nanostructures for the photocatalytic mineralization of the highly recalcitrant pollutant iopromide in pure and tap water. *Catal. Today* **2020,** *341*, 71-81.
49. a) Daghrir, R.; Drogui, P.; Robert, D., Modified TiO2 For Environmental Photocatalytic Applications: A Review. *Ind. Eng. Chem. Res.* **2013,** *52*, 3581-3599; b) Xu, X.; Lai, L.; Jiang, J.; He, Z.; Song, S., C,N-Codoped TiO2 with a Nitrogen-Doped Carbon Coating Derived from 2,6-Diaminopyridine for Visible Light-Induced Photocatalytic Hydrogen Evolution. *The Journal of Physical Chemistry C* **2019,** *123*, 9702-9712; c) Beydoun, N.; Farhat, R.; Halaoui, L. I., Enhanced Solar Light Harvesting with Q-CdTe/Se Sensitized Inverse Opal TiO2. *ACS Applied Energy Materials* **2020,** *3*, 3104-3119.
50. a) Qin, L.; Chen, H.-Z.; Lei, J.; Wang, Y.-Q.; Ye, T.-Q.; Zheng, H.-G., Photodegradation of Some Organic Dyes over Two Metal–Organic Frameworks with Especially High Efficiency for Safranine T. *Cryst. Growth Des.* **2017,** *17*, 1293-1298; b) Sabri, M.; Habibi-Yangjeh, A.; Ghosh, S., Novel ZnO/CuBi2O4 heterostructures for persulfate-assisted photocatalytic degradation of dye contaminants under visible light. *Journal of Photochemistry and Photobiology A: Chemistry* **2020,** *391*, 112397; c) Gao, Y.; Li, S.; Li, Y.; Yao, L.; Zhang, H., Accelerated photocatalytic degradation of organic pollutant over metal-organic framework MIL-53(Fe) under visible LED light mediated by persulfate. *Appl. Catal., B* **2017,** *202*, 165-174.
51. Shen, L.; Luo, M.; Huang, L.; Feng, P.; Wu, L., A Clean and General Strategy To Decorate a Titanium Metal–Organic Framework with Noble-Metal Nanoparticles for Versatile Photocatalytic Applications. *Inorg. Chem.* **2015,** *54*, 1191-1193.
52. a) Piscopo, A.; Robert, D.; Weber, J. V., Influence of pH and chloride anion on the photocatalytic degradation of organic compounds: Part I. Effect on the benzamide and para-hydroxybenzoic acid in TiO2 aqueous solution. *Appl. Catal., B* **2001,** *35*, 117-124; b) Mangrulkar, P. A.; Kamble, S. P.; Joshi, M. M.; Meshram, J. S.; Labhsetwar, N. K.; Rayalu, S. S., Photocatalytic Degradation of Phenolics by N-Doped Mesoporous Titania under Solar Radiation. *Int. J. photoenergy* **2012,** *2012*.

53. a) Azeez, F.; Al-Hetlani, E.; Arafa, M.; Abdelmonem, Y.; Nazeer, A. A.; Amin, M. O.; Madkour, M., The effect of surface charge on photocatalytic degradation of methylene blue dye using chargeable titania nanoparticles. *Sci. Rep.* **2018,** *8*, 7104; b) Suda, Y.; Morimoto, T., Molecularly adsorbed water on the bare surface of titania (rutile). *Langmuir* **1987,** *3*, 786-788.
54. Jeon, T. H.; Koo, M. S.; Kim, H.; Choi, W., Dual-Functional Photocatalytic and Photoelectrocatalytic Systems for Energy- and Resource-Recovering Water Treatment. *ACS Catal.* **2018,** *8*, 11542-11563.
55. a) Kawai, T.; Sakata, T., Hydrogen evolution from water using solid carbon and light energy. *Nature* **1979,** *282*, 283-284; b) Kawai, T.; Sakata, T., Conversion of carbohydrate into hydrogen fuel by a photocatalytic process. *Nature* **1980,** *286*, 474; c) Hashimoto, K.; Kawai, T.; Sakata, T., Photocatalytic reactions of hydrocarbons and fossil fuels with water. Hydrogen production and oxidation. *The Journal of Physical Chemistry* **1984,** *88*, 4083-4088.
56. a) Rossetti, I., Hydrogen Production by Photoreforming of Renewable Substrates. *ISRN Chemical Engineering* **2012,** *2012*, 21; b) Uekert, T.; Kasap, H.; Reisner, E., Photoreforming of Nonrecyclable Plastic Waste over a Carbon Nitride/Nickel Phosphide Catalyst. *J. Am. Chem. Soc.* **2019,** *141*, 15201-15210.
57. a) Ayodele, B. V.; Ghazali, A. A.; Mohd Yassin, M. Y.; Abdullah, S., Optimization of hydrogen production by photocatalytic steam methane reforming over lanthanum modified Titanium (IV) oxide using response surface methodology. *Int J Hydrogen Energy* **2018**, https://doi.org/10.1016/j.ijhydene.2018.06.185; b) Bowker, M.; Morton, C.; Kennedy, J.; Bahruji, H.; Greves, J.; Jones, W.; Davies, P. R.; Brookes, C.; Wells, P. P.; Dimitratos, N., Hydrogen production by photoreforming of biofuels using Au, Pd and Au–Pd/TiO2 photocatalysts. *Journal of Catalysis* **2014,** *310*, 10-15; c) Zhang, X.; Luo, L.; Yun, R.; Pu, M.; Zhang, B.; Xiang, X., Increasing the Activity and Selectivity of TiO2-Supported Au Catalysts for Renewable Hydrogen Generation from Ethanol Photoreforming by Engineering Ti3+ Defects. *ACS Sustain. Chem. Eng.* **2019,** *7*, 13856-13864.
58. Zhang, L.; Jiang, D.; Irfan, R. M.; Tang, S.; Chen, X.; Du, P., Highly efficient and selective photocatalytic dehydrogenation of benzyl alcohol for simultaneous hydrogen and benzaldehyde production over Ni-decorated Zn0.5Cd0.5S solid solution. *Journal of Energy Chemistry* **2018,** *30*, 71-77.
59. a) Lu, D.; Wang, H.; Zhao, X.; Kondamareddy, K. K.; Ding, J.; Li, C.; Fang, P., Highly Efficient Visible-Light-Induced Photoactivity of Z-Scheme g-C3N4/Ag/MoS2 Ternary Photocatalysts for Organic Pollutant Degradation and Production of Hydrogen. *ACS Sustainable Chemistry & Engineering* **2017,** *5*, 1436-1445; b) Hou, H.-J.; Zhang, X.-H.; Huang, D.-K.; Ding, X.; Wang, S.-Y.; Yang, X.-L.; Li, S.-Q.; Xiang, Y.-G.; Chen, H., Conjugated microporous poly(benzothiadiazole)/TiO2 heterojunction for visible-light-driven H2 production and pollutant removal. *Applied Catalysis B: Environmental* **2017,** *203*, 563-571.
60. Furukawa, H.; Cordova, K. E.; O'Keeffe, M.; Yaghi, O. M., The Chemistry and Applications of Metal-Organic Frameworks. *Science* **2013,** *341*, 1230444.
61. Yaghi, O. M.; Li, G.; Li, H., Selective binding and removal of guests in a microporous metal-organic framework. *Nature* **1995,** *378*, 703-706.
62. Farha, O. K.; Eryazici, I.; Jeong, N. C.; Hauser, B. G.; Wilmer, C. E.; Sarjeant, A. A.; Snurr, R. Q.; Nguyen, S. T.; Yazaydın, A. Ö.; Hupp, J. T., Metal–Organic Framework Materials with Ultrahigh Surface Areas: Is the Sky the Limit? *J. Am. Chem. Soc.* **2012,** *134*, 15016-15021.
63. a) Li, B.; Wen, H.-M.; Cui, Y.; Zhou, W.; Qian, G.; Chen, B., Emerging Multifunctional Metal–Organic Framework Materials. *Adv. Mater.* **2016,** *28*, 8819–8860; b) Thorarinsdottir, A. E.; Harris, T. D., Metal–Organic Framework Magnets. *Chem. Rev.* **2020**; c) Xie, L. S.; Skorupskii, G.; Dincă, M., Electrically Conductive Metal–Organic Frameworks. *Chem. Rev.* **2020**.
64. a) Bordiga, S.; Lamberti, C.; Ricchiardi, G.; Regli, L.; Bonino, F.; Damin, A.; Lillerud, K. P.; Bjorgen, M.; Zecchina, A., Electronic and vibrational properties of a MOF-5 metal–organic framework: ZnO quantum dot behaviour. *Chem. Commun.* **2004**, 2300-2301; b) Alvaro, M.; Carbonell, E.; Ferrer, B.; Llabrés i Xamena, F. X.; Garcia, H., Semiconductor Behavior of a Metal-Organic Framework (MOF). *Chem.: Eur. J.* **2007,** *13*, 5106-5112; c) Silva, C. G.; Corma, A.; García, H., Metal–organic frameworks as semiconductors. *J. Mater. Chem.* **2010,** *20*, 3141-3156.
65. a) Kataoka, Y.; Sato, K.; Miyazaki, Y.; Masuda, K.; Tanaka, H.; Naito, S.; Mori, W., Photocatalytic hydrogen production from water using porous material [Ru2(p-BDC)2]n. *Energy Environ. Sci.* **2009,** *2*, 397-400; b) Gomes Silva, C.; Luz, I.; Llabrés i Xamena, F. X.; Corma, A.; García, H., Water stable Zr–benzenedicarboxylate metal–organic frameworks as photocatalysts for hydrogen generation. *Chemistry–A European Journal* **2010,** *16*, 11133-11138.
66. a) Zhang, T.; Lin, W., Metal-organic frameworks for artificial photosynthesis and photocatalysis. *Chemical Society Reviews* **2014,** *43*, 5982-5993; b) Wang, C.-C.; Du, X.-D.; Li, J.; Guo, X.-X.; Wang, P.; Zhang, J., Photocatalytic Cr(VI) reduction in metal-organic frameworks: A mini-review. *Appl. Catal., B* **2016,** *193*, 198-216; c) Wang, C.-C.; Li, J.-R.; Lv, X.-L.; Zhang, Y.-Q.; Guo, G., Photocatalytic organic pollutants degradation in metal-organic frameworks. *Energy Environ. Sci.* **2014,** *7*, 2831-2867; d) Alkhatib, I. I.; Garlisi, C.; Pagliaro, M.; Al-Ali,

K.; Palmisano, G., Metal-organic frameworks for photocatalytic CO2 reduction under visible radiation: A review of strategies and applications. *Catal. Today* **2020,** *340*, 209-224; e) Liu, S.; Zhang, C.; Sun, Y.; Chen, Q.; He, L.; Zhang, K.; Zhang, J.; Liu, B.; Chen, L.-F., Design of metal-organic framework-based photocatalysts for hydrogen generation. *Coord. Chem. Rev.* **2020,** *413*, 213266.

67. Kalyanasundaram, K., 7 - Semiconductor Particulate Systems for Photocatalysis and Photosynthesis: An Overview A2 - Grätzel, Michael. In *Energy Resources Through Photochemistry and Catalysis*, Academic Press: 1983; pp 217-260.

68. a) Yang, X.; Liu, R.; He, Y.; Thorne, J.; Zheng, Z.; Wang, D., Enabling practical electrocatalyst-assisted photoelectron-chemical water splitting with earth abundant materials. *Nano Res.* **2015,** *8*, 56-81; b) Kudo, A.; Miseki, Y., Heterogeneous photocatalyst materials for water splitting. *Chem. Soc. Rev.* **2009,** *38*, 253-278; c) Zou, Z.; Ye, J.; Sayama, K.; Arakawa, H., Direct splitting of water under visible light irradiation with an oxide semiconductor photocatalyst. *Nature* **2001,** *414*, 625-627.

69. a) Majewski, M. B.; Peters, A. W.; Wasielewski, M. R.; Hupp, J. T.; Farha, O. K., Metal–Organic Frameworks as Platform Materials for Solar Fuels Catalysis. *ACS Energy Lett.* **2018,** *3*, 598-611; b) Nasalevich, M. A.; Becker, R.; Ramos-Fernandez, E. V.; Castellanos, S.; Veber, S. L.; Fedin, M. V.; Kapteijn, F.; Reek, J. N. H.; van der Vlugt, J. I.; Gascon, J., Co@NH2-MIL-125(Ti): cobaloxime-derived metal-organic framework-based composite for light-driven H2 production. *Energy & Environmental Science* **2015,** *8*, 364-375.

70. Baker, F. B.; Newton, T. W.; Kahn, M., THE KINETICS OF THE REACTION BETWEEN URANIUM(IV) AND CERIUM(IV)1. *J. Phys. Chem.* **1960,** *64*, 109-112.

71. Li, H.; Eddaoudi, M.; O'Keeffe, M.; Yaghi, O. M., Design and synthesis of an exceptionally stable and highly porous metal-organic framework. *Nature* **1999,** *402*, 276-279.

72. Dan-Hardi, M.; Serre, C.; Frot, T.; Rozes, L.; Maurin, G.; Sanchez, C.; Férey, G., A New Photoactive Crystalline Highly Porous Titanium(IV) Dicarboxylate. *J. Am. Chem. Soc.* **2009,** *131*, 10857-10859.

73. Férey, G.; Mellot-Draznieks, C.; Serre, C.; Millange, F.; Dutour, J.; Surblé, S.; Margiolaki, I., A Chromium Terephthalate-Based Solid with Unusually Large Pore Volumes and Surface Area. *Science* **2005,** *309*, 2040-2042.

74. Cavka, J. H.; Jakobsen, S.; Olsbye, U.; Guillou, N.; Lamberti, C.; Bordiga, S.; Lillerud, K. P., A New Zirconium Inorganic Building Brick Forming Metal Organic Frameworks with Exceptional Stability. *J. Am. Chem. Soc.* **2008,** *130*, 13850-13851.

75. Liao, P.-Q.; Zhou, D.-D.; Zhu, A.-X.; Jiang, L.; Lin, R.-B.; Zhang, J.-P.; Chen, X.-M., Strong and Dynamic CO2 Sorption in a Flexible Porous Framework Possessing Guest Chelating Claws. *J. Am. Chem. Soc.* **2012,** *134*, 17380-17383.

76. Taylor, J. M.; Vaidhyanathan, R.; Iremonger, S. S.; Shimizu, G. K. H., Enhancing Water Stability of Metal–Organic Frameworks via Phosphonate Monoester Linkers. *J. Am. Chem. Soc.* **2012,** *134*, 14338-14340.

77. Anderson, S.; Tiana, D.; Ireland, C.; Capano, G.; Fumanal, M.; Gladysiak, A.; Kampouri, S.; Rahmanudin, A.; Guijarro, N.; Sivula, K.; Stylianou, K.; Smit, B., Taking Lanthanides out of isolation: tuning the optical properties of metal-organic frameworks. *Chem. Sci.* **2020**, DOI: 10.1039/D0SC00740D.

78. Lustig, W. P.; Wang, F.; Teat, S. J.; Hu, Z.; Gong, Q.; Li, J., Chromophore-Based Luminescent Metal–Organic Frameworks as Lighting Phosphors. *Inorg. Chem.* **2016,** *55*, 7250-7256.

79. a) Yuan, Y.-P.; Yin, L.-S.; Cao, S.-W.; Xu, G.-S.; Li, C.-H.; Xue, C., Improving photocatalytic hydrogen production of metal–organic framework UiO-66 octahedrons by dye-sensitization. *Applied Catalysis B: Environmental* **2015,** *168–169*, 572-576; b) Chen, Q.; Feng, Y.; Tian, R.; Chen, J.; Wang, A.; Yao, J., Defect Rich UiO-66 with Enhanced Adsorption and Photosensitized Reduction of Cr(VI) under Visible Light. *Industrial & Engineering Chemistry Research* **2019,** *58*, 21562-21568.

80. Hendon, C. H.; Tiana, D.; Fontecave, M.; Sanchez, C. m.; D'arras, L.; Sassoye, C.; Rozes, L.; Mellot-Draznieks, C.; Walsh, A., Engineering the optical response of the titanium-MIL-125 metal–organic framework through ligand functionalization. *J. Am. Chem. Soc.* **2013,** *135*, 10942-10945.

81. Xiao, Y.; Qi, Y.; Wang, X.; Wang, X.; Zhang, F.; Li, C., Visible-Light-Responsive 2D Cadmium–Organic Framework Single Crystals with Dual Functions of Water Reduction and Oxidation. *Adv. Mater.* **2018,** *30*, 1803401.

82. Fateeva, A.; Chater, P. A.; Ireland, C. P.; Tahir, A. A.; Khimyak, Y. Z.; Wiper, P. V.; Darwent, J. R.; Rosseinsky, M. J., A Water-Stable Porphyrin-Based Metal–Organic Framework Active for Visible-Light Photocatalysis. *Angew. Chem.* **2012,** *124*, 7558-7562.

83. O'Regan, B.; Graetzel, M., A low-cost, high-efficiency solar cell based on dye-sensitized. *nature* **1991,** *353*, 737-740.

84. He, J.; Wang, J.; Chen, Y.; Zhang, J.; Duan, D.; Wang, Y.; Yan, Z., A dye-sensitized Pt@ UiO-66 (Zr) metal–organic framework for visible-light photocatalytic hydrogen production. *Chemical Communications* **2014,** *50*, 7063-7066.

85. a) Xiao, J. D.; Shang, Q.; Xiong, Y.; Zhang, Q.; Luo, Y.; Yu, S. H.; Jiang, H. L., Boosting photocatalytic hydrogen production of a metal–organic framework decorated with platinum nanoparticles: The platinum location matters. *Angew. Chem. Int. Ed.* **2016,** *128*, 9535-9539; b) Wang, D.; Song, Y.; Cai, J.; Wu, L.; Li, Z., Effective photo-reduction to deposit Pt nanoparticles on MIL-100 (Fe) for visible-light-induced hydrogen evolution. *New Journal of Chemistry* **2016,** *40*, 9170-9175; c) Wang, C.; deKrafft, K. E.; Lin, W., Pt Nanoparticles@Photoactive Metal–Organic Frameworks: Efficient Hydrogen Evolution via Synergistic Photoexcitation and Electron Injection. *J. Am. Chem. Soc.* **2012,** *134*, 7211-7214; d) Guo, W.; Shu, S.; Zhang, T.; Jian, Y.; Liu, X., Stable d10 Metal–Organic Framework Exhibiting Bifunctional Properties of Photocatalytic Hydrogen and Oxygen Evolution. *ACS Appl. Energy Mater.* **2020,** *3*, 2983-2988.

86. Kampouri, S.; Nguyen, T. N.; Ireland, C. P.; Valizadeh, B.; Ebrahim, F. M.; Capano, G.; Ongari, D.; Mace, A.; Guijarro, N.; Sivula, K.; Sienkiewicz, A.; Forro, L.; Smit, B.; Stylianou, K. C., Photocatalytic Hydrogen Generation from a Visible-Light Responsive Metal-Organic Framework System: The Impact of Nickel Phosphide Nanoparticles. *J. Mater. Chem. A* **2018,** *6*, 2476-2481.

87. Kampouri, S.; Nguyen, T. N.; Spodaryk, M.; Palgrave, R. G.; Züttel, A.; Smit, B.; Stylianou, K. C., Concurrent Photocatalytic Hydrogen Generation and Dye Degradation Using MIL-125-NH2 under Visible Light Irradiation. *Adv. Funct. Mater.* **2018,** *28*, 1806368.

88. a) Gomes Silva, C.; Luz, I.; Llabrés i Xamena, F. X.; Corma, A.; García, H., Water Stable Zr–Benzenedicarboxylate Metal–Organic Frameworks as Photocatalysts for Hydrogen Generation. *Chemistry – A European Journal* **2010,** *16*, 11133-11138; b) Zhang, F.; Zhang, B.; Feng, J.; Tan, X.; Liu, L.; Liu, L.; Han, B.; Zheng, L.; Zhang, J.; Tai, J.; Zhang, J., Highly Mesoporous Ru-MIL-125-NH2 Produced by Supercritical Fluid for Efficient Photocatalytic Hydrogen Production. *ACS Appl. Energy Mater.* **2019,** *2*, 4964-4970; c) Zhao, C.; Zhang, Y.; Jiang, H.; Chen, J.; Liu, Y.; Liang, Q.; Zhou, M.; Li, Z.; Zhou, Y., Combined Effects of Octahedron NH2-UiO-66 and Flowerlike ZnIn2S4 Microspheres for Photocatalytic Dye Degradation and Hydrogen Evolution under Visible Light. *J. Phys. Chem. C* **2019,** *123*, 18037-18049; d) Toyao, T.; Saito, M.; Dohshi, S.; Mochizuki, K.; Iwata, M.; Higashimura, H.; Horiuchi, Y.; Matsuoka, M., Development of a Ru complex-incorporated MOF photocatalyst for hydrogen production under visible-light irradiation. *Chemical Communications* **2014,** *50*, 6779-6781.

89. a) Shi, D.; Zheng, R.; Sun, M.-J.; Cao, X.; Sun, C.-X.; Cui, C.-J.; Liu, C.-S.; Zhao, J.; Du, M., Semiconductive Copper(I)–Organic Frameworks for Efficient Light-Driven Hydrogen Generation Without Additional Photosensitizers and Cocatalysts. *Angewandte Chemie International Edition* **2017,** *56*, 14637-14641; b) Wu, Z.-L.; Wang, C.-H.; Zhao, B.; Dong, J.; Lu, F.; Wang, W.-H.; Wang, W.-C.; Wu, G.-J.; Cui, J.-Z.; Cheng, P., A Semi-Conductive Copper–Organic Framework with Two Types of Photocatalytic Activity. *Angewandte Chemie International Edition* **2016,** *55*, 4938-4942; c) Dong, X.-Y.; Zhang, M.; Pei, R.-B.; Wang, Q.; Wei, D.-H.; Zang, S.-Q.; Fan, Y.-T.; Mak, T. C. W., A Crystalline Copper(II) Coordination Polymer for the Efficient Visible-Light-Driven Generation of Hydrogen. *Angewandte Chemie International Edition* **2016,** *55*, 2073-2077.

90. a) Horiuchi, Y.; Toyao, T.; Saito, M.; Mochizuki, K.; Iwata, M.; Higashimura, H.; Anpo, M.; Matsuoka, M., Visible-Light-Promoted Photocatalytic Hydrogen Production by Using an Amino-Functionalized Ti(IV) Metal–Organic Framework. *The Journal of Physical Chemistry C* **2012,** *116*, 20848-20853; b) Fateeva, A.; Chater, P. A.; Ireland, C. P.; Tahir, A. A.; Khimyak, Y. Z.; Wiper, P. V.; Darwent, J. R.; Rosseinsky, M. J., A Water-Stable Porphyrin-Based Metal–Organic Framework Active for Visible-Light Photocatalysis. *Angewandte Chemie International Edition* **2012,** *51*, 7440-7444.

91. a) Horiuchi, Y.; Toyao, T.; Saito, M.; Mochizuki, K.; Iwata, M.; Higashimura, H.; Anpo, M.; Matsuoka, M., Visible-Light-Promoted Photocatalytic Hydrogen Production by Using an Amino-Functionalized Ti(IV) Metal-Organic Framework. *J. Phys. Chem. C* **2012,** *116*, 20848-20853; b) Meyer, K.; Bashir, S.; Llorca, J.; Idriss, H.; Ranocchiari, M.; van Bokhoven, J. A., Photocatalyzed Hydrogen Evolution from Water by a Composite Catalyst of NH2-MIL-125 (Ti) and Surface Nickel (II) Species. *Chem.: Eur. J* **2016,** *22*, 13894-13899.

92. a) Hendon, C. H.; Tiana, D.; Fontecave, M.; Sanchez, C.; D'arras, L.; Sassoye, C.; Rozes, L.; Mellot-Draznieks, C.; Walsh, A., Engineering the Optical Response of the Titanium-MIL-125 Metal–Organic Framework through Ligand Functionalization. *J. Am. Chem. Soc.* **2013,** *135*, 10942-10945; b) Zhang, B.; Zhang, J.; Tan, X.; Shao, D.; Shi, J.; Zheng, L.; Zhang, J.; Yang, G.; Han, B., MIL-125-NH2@TiO2 Core–Shell Particles Produced by a Post-Solvothermal Route for High-Performance Photocatalytic H2 Production. *ACS Appl. Energy Mater.* **2018,** *10*, 16418-16423.

93. a) Dhakshinamoorthy, A.; Li, Z.; Garcia, H., Catalysis and photocatalysis by metal organic frameworks. *Chem. Soc. Rev.* **2018,** *47*, 8134-8172 ; b) Wang, J.-L.; Wang, C.; Lin, W., Metal–Organic Frameworks for Light Harvesting and Photocatalysis. *ACS Catalysis* **2012,** *2*, 2630-2640; c) Li, Y.; Xu, H.; Ouyang, S.; Ye, J., Metal–organic frameworks for photocatalysis. *Phys. Chem. Chem. Phys.* **2016,** *18*, 7563-7572; d) Wang, S.; Wang, X., Multifunctional Metal–Organic Frameworks for Photocatalysis. *Small* **2015,** *11*, 3097-3112; e) Fu, Y.; Yang, H.;

Du, R.; Tu, G.; Xu, C.; Zhang, F.; Fan, M.; Zhu, W., Enhanced photocatalytic CO2 reduction over Co-doped NH2-MIL-125(Ti) under visible light. *RSC Adv.* **2017,** *7*, 42819-42825.
94. Nasalevich, M. A.; Becker, R.; Ramos-Fernandez, E. V.; Castellanos, S.; Veber, S. L.; Fedin, M. V.; Kapteijn, F.; Reek, J. N. H.; van der Vlugt, J. I.; Gascon, J., Co@NH2-MIL-125(Ti): cobaloxime-derived metal-organic framework-based composite for light-driven H2 production. *Energy Environ. Sci.* **2015,** *8*, 364-375.
95. Kumar, D. P.; Choi, J.; Hong, S.; Reddy, D. A.; Lee, S.; Kim, T. K., Rational Synthesis of Metal–Organic Framework-Derived Noble Metal-Free Nickel Phosphide Nanoparticles as a Highly Efficient Cocatalyst for Photocatalytic Hydrogen Evolution. *ACS Sustainable Chemistry & Engineering* **2016,** *4*, 7158-7166.
96. Jagadeesh, R. V.; Murugesan, K.; Alshammari, A. S.; Neumann, H.; Pohl, M.-M.; Radnik, J.; Beller, M., MOF-derived cobalt nanoparticles catalyze a general synthesis of amines. *Science* **2017**.
97. Rui, W.; Xi-Yan, D.; Jiao, D.; Jin-Yan, Z.; Shuang-Quan, Z., MOF-Derived Bifunctional Cu3P Nanoparticles Coated by a N,P-Codoped Carbon Shell for Hydrogen Evolution and Oxygen Reduction. *Advanced Materials* **2018,** *30*, 1703711.
98. Yu, Z.; Bai, Y.; Zhang, S.; Liu, Y.; Zhang, N.; Wang, G.; Wei, J.; Wu, Q.; Sun, K., Metal–Organic Framework-Derived Co3ZnC/Co Embedded in Nitrogen-Doped Carbon Nanotube-Grafted Carbon Polyhedra as a High-Performance Electrocatalyst for Water Splitting. *ACS Appl. Mater. Interfaces* **2018,** *10*, 6245-6252.
99. Li, L.; Li, X.; Ai, L.; Jiang, J., MOF-derived nanostructured cobalt phosphide assemblies for efficient hydrogen evolution reaction. *RSC Advances* **2015,** *5*, 90265-90271.
100. Pradhan, B.; Kumar, G. S.; Dalui, A.; Khan, A. H.; Satpati, B.; Ji, Q.; Shrestha, L. K.; Ariga, K.; Acharya, S., Shape-controlled cobalt phosphide nanoparticles as volatile organic solvent sensor. *J. Mater. Chem. C* **2016,** *4*, 4967-4977.
101. Hou, C.; Xu, Q.; Wang, Y.; Hu, X., Synthesis of Pt@NH2-MIL-125(Ti) as a photocathode material for photoelectrochemical hydrogen production. *RSC Adv.* **2013,** *3*, 19820-19823.
102. Xiao, J.-D.; Shang, Q.; Xiong, Y.; Zhang, Q.; Luo, Y.; Yu, S.-H.; Jiang, H.-L., Boosting Photocatalytic Hydrogen Production of a Metal–Organic Framework Decorated with Platinum Nanoparticles: The Platinum Location Matters. *Angew. Chem. Int. Ed.* **2016,** *128*, 9535-9539.
103. a) Kuhn, H. B., S.; Schmidt, R. , *Pure Appl. Chem.* **2004,** *76.*, 2105-2146; b) Hatchard, C. P., C. A. , *Proc. Royal Soc. A* **1956,** *235*, 518.
104. Shen, L.; Luo, M.; Liu, Y.; Liang, R.; Jing, F.; Wu, L., Noble-metal-free MoS2 co-catalyst decorated UiO-66/CdS hybrids for efficient photocatalytic H2 production. *Appl. Catal., B* **2015,** *166–167*, 445-453.
105. a) Maeda, K.; Teramura, K.; Lu, D.; Takata, T.; Saito, N.; Inoue, Y.; Domen, K., Photocatalyst releasing hydrogen from water. *Nature* **2006,** *440*, 295-295; b) Chen, X.; Shen, S.; Guo, L.; Mao, S. S., Semiconductor-based Photocatalytic Hydrogen Generation. *Chem. Rev.* **2010,** *110*, 6503-6570.
106. Zhang, B.; Xue, Y.; Sun, H.; Jiang, A.; Li, Z.; Hao, J., A green synthesis of "naked" Pt and PtPd catalysts for highly efficient methanol electrooxidation. *RSC Adv.* **2016,** *6*, 56083-56090.
107. a) Sun, D.; Liu, W.; Fu, Y.; Fang, Z.; Sun, F.; Fu, X.; Zhang, Y.; Li, Z., Noble Metals Can Have Different Effects on Photocatalysis Over Metal–Organic Frameworks (MOFs): A Case Study on M/NH2-MIL-125(Ti) (M=Pt and Au). *Chem. Eur. J.* **2014,** *20*, 4780-4788; b) Toyao, T.; Saito, M.; Horiuchi, Y.; Mochizuki, K.; Iwata, M.; Higashimura, H.; Matsuoka, M., Efficient hydrogen production and photocatalytic reduction of nitrobenzene over a visible-light-responsive metal-organic framework photocatalyst. *Catal. Sci. Technol.* **2013,** *3*, 2092-2097.
108. Xinzuo, F.; Qichao, S.; Yu, W.; Long, J.; Tao, Y.; Yafei, L.; Qun, Z.; Yi, L.; Hai-Long, J., Single Pt Atoms Confined into a Metal–Organic Framework for Efficient Photocatalysis. *Advanced Materials* **2018,** *30*, 1705112.
109. Schneider, J.; Bahnemann, D. W., Undesired Role of Sacrificial Reagents in Photocatalysis. *The Journal of Physical Chemistry Letters* **2013,** *4*, 3479-3483.
110. Wang, Y.; Vogel, A.; Sachs, M.; Sprick, R. S.; Wilbraham, L.; Moniz, S. J. A.; Godin, R.; Zwijnenburg, M. A.; Durrant, J. R.; Cooper, A. I.; Tang, J., Current understanding and challenges of solar-driven hydrogen generation using polymeric photocatalysts. *Nat. Energy* **2019,** *4*, 746-760.
111. a) Cho, Y.-J.; Moon, G.-h.; Kanazawa, T.; Maeda, K.; Choi, W., Selective dual-purpose photocatalysis for simultaneous H2 evolution and mineralization of organic compounds enabled by a Cr2O3 barrier layer coated on Rh/SrTiO3. *Chem. Commun.* **2016,** *52*, 9636-9639; b) Kim, J.; Monllor-Satoca, D.; Choi, W., Simultaneous production of hydrogen with the degradation of organic pollutants using TiO2 photocatalyst modified with dual surface components. *Energy & Environmental Science* **2012,** *5*, 7647-7656.
112. Zhou, J.-J.; Wang, R.; Liu, X.-L.; Peng, F.-M.; Li, C.-H.; Teng, F.; Yuan, Y.-P., In situ growth of CdS nanoparticles on UiO-66 metal-organic framework octahedrons for enhanced photocatalytic hydrogen production under visible light irradiation. *Appl. Surf. Sci.* **2015,** *346*, 278-283.

113. a) Yu, K.; Yang, S.; He, H.; Sun, C.; Gu, C.; Ju, Y., Visible Light-Driven Photocatalytic Degradation of Rhodamine B over NaBiO3: Pathways and Mechanism. *J. Phys. Chem. A* **2009,** *113*, 10024-10032; b) Hassanpour, M.; Safardoust-Hojaghan, H.; Salavati-Niasari, M., Degradation of methylene blue and Rhodamine B as water pollutants via green synthesized Co3O4/ZnO nanocomposite. *J. Mol. Liq.* **2017,** *229*, 293-299.

114. a) Xia, Q.; Yu, X.; Zhao, H.; Wang, S.; Wang, H.; Guo, Z.; Xing, H., Syntheses of Novel Lanthanide Metal–Organic Frameworks for Highly Efficient Visible-Light-Driven Dye Degradation. *Cryst. Growth Des.* **2017**; b) Ai, L.; Zhang, C.; Li, L.; Jiang, J., Iron terephthalate metal–organic framework: Revealing the effective activation of hydrogen peroxide for the degradation of organic dye under visible light irradiation. *Appl. Catal., B* **2014,** *148–149*, 191-200; c) Fan, K.; Nie, W.-X.; Wang, L.-P.; Liao, C.-H.; Bao, S.-S.; Zheng, L.-M., Defective Metal–Organic Frameworks Incorporating Iridium-Based Metalloligands: Sorption and Dye Degradation Properties. *Chem.: Eur. J.* **2017,** *23*, 6615-6624.

115. Baldev, E.; MubarakAli, D.; Ilavarasi, A.; Pandiaraj, D.; Ishack, K. A. S. S.; Thajuddin, N., Degradation of synthetic dye, Rhodamine B to environmentally non-toxic products using microalgae. *Colloids Surf B Biointerfaces* **2013,** *105*, 207-214.

116. a) Li, Y.; Lu, G.; Li, S., Photocatalytic hydrogen generation and decomposition of oxalic acid over platinized TiO2. *Appl. Catal., A* **2001,** *214*, 179-185; b) Li, Y.; Lu, G.; Li, S., Photocatalytic production of hydrogen in single component and mixture systems of electron donors and monitoring adsorption of donors by in situ infrared spectroscopy. *Chemosphere* **2003,** *52*, 843-850; c) Li, Y.; Xie, Y.; Peng, S.; Lu, G.; Li, S., Photocatalytic hydrogen generation in the presence of chloroacetic acids over Pt/TiO2. *Chemosphere* **2006,** *63*, 1312-1318; d) Patsoura, A.; Kondarides, D. I.; Verykios, X. E., Enhancement of photoinduced hydrogen production from irradiated Pt/TiO2 suspensions with simultaneous degradation of azo-dyes. *Appl. Catal., B* **2006,** *64*, 171-179; e) Patsoura, A.; Kondarides, D. I.; Verykios, X. E., Photocatalytic degradation of organic pollutants with simultaneous production of hydrogen. *Catal. Today* **2007,** *124*, 94-102; f) Kim, J.; Choi, W., Hydrogen producing water treatment through solar photocatalysis. *Energy Environ. Sci.* **2010,** *3*, 1042-1045.

117. a) Wang, H.; Zhang, L.; Chen, Z.; Hu, J.; Li, S.; Wang, Z.; Liu, J.; Wang, X., Semiconductor heterojunction photocatalysts: design, construction, and photocatalytic performances. *Chem. Soc. Rev.* **2014,** *43*, 5234-5244; b) Moniz, S. J. A.; Shevlin, S. A.; Martin, D. J.; Guo, Z.-X.; Tang, J., Visible-light driven heterojunction photocatalysts for water splitting – a critical review. *Energy Environ. Sci.* **2015,** *8*, 731-759.

118. Low, J.; Yu, J.; Jaroniec, M.; Wageh, S.; Al-Ghamdi, A. A., Heterojunction Photocatalysts. *Adv. Mater.* **2017,** *29*, 1601694.

119. a) Sun, D.; Jang, S.; Yim, S.-J.; Ye, L.; Kim, D.-P., Metal Doped Core–Shell Metal-Organic Frameworks@Covalent Organic Frameworks (MOFs@COFs) Hybrids as a Novel Photocatalytic Platform. *Adv. Funct. Mater.* **2018,** *28*, 1707110; b) Zhang, C.-F.; Qiu, L.-G.; Ke, F.; Zhu, Y.-J.; Yuan, Y.-P.; Xu, G.-S.; Jiang, X., A novel magnetic recyclable photocatalyst based on a core–shell metal–organic framework Fe3O4@MIL-100(Fe) for the decolorization of methylene blue dye. *J. Mater. Chem. A* **2013,** *1*, 14329-14334; c) Liang, Y.; Shang, R.; Lu, J.; Liu, L.; Hu, J.; Cui, W., Ag3PO4@UMOFNs Core–Shell Structure: Two-Dimensional MOFs Promoted Photoinduced Charge Separation and Photocatalysis. *ACS Appl. Energy Mater.* **2018,** *10*, 8758-8769; d) Tilgner, D.; Kempe, R., A Plasmonic Colloidal Photocatalyst Composed of a Metal–Organic Framework Core and a Gold/Anatase Shell for Visible-Light-Driven Wastewater Purification from Antibiotics and Hydrogen Evolution. *Chem.: Eur. J.* **2017,** *23*, 3184-3190; e) He, X.; Wang, W.-N., MOF-based ternary nanocomposites for better CO2 photoreduction: roles of heterojunctions and coordinatively unsaturated metal sites. *J. Mater. Chem. A* **2018,** *6*, 932-940; f) Crake, A.; Christoforidis, K. C.; Gregg, A.; Moss, B.; Kafizas, A.; Petit, C., The Effect of Materials Architecture in TiO2/MOF Composites on CO2 Photoreduction and Charge Transfer. *Small* **2019,** *15*, 1805473; g) Garzón-Tovar, L.; Pérez-Carvajal, J.; Yazdi, A.; Hernández-Muñoz, J.; Tarazona, P.; Imaz, I.; Zamora, F.; Maspoch, D., A MOF@COF Composite with Enhanced Uptake through Interfacial Pore Generation. *Angew. Chem.* **2019,** *131*, 9612-9616.

120. a) McDonald, K. A.; Feldblyum, J. I.; Koh, K.; Wong-Foy, A. G.; Matzger, A. J., Polymer@MOF@MOF: "grafting from" atom transfer radical polymerization for the synthesis of hybrid porous solids. *Chem. Commun.* **2015,** *51*, 11994-11996; b) Wu, S.; Zhuang, G.; Wei, J.; Zhuang, Z.; Yu, Y., Shape control of core–shell MOF@MOF and derived MOF nanocages via ion modulation in a one-pot strategy. *J. Mater. Chem. A* **2018,** *6*, 18234-18241; c) Zhang, L.; Wang, J.; Ren, X.; Zhang, W.; Zhang, T.; Liu, X.; Du, T.; Li, T.; Wang, J., Internally extended growth of core–shell NH2-MIL-101(Al)@ZIF-8 nanoflowers for the simultaneous detection and removal of Cu(ii). *J. Mater. Chem. A* **2018,** *6*, 21029-21038; d) Zhang, M.; Wu, D.; Ye, Y.; Wu, L.; Yao, Z.; Ma, X.; Wang, L.; Zhang, Z.; Xiang, S., Thermal Conversion of MOF@MOF: Synthesis of an N-Doped Carbon Material with Excellent ORR Performance. *Chem. Phys. Chem.* **2018,** *83*, 1044-1051; e) Gong, Y.; Yuan, Y.; Chen, C.; Zhang, P.; Wang, J.; Khan, A.; Zhuiykov, S.; Chaemchuen, S.; Verpoort, F., Enhancing catalytic performance via structure core-shell metal-organic frameworks. *J. Catal.* **2019,** *375*, 371-379; f) Gong, Y.; Yuan, Y.; Chen, C.; Zhang, P.; Wang, J.;

Zhuiykov, S.; Chaemchuen, S.; Verpoort, F., Core-shell metal-organic frameworks and metal functionalization to access highest efficiency in catalytic carboxylation. *J. Catal.* **2019,** *371*, 106-115; g) Gu, Y.; Wu, Y.-n.; Li, L.; Chen, W.; Li, F.; Kitagawa, S., Controllable Modular Growth of Hierarchical MOF-on-MOF Architectures. *Angew. Chem. Int. Edit.* **2017,** *56*, 15658-15662.

121. Assi, H.; Pardo Pérez, L. C.; Mouchaham, G.; Ragon, F.; Nasalevich, M.; Guillou, N.; Martineau, C.; Chevreau, H.; Kapteijn, F.; Gascon, J.; Fertey, P.; Elkaim, E.; Serre, C.; Devic, T., Investigating the Case of Titanium(IV) Carboxyphenolate Photoactive Coordination Polymers. *Inorg. Chem.* **2016,** *55*, 7192-7199.

122. Sun, X.; Yu, Q.; Zhang, F.; Wei, J.; Yang, P., A dye-like ligand-based metal–organic framework for efficient photocatalytic hydrogen production from aqueous solution. *Catal. Sci. Technol.* **2016,** *6*, 3840-3844.

123. Nasalevich, M. A.; Hendon, C. H.; Santaclara, J. G.; Svane, K.; van der Linden, B.; Veber, S. L.; Fedin, M. V.; Houtepen, A. J.; van der Veen, M. A.; Kapteijn, F.; Walsh, A.; Gascon, J., Electronic origins of photocatalytic activity in d0 metal organic frameworks. *Sci. Rep.* **2016,** *6*, 23676.

124. Kampouri, S.; Ireland, C. P.; Valizadeh, B.; Oveisi, E.; Schouwink, P.; Mensi, M.; Stylianou, K. C., Mixed-phase MOF-derived Titanium Dioxide for Photocatalytic Hydrogen Evolution: The Impact of the Templated Morphology. *ACS Appl. Energy Mater.* **2018,** *1*, 6541-6548.

125. Schrauzer, G. N.; Guth, T. D., Photocatalytic Reactions. 1. Photolysis of Water and Photoreduction of Nitrogen on Titanium Dioxide. *J. Am. Chem. Soc.* **1977,** *99*, 7189-7193.

126. a) Dahl, M.; Liu, Y.; Yin, Y., Composite Titanium Dioxide Nanomaterials. *Chem. Rev.* **2014,** *114*, 9853-9889; b) Shi, L.; Li, Z.; Dao, T. D.; Nagao, T.; Yang, Y., A Synergistic Interaction between Isolated Au Nanoparticles and Oxygen Vacancies in an Amorphous Black TiO2 Nanoporous Film: toward Enhanced Photoelectrochemical Water Splitting. *J. Mater. Chem. A* **2018,** *6*, 12978-12984; c) Li, Z.; Shi, L.; Franklin, D.; Koul, S.; Kushima, A.; Yang, Y., Drastic Enhancement of Photoelectrochemical Water Splitting Performance over Plasmonic Al@TiO2 Heterostructured Nanocavity Arrays. *Nano Energy* **2018,** *51*, 400-407.

127. Schneider, J.; Matsuoka, M.; Takeuchi, M.; Zhang, J.; Horiuchi, Y.; Anpo, M.; Bahnemann, D. W., Understanding TiO_2 Photocatalysis: Mechanisms and Materials. *Chem. Rev.* **2014,** *114*, 9919-9986.

128. Bourikas, K.; Kordulis, C.; Lycourghiotis, A., Titanium Dioxide (Anatase and Rutile): Surface Chemistry, Liquid–Solid Interface Chemistry, and Scientific Synthesis of Supported Catalysts. *Chem. Rev.* **2014,** *114*, 9754-9823.

129. Carp, O.; Huisman, C. L.; Reller, A., Photoinduced Reactivity of Titanium Dioxide. *Prog. Solid State Chem.* **2004,** *32*, 33-177.

130. a) Bickley, R. I.; Gonzalez-Carreno, T.; Lees, J. S.; Palmisano, L.; Tilley, R. J. D., A Structural Investigation of Titanium Dioxide Photocatalysts. *J. Solid State Chem.* **1991,** *92*, 178-190; b) Kho, Y. K.; Iwase, A.; Teoh, W. Y.; Mädler, L.; Kudo, A.; Amal, R., Photocatalytic H2 Evolution over TiO2 Nanoparticles. The Synergistic Effect of Anatase and Rutile. *The Journal of Physical Chemistry C* **2010,** *114*, 2821-2829; c) Li, G.; Richter, C. P.; Milot, R. L.; Cai, L.; Schmuttenmaer, C. A.; Crabtree, R. H.; Brudvig, G. W.; Batista, V. S., Synergistic Effect between Anatase and Rutile TiO_2 Nanoparticles in Dye-Sensitized Solar Cells. *Dalton Trans.* **2009**, 10078-10085; d) Ohtani, B.; Prieto-Mahaney, O. O.; Li, D.; Abe, R., What is Degussa (Evonik) P25? Crystalline Composition Analysis, Reconstruction from Isolated Pure Particles and Photocatalytic Activity Test. *J. Photochem. Photobiol. A* **2010,** *216*, 179-182; e) Nosaka, Y.; Nosaka, A. Y., Reconsideration of Intrinsic Band Alignments within Anatase and Rutile TiO_2. *J. Phys. Chem. Lett.* **2016,** *7*, 431-434.

131. Scanlon, D. O.; Dunnill, C. W.; Buckeridge, J.; Shevlin, S. A.; Logsdail, A. J.; Woodley, S. M.; Catlow, C. R. A.; Powell, M. J.; Palgrave, R. G.; Parkin, I. P.; Watson, G. W.; Keal, T. W.; Sherwood, P.; Walsh, A.; Sokol, A. A., Band alignment of Rutile and Anatase TiO_2. *Nat. Mater.* **2013,** *12*, 798.

132. a) Su, R.; Bechstein, R.; Sø, L.; Vang, R. T.; Sillassen, M.; Esbjörnsson, B.; Palmqvist, A.; Besenbacher, F., How the Anatase-to-Rutile Ratio Influences the Photoreactivity of TiO_2. *J. Phys. Chem. C* **2011,** *115*, 24287-24292; b) Sun, B.; Smirniotis, P. G., Interaction of Anatase and Rutile TiO_2 Particles in Aqueous Photooxidation. *Catal. Today* **2003,** *88*, 49-59.

133. Malekshahi Byranvand, M.; Nemati Kharat, A.; Fatholahi, L.; Malekshahi Beiranvand, Z., A Review on Synthesis of Nano-TiO_2 via Different Methods. *J. Nanostruct.* **2013,** *3*, 1-9.

134. a) Jagadeesh, R. V.; Murugesan, K.; Alshammari, A. S.; Neumann, H.; Pohl, M.-M.; Radnik, J.; Beller, M., MOF-Derived Cobalt Nanoparticles Catalyze a General Synthesis of Amines. *Science* **2017,** *358*, 326–332; b) Tian, T.; Ai, L.; Jiang, J., Metal–Organic Framework-derived Nickel Phosphides as Efficient Electrocatalysts toward Sustainable Hydrogen Generation from Water Splitting. *RSC Adv.* **2015,** *5*, 10290-10295; c) Xiu, Z.; Alfaruqi, M. H.; Gim, J.; Song, J.; Kim, S.; Thi, T. V.; Duong, P. T.; Baboo, J. P.; Mathew, V.; Kim, J., Hierarchical Porous Anatase TiO_2 Derived from a Titanium Metal–Organic Framework as a Superior Anode Material for Lithium Ion Batteries. *Chem. Commun.* **2015,** *51*, 12274-12277.

135. a) Oar-Arteta, L.; Wezendonk, T.; Sun, X.; Kapteijn, F.; Gascon, J., Metal organic frameworks as precursors for the manufacture of advanced catalytic materials. *Materials Chemistry Frontiers* **2017,** *1*, 1709-1745; b) Zhao, S.-N.; Song, X.-Z.; Song, S.-Y.; Zhang, H.-j., Highly Efficient Heterogeneous Catalytic Materials Derived from Metal-Organic Framework Supports/Precursors. *Coord. Chem. Rev.* **2017,** *337*, 80-96.
136. Bhadra, B. N.; Song, J. Y.; Khan, N. A.; Jhung, S. H., TiO_2-Containing Carbon Derived from a Metal–Organic Framework Composite: A Highly Active Catalyst for Oxidative Desulfurization. *ACS Appl. Mater. Interfaces* **2017,** *9*, 31192-31202.
137. a) Khaletskaya, K.; Pougin, A.; Medishetty, R.; Rösler, C.; Wiktor, C.; Strunk, J.; Fischer, R. A., Fabrication of Gold/Titania Photocatalyst for CO_2 Reduction Based on Pyrolytic Conversion of the Metal–Organic Framework NH_2-MIL-125(Ti) Loaded with Gold Nanoparticles. *Chem. Mater.* **2015,** *27*, 7248-7257; b) Yan, B.; Zhang, L.; Tang, Z.; Al-Mamun, M.; Zhao, H.; Su, X., Palladium-Decorated Hierarchical Titania Constructed from the Metal-Organic Frameworks NH_2-MIL-125(Ti) as a Robust Photocatalyst for Hydrogen Evolution. *Appl. Catal., B* **2017,** *218*, 743-750.
138. Hanaor, D. A. H.; Sorrell, C. C., Review of the Anatase to Rutile Phase Transformation. *J. Mater. Sci.* **2011,** *46*, 855-874.
139. Particle Size Effects on Transformation Kinetics and Phase Stability in Nanocrystalline TiO_2. *Am. Mineral.* **1997,** *82*, 717-728.
140. Zhang, Z.; Brown, S.; Goodall, J. B. M.; Weng, X.; Thompson, K.; Gong, K.; Kellici, S.; Clark, R. J. H.; Evans, J. R. G.; Darr, J. A., Direct Continuous Hydrothermal Synthesis of High Surface Area Nanosized Titania. *J. Alloys Compd.* **2009,** *476*, 451-456.
141. Kapilashrami, M.; Zhang, Y.; Liu, Y.-S.; Hagfeldt, A.; Guo, J., Probing the Optical Property and Electronic Structure of TiO_2 Nanomaterials for Renewable Energy Applications. *Chem. Rev.* **2014,** *114*, 9662-9707.
142. Ohno, T.; Sarukawa, K.; Tokieda, K.; Matsumura, M., Morphology of a TiO2 Photocatalyst (Degussa, P-25) Consisting of Anatase and Rutile Crystalline Phases. *J. Catal.* **2001,** *203*, 82-86.
143. Qureshi, M.; Takanabe, K., Insights on Measuring and Reporting Heterogeneous Photocatalysis: Efficiency Definitions and Setup Examples. *Chem. Mater.* **2017,** *29*, 158-167.
144. Emeline, A. V.; Ryabchuk, V. K.; Serpone, N., Dogmas and Misconceptions in Heterogeneous Photocatalysis. Some Enlightened Reflections. *J. Phys. Chem. B* **2005,** *109*, 18515-18521.
145. Kumar, D. P.; Choi, J.; Hong, S.; Reddy, D. A.; Lee, S.; Kim, T. K., Rational Synthesis of Metal–Organic Framework-Derived Noble Metal-Free Nickel Phosphide Nanoparticles as a Highly Efficient Cocatalyst for Photocatalytic Hydrogen Evolution. *ACS Sustain. Chem. Eng.* **2016,** *4*, 7158-7166.
146. a) Hatchard, C.; Parker, C. A., A new sensitive chemical actinometer. II. Potassium ferrioxalate as a standard chemical actinometer. *Proc. R. Soc. London, Ser. A* **1956,** *235*, 518-536; b) Kuhn, H.; Braslavsky, S.; Schmidt, R., Chemical actinometry (IUPAC technical report). *Pure and Applied Chemistry* **2004,** *76*, 2105-2146.
147. Horiuchi, Y.; Toyao, T.; Saito, M.; Mochizuki, K.; Iwata, M.; Higashimura, H.; Anpo, M.; Matsuoka, M., Visible-light-promoted photocatalytic hydrogen production by using an amino-functionalized Ti (IV) metal–organic framework. *J. Phys. Chem. C* **2012,** *116*, 20848-20853.
148. Sun, D.; Liu, W.; Qiu, M.; Zhang, Y.; Li, Z., Introduction of a mediator for enhancing photocatalytic performance via post-synthetic metal exchange in metal–organic frameworks (MOFs). *Chemical Communications* **2015,** *51*, 2056-2059.
149. Toyao, T.; Saito, M.; Horiuchi, Y.; Mochizuki, K.; Iwata, M.; Higashimura, H.; Matsuoka, M., Efficient hydrogen production and photocatalytic reduction of nitrobenzene over a visible-light-responsive metal–organic framework photocatalyst. *Catal. Sci. Technol.* **2013,** *3*, 2092-2097.
150. Shen, L.; Luo, M.; Huang, L.; Feng, P.; Wu, L., A Clean and General Strategy To Decorate a Titanium Metal–Organic Framework with Noble-Metal Nanoparticles for Versatile Photocatalytic Applications. *Inorg. Chem.* **2015,** *54*, 1191-1193.
151. Zhou, T.; Du, Y.; Borgna, A.; Hong, J.; Wang, Y.; Han, J.; Zhang, W.; Xu, R., Post-synthesis modification of a metal–organic framework to construct a bifunctional photocatalyst for hydrogen production. *Energy Environ. Sci.* **2013,** *6*, 3229-3234.
152. Shen, J.-Q.; Zhang, Y.; Zhang, Z.-M.; Li, Y.-G.; Gao, Y.-Q.; Wang, E.-B., Polyoxoniobate-based 3D framework materials with photocatalytic hydrogen evolution activity. *Chemical Communications* **2014,** *50*, 6017-6019.
153. Wang, C.; DeKrafft, K. E.; Lin, W., Pt nanoparticles@ photoactive metal–organic frameworks: efficient hydrogen evolution via synergistic photoexcitation and electron injection. *J. Am. Chem. Soc.* **2012,** *134*, 7211-7214.
154. Gomes Silva, C.; Luz, I.; Llabrés i Xamena, F. X.; Corma, A.; García, H., Water stable Zr–benzenedicarboxylate metal–organic frameworks as photocatalysts for hydrogen generation. *Chemistry-A European Journal* **2010,** *16*, 11133-11138.

155. Dong, X. Y.; Zhang, M.; Pei, R. B.; Wang, Q.; Wei, D. H.; Zang, S. Q.; Fan, Y. T.; Mak, T. C., A Crystalline Copper (II) Coordination Polymer for the Efficient Visible-Light-Driven Generation of Hydrogen. *Angewandte Chemie International Edition* **2016,** *55*, 2073-2077.
156. Sasan, K.; Lin, Q.; Mao, C.; Feng, P., Incorporation of iron hydrogenase active sites into a highly stable metal–organic framework for photocatalytic hydrogen generation. *Chemical Communications* **2014,** *50*, 10390-10393.
157. Pullen, S.; Fei, H.; Orthaber, A.; Cohen, S. M.; Ott, S., Enhanced photochemical hydrogen production by a molecular diiron catalyst incorporated into a metal–organic framework. *J. Am. Chem. Soc.* **2013,** *135*, 16997-17003.
158. Zhang, Z.-M.; Zhang, T.; Wang, C.; Lin, Z.; Long, L.-S.; Lin, W., Photosensitizing metal–organic framework enabling visible-light-driven proton reduction by a Wells–Dawson-type polyoxometalate. *J. Am. Chem. Soc.* **2015,** *137*, 3197-3200.
159. Han, L.; Ju, H.; Xu, Y., Ethanol electro-oxidation: Cyclic voltammetry, electrochemical impedance spectroscopy and galvanostatic oscillation. *International Journal of Hydrogen Energy* **2012,** *37*, 15156-15163.
160. Perdew, J. P.; Burke, K.; Ernzerhof, M., Generalized Gradient Approximation Made Simple [Phys. Rev. Lett. 77, 3865 (1996)]. *Phys. Rev. Lett.* **1997,** *78*, 1396-1396.
161. Grimme, S.; Antony, J.; Ehrlich, S.; Krieg, H., A consistent and accurate ab initio parametrization of density functional dispersion correction (DFT-D) for the 94 elements H-Pu. *J. Chem. Phys.* **2010,** *132*, 154104.
162. Goedecker, S.; Teter, M.; Hutter, J., Separable dual-space Gaussian pseudopotentials. *Phys. Rev. B* **1996,** *54*, 1703-1710.
163. VandeVondele, J.; Hutter, J., Gaussian basis sets for accurate calculations on molecular systems in gas and condensed phases. *J. Chem. Phys.* **2007,** *127*, 114105.
164. Guidon, M.; Hutter, J.; VandeVondele, J., Auxiliary Density Matrix Methods for Hartree−Fock Exchange Calculations. *Journal of Chemical Theory and Computation* **2010,** *6*, 2348-2364.
165. Butler, K. T.; Hendon, C. H.; Walsh, A., Electronic Chemical Potentials of Porous Metal–Organic Frameworks. *J. Am. Chem. Soc.* **2014,** *136*, 2703-2706.
166. Zong, X.; Wu, G.; Yan, H.; Ma, G.; Shi, J.; Wen, F.; Wang, L.; Li, C., Photocatalytic H2 Evolution on MoS2/CdS Catalysts under Visible Light Irradiation. *J. Phys. Chem. C* **2010,** *114*, 1963-1968.
167. Yu, W.; Zhang, D.; Guo, X.; Song, C.; Zhao, Z., Enhanced visible light photocatalytic non-oxygen coupling of amines to imines integrated with hydrogen production over Ni/CdS nanoparticles. *Catal. Sci. Technol.* **2018,** *8*, 5148-5154.
168. Advanced Functional MaterialsMahshid, S.; Askari, M.; Ghamsari, M. S., Synthesis of TiO_2 Nanoparticles by Hydrolysis and Peptization of Titanium Isopropoxide Solution. *J. Mater. Process. Technol.* **2007,** *189*, 296-300.

Curriculum Vitae

Personal information

Full Name	Stavroula Alina Kampouri
Date of Birth	11/11/1992
Nationality	Greece

(+41)786794641 alina_kampouri5@gmail.com ORCID: 0000-0003-3792-1092
Scopus Author ID: 57188752917

Education

Oct. 2016 - today

Ph.D. in Chemistry and Chemical Engineering (EDCH) at École Polytechnique Fédérale de Lausanne (EPFL) Valais, Switzerland.
Thesis: 'Synthesis, development and characterization of light-responsive Metal-Organic Frameworks and their Application in Photocatalysis'.
Strategic design and characterization of Metal-Organic Framework-based systems with enhanced light absorption properties and charge separation efficiencies. Their application involves the photocatalytic hydrogen evolution reaction and dual-functional photocatalysis for Simultaneous organic pollutant degradation and hydrogen evolution.
Laboratory of Molecular Simulation (LSMO),
Supervisors: Prof. B. Smit and Dr. K. Stylianou.

Sep. 2010 - 2015

Diploma in Environmental Engineering at Technical University of Crete (TUC), Greece.
Thesis: 'Catalytic Decomposition of Nitrous Oxide (N_2O) on Ir-based and Metal Phosphide Catalysts' (7 months).
Synthesis and characterization of metal phosphide and Iridium-based catalysts supported on mixed metal-oxides, and their investigation for the catalytic decomposition of nitrous oxide.
Laboratory of Physical and Chemical Processes,
Supervisor: Prof. I.V. Yentekakis.

Employment History

Sept. - Nov. 2015

Internship within the Laboratory of Physical and Chemical Processes, under the supervision of Profs. I. V. Yentekakis and P. Panagiotopoulou at the Technical University of Crete (TUC), in Greece. Project related to the synthesis of different mixed-metal oxides as supports for Iridium catalysts.

May - Jun. 2016

Internship within the Water and Air Quality Laboratory, under the supervision of Prof. A. Stasinakis at the University of the Aegean, in Greece. Project related to the investigation of duckweed Lemna minor as a wastewater treatment system.

Teaching Experience

Spring Semesters 2017 - 2019	**Teaching assistant**, Chemical engineering practical work for 1st and 2nd year bachelor students, *TP: Mass Transfer Phenomena*, EPFL.
Nov. - Dec. 2019	**Supervision** of visiting student Matthew Garvin, from the Heriot-Watt University (United Kingdom). *Project related to the design and characterization of metal-organic framework/semiconductor heterojunctions for photocatalysis*, EPFL.
Jul. - Aug. 2019	**Supervision** of visiting bachelor student Aylin Kinik, from the Istanbul Technical University (Turkey). *Project related to the synthesis of metal-organic framework-derived TiO_2 for photocatalysis*, EPFL.
Nov. 2018 - Jul. 2019	**Supervision** of visiting student Farrokh Mohammadnezhad, from the Razi University (Iran). *Project related to the investigation of the impact of linker doping on the optoelectronic properties and photocatalytic activity of Metal-Organic Frameworks*, EPFL.
Winter Semester 2018	**Teaching Assistant**, Advanced practical work of physics for 3rd year bachelor students, *TP: Internal photoemission - Schottky barrier*, EPFL.
Winter Semester 2018	**Teaching Assistant**, Advanced practical work of physics for 3rd year bachelor students, *TP: Optical Spectroscopy*, EPFL.

Prizes and Awards

- **Chemistry Travel Award**, Platform Chemistry of Swiss Academy of Sciences SCNAT and Swiss Chemical Society (SCS), 2019 (Sion, Switzerland).
- **Best Poster Prize** at 12th Int. Symposium Hydrogen & Energy 2018 (Lausanne, Switzerland).
- **Best Poster Prize** at EuroMOF conference 2017 (Delft, Netherlands).
- Award from **Mathematical Olympiad of Greece** E.M.E. Thales 2007 (Mytilene, Greece).

Personal Skills

Languages:

Greek *ILR Level 5* Native or bilingual proficiency.

English *ILR Level* 5 Native or bilingual proficiency.

French *ILR Level 2* Limited working proficiency
(*Diplôme d'Etudes en langue Françaises, DELF B1).*

Job-related skills:

Software: Excellent competence in Microsoft Office, ChemDraw, Diamond, CCDC software package (e.g., Mercury) Origin.

Instrumentation: Excellent command of Gas Chromatograph, Uv-vis Absorption and Photoluminescence Spectrophotometers, Powder X-ray Diffractometer (**PXRD**) and Scanning Electron Microscopy (**SEM**). Good command of Transient Absorption Spectrometer (**TAS**), Fourier-Transform Infrared (**FTIR**) Spectrometer and Gas Adsorption Analyzer.

Outreach activity: **Scientastic Festival EPFL Valais** (2017-2019). Swiss annual festival to communicate science and technology to young people and the general public. Tasks included presenting my research projects in simple, straightforward terms and organizing the LSMO laboratory space for the event.

Contributions to International Conferences

1. MRS Fall **2019**, Material Research Society Fall Meeting and Exhibit (Boston, U.S.A.).
Oral presentation: 'Concurrent Photocatalytic Hydrogen Generation and Dye Degradation Using MIL-125-NH_2 under Visible Light Irradiation'.

2. AAAFM **2019**, American Association for Advances in Functional Materials (Los Angeles, U.S.A.).
Oral presentation: 'Concurrent Photocatalytic Hydrogen Generation and Dye Degradation Using MIL-125-NH_2 under Visible Light Irradiation'.

3. MOF **2018**, 6th International Conference on Metal-Organic Frameworks and Open Framework Compounds (Auckland, New Zealand).
Poster presentation: 'Concurrent Photocatalytic Hydrogen Generation and Dye Degradation Using MIL-125-NH_2 under Visible Light Irradiation'.

4. NAGC **2018**, 8th North America-Greece-Cyprus Workshop on Paramagnetic Materials (Sparta, Greece).
Oral presentation*:* 'Concurrent Photocatalytic Hydrogen Generation and Dye Degradation Using MIL-125-NH_2 under Visible Light Irradiation'.

5. Latsis symposium: 12th Int. Symposium Hydrogen & Energy **2018** (Lausanne, Switzerland)
Oral and poster presentation*:* 'Photocatalytic Hydrogen Generation from a Visible-Light Responsive Metal-Organic Framework System: The Impact of Nickel Phosphide Nanoparticles'.

6. EuroMOF **2017**, 2nd International Conference on Metal Organic Frameworks and Porous Polymers (Delft, Netherlands).
Poster presentation*:* 'Photocatalytic Hydrogen Generation from a Visible-Light Responsive Metal-Organic Framework System: The Impact of Nickel Phosphide Nanoparticles'.

Published/Submitted Work

1. **Unraveling the Synergy between Metal Organic Frameworks and Co-Catalysts**, S. Falletta, P. Gono, Z. Guo, S. Kampouri, K. C. Stylianou, A. Pasquarello, *Submitted*, **2020**.

2. **Development of a MOF/MOF Heterojunction for Enhanced Photocatalytic Performance**, S. Kampouri, F. M. Ebrahim, M. Fumanal, P. A. Schouwink, C. P. Ireland, B. Smit, K. C. Stylianou, *Submitted*, **2020**.

3. **Taking Lanthanides out of Isolation: Tuning the Optical Properties of Metal–Organic Frameworks**, S. L. Anderson, D. Tiana, C. P. Ireland, G. Capano, M. Fumanal, A. Gładysiak, S. Kampouri, A. Rahmanudin, N. Guijarro, K. Sivula, K. C. Stylianou, B. Smit, *Chemical Science*, **2020**, 11, 4164–4170. https://pubs.rsc.org/en/content/articlepdf/2020/sc/d0sc00740d

4. **A Novel Integrated Cr(VI) Adsorption-Photoreduction System using MOF@Polymer Composite Beads**, B. Valizadeh, T. N. Nguyen, S. Kampouri, D. T. Sun, M. D. Mensi, K. Stylianou, B. Smit, W. L. Queen, *Journal of Materials Chemistry A*, **2020**, 8, 9629–9637.
https://pubs.rsc.org/en/content/articlepdf/2020/ta/d0ta01046d

5. **On the Electronic and Optical Properties of Metal-Organic Frameworks: Case Study of MIL-125 and MIL-125-NH_2**, G. Capano, F. Ambrosio, S. Kampouri, K. C. Stylianou, A. Pasquarello, B. Smit, *The Journal of Physical Chemistry C*, **2020**, 124, 4065–4072. https://pubs.acs.org/doi/abs/10.1021/acs.jpcc.9b09453

6. **Dual-Functional Photocatalysis for Simultaneous Hydrogen Production and Oxidation of Organic Substances**, S. Kampouri, K. C. Stylianou, *ACS Catalysis*, **2019**, 9, 4247–4270. https://pubs.acs.org/doi/10.1021/acscatal.9b00332

7. **Concurrent Photocatalytic Hydrogen Generation and Dye Degradation Using MIL-125-NH_2 under Visible Light Irradiation**, S. Kampouri, T. N. Nguyen, M. Spodaryk, R. G. Palgrave, A. Züttel, B. Smit, K. C. Stylianou, *Advanced Functional Materials*, **2018**, 28, 1806368. https://onlinelibrary.wiley.com/doi/full/10.1002/adfm.201806368

8. **Mixed-phase MOF-derived Titanium Dioxide for Photocatalytic Hydrogen Evolution: The Impact of the Templated Morphology**, S. Kampouri, C. P. Ireland, B. Valizadeh, E. Oveisi, P. A. Schouwink, M. Mensi, K. C. Stylianou, *ACS Applied Energy Materials*, **2018**, 1, 6541–6548. https://pubs.acs.org/doi/abs/10.1021/acsaem.8b01445

9. **Photocatalytic Hydrogen Generation from a Visible-light Responsive Metal-organic Framework: Stability versus Activity of Molybdenum Sulfide Cocatalysts**, T. N. Nguyen, S. Kampouri, B. Valizadeh, W. Luo, D. Ongari, O. M. Planes, A. Zuttel, K. Severin, B. Smit, K. C. Stylianou. *ACS Applied Materials and Interfaces*, **2018**, 10, 30035–30039. https://pubs.acs.org/doi/10.1021/acsami.8b10010

10. **Photocatalytic Hydrogen Generation from a Visible-Light Responsive Metal-Organic Framework System: The Impact of Nickel Phosphide Nanoparticles**, S. Kampouri, T. N. Nguyen, C. P. Ireland, B. Valizadeh, F. M. Ebrahim, G. Capano, D. Ongari, A. Mace, B. Smit, K. C. Stylianou. *Journal of Materials Chemistry A*, **2018**, 6, 2476–2481. https://pubs.rsc.org/en/content/articlelanding/2018/ta/c7ta10225a#!divAbstract

11. **Ir-Catalysed Nitrous oxide (N_2O) Decomposition: Effect of Ir Particle Size and Metal–Support Interactions**, I. V. Yentekakis, G. Goula, S. Kampouri, I. Betsi-Argyropoulou, P. Panagiotopoulou, M. J. Taylor, G. Kyriakou, R. M. Lambert. *Catalysis Letters*, **2018**, 148, 341–347. https://link.springer.com/article/10.1007/s10562-017-2233-z

12. **Stabilization of Catalyst Particles against Sintering on Oxide Supports with High Oxygen Ion Lability Exemplified by Ir-Catalyzed Decomposition of N_2O**, I.V. Yentekakis, G. Goula, P. Panagiotopoulou, S. Kampouri, M. J. Taylor, G. Kyriakou, R. M. Lambert. *Applied Catalysis B: Environmental*, **2016**, 192, 357–364. https://www.sciencedirect.com/science/article/pii/S0926337316302740

13. Book Chapter: **Porous Metal-Organic Frameworks for Advanced Applications**, F. P. Kinik, S. Kampouri, F. M. Ebrahim, B. Valizadeh, K. C. Stylianou. *In press* **2020**.

Patents

K. C. Stylianou, B. Smit, S. Kampouri, C. P. Ireland, T. N. Nguyen, *Noble-Metal-Free Photocatalytic Systems for Hydrogen Evolution Under Visible Light*, N° PCT/IB2018/054997 (filed on July 6, 2018).

Publications Under Preparation

Tuning the Optoelectronic Properties of MIL-125-NH_2 through Ligand Doping for Photocatalytic Hydrogen Evolution, S. Kampouri, F. Mohammadnezhad, G. Capano, M. Feyzi, B. Smit, C. P. Ireland, K. C. Stylianou.